

UNIVERSITY OF ALBERTA

**AXIAL MOLECULAR BEAM TUNABLE DIODE LASER
SPECTROMETER**

BY

HANS D. OSTHOFF



A THESIS SUBMITTED TO THE FACULTY OF GRADUATE STUDIES AND
RESEARCH IN PARTIAL FULFILLMENT OF THE REQUIREMENTS FOR THE
DEGREE OF

DOCTOR OF PHILOSOPHY

DEPARTMENT OF CHEMISTRY

EDMONTON, ALBERTA

SPRING 2004



Library and
Archives Canada

Bibliothèque et
Archives Canada

Published Heritage
Branch

Direction du
Patrimoine de l'édition

395 Wellington Street
Ottawa ON K1A 0N4
Canada

395, rue Wellington
Ottawa ON K1A 0N4
Canada

Your file *Votre référence*

ISBN: 0-612-96312-8

Our file *Notre référence*

ISBN: 0-612-96312-8

The author has granted a non-exclusive license allowing the Library and Archives Canada to reproduce, loan, distribute or sell copies of this thesis in microform, paper or electronic formats.

L'auteur a accordé une licence non exclusive permettant à la Bibliothèque et Archives Canada de reproduire, prêter, distribuer ou vendre des copies de cette thèse sous la forme de microfiche/film, de reproduction sur papier ou sur format électronique.

The author retains ownership of the copyright in this thesis. Neither the thesis nor substantial extracts from it may be printed or otherwise reproduced without the author's permission.

L'auteur conserve la propriété du droit d'auteur qui protège cette thèse. Ni la thèse ni des extraits substantiels de celle-ci ne doivent être imprimés ou autrement reproduits sans son autorisation.

In compliance with the Canadian Privacy Act some supporting forms may have been removed from this thesis.

Conformément à la loi canadienne sur la protection de la vie privée, quelques formulaires secondaires ont été enlevés de cette thèse.

While these forms may be included in the document page count, their removal does not represent any loss of content from the thesis.

Bien que ces formulaires aient inclus dans la pagination, il n'y aura aucun contenu manquant.

Canada

ABSTRACT

A mid-infrared tunable diode laser molecular beam spectrometer for the purpose of trace gas sensing and the study of van der Waals complexes is described. The spectrometer employs a Herriott multipass cell with up to 72 passes. The sample gas is injected parallel to the optical axis through a hole at the center of the far mirror. The molecular absorption transitions are Doppler split, resulting from the laser beam propagating parallel and antiparallel to the molecular beam expansion. The axial expansion leads to narrower line widths and increased sensitivity compared to the traditional vertical injection method as a result of selective sampling of the central part of the molecular expansion with reduced Doppler broadening and longer residence time of the molecular sample in the laser beam. The molecular expansion leads also to selective signal enhancement of low J transitions, as demonstrated for the ν_3 asymmetric stretch vibration of CO_2 and ^{18}OCO . The spectrometer performance was evaluated by recording spectra of the $\text{CO}_2\text{-Ar}$, $(\text{CO}_2)_2$, $\text{CO}_2\text{-He}$, $\text{CO}_2\text{-SO}_2$ and $\text{CO}_2\text{-CH}_4$ van der Waals complexes near the R(0) transition of the ν_3 band of CO_2 around 2349 cm^{-1} . $\text{CO}_2\text{-CH}_4$ was also studied by Fourier transform microwave spectroscopy, and its equilibrium structure was determined to be T-shaped. A microwave horn antenna was implemented into the spectrometer to enable microwave-infrared double resonance experiments on $\text{CO}_2\text{-SO}_2$ and $\text{CO}_2\text{-CH}_4$, which greatly simplified the spectral assignment. In addition, the previously unknown spectra of $^{18}\text{OCO-N}_2$, $^{18}\text{OCO-Ne}$, and $^{18}\text{OCO-He}$ were recorded and analyzed. Digital filtering techniques, including the Wiener and Kalman filters, were implemented and evaluated. The feasibility of using a pulsed molecular expansion for trace gas sensing is explored.

ACKNOWLEDGMENTS

Many individuals have helped make this thesis a reality. First, I would like to thank my supervisor, Dr. Wolfgang Jäger for his support, guidance, and patience during all phases of my Ph. D. project. I am also thankful to the many individuals who have worked directly on the construction of the spectrometer. This project was in part a collaboration with Johnathon Walls and William van Wijngaarden of York University. I would like to thank Johnathon in particular, because he spent several months in Edmonton and assisted me in the early phases of this project. I would also like to thank Roman Lipiecki, Hubert Hoffman, and Dieter Starke at the department's machine shop, Ed Feschuk, Kim Do, and Al Chilton at the electronics shop, and Larry Coulson of the IT group, for constructing several parts of the spectrometer and offering plenty of advice.

After the construction of the spectrometer, the focus of this project shifted to the interpretation of the acquired spectra. During this phase, I received a lot of support from all members of the Jäger group, especially from Yunjie Xu, Yaqian Liu, Jennifer van Wijngaarden, and Kai Brendel of the Universität Kiel.

Foremost, I have to thank my family and friends for their continuing love and support, without which I could not have imagined finishing this degree: My parents, my sister Sabine, Christie, Rob and Lesley, Apollo, Blacky, and Babsie, and all other family members and friends, whether in Edmonton or elsewhere in the world.

TABLE OF CONTENTS

Chapter 1: An introduction to mid-infrared tunable diode laser gas spectroscopy

1.1 Motivation

1.1.1 Air pollution and climate	1
1.1.2 Gas sensing	2
1.1.3 Signal enhancement in a molecular beam	3
1.1.4 Objectives	6

1.2 Fundamentals of ro-vibrational spectroscopy

1.2.1 Beer-Lambert law	7
1.2.2 Line shapes	
1.2.2.1 Absorption	8
1.2.2.2 Laser Emission	10
1.2.3 Labeling of energy levels	12
1.2.4 Transitions and Selection rules	14

1.3 Laser spectroscopic techniques in the mid-infrared

1.3.1 Sources of infrared light	15
1.3.2 Optical path length enhancements	17
1.3.3 Detection of infrared light.....	18
1.3.4 Noise sources in TDLAS	18

1.4 Carbon dioxide

1.4.1 Relevance	20
1.4.2 Spectroscopy of CO ₂	24

1.5 Weakly bound complexes	26
1.5.1 Weakly bound complexes of CO ₂	27
1.6 Thesis Outline	28
 Chapter 2: Spectrometer design and operation	
2.1 Introduction	30
2.2 General description	31
2.3 Optics	
2.3.1 General	35
2.3.2 Optical multipass cell	36
2.4 Sampling	
2.4.1 Static gas cells	40
2.4.2 Free jet expansions	42
2.5 Laser modulation and detection schemes	
2.5.1 General	44
2.5.2 Direct absorption: fast-scan technique	44
2.5.2.1 Frequency locking mechanism	45
2.5.3 Frequency modulation method	46
2.5.4 Measurement of molecular expansion spectra	47
2.5.5 Microwave-infrared double resonance experiments	52
2.5.6 Frequency calibration	52

Chapter 3: Spectrometer performance

3.1 Introduction	55
3.2 Experiments using static cells	
3.2.1 Evaluation of diode laser characteristics	56
3.2.2 Performance of modulation and detection schemes	
3.2.2.1 Sample H ₂ S spectrum	61
3.2.2.2 Performance of fast-scan technique	64
3.3 Experiments with molecular beams	
3.3.1 Signal enhancement and selectivity	66
3.3.2 Pulse reproducibility	68
3.3.3 Axial vs. perpendicular expansion	67
3.3.4 Line shape model	71
3.3.5 Beam evolution, speed and lifetime	76
3.3.6 Line intensities in the molecular beam	80
3.3.7 Spectra of van der Waals complexes	85
3.4 Summary	91

Chapter 4: The mid-infrared spectrum of CO₂-SO₂

4.1 Introduction	92
4.2 Molecular Symmetry (MS) group analysis	
4.2.1 Choice of MS group	93
4.2.2 Nuclear spin statistics	98
4.2.3 Classification of the vibrational wavefunctions	99

4.2.4 Classification of the rotational wavefunctions	100
4.2.5 Energy levels and selection rules	100
4.3 Experimental	103
4.4 Results	
4.4.1 Spectral analysis and assignment	104
4.4.2 <i>ab initio</i> Calculations	117
4.5 Discussion	
4.5.1 Structural Analysis	121
4.5.2 Unassigned lines	127
4.6 Summary	128
Chapter 5: Microwave, infrared and microwave-infrared double resonance spectra of the weakly bound complex CO₂-CH₄	
5.1 Introduction	129
5.2 <i>ab initio</i> Theoretical predictions	131
5.3 Symmetry considerations	135
5.4 Results	
5.4.1 Infrared spectrum	144
5.4.2 Microwave spectrum	145
5.4.3 Microwave-infrared double resonance spectra	147
5.4.4 Analysis of the infrared spectrum and spectral fit	155
5.4.5 Structural parameters and moment of inertia defects	165
5.5 Discussion	170

5.6 Summary and future work	177
-----------------------------------	-----

Chapter 6: Mid-infrared spectra of the weakly bound complexes $^{18}\text{OCO-Ne}$, $^{18}\text{OCO-N}_2$ and $^{18}\text{OCO-He}$

6.1 Introduction	178
6.2 Experimental	179
6.3 Results and Discussion	
6.3.1 $\text{N}_2\text{-}^{18}\text{OCO}$	180
6.3.2 $\text{Ne-}^{18}\text{OCO}$	185
6.3.3 $\text{He-}^{18}\text{OCO}$	190
6.3.4 Derivation of molecular structures	195
6.3.5 Internal motions	199
6.4 Summary	200

Chapter 7: Post-data acquisition digital filtering

7.1 Introduction	201
7.2 Description of algorithms	
7.2.1 Boxcar integration	202
7.2.2 Low- and high-pass filter	202
7.2.3 Wiener filter	202
7.2.4 Low-pass Wiener filter	203
7.2.5 Kalman filter	204
7.3 Filter performance in rapid sweep mode	206

7.3.1 Boxcar integration	211
7.3.2 Low-pass filter	211
7.3.3 Wiener filter	212
7.3.4 Low-pass Wiener filter	212
7.3.5 Kalman filter	212
7.4 Conclusions	214
Chapter 8: Gas sensing with a free jet expansion IR spectrometer	
8.1 Introduction	215
8.2 Experimental	
8.2.1 General	216
8.2.2 Laser modulation and detection	218
8.2.2.1 Response function of the 2f-detection scheme	220
8.2.3 Laser stabilization	221
8.2.4 Post-data acquisition digital filtering	225
8.3 Quantitative measurements	
8.3.1 Calibration and typical signals	227
8.3.2 Limit of detection (LOD)	234
8.3.3 Concentration monitoring	236
8.4 Discussion	
8.4.1 TDL stability	236
8.4.2 Gas sampling with a molecular beam	241
8.5 Summary and future work	244

Chapter 9: General conclusions and future work	245
Bibliography	248
Appendix A. Supplementary data	261
Appendix B. Maple input files	277
Appendix C. Screen shot of the data acquisition software	278
Appendix D. Photograph of the laboratory	279

LIST OF TABLES

Table 1.1	Isotopomers of carbon dioxide	21
Table 1.2	Normal modes of carbon dioxide	25
Table 1.3	Molecular parameters of CO ₂ and ¹⁸ OCO	25
Table 2.1	Mirror positions resulting in narrow interference fringes in a Herriott cell	41
Table 2.2	4 th order polynomial parameters relating frequency and position in computer memory	54
Table 3.1	H ₂ S transitions observed in Fig. 3.4	63
Table 3.2	Comparison of measured frequencies of selected CO ₂ , (CO ₂) ₂ and He-CO ₂ transitions to literature values	88
Table 3.3	Summary of observed line widths of selected CO ₂ , (CO ₂) ₂ and He-CO ₂ transitions	89
Table 4.1	Previously observed microwave transitions of CO ₂ -SO ₂	95
Table 4.2	The molecular symmetry group G ₄ (M)	93
Table 4.3	Symmetries of the ro-vibrational wavefunctions of CO ₂ -SO ₂	101
Table 4.4	Observed and assigned infrared transition frequencies of the CO ₂ -SO ₂ van der Waals complex	112-113
Table 4.5	Unassigned transitions in the expansion spectra of the CO ₂ -SO ₂ van der Waals complex	114
Table 4.6	Spectral parameters of CO ₂ -SO ₂	115
Table 4.7	Calculation of structural parameters of CO ₂ -SO ₂	124

Table 4.8	Revised calculation of structural parameters	125
Table 4.9	Comparison of asymmetric stretching band origins of CO ₂ complexes ..	126
Table 5.1	Molecular symmetry group used for CO ₂ -CH ₄	136
Table 5.2	The T(M), and T _d (M) molecular symmetry groups of CH ₄	137
Table 5.3	Nuclear spin statistics of CH ₄	137
Table 5.4	Symmetries and spin statistical weights of ro-vibrational energy levels of CO ₂ -CH ₄	142-143
Table 5.5	Observed microwave transitions of the CO ₂ -CH ₄ complex	146
Table 5.6	Observed microwave-infrared double resonance transitions of CO ₂ -CH ₄ in the A and F nuclear spin states	153
Table 5.7	Observed microwave-infrared double resonance transitions of CO ₂ -CH ₄ in the E nuclear spin state	154
Table 5.8	Assigned infrared transitions of CO ₂ -CH ₄ in the A and F nuclear spin states	160
Table 5.9	Observed infrared transitions of CO ₂ -CH ₄ in the E state nuclear spin state	161
Table 5.10	Molecular constants derived from a fit of a Watson's A-reduction Hamiltonian to the assigned FTMW transitions	162
Table 5.11	Molecular constants derived from a fit of Watson's A-reduction Hamiltonian to the assigned FTMW and IR transitions	163
Table 5.12	Experimental moments of inertia and inertial defects of CO ₂ -CH ₄ (uncorrected)	166

Table 5.13	Experimental moments of inertia and inertial defects of CO ₂ -CH ₄ (revised)	167
Table 5.14a	Effective structural parameters of the CO ₂ -CH ₄ weakly bound complex calculated by a least-squares error fit to the observed moments of inertia	168
Table 5.14b	Effective structural parameters of the CO ₂ -CH ₄ weakly bound complex calculated using Howard's method for Rg-CO ₂ complexes	168
Table 5.15	Comparison of asymmetric stretching frequencies of CO ₂ and several of its T-shaped weakly bound complexes	169
Table 6.1	Observed infrared transitions of the N ₂ - ¹⁸ OCO complex	181-182
Table 6.2	Spectroscopic constants of N ₂ - ¹⁸ OCO and N ₂ -CO ₂	183
Table 6.3	Assigned infrared transitions of the Ne- ¹⁸ OCO complex	186
Table 6.4	Assigned microwave transitions of the Ne- ¹⁸ OCO complex	187
Table 6.5	Spectroscopic constants of Ne- ¹⁸ OCO and selected Ne-CO ₂ isotopomers	188
Table 6.6	Assigned mid-infrared transitions of the He- ¹⁸ OCO complex	192
Table 6.7	Spectroscopic constants of He- ¹⁸ OCO and He-CO ₂	193
Table 6.8	Comparison of structural constants calculated using Howard's equations	196
Table 6.9	Location of O atom in the complexes derived from Kraitchman equations	196
Table 6.10	Comparison of inertial defects	198
Table 7.1	Comparison of digital filter performance	210

Table 8.1	Signal intensity of the CO ₂ R(0) line	229
Table 8.2	Signal intensity of the ¹⁸ OCO R(1) line	231
Table 8.3	Kalman filtered signal intensity of the ¹⁸ OCO R(1) data	232
Table 8.4	Detection limits for the R(1) transition of ¹⁸ OCO in standard air	235
Table A3.1	Coding of CO ₂ vibrational levels in Hitran	261
Table A3.2	Assigned transitions of a continuous mode of the diode F-2462-GMP	262
Table A3.3	Assigned transitions of a continuous mode of the diode IR-2333	264
Table A4.1	Single point calculations on the potential energy surface of CO ₂ -SO ₂ ...	267
Table A4.2	Single point calculations on the potential energy surface of CO ₂ -SO ₂ ...	268
Table A4.3	Calculations to estimate internal rotation barrier height of CO ₂ -SO ₂	269
Table A5.1	Intermolecular <i>ab initio</i> interaction energy (Surface A) of CO ₂ -CH ₄ ...	270
Table A5.2	Intermolecular <i>ab initio</i> interaction energy (Surface B) of CO ₂ -CH ₄	272
Table A5.3	Intermolecular <i>ab initio</i> interaction energy (Surface C) of CO ₂ -CH ₄	273
Table A5.4	Intermolecular <i>ab initio</i> interaction energy (Surface D) of CO ₂ -CH ₄ ...	275

LIST OF FIGURES

Fig. 1.1	Population of rotational energy levels of CO ₂ as a function of temperature5	5
Fig. 1.2	Global carbon cycle22	22
Fig. 1.3	Correlation of ¹⁸ OCO with seasonal biological activity23	23
Fig. 2.1	Schematic diagram of the spectrometer34	34
Fig. 2.2	Example of a Herriott multipass cell37	37
Fig. 2.3	Circular spot patterns on the spherical mirrors of a Herriott cell38	38
Fig. 2.4	Sketch of the Herriott multipass cell in the vacuum chamber43	43
Fig. 2.5	Timing sequence for single resonance experiments50	50
Fig. 2.6	Timing sequence for double resonance experiments51	51
Fig. 2.7	Typical frequency calibration curve53	53
Fig. 3.1	Example of mode hop and multimode lasing57	57
Fig. 3.2	Rapid sweep spectrum of CO ₂ in a 10 cm long reference cell near 2350 cm ⁻¹59	59
Fig. 3.3	Rapid sweep spectrum of CO ₂ in a 10 cm long reference cell near 2333 cm ⁻¹60	60
Fig. 3.4	Spectra of ~1 torr H ₂ S in a 2 m absorption path62	62
Fig. 3.5	Demonstration of selective signal enhancement67	67
Fig. 3.6	The R(0) transition of CO ₂ in air at ambient pressure observed with the nozzle in the axial position and in the perpendicular position70	70
Fig. 3.7	Definition of the coordinate system for the axial line shape model72	72

Fig. 3.8	Comparison of the calculated Doppler line shape with the observed line shape of the R(1) transition of ^{18}OCO75
Fig. 3.9	Time evolution of a pulse of ambient air characterized by fast scan and lock-in amplification methods79
Fig. 3.10	Molecular expansion spectrum of the Ar-CO ₂ van der Waals complex near 2349 cm ⁻¹82
Fig. 3.11	Intensity of the CO ₂ R(0) transition as a function of backing pressure ...83
Fig. 3.12	Intensities of selected (CO ₂) ₂ lines as a function of backing pressure84
Fig. 3.13	A portion of the Ar-CO ₂ spectrum near 2349 cm ⁻¹87
Fig. 3.14	Spectrum of He _N CO ₂ showing the R(0) transitions of N=1..490
Fig. 4.1	Proposed equilibrium structure of the CO ₂ -SO ₂ van der Waals complex94
Fig. 4.2	Feasible symmetry operations of CO ₂ -SO ₂97
Fig. 4.3	Energy level diagram and representative transitions of CO ₂ -SO ₂102
Fig. 4.4a-c	Mid-infrared expansion spectrum of the CO ₂ -SO ₂ van der Waals complex107-109
Fig. 4.5	The ^R R ₀ branch of CO ₂ -SO ₂ observed by MW-IR double resonance ...110
Fig. 4.6	The ^R Q ₀ branch of CO ₂ -SO ₂ , observed by single resonance IR and MW-IR double resonance111
Fig. 4.7	Comparison between experimental and model stick spectra of CO ₂ -SO ₂116
Fig. 4.8	Cuts through the potential energy surface of CO ₂ -SO ₂ as a function of intermolecular separation119

Fig. 4.9	Cuts through the intermolecular potential energy surface of CO ₂ -SO ₂ along the internal rotation coordinate τ_{tor}	120
Fig. 5.1	Definition of structural parameters of the CO ₂ -CH ₄ complex	132
Fig. 5.2	Input structures for the <i>ab initio</i> calculations	133
Fig. 5.3	Cut B through the potential energy surface of CO ₂ -CH ₄	134
Fig. 5.4	The effects of the MS group operations on CO ₂ -CH ₄	139
Fig. 5.5	High resolution MW-IR double resonance experiment on CO ₂ -CH ₄	149
Fig. 5.6	MW-IR double resonance experiments on CO ₂ -CH ₄ in the A state	150
Fig. 5.7	MW-IR double resonance experiments on CO ₂ -CH ₄ in the F state	151
Fig. 5.8	MW-IR double resonance experiments on CO ₂ -CH ₄ in the E state	152
Fig. 5.9a-c	Mid-infrared expansion spectrum of the CO ₂ -CH ₄ van der Waals complex	157-159
Fig. 5.10	Stick spectrum comparison between experimental and simulated spectrum of CO ₂ -CH ₄	164
Fig. 5.11	Energy level diagram of Ar-SiH ₄	172
Fig. 5.12	Moments of inertia defects as a function of internal rotational level <i>j</i>	174
Fig. 6.1	Portion of the mid-infrared spectrum of N ₂ - ¹⁸ OCO	184
Fig. 6.2	Portion of the mid-infrared spectrum of Ne- ¹⁸ OCO lines	189
Fig. 6.3	Portion of the mid-infrared spectrum of He- ¹⁸ OCO lines	194
Fig. 7.1	Effect of digital filtering on a sample rapid-sweep spectrum: Boxcar averaging and low-pass filtering	207

Fig. 7.2	Effect of digital filtering on a sample rapid-sweep spectrum: Wiener and low-pass Wiener filters	208
Fig. 7.3	Effect of Kalman digital filtering on a sample rapid-sweep spectrum ...	209
Fig. 8.1	Sketch of the spectrometer modified for gas measurements	217
Fig. 8.2	The modulation of the laser in terms of laser output frequency ν and time domain	219
Fig. 8.3	Theoretical detector response and the 1f- and 2f-demodulation reference signals	222
Fig. 8.4	Actual and simulated spectra using 2f-demodulation detection	223
Fig. 8.5	Diagram of feedback circuit	226
Fig. 8.6	Representative response curves of the spectrometer operated in frequency – 2f-demodulation mode, averaged over 100 molecular pulses	228
Fig. 8.7	Instrument response to a series of gas standards	230
Fig. 8.8	Calibration curves	233
Fig. 8.9	Concentration measurements during a 3.5 hr period	237
Fig. 8.10	Concentration measurements during a 3.5 hr period, corrected for laser power fluctuations	238
Fig. 8.11	Allan plot of the 2f-demodulated signal of the reference cell during a 3.5 hour measurement	240
Fig. A5.1	Cut A through the potential energy surface of CO ₂ -CH ₄	271
Fig. A5.2	Cut C through the potential energy surface of CO ₂ -CH ₄	274
Fig. A5.3	Cut D through the potential energy surface of CO ₂ -CH ₄	276

LIST OF ABBREVIATIONS

Abbreviation	Full name
a.u.	arbitrary units
CNPI	Complete nuclear permutation inversion
CRD	Cavity ring-down
CEAS	Cavity enhanced absorption spectroscopy
cw	continuous wave
DFG	Difference frequency generation
e.s.	Excited state
FM	Frequency modulation
FSR	Free spectral range
FTIR	Fourier transform infrared
FTMW	Fourier transform microwave
FWHM	Full width at half maximum
g.s.	Ground state
ICOS	Integrated cavity output spectroscopy
IR	Infrared
LOD	Limit of detection
MCT	Mercury Cadmium Telluride
MI	Matrix isolation
MS	Molecular symmetry
MW	Microwave
MW-IR	Microwave-infrared
o-c	observed - calculated
PES	Potential energy surface
ppm	parts-per-million per volume ($\mu\text{mol/mol}$)
QC	Quantum cascade
RAM	Residual amplitude modulation
Rg	Rare gas, noble gas
rms	Root-mean-square
RSD	Relative standard deviation
S/N	Signal-to-noise ratio
TDL	Tunable diode laser
TDLAS	Tunable diode laser absorption spectroscopy
UV/Vis	Ultraviolet and visible
VCSEL	Vertical-cavity-surface emitting laser
WM	Wavelength modulation

LIST OF SYMBOLS

Symbol	Meaning
α	angle of CO ₂ wrt center-of-mass of the binding partner
Γ (Γ_{ns})	character (of nuclear spin wavefunction)
δ	isotope abundance ratio
δv_b	Gaussian distribution beam speed
Δ	inertial defect
$\Delta\Delta$	change in inertial defect
Δ_A	Fabry-Pérot cavity (laser) line width
$\Delta(\alpha - \beta)$	Difference between two quantities α and β
Δm	change of mass due to isotopic substitution
Δr	cartesian displacement coordinate
Δs	path length difference
$\Delta\xi$	phase difference upon reflection
Δv	Doppler split
Δv_D	full-width-at-half-maximum of a Doppler line shape
Δv_L	full-width-at-half-maximum of a Lorentzian line shape
Δv_V	full-width-at-half-maximum of a Voigt line shape
ϵ_0	vacuum permittivity
ϕ_i	recursive Kalman parameter
ϕ_H	defined in Figure 5.1
ξ	phase
η	refractive index
λ	wavelength
μ	reduced mass
μ_{fi}	transition dipole moment
ν	frequency
ν_0	line center frequency
$\nu(0)$	intercept of polynomial function relating frequency and acquisition channel
ρ	gas density
Θ	505376 MHz / amu Å ²
θ_b	angular distribution of molecular beam
θ_H	defined in Figure 5.1
θ_m	angle between consecutive mirror reflections in a Herriott cell
σ	absorption cross section
σ_b	molecular beam angular spread
σ_D	Doppler line width
σ_{bl}	standard deviation of a blank run

LIST OF SYMBOLS (CONT'D)

Symbol	Meaning
σ_{obs}	observed standard deviation
σ_{avg}	standard deviation of the mean
σ_{rms}	standard deviation of the fit
σ_{shot}	standard deviation of single-pulse data
$\langle \sigma_A^2 \rangle$	Allan variance
τ	integration time constant
τ_{tor}	torsional coordinate
Ψ_{tot} (Ψ_{tor} , Ψ_{rot} , Ψ_{vib} , Ψ_{elec} , Ψ_{nucl})	total (torsional, rotational, vibrational, electronic, nuclear) wavefunction
ω	noise superimposed on the "true" signal
A	rotational constant (around a -axis)
A_{foo}	averaged signal in bin foo
b	pressure broadening coefficient
bar	number of bins of size foo
B	rotational constant (around b -axis)
c	speed of light
c_{white} , $c_{1/f}$, c_{drift}	coefficients for white, 1/f and drift noise
C	rotational constant (around c -axis)
$\text{cor}(t)$, $\text{COR}(f)$	corrupted signal in time and frequency domain
d_{m}	mirror separation in Herriott multipass cell
d_{TDL}	length of a tunable diode laser
E''	ground state energy
E_J , E_V	rotational (vibrational) energy
f	frequency
foo	bin index
$f(v_x)$	velocity distribution function
$f(s, \text{os})$	error function for frequency lock
FSR	free spectral range
g	line shape function
h	Planck's constant
$H(f)$	Wiener response function
i	index variable
I_A , I_B , I_C	moments of inertia in the principal axis system
I_{xx} , I_{yy} , I_{zz}	moments of inertia in the molecular axis system
I_0	incident (laser) intensity
I_H	proton nuclear spin
I_T	transmitted intensity
$I(v)$	intensity

LIST OF SYMBOLS (CONT'D)

Symbol	Meaning
$I(\nu_0)$	intensity at line center frequency
j	internal rotation quantum number
J	rotational quantum number
J_{\max}	highest bound rotational state
\hat{J}	angular momentum operator
k	Boltzmann's constant
$K_a (K_c)$	K quantum number for prolate (oblate) rotor
L	optical absorption path length
m	mass
m_i	i^{th} order polynomial expansion coefficient
M	total mass of the parent molecule
M_m	number of complete orbits in a Herriott cell
n	number of molecular pulses or measurements
$n(\nu_z)$	number of molecules traveling with velocity component ν_z
n_{obs}	number of observations
N	number density of molecules
N	number of He atoms in a complex
N_i, N_f	number density of the initial (final) state
N_J, N_V	number density of molecules in a rotational (vibrational) level
$\text{noi}(t), \text{NOI}(f)$	noise in time and frequency domain
N_m	Number of complete laser passes in a Herriott cell
os	DC offset
P	pressure
P'	Kalman variance
$q_{\text{rot}}, q_{\text{vib}}$	rotational (vibrational) partition function
Q'	signal variance
R'	noise variance
R	(power) reflectivity
R_{std}	isotopic ratio of a traceable standard
R_m	radius of curvature
R_{sample}	isotopic ratio of a sample
r_{cm}	intermolecular center-of-mass separation
$r_{\text{cm}}(\text{H})$	r_{cm} calculated using Howard's equations
$r_{\text{cm}}(\text{K})$	r_{cm} calculated using Kraitchman's equations
r_{H}	radius of Herriott spot pattern
$r(z)^{\text{para}}, r(z)^{\text{dia}}$	distance of parallel (diagonal) laser beam from optical axis
$r_0 (r_{\text{CO}}, r_{\text{SO}}, r_{\text{CH}})$	effective bond length (atoms indicated)
r_e	equilibrium bond length
s	frequency shift

LIST OF SYMBOLS (CONT'D)

Symbol	Meaning
$\text{sig}(t)$, $\text{SIG}(f)$	"true" signal in time and frequency domain
$\text{SIG}'(f)$	best estimate of "true" signal in frequency domain
$\text{sig}'(t)$	best estimate of "true" signal in time domain
$\text{sig}_e(t)$	best estimate of the next signal measured
S_m	number of visible spots on the mirrors of a Herriott cell
t	time
T	temperature
T_{ax} , T_{perp}	axial (perpendicular) translational temperature
T_{rot} , T_{vib}	rotational (vibrational) temperature
u	average velocity (parallel to the optical axis)
v	vibrational quantum number
v_b	beam speed
v_0	average beam speed
v_{max}	highest bound vibrational state
v_{eff}	velocity component projected onto the laser beam
v_x , v_y	velocity components perpendicular to the optical axis
v_z	velocity component parallel to the optical axis
V (V_{avg})	integrated signal (averaged)
V_{bl}	blank signal
w_0	beam waist of collimated beam
x	cartesian coordinate
x_n	array in computer memory containing data from the n^{th} molecular pulse
x_{ref}	array in computer memory containing data the reference spectrum
y	cartesian coordinate
z	cartesian coordinate
Z_R	Rayleigh range

CHAPTER 1

AN INTRODUCTION TO MID-INFRARED TUNABLE DIODE LASER GAS SPECTROSCOPY

1.1 Motivation

1.1.1 Air pollution and climate change

One of the first reports on the impact of air pollution on human health was made by J. Evelyn of London, England, in 1661.¹ At the time, the citizens of London suffered from the effects of using high-sulfur coal as their primary heating source:²

*"It is this horrid Smoake which obscures our Church and makes our palaces look old, which fouls our Cloth and corrupts the Waters, so as the very Rain, and refreshing Dews which fall in the several Seasons, precipitate to impure vapour, which, with its black and tenacious quality, spots and contaminates whatever is exposed to it . . . the constant and unremitting Poison is communicated by the foul Air, which, as the Town still grows larger, has made regular and steady advances in its fatal influence."*³

It would take more than a hundred years after Evelyn's observations before nitrogen, initially called "noxious" or "phlogisticated" air, was identified as the major component of the atmosphere in 1772. Soon after, J. Priestley and others discovered a whole host of major chemical components of the atmosphere, including oxygen, carbon dioxide, sulfur dioxide, nitric oxide and ammonia.¹

In the late 19th and early 20th century, attention turned to so-called trace gases,

which are present in concentrations up to the parts-per-million (ppm) level. In spite of their low concentrations, many of these trace constituents are now known to cause a whole range of phenomena, including photochemical smog, acid rain, and climate change.⁴ There is also strong evidence that the composition of the atmosphere is gradually changing.⁴ Associated with climate change in particular are the greenhouse gases CO₂, CH₄ and N₂O.⁴ The changing atmosphere and especially the discovery of the Antarctic ozone hole⁵ have led to the signing of international treaties like the Montreal protocol,⁶ the Rio declaration⁷ and the Kyoto protocol.⁸

1.1.2 Gas sensing

Much of our current understanding of atmospheric chemistry depends on accurate data on the geographical and temporal distribution of trace gases. Historically, atmospheric trace gas concentrations were measured using wet chemical techniques.² Wet chemical techniques suffer from many deficiencies, including lack of sensitivity and nonspecificity. Today, spectroscopic techniques such as Fourier transform infrared (FTIR), tunable diode laser absorption (TDLAS), matrix isolation (MI), or UV/Vis absorption spectroscopy are most commonly used for measuring pollutants, trace gases and particles in air.² We now know that the atmosphere contains a multitude of trace species, some at concentrations as low as the parts-per-trillion (ppt) level.⁴ These low concentrations continue to drive the development of ever more sensitive instrumentation for the detection and quantification of these compounds. In addition to field measurements, studies and method development in the laboratory also play critical roles in elucidating the fundamental processes in the atmosphere.

1.1.3 Signal enhancement in a molecular beam

Molecular beam spectroscopy is a very common and sensitive instrumental technique and has been the subject of entire books⁹ and book chapters.¹⁰ Even though numerous molecular beam instruments are employed in many laboratories for the study of weak interactions in the gas phase, their great sensitivity and specificity are only now starting to be exploited for atmospheric gas sensing.¹¹

Molecular expansions are typically used to generate cold environments by population redistribution into lower translational, rotational and vibrational energy levels. However, the concept of a "beam temperature" is strictly speaking incorrect. Due to the absence of collisions in the later stages of the molecular expansion, thermal equilibrium within the beam is not reached. Population distributions corresponding to different effective translational, rotational and vibrational temperatures are created and preserved in the jet because the collisional cross-sections are different for the three cooling processes. For example, particularly narrow velocity distributions are achieved in parallel to the direction of the gas flow. If the molecular velocities v_z are distributed normally around an average velocity u , the axial translational temperature T_{ax} can be derived from

$$n(v_z) \propto e^{\frac{-m(v_z-u)^2}{2kT_{ax}}} \quad (1.1)$$

$n(v_z)$ is the number of molecules traveling at velocity v_z , m is the molecular mass, and k is Boltzmann's constant. The translational temperature associated with the velocity distribution along the beam axis T_{ax} is usually less than 1 K. The translational temperature T_{perp} associated with the distribution of velocities v_x and v_y perpendicular to

the flow direction is typically higher.¹⁰

The molecular expansion also compresses the populations of the rotational and vibrational energy levels. At equilibrium, the population distribution is described by the Boltzmann equation. The rotational temperature T_{rot} can be obtained from the relative populations N_J of the rotational energy levels:¹²

$$\frac{N_J}{N} = \frac{(2J+1)e^{\frac{-E_J}{kT_{\text{rot}}}}}{q_{\text{rot}}} \quad (1.2)$$

N is the number of molecules in the accessible states, E_J is the energy of a particular level with rotational quantum number J , and q_{rot} is the rotational partition function:¹²

$$q_{\text{rot}} = \sum_J^{J_{\text{max}}} (2J+1)e^{\frac{-E_J}{kT_{\text{rot}}}} \quad (1.3)$$

The corresponding equations for vibrational energy levels are:¹²

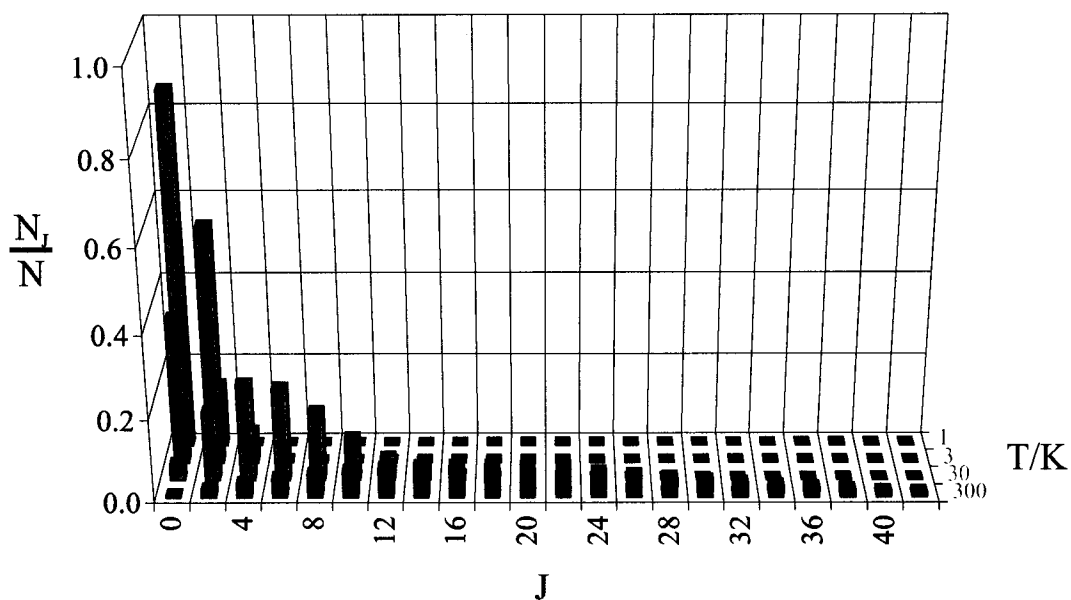
$$\frac{N_v}{N} = \frac{e^{\frac{-E_v}{kT_{\text{vib}}}}}{q_{\text{vib}}} \quad (1.4)$$

$$q_{\text{vib}} = \sum_v^{v_{\text{max}}} e^{\frac{-E_v}{kT_{\text{vib}}}} \quad (1.5)$$

In the above equations, J_{max} and v_{max} are the highest bound rotational and vibrational energy states, respectively. In a molecular beam, T_{rot} is typically between 1 K and 5 K, and the vibrational temperature T_{vib} is between 50 K and 100 K.

Figure 1.1

Population of rotational energy levels of CO₂ at the rotational temperatures $T_{\text{rot}} = 300, 30, 3,$ and 1 K. The ground state population of the $J=0$ level increases several orders of magnitude under conditions found in molecular beams (i.e. $T_{\text{rot}} = 1$ K).



In Fig. 1.1, the relative populations of rotational levels of CO₂ are plotted as a function of rotational temperature. In this example, the population of the lowest energy level increases by several orders of magnitude under conditions typical of a free jet expansion environment ($T_{\text{rot}} \approx 1$ K). The redistribution into the lowest ro-vibrational states causes the selective signal enhancement in a molecular beam.

1.1.4 Objectives

In spite of the high sensitivity of molecular beam spectroscopy, molecular beams are currently underutilized in field applications such as gas sensing.¹¹ One of the objectives of this thesis was therefore to determine if a molecular beam can be used as a tool for selective signal enhancement in a mid-infrared trace gas sensor. For this purpose, a mid-infrared molecular beam tunable lead salt diode laser absorption spectrometer was assembled. Regions containing low J transitions of an inert test molecule (CO₂) were identified. Optimized sample introduction, laser modulation and detection, calibration, and post-data acquisition digital filtering schemes were implemented and evaluated.

To evaluate the instrument sensitivity, calibration curves were constructed. In addition, the suitability of the spectrometer to record molecular expansion spectra of weakly bound gas phase clusters in the mid-infrared was explored. The instrument was used to record mid-infrared spectra of several weakly bound complexes in the gas phase containing the CO₂ subunit. The study of weak interactions in the gas phase is an important area of research, because insight into the structure and internal dynamics of weakly bound clusters can be obtained from the observed spectra.¹³⁻²¹

1.2 Fundamentals of ro-vibrational spectroscopy

Spectroscopic techniques, in particular in the infrared, have been extensively used for trace gas sensing. The main advantages of IR spectroscopy are a high level of selectivity, sensitivity, accuracy, precision and speed, which enables time and space resolved gas measurements. In the following paragraphs, the fundamental concepts of infrared spectroscopy are briefly summarized and important equations are defined.

1.2.1 Beer-Lambert law

The transmission intensity I_T of a gas is given by the Beer-Lambert law:²²

$$I_T = I_0 e^{-\sigma(N_i - N_f)L} \quad (1.6)$$

I_0 is the initial intensity of the probing light, L is the optical absorption path length, N_i and N_f are the number densities of molecules in the lower and upper state, and the absorption cross section σ is given by:²²

$$\sigma = \frac{2\pi^2\mu_{fi}^2}{3\epsilon_0hc} \nu_0 g \quad (1.7)$$

ϵ_0 is the permittivity of vacuum ($8.854187 \cdot 10^{-12} \text{ C}^2\text{N}^{-1}\text{m}^{-2}$), μ_{fi} is the transition dipole moment, ν_0 is the absorption frequency, h is Planck's constant, c is the speed of light and g is the line shape function.²² An understanding of the line shape function is important to extract quantitative information from the observed signal.

1.2.2 Line shapes

1.2.2.1 Absorption

The velocity distribution of gas molecules $f(v_z)$ in a reduced-pressure (<10 torr) static gas cell closely resembles the Maxwell-Boltzmann²³ distribution of an ideal mono-atomic gas:

$$f(v_z) = \left(\frac{m}{2\pi kT} \right)^{\frac{1}{2}} e^{-\frac{mv_z^2}{2kT}} \quad (1.8)$$

In the above equation, T is the gas temperature, and v_z is the velocity along the absorption path. Because of the Doppler effect, the molecules in the static gas cell absorb at a range of absorption frequencies ν , which can be derived from the Doppler equation:

$$\nu = \nu_0 (1 + v_z/c) \quad (1.9)$$

where ν_0 is the line center frequency. The width σ_D of the resulting Gaussian line shape function is given by:²⁴

$$\sigma_D = \nu_0 \sqrt{\frac{kT}{mc^2}} \quad (1.10)$$

and the overall line shape function is a Gaussian equation of the form:¹⁰

$$I(\nu) = I(\nu_0) e^{-\frac{(\nu - \nu_0)^2}{2\sigma_D^2}} \quad (1.11)$$

The full-width-at-half-maximum (FWHM) of a Doppler-broadened line $\Delta\nu_D$ is given by:¹⁰

$$\Delta\nu_D = (8 \ln 2)^{1/2} \sigma_D \approx 7.16 \cdot 10^{-7} (T/m)^{1/2} \nu_0 \text{ [Hz]} \quad (1.12)$$

If the pressure in the sample cell exceeds 100 torr, collisional broadening becomes dominant. Lines broadened by collisions have a Lorentzian profile,¹⁰ which normalized to the peak intensity at peak center takes the form:

$$I(\nu) = I(\nu_0) \frac{\Delta\nu_L^2}{(\nu - \nu_0)^2 + \left(\frac{\Delta\nu_L}{2}\right)^2} \quad (1.13)$$

with full-width-at-half-maximum (FWHM) $\Delta\nu_L$. An empirical equation for $\Delta\nu_L$ is given by Sigrist:²⁵

$$\Delta\nu_L = 2 b P \quad (1.14)$$

P is the gas pressure and b is a pressure broadening coefficient. For pressures between 10 and 100 torr, the line shape and width are described by a convolution of Doppler (Gaussian function) and pressure broadening (Lorentzian function). This

pressure range is known as the Voigt regime. Under these conditions, the FWHM Δv_V can be calculated from:²⁵

$$\Delta v_V^2 \approx \Delta v_D^2 + \Delta v_L^2 \quad (1.15)$$

Atmospheric absorption experiments in the IR are usually carried out in the Voigt regime. Under certain conditions, the observed absorption line shapes may also be affected by lifetime or transit broadening, and second order effects such as Dicke narrowing.¹⁰

1.2.2.2 Laser emission

The observed absorption lines may be broadened as a result of the finite laser line width. Many mid-infrared lasers, including lead salt diodes, are Fabry-Pérot devices.²⁵ In this case, the emitted laser line shape is given by the Airy function:¹⁰

$$I_T = I_0 \frac{1}{1 + \frac{4R}{(1-R)^2} \sin^2\left(\frac{\xi}{2}\right)} \quad (1.16)$$

R is the internal reflectivity of the diode faces at either end, and ξ is the phase difference between successively reflected waves within the resonator:

$$\xi = 2\pi \Delta s / \lambda + \Delta\xi \quad (1.17)$$

λ is the wavelength of the radiation, Δs is the optical path difference between successively reflected waves within the resonator, and $\Delta\xi$ accounts for the possible phase change upon reflection.

Because tunable lead salt diode lasers are used in this spectrometer, it is worthwhile at this point to focus on the emission of TDLs in more detail. Typical lead salt diodes are $d_{\text{TDL}} = 400 \mu\text{m}$ long.²⁵ Assuming the refractive index η is ~ 6 , $\Delta s = 2\eta d_{\text{TDL}}$ is $\sim 4.8 \text{ mm}$.²⁴ The free spectral range (FSR) of a lead salt diode, i.e. the spacing between longitudinal modes is approximately:

$$\text{FSR} = c/2\eta d_{\text{TDL}} \approx 6.2 \cdot 10^{10} \text{ Hz} \approx 2 \text{ cm}^{-1} \quad (1.18)$$

The FWHM (in frequency units) of the laser output is given by:¹⁰

$$\Delta_A = \text{FSR} (1-R) R^{-1/2} / \pi \quad (1.19)$$

The manufacturer specifies the average laser line width Δ_A as $\sim 20 \text{ MHz}$ ($\sim 0.00066 \text{ cm}^{-1}$) at 2350 cm^{-1} .²⁶ From equation 1.19 it follows that the reflectivity of the diode faces R is $>99.8\%$. It has been shown²⁷ that the observed line width of tunable lead salt diodes is actually a temporal average of many narrow, short-lived emission modes, so that the actual reflectivity of the diode facets is higher. At 20 MHz , the laser line width of a lead salt diode is significantly less than a Doppler-broadened absorption line at room temperature.

1.2.3 Labeling of energy levels

The rigid rotor rotational energy levels are determined from Schrödinger's equation using the rigid asymmetric rotor Hamiltonian and the rotational angular momentum operator \hat{J} in the principal axis system:²²

$$\hat{H}_r = \frac{\hat{J}_a^2}{2I_A} + \frac{\hat{J}_b^2}{2I_B} + \frac{\hat{J}_c^2}{2I_C} \quad (1.20)$$

Structural information is contained in the principal moments of inertia, which are related to the spectroscopic constants A , B and C by:²⁸

$$A = 505376 \text{ (MHz/amu}\mathring{\text{A}}^2) / I_A \quad (1.21a)$$

$$B = 505376 \text{ (MHz/amu}\mathring{\text{A}}^2) / I_B \quad (1.21b)$$

$$C = 505376 \text{ (MHz/amu}\mathring{\text{A}}^2) / I_C \quad (1.21c)$$

It is useful to distinguish between near-prolate ($I_A > I_B \approx I_C$) and near-oblate ($I_A \approx I_B < I_C$) rotors. In a near-prolate system, a so-called right-handed type Γ coordinate system is chosen, where $abc = zxy$. The moments of inertia are defined (in the molecular frame) as

$$I_{xx} = \sum m_i (y_i^2 + z_i^2) \quad (1.22a)$$

$$I_{yy} = \sum m_i (x_i^2 + z_i^2) \quad (1.22b)$$

$$I_{zz} = \sum m_i (x_i^2 + y_i^2) \quad (1.22c)$$

An analytical solution for Schrödinger's equation with the Hamiltonian in equation 1.20 does not exist. The solutions to the asymmetric top Hamiltonian can be approximated using a symmetric top basis set, and the asymmetric rotor energy levels are correlated between prolate ($I_B = I_C$) and oblate ($I_A = I_B$) energy levels. The energy levels of the prolate and oblate symmetric tops are given by:²¹

$$E_p \approx (A-B) K_a^2 + BJ(J+1) \quad (1.23a)$$

$$E_o \approx (C-B) K_c^2 + BJ(J+1) \quad (1.23b)$$

K_a and K_c are defined as the projections of the total rotational angular momentum onto the a - and c -axis, respectively.²¹ Additional terms, which are referred to as distortion constants, are added to the above expressions because of non-rigidity of real systems.²²

The energies of the vibrational energy levels may be derived (in first approximation) from the harmonic oscillator Schrödinger equation. Because nuclear motions are assumed to be separable into rotations and vibrations, the total energies are then obtained by simple addition. The combined energy levels of an asymmetric rotor are labeled $J_{K_a K_c}'$ or $J_{K_a K_c}''$. The prime and double prime refer to the vibrational upper and lower state, respectively.

1.2.4 Transitions and selection rules

It is convenient to identify "normal" modes of vibration. Normal coordinates are chosen so that they are linear functions of Cartesian displacement coordinates. All normal vibrations that are connected with a *change of dipole moment* are infrared active.

In the harmonic oscillator approximation, only the fundamental transitions (i.e. the normal modes) appear in the infrared spectra. Much weaker overtone and combination bands arise due to the anharmonicity of the intermolecular potential.²⁹ In gas sensing applications, the transitions of normal vibrational modes should therefore be chosen, if possible.

The vibration-rotation transitions of asymmetric tops are classified as *a*-type, *b*-type or *c*-type, depending on the orientation of the transition dipole moment relative to the principal axes. The selection rules are as follows:²²

$$a\text{-type: } \Delta K_a = 0, \Delta K_c = \pm 1, \Delta J = 0, \pm 1 \quad (1.24a)$$

$$b\text{-type: } \Delta K_a = \pm 1, \Delta K_c = \pm 1, \Delta J = 0, \pm 1 \quad (1.24b)$$

$$c\text{-type: } \Delta K_a = \pm 1, \Delta K_c = 0, \Delta J = 0, \pm 1 \quad (1.24c)$$

It is common practice to label ro-vibrational transitions of asymmetric tops using ΔJ ($P = -1, Q = 0, R = +1$, etc.) as the main letter with ΔK_a as a preceding superscript and K_a as a following subscript, followed by J in brackets. For example, the $2_{20} \leftarrow 3_{12}$ transition is labeled as ${}^R P_1(3)$.

1.3 Laser spectroscopic techniques in the mid-infrared

1.3.1 Sources of infrared light

Traditional broad-band emission sources, such as the Nernst glower or the globar, are still being used in FTIR spectrometers.³⁰ In many mid-infrared absorption spectrometers, narrow-band lasers serve as the sources of infrared light. In the 10 μm region, the CO_2 laser, which was developed at Bell laboratories in 1964,^{31,32} has been popular both as a welding tool and for gas sensing applications. Tunable lead telluride diode lasers (TDLs) were invented nearly concurrently with the CO_2 laser.^{33,34} The band gaps in $\text{Pb}_2\text{Sn}_{1-z}\text{Te}$ or $\text{Pb}_x\text{Eu}_{1-x}\text{Se}_{1-y}\text{Te}_y$ vary for different values of x , y and z , giving coverage between 3 and 50 μm .³⁵⁻³⁷ The near-infrared between 0.6 and 4.0 μm is covered by gallium arsenide lasers.³⁸ Various laser fabrication schemes have been developed, resulting in different laser performances. At first, crystals were synthesized using the diffusion growth technique, a process that is difficult to make reproducible. Improved performance was achieved after the advent of molecular beam epitaxy techniques, which are now the methods of choice.²⁵ The laser designs include homo junction lasers made from a single semiconductor compound, double heterostructures, buried heterostructures, vertical-cavity surface-emitting lasers (VCSEL),³⁹ and quantum well lasers.³⁵ Recently, quantum cascade (QC) lasers⁴⁰ and difference frequency generation (DFG) lasers⁴¹⁻⁴⁴ have been proposed as viable alternatives to lead salt diodes.

Tunable diode laser absorption spectroscopy (TDLAS) has now established itself as one of the leading techniques for trace gas sensing, and several reviews have appeared in the literature on the subject.^{35-37,45-47} In the last decade, diode laser

spectroscopy benefitted immensely from the popularity of laser printers, CD and DVD players and recorders, and the boom in the telecommunication industry, which provided affordable mass-produced diodes in the near-infrared and accessories like fiber-optic couplers etc. However, in the mid-infrared, the only options are still lead salt diodes or quantum cascade lasers. Diodes and quantum cascade lasers alike are pumped by electric currents up to several Amperes, and ohmic heating remains a problem. Often, liquid nitrogen or helium cooling and/or pulsed operation are therefore required. Cooling systems tend to be expensive, cumbersome, heavy, and power-consuming, which are all undesirable in typical field applications.²⁵ Quantum cascade lasers operating continuously (cw) at room temperatures will no doubt be the way of the future, if technical problems like long-term stability can be overcome.

Lead salt diode lasers are overall a good choice as a mid-infrared laser source. The manufacturing process has matured enough so that well-characterized diodes are commercially available, even though diode prices have been rising steadily since the market recently became a quasi-monopoly owned by Laser Components. Stable current sources with built-in modulation schemes, dewars, and collimating optics are commercially available, which make lead salt diode systems easy to implement. The emission line widths of the diodes are very narrow ($\sim 10^{-5} \text{ cm}^{-1}$) when operated in cw mode, so that spectral resolution on the order of $1:10^8$ are routine. The high laser resolution gives TDL spectroscopy an extremely high selectivity. Such narrow emission line widths can only be achieved with great difficulty in QC lasers.⁴⁸ The tuning range of diodes can be as large as 200 cm^{-1} , but is patchy as a result of mode hops. Often, a single lead salt diode can be used in the simultaneous measurement of several atmospheric

components. Single mode emission can often only be achieved near threshold conditions, so that the output powers are typically in the low μW range. With a good diode though, the output power can be rough-selected by setting the operating temperature. One of the chief advantages of the lead salt diodes is the very fast response times to the applied current up to the GHz region. This allows a variety of different modulation and detection schemes to be used, including amplitude modulation, frequency modulation,⁴⁹ sweep integration,⁵⁰ and heterodyne techniques.⁵¹⁻⁵³ At present, TDLs are still the preferred sources of laser light in routine measurements, but QC lasers show promise due to their higher output power, room temperature operation, and greater accessible spectroscopic range down to the THz region.^{54,55}

1.3.2 Optical path length enhancements

It is self-evident from the Beer-Lambert law (equation 1.6) that the sensitivity of a spectrometer depends on the sampled optical path length. Various schemes exist by which the optical path length can be increased. In direct absorption measurements, optical multipass cells such as the Herriott⁵⁶⁻⁵⁸ cell, the White^{59,60} cell and astigmatic designs^{61,62} have been popular. A relatively recent but promising technique is cavity ring-down (CRD) spectroscopy.⁶³ In CRD spectroscopy, the ring-down time of a resonant cavity is shortened by the presence of an optical absorber. Equivalent optical path lengths in excess of several km have been achieved by CRD. Variations of the CRD technique include cavity leak-out spectroscopy,^{64,65} cavity enhanced absorption spectroscopy (CEAS),⁶⁶⁻⁶⁸ and integrated cavity output spectroscopy (ICOS).^{69,70} Finally,

photoacoustics, a technique originally discovered by Alexander Graham Bell in the 19th century, is re-emerging in part because of the advent of high-power infrared lasers such as the quantum cascade laser.⁷¹ In this technique, the absorbed energy of a modulated laser beam produces heat, generating acoustic waves, which are picked up by a sensitive microphone.^{72,73}

1.3.3 Detection of infrared light

Most commonly used materials for photodetectors in the mid-infrared are indium antimonide (InSb) below 5 μm and mercury cadmium telluride (MCT, $\text{Hg}_{1-x}\text{Cd}_x\text{Te}$), which can be used between 2 and 24 μm . MCT detectors are particularly useful because of their fast frequency response (>1.5 GHz). Detectors can be operated in either photovoltaic or photoconductive mode. In a photoconductive detector, an external reverse bias voltage is applied, and the internal resistance is measured as a function of incident photon flux. In photovoltaic devices, the photovoltage or photocurrent is measured directly using a high impedance preamplifier.²⁵ The response time of a photodetector is larger in photoconductive mode, but the dark noise level is lower when the diode is operated in photovoltaic mode.

1.3.4 Noise sources in TDLAS

The term noise refers to the sum of all unwanted signals obtained at the output of a detection system. In TDLAS, the dominant noise sources are detector noise, laser excess noise resulting from fluctuations in laser power and frequency, and interference

fringes arising from reflecting or scattering parallel surfaces, which form Fabry-Pérot cavities.²⁵

Detector noise arises from frequency independent thermal or Johnson noise, detector 1/f noise (<1 kHz), and on rare occasions, shot noise. Thermal noise decreases with $T^{1/2}$, and is significantly reduced by cooling the detector with liquid nitrogen. Since all three detector noise sources depend linearly on the bandwidth, detector noise can be reduced by band pass filtering or signal integration.²⁵ In addition to noise created directly at the detection element, noise may be picked up at the leads, at the pre-amplifier stage, and at digitization.

Laser excess noise is due to intrinsic output power fluctuations or caused externally by injection current noise, optical feedback and temperature instability. Intrinsic laser noise can be caused by mode competition, photon and carrier density or refractive index fluctuations. In high-frequency applications, residual amplitude modulation (RAM), which arises from the simultaneous modulation of frequency and output power, and phase instabilities⁴⁹ often become the limiting source of noise.²⁵

1.4 Carbon dioxide

1.4.1 Relevance

Carbon dioxide is known as the earth's dominant greenhouse gas, because of its abundance and strong infrared absorption bands. The annual average tropospheric concentration of CO₂ has risen from 280 ppm in the pre-1750 era to 372 ppm in the year 2001.⁷⁴ Most of the sources and sinks of CO₂ are natural (Fig 1.2), but human activity is believed to disturb this equilibrium. The continuing rise of ambient CO₂ concentrations in the last 200 years has become a cause of grave concern, and international treaties have been signed to limit the production of CO₂.⁸ There is even one web site whose sole purpose is to report on the current status of CO₂ (<http://cdiac.esd.ornl.gov/home.html>).

Some of the more recent research has focused on the isotopomers of CO₂. The abundances of naturally occurring isotopomers of CO₂ are summarized in Table 1.1. ¹³CO₂ has been used as a tracer for the burning of (lighter) fossil fuel⁷⁵ and ¹⁸OCO has been used as a trace molecule for biological activity.⁷⁶ The abundance of an isotope is defined on a "per mil" scale and can be written as:⁷⁵

$$\delta(\text{‰}) = 1000 \frac{R_{\text{sample}} - R_{\text{std}}}{R_{\text{std}}} \quad (1.25)$$

R_{std} is the isotopic ratio of a standard traceable to a marine limestone, Pee Dee Belemnite.⁷⁵ Important isotopic ratios of CO₂ are $\delta^{13}\text{C}$, $\delta^{14}\text{C}$ and $\delta^{18}\text{O}$. Fig. 1.3 shows sample data on the annual fluctuations of these isotopic ratios.

Table 1.1

Isotopomers of carbon dioxide.

Number	Isotope	Natural Abundance ⁷⁷
1	$^{12}\text{C}^{16}\text{O}_2$	0.9840
2	$^{13}\text{C}^{16}\text{O}_2$	0.01106
3	$^{12}\text{C}^{16}\text{O}^{18}\text{O}$	0.0039471
4	$^{12}\text{C}^{16}\text{O}^{17}\text{O}$	0.000734
5	$^{13}\text{C}^{16}\text{O}^{18}\text{O}$	0.00004434
6	$^{13}\text{C}^{16}\text{O}^{17}\text{O}$	0.00000825
7	$^{12}\text{C}^{18}\text{O}_2$	0.0000039573
8	$^{12}\text{C}^{17}\text{O}^{18}\text{O}$	0.00000147

Figure 1.2

Global carbon cycle. Units are Gt for reservoirs, and Gt/yr for fluxes. The acronym DOC means "dissolved organic carbon". Source: Seinfeld and Pandis.⁴

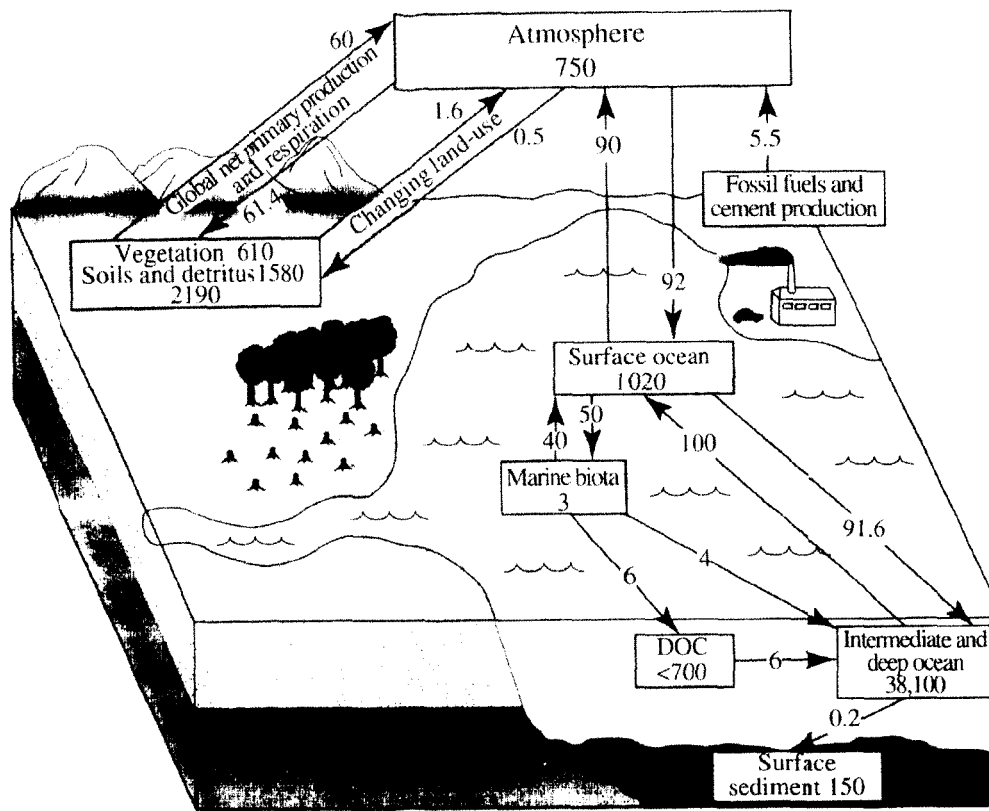
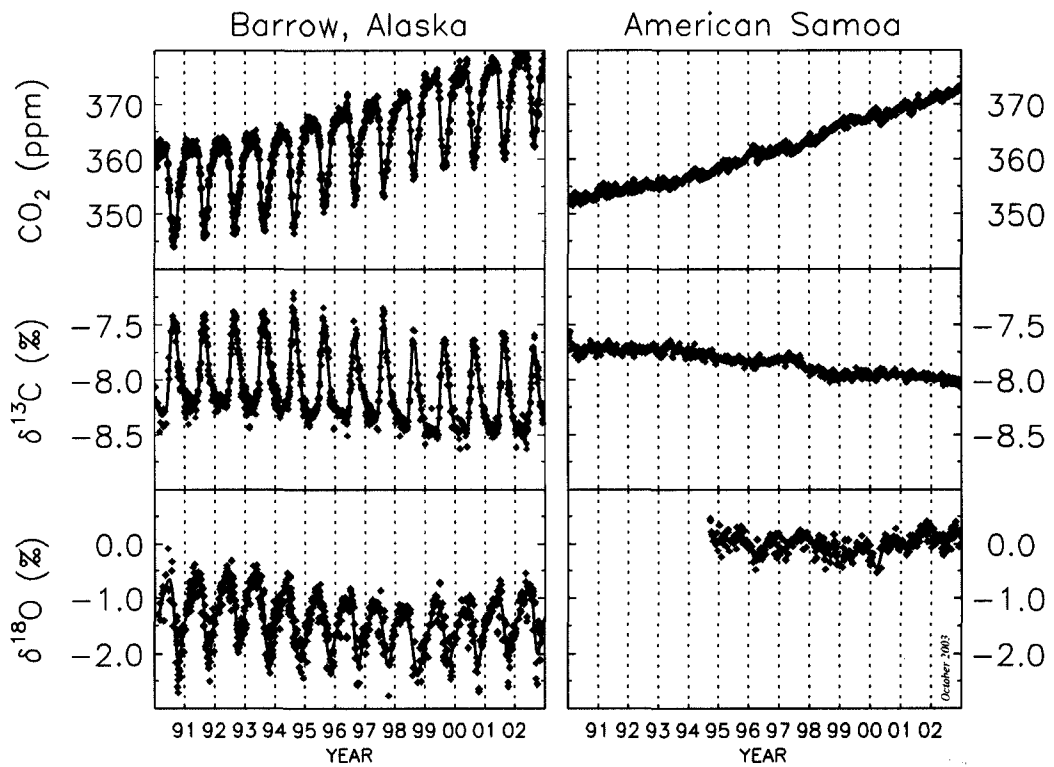


Figure 1.3

Correlation of ^{18}O CO with seasonal biological activity. Source: "Climate Monitoring & Diagnostics Laboratory", NOAA (<http://www.cmdl.noaa.gov/>)



Time series showing the relationships between atmospheric carbon dioxide (upper panel), carbon-13 (middle panel) and oxygen-18 (lower panel) isotopic composition in the marine boundary layer. The measurements were made at NOAA CMDL and the University of Colorado INSTAAR using samples provided by the NOAA CMDL cooperative air sampling network. Data are shown for Barrow and Samoa, revealing the greater seasonal variations at high northern latitudes driven by the terrestrial biosphere. The isotope data are expressed as deviations of the carbon-13/carbon-12 ratio in carbon dioxide from the VPDB-CO₂ standard, in per mil (parts per thousand). Contact: Dr. Jim White, CU-INSTAAR, Boulder, Colorado, (303) 492-5494. James.white@colorado.edu.

In this thesis, particular emphasis is placed on carbon dioxide because of its high natural abundance, non-toxicity, strong mid-infrared absorption bands, importance as a greenhouse gas, ready availability in the form of commercial CO₂ gas standards, and because of good diode frequency coverage of several low J ro-vibrational transitions of CO₂.

1.4.2 Spectroscopy of CO₂

Carbon dioxide has been extensively studied by spectroscopic means. As a linear triatomic (N=3) molecule, it possesses $3N-5 = 4$ normal modes. Two of the bending modes are degenerate. The three fundamental bands (Table 1.2) are located at $\nu_1=1340\text{ cm}^{-1}$ (symmetric stretch, Raman active), $\nu_2=667.3\text{ cm}^{-1}$ (bend, IR active perpendicular band), and $\nu_3=2349\text{ cm}^{-1}$ (asymmetric stretch, IR active parallel band). The Raman band is split into two "lines" at 1285.5 and 1388.3 due to a Fermi resonance with $2\nu_2$. In addition to the three fundamentals, many overtone and combination bands have been identified.²⁹ In the main isotopomer of CO₂, the two ¹⁶O nuclei are equivalent. Bose-Einstein statistics requires the total wavefunction to be symmetric with respect to an exchange of the two equivalent spin 0 bosons. As a result, rotational energy levels with odd (even) J in the vibrational ground (upper) state are not populated. Entire branches are therefore absent in the ro-vibrational spectrum of CO₂. This rule does not apply to unsymmetrically substituted isotopomers like ¹⁸OCO.

Table 1.2

Normal modes of carbon dioxide.²⁹

	Ground state	ν_1	ν_2	ν_3
Band origin /cm ⁻¹	-	1388.3	667.3	2349.3
B /cm ⁻¹	0.38950	0.38971	0.38995	0.38660
Symmetry	Σ_g^+	Σ_g^+	Π_u	Σ_u^+

Table 1.3

Molecular parameters of CO₂ and ¹⁸OCO.⁷⁸

	¹² C ¹⁶ O ₂ g.s.	¹² C ¹⁶ O ₂ ν_3	¹² C ¹⁶ O ¹⁸ O g.s.	¹² C ¹⁶ O ¹⁸ O ν_3
ν_0 /cm ⁻¹	-	2349.14326	-	2332.1127
B /MHz	11698.47	11606.207	11037.89	10950.4
r_{CO} /Å	1.162	1.166	1.163	1.165

1.5 Weakly bound complexes

Weakly bound complexes of neutral molecules in the gas phase are commonly referred to as van der Waals complexes, after Johannes Diderik van der Waals, who was awarded the Nobel Prize for physics in 1910 "for his work on the equation of state for gases and liquids".²⁴ Van der Waals complexes are usually generated and stabilized in molecular beams, but also occur naturally. For example, the weakly bound water dimer was recently observed in the atmosphere.⁷⁹

Weakly bound complexes are usually investigated by high-resolution spectroscopy complemented by high level quantum chemical calculations. In van der Waals compounds, the energy levels and therefore the locations of the molecular transitions are extremely sensitive to the shallow intermolecular potentials. Often, the intermolecular interaction can be fine-tuned by isotopic and atomic substitutions. Van der Waals complexes have therefore emerged as ideal probes of intermolecular interaction potentials and dynamics, with tremendous implications for macroscopic phenomena such as chemical reactions, protein folding and superfluidity.^{14,20} In the last 15 years alone, three special issues of *Chemical Reviews* were dedicated to the subject of weakly bound clusters.⁸⁰⁻⁸² Weakly bound clusters, especially those of the major atmospheric constituents like H₂O, N₂, O₂ and CO₂, are now believed to play an important role in atmospheric extinction, nucleation, particle growth, and as precursors in important atmospheric chemical reactions, in particular at the reduced pressures and low temperatures found in the stratosphere.^{79,83,84} The complexes studied in this thesis in particular (CO₂-SO₂ and CO₂-CH₄) may be of importance as intermediates in the early stages of smog formation and as contributing factors in the Earth's radiation balance.⁴

In the mid-infrared, most experiments on weakly bound complexes are performed using tunable diode laser absorption spectroscopy with pulsed molecular beams. The absorption frequency of an infrared active mode of one of the cluster constituents is only slightly perturbed by complex formation, and the *B* rotational constants are often small because of the typically large intermolecular separations. Thus, infrared spectra of complexes usually fall within a few wavenumbers of the band origin of the respective monomer vibration. Because of the occurrence of many closely spaced lines within the tuning range of the diode laser and because only a small percentage of monomer will form gas adducts in a molecular beam, van der Waals complexes are ideal test molecules to evaluate the performance of an infrared molecular beam spectrometer in terms of sensitivity, diode laser tunability, and beam temperature.

1.5.1 Weakly bound complexes of CO₂

Weakly bound complexes that contain the CO₂ subunit have been the subject of numerous spectroscopic studies in the last 15 years. In the mid-infrared, most experiments were performed in the region near the ν_3 asymmetric stretch of the CO₂ monomer. Howard and coworkers investigated (CO₂)₂⁸⁵ in this manner, as well as CO₂ complexes with the rare gases Ne through Xe,⁸⁶ N₂,⁸⁷ and CO.⁸⁸ The CO₂-CO complex has also been investigated in the CO fundamental stretching region.⁸⁹ The Beaudet group reported ro-vibrational spectra of CO₂-Ar,^{90,91} CO₂-HCl,⁹² CO₂-HBr,⁹² CO₂-N₂O,⁹³ CO₂-Br₂⁹⁴ and CO₂-CS₂.⁹⁵ Miller and coworkers investigated several CO₂ containing systems, including CO₂-H₂O,⁹⁶ CO₂-C₂H₄,⁹⁷ CO₂-HCl,⁹⁸ and CO₂-HCN,⁹⁹ while making

use of vibrational frequencies of the non-CO₂ subunits. The group led by Nesbitt studied the trimer species (CO₂)₃^{100,101} and Ar₂-CO₂¹⁰² as well as CO₂-He,¹⁰³ which exhibits very large amplitude internal motions. There has been even one report¹⁰⁴ of an infrared study of the non-symmetrically substituted complexes ¹⁸OCO-Ar and C¹⁸O₂-Ar.

Weakly bound CO₂ containing dimers were found to have a number of different equilibrium structures. Most dimers are T-shaped, but linear (e.g. CO₂-HF,⁹² CO₂-Br₂⁹⁴), slipped parallel (e.g. CO₂-CO₂,⁸⁵ CO₂-N₂O⁹³), and X-shaped structures (CO₂-CS₂⁹⁵ and CO₂-SO₂¹⁰⁵) have also been found. Crossed geometries were rationalized in terms of the interaction of the negative quadrupole moment of CO₂ with either the quadrupole moment (CS₂) or dipole moment (SO₂) of the binding partner. In rare cases, multiple structural isomers were found for the same complex (e.g. CO₂-HCN).^{99,106}

1.6 Thesis outline

In this thesis, a new mid-infrared molecular beam tunable diode laser spectrometer for the purpose of gas sensing and the study of weak interactions in the gas phase is described. In Chapter 2, the setup and operation of the spectrometer are described in detail. The optimized spectrometer design is similar to the instruments used by Howard,⁸⁵⁻⁸⁸ Miller,⁹⁶⁻⁹⁹ Nesbitt,¹⁰⁰⁻¹⁰³ Beaudet,⁹⁰⁻⁹⁵ and McKellar¹⁰⁷⁻¹¹² for the study of weakly bound complexes in the gas phase. The spectrometer's adaptability towards recording spectra of weakly bound complexes is evaluated in Chapter 3, using several known weakly bound complexes of CO₂. The spectrometer performance was so encouraging that the previously unknown mid-infrared spectra of CO₂-SO₂ (Chapter 4), CO₂-CH₄ (Chapter 5) and various ¹⁸OCO complexes, including N₂-¹⁸OCO, Ne-¹⁸OCO and

He-¹⁸OCO (Chapter 6) were also recorded and analyzed. These studies were supplemented by high level *ab initio* calculations, Fourier transform microwave (FTMW) spectroscopy¹¹³ and microwave-infrared double resonance spectroscopy.

To further enhance the instrument sensitivity, several post-data acquisition digital filtering tools (Chapter 7) were implemented and evaluated. The conversion of the spectrometer into a pure trace gas sensing instrument is described in detail in Chapter 8. The spectrometer's suitability for trace gas sensing at the part-per-million level is demonstrated by monitoring ¹⁸OCO in natural abundance. Chapter 9 concludes the thesis with a short summary of the major findings and potential future work.

CHAPTER 2

SPECTROMETER DESIGN AND OPERATION*

* Condensed versions of this Chapter have been published in *Proceedings of SPIE 2002*, 4817, 249 and in *Review of Scientific Instruments 2004*, 75, 46.

2.1 Introduction

Many mid-infrared tunable diode laser (TDL) spectrometers have been built in the last two decades for laboratory and field applications. TDL spectrometers are frequently employed to measure high resolution ro-vibrational spectra of weakly bound complexes in molecular beams.^{50,114-116} Sensitivity enhancement is achieved from redistributing the molecules into the lowest ro-vibrational energy levels during the molecular expansion. Typically, lead salt diode lasers that operate continuously at cryogenic temperatures are the radiation source in these instruments. Multipass cells of Herriott,⁵⁶⁻⁵⁸ White,^{59,60} Perry,¹¹⁷ or astigmatic designs^{61,62} increase the absorption path length and lead to significant sensitivity enhancement. Various modulation schemes, including the fast scanning technique,⁵⁰ have been introduced to further increase the instrument sensitivity.

Mid-infrared tunable diode laser spectrometers are also used in atmospheric trace gas sensing applications.^{37,45} In this case, the sample gas is often continuously pumped through a multipass cell under reduced pressure or, in the case of aircraft mounted instruments, sampled *in situ* in the low-pressure environment at high altitude.

Sampling at reduced pressure has been shown²⁵ to result in greater instrument selectivity and sensitivity due to narrower line widths and reduced overlap with atmospheric water and carbon dioxide transitions. Even greater selectivity and sensitivity enhancement for low J transitions can be expected from sampling with a molecular beam, which was recently demonstrated in the microwave region by Suenram *et al.*¹¹

In this Chapter, a new state-of-the-art laboratory molecular beam mid-infrared tunable diode laser spectrometer is described. This instrument is the first molecular beam TDL spectrometer designed for the purpose of trace gas sensing. One of the goals of this work was to improve upon existing spectrometers in terms of instrument sensitivity by using a molecular beam. To achieve this goal, the designs of current molecular beam spectrometers were studied, and the most sensitive components and setups were chosen. In our approach, the optical absorption path was increased with a Herriott⁵⁶⁻⁵⁸ multipass cell (Section 2.3), and a pulsed pinhole nozzle was placed in the axial position (Section 2.4). The fast-scan modulation method⁵⁰ was implemented for frequency calibration and spectral acquisition (Section 2.5).

2.2 General description

A schematic diagram of the instrument is shown in Fig. 2.1. Up to two tunable lead salt semiconductor diodes (Laser Components, Wilmington, MA) are housed in a liquid nitrogen cooled dewar (Laser Photonics L5740). The operating temperature can be lowered by reducing the pressure above the liquid nitrogen to ~ 0.5 atm. The laser temperature and therefore its coarse output frequency is controlled by a Laser Components L5830 control unit, which also acts as the current source. A Stanford

Research Systems (Sunnyvale, CA) function generator (DS345) is used to generate the laser current modulation signal.

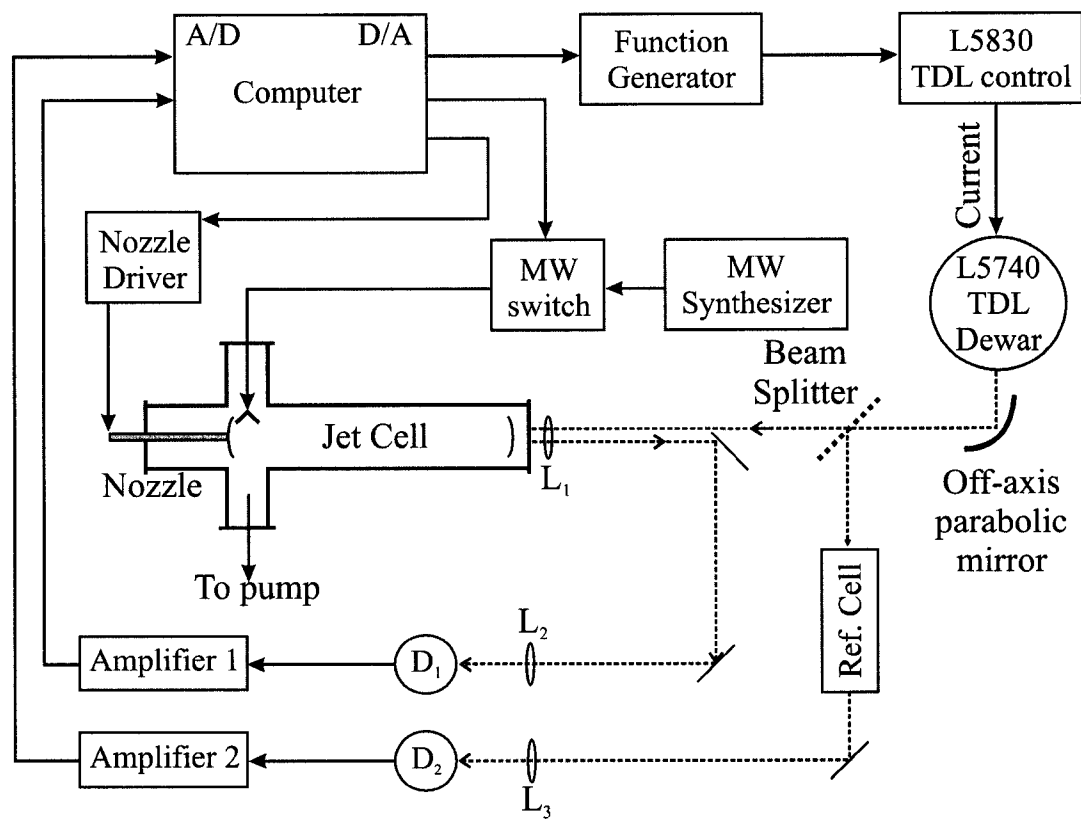
For improved performance, the optical elements outside the vacuum system can be kept under nitrogen to reduce atmospheric absorption. The laser beam is collected and focused by an off-axis parabolic mirror (Laser Components L2018), which can be moved laterally to collect the output of either laser. Part of the beam (~8%) is diverted by a pellicle beam splitter (Oriel Instruments 37400, Stratford, CT) and passed through a 10 cm long reduced pressure reference cell for frequency calibration. Alternatively, a 2.54 cm long temperature-stabilized Germanium tuning rate étalon (Laser Analytics L5940) can be employed. The calibration beam is focused with a 100 mm focal length CaF₂ lens L₃ (Janos Technologies A1404-110, Townshend, VT) onto a liquid nitrogen cooled InSb detector D₂ (Infrared Associates, Stuart, FL). The main beam (92%) is mildly focused using a 500 mm focal length CaF₂ lens L₁ (Janos Technologies A1404-350) and enters, through a CaF₂ Brewster angle window, the vacuum chamber that houses the multipass sample cell. The multipass cell mirrors are 50.8 mm diameter gold-coated spherical mirrors with either 101.6 mm or 508.0 mm common focal lengths (Edmund Industrial Optics K32-816 or K32-822, Barrington, NJ). The vacuum chamber is evacuated by a diffusion pump with liquid nitrogen baffle (Edwards Diffstak® CR160-700, Wilmington, MA) backed by a dual-stage backing pump (Edwards E2M18). The sample gas is injected into the sample cell using a pulsed nozzle (General Valve Series 9, Brookshire, TX) with an in-house constructed aluminum nozzle head with spherical orifice (diameter 0.8 mm). The nozzle can be moved to a position perpendicular to the optical axis of the multipass cell, but is commonly placed along the optical axis, with the nozzle head sitting

in a 2 cm coupling hole in one of the mirrors. The nozzle is controlled by a custom-made pulsed nozzle driver (CPC Consulting PND-2, Vancouver, BC). The laser beam enters and exits the Herriott multipass cell through a coupling hole in the second mirror at slightly different angles. The exiting beam is focused with a 75 mm focal length CaF_2 lens L_2 (Janos Technologies A1407-3081) onto an InSb detector D_1 (Electro-Optical Systems IS-010-LN4, Phoenixville, PA). Both main and reference signals are amplified using fast (DC to 250 kHz) amplifiers and A/D-converted and stored using a dual-channel 12-bit, 50 MS/s PCI data acquisition board (Gage CompuScope 1250, Lachine, QC). The two data acquisition channels are interleaved, so that data from both signals are acquired nearly simultaneously, offset by 40 ns, at an effective sampling rate of 25 MHz. Data acquisition and the operation of the spectrometer are controlled by a personal computer, running the Windows 2000 operating system and using software written in Delphi 5 (Borland, Scotts Valley, CA). Events are triggered by TTL signals generated with an Iotech (Cleveland, OH) DaqBoard 2000 I/O card.

For microwave-infrared double resonance experiments, an X-band microwave horn antenna is mounted perpendicularly to the optical axis near the nozzle head. A Watkins-Johnson (San Jose, CA) 1250 synthesizer is used as the microwave source. The microwave pump signal is on/off-modulated with a microwave PIN diode switch (SMT SFS0518, Georgetown, TX).

Figure 2.1

Schematic diagram of the lead salt diode laser mid-infrared spectrometer. For a description, see Section 2.2.



2.3 Optics

2.3.1 General

The typical output power of a TDL is only in the μW to low mW range. The intensity of the laser beam is further reduced by an elliptical and highly divergent beam profile.²⁵ In the spectrometer described here, the laser beam is collimated with an off-axis parabolic mirror which was purchased from Laser Components. The collimated laser beam has an approximate waist w_0 between 1 and 1.5 mm, judged by moving the detector laterally through the laser beam, and was unpolarized. An important quantity to determine is the Rayleigh range z_R , which is the distance after which the spot size of a collimated Gaussian laser beam has increased by a factor of $2^{1/2}$.¹⁰

$$z_R = \pi w_0^2 \nu / c \quad (2.1)$$

ν is the laser frequency and c is the speed of light. At 2350 cm^{-1} and with a beam waist between 1.0 and 1.5 mm, z_R of our diodes is estimated to be between 0.78 and 1.7 m. It was therefore necessary to slightly refocus the laser beam with a weak lens located just outside the vacuum chamber to keep the beam waist from expanding and the signal from deteriorating. In the multipass cell, the laser beam is continuously refocused at either mirror.

Optical fringing often sets a lower limit of detection in laser based instruments, and many schemes, including complicated laser and mirror modulation patterns,^{118,119} have been developed to combat this kind of noise. In setting up this spectrometer, optical

elements such as mirrors and lenses were inserted at slight angles ($<1^\circ$) to minimize optical feedback and unwanted étalons.

2.3.2 Optical multipass cell

The optical absorption path within the vacuum chamber can be greatly increased with a multipass cell. The maximum useful optical absorption path length in each of these cells is limited primarily by the mirror reflectivity, which is determined by the quality of the mirror coatings. The most popular designs are the Herriott (Fig. 2.2),⁵⁶⁻⁵⁸ White,^{59,60} and astigmatic^{61,62} cells.

For this spectrometer, the Herriott design was chosen because it is the simplest to set up and allows the placement of a pinhole in a hole drilled into the center of one of the mirrors. The nozzle is then surrounded by the circular spot pattern traced out by the laser beam (Fig. 2.3). The Herriott cell is constructed from two spherical mirrors and requires an off-axis coupling hole through which the laser beam enters and exits (Fig. 2.2). The number of spots and therefore the number of optical passes can be controlled by varying the separation of the two mirrors.⁵⁶⁻⁵⁸ The mirror separation can be adjusted by sliding one of the mirrors along the cavity axis. The orientation relative to the other mirror does not need to be altered during this process. Once in place, the positions of the mirrors are secured with set-screws. This procedure allows quick changes of the optical absorption path.

Figure 2.2

Example of a Herriott multipass cell (adapted from Altmann *et al.*⁵⁷). The spherical mirrors are separated by roughly twice their common focal length. Varying the distance between the two mirrors changes the number of optical passes.

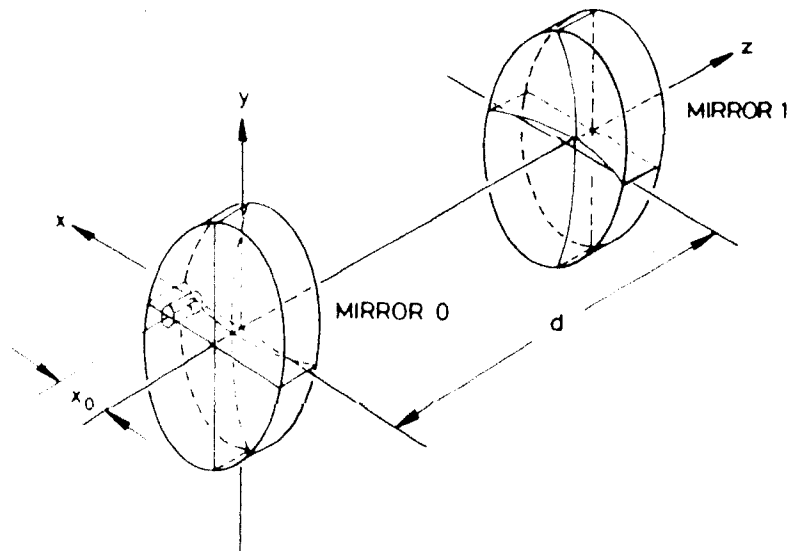
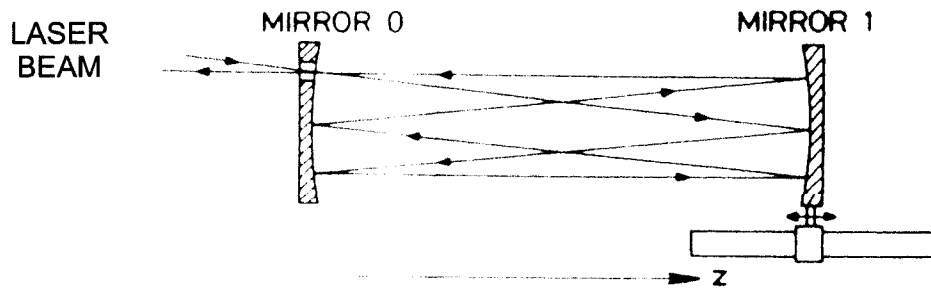
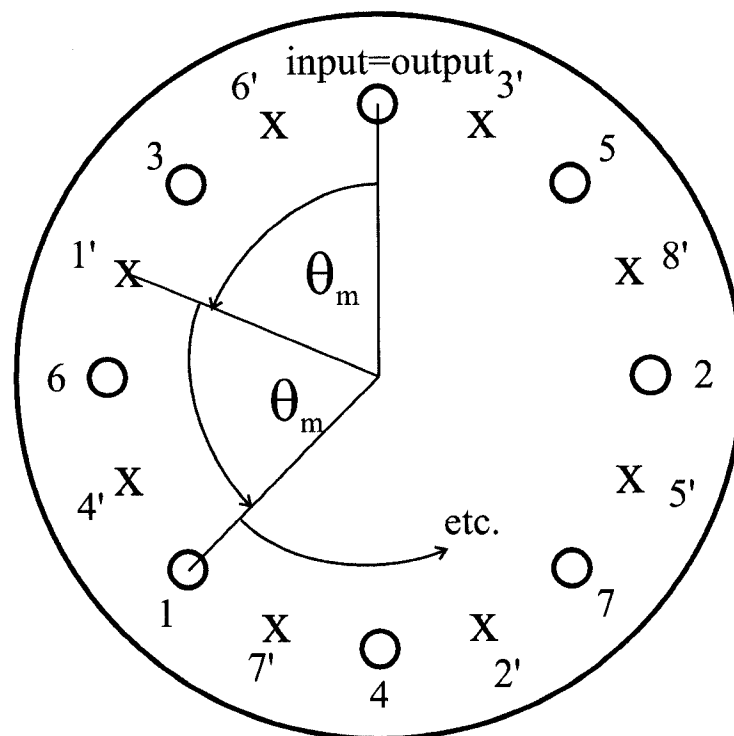


Figure 2.3

Illustration of the circular spot patterns on the spherical mirrors of a Herriott cell. The example chosen is for $M_m=3$ complete orbits, $N_m=16$ passes and $S_m=8$ spots on the mirrors. The circles mark the location of the spots on the coupling mirror, the X's mark the spots on the far mirror. The spherical spot pattern allows the placement of a pulsed nozzle in a hole at the center of either mirror.



The movement of the mirror can in principle be automated, for example by mounting it on a motor-driven sled. The functional dependence of the optical path on the mirror separation and tips for reduction of optical fringing were addressed in a paper McManus *et al.*,⁵⁸ who recommended that the number of visible spots on the mirror should be a multiple of four. The corresponding mirror separation distances can be calculated from the re-entry condition equation originally derived by Herriott:⁵⁶

$$\cos(\theta_m) = 1 - d_m/R_m \quad (2.2)$$

θ_m equals the change of the angular coordinate of the beam spot with each reflection, d_m is the distance separating the two spherical mirrors, and R_m is the mirrors' common radius of curvature. The number of passes N_m relates to the number of complete orbits M_m by

$$N_m \theta_m = \pm 2\pi M_m \quad (2.3)$$

McManus *et al.*⁵⁸ found that especially narrow interference fringes occur if M_m is odd and

$$N_m = 4M_m \pm 4 \quad (2.4)$$

In this instrument, the spherical mirrors were kept at a distance of just below twice their common focal length (i.e. in the $N_m = 4M_m + 4$ regime) yielding up to 72

passes of the laser beam, which corresponds to 36 spots on either mirror and $M_m=17$ completed orbits of the laser beam. Since the focal length was approximately 90 cm, the maximum total optical absorption path length was 64 m. In most experiments, the cell was set up with 40 passes of the laser beam, yielding a 36 m absorption path length.

2.4 Sampling

2.4.1 Static gas cells

In traditional gas sensing applications, the sample gas is continuously pumped through the optical multipass cell at slightly reduced pressures.³⁷ The gas exchange rates are typically slow enough such that the motion of the gas molecules does not result in observable Doppler shifting or broadening of the line (for example through formation of eddies). Over short time periods, the sampling conditions are therefore equivalent to those of a static gas. In this instrument, static gas samples were employed for two purposes: Using the steady absorption signals of the static gas cell, the operating parameters of the instrument, such as laser scan rate and frequency locks, were optimized. In addition, the signals obtained with static gases serve as a frequency reference for comparison with those obtained in molecular beam experiments.

Table 2.1

Mirror positions resulting in narrow interference fringes in a Herriott cell.⁵⁸ M_m is the number of complete orbits, N_m is the number of complete laser passes, S_m is the number of visible spots on the mirrors, θ_m is the angle as defined in Fig. 2.3, and d_m/R_m is the mirror separation as a fraction of the common radius of curvature.

M_m	N_m	S_m	$\theta_m / ^\circ$	d_m/R_m
1	8	4	45.00	0.2929
3	16	8	67.50	0.6173
5	24	12	75.00	0.7412
7	32	16	78.75	0.8049
9	40	20	81.00	0.8436
11	48	24	82.50	0.8695
13	56	28	83.57	0.8880
15	64	32	84.38	0.9020
17	72	36	85.00	0.9128
19	80	40	85.50	0.9215
21	88	44	85.91	0.9287
23	96	48	86.25	0.9346
25	104	52	86.54	0.9396

2.4.2 Free jet expansions

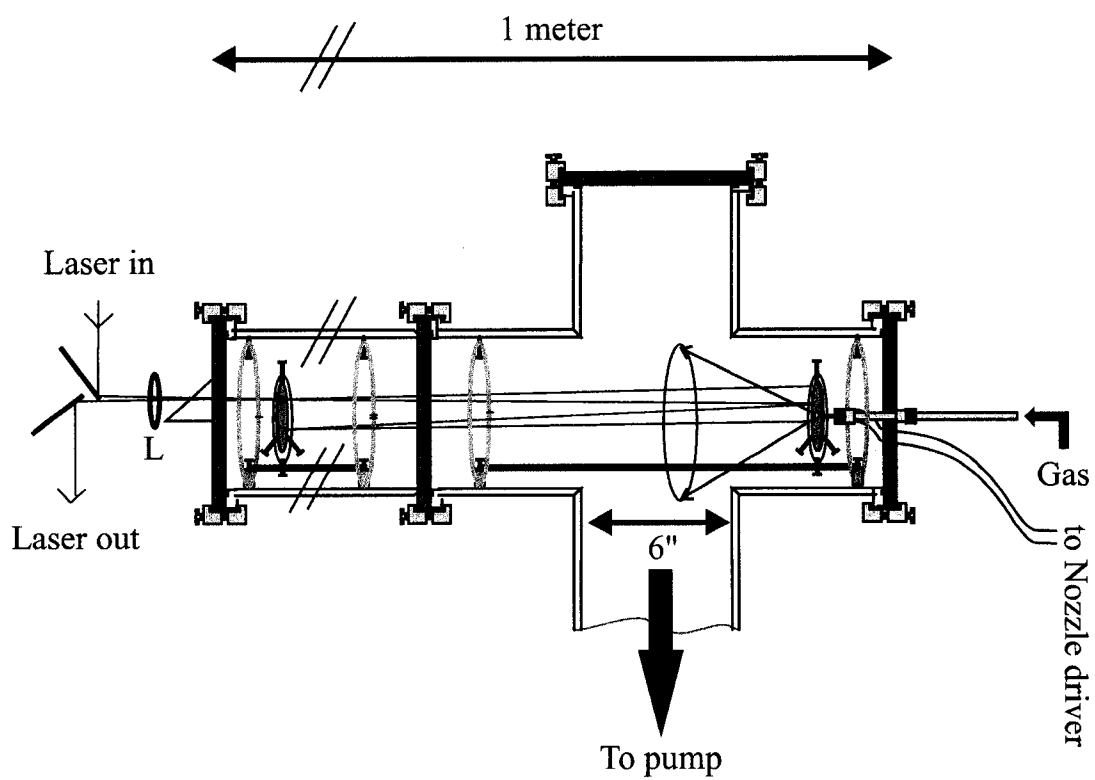
Cold pulsed molecular beams are usually generated with nozzles of circular or slit orifice. Slit nozzles, such as described by Lovejoy *et al.*¹²⁰, are commonly set up perpendicularly to the optical axis because of the geometric confinement of larger quantities of sample gas along the optical axis. Narrow line widths are obtained with slit nozzles because of partial skimming of the expanding gas at the edges of the slit. However, the slit edges disturb the free expansion of the gas and decreases the overall cooling efficiency. As a result, rotational temperatures in slit nozzles (5 - 10 K) are up to a magnitude larger than in free jet expansions using pinhole nozzles (0.5 - 1.5 K).

For gas sensing purposes, the lower beam temperature of pinhole nozzles are highly desirable, because greater signal enhancement for low J transitions can be expected from the more efficient redistribution of molecules into lower energy levels. Because of the difference between transverse and axial translational temperatures, free jet expansions with spherical pinhole nozzles are best performed in parallel to the probing laser beam, in order to avoid excessive Doppler broadening. Surprisingly, such a parallel arrangement was not implemented in an infrared molecular beam spectrometer prior to this work, but comparable microwave^{15,18} and millimeter-wave¹²¹ setups exist.

In this spectrometer, axial sample injection is achieved by mounting the injection nozzle in a hole drilled into the center of the spherical mirror used in the Herriott multipass cell. The setup is shown schematically in Fig. 2.4.

Figure 2.4

Sketch of the Herriott multipass cell in the vacuum chamber, showing the pinhole nozzle in the axial position. For a description, see Section 2.3.2.



2.5 Laser modulation and detection schemes

2.5.1 General

Tunable lead salt diodes exhibit a remarkable fast response to modulation signals up to the GHz range. The modulation signals are usually superimposed onto the diode current, but pressure and temperature modulation of the diodes is also possible. Most commonly, high frequency sinusoidal waveforms are used for current modulation, and the detector signal is demodulated with a phase sensitive lock-in amplifier. The laser is then slowly scanned through the spectrum by superimposing an additional ramp onto the diode current modulation. It has become custom in the TDL community to distinguish two frequency regimes, which are called wavelength modulation (WM) and frequency modulation (FM). In "wavelength modulation", the applied modulation frequencies are less than the cut-off point for 1/f noise, while the modulation frequencies in "frequency modulation" are higher. Unfortunately, this cut-off point is ill-defined. For example, Sigrist¹⁵ puts this point at 100 kHz, whereas Silver¹²² recommends between 10 and 100 MHz. The distinction between WM and FM can give rise to confusion, since wavelength and frequency are often used as synonyms related by $c = \lambda\nu$ and the boundaries are poorly defined. In this thesis, sinusoidal modulation of the laser diode current at any frequency will be referred to as frequency modulation (FM).

2.5.2 Direct absorption: Fast-scan technique

An alternative to the frequency modulation method is the so-called "sweep integration" technique. De Piante *et al.*⁵⁰ were the among the first to apply this technique

to record the spectrum of a van der Waals complex. In this direct absorption method, the diode laser output is rapidly swept through the spectral region of interest and many spectra are averaged. Typically, the laser is scanned through a single mode (which can encompass up to 3 cm^{-1}) in about a millisecond. Sweeps can therefore be repeated several thousand times in a matter of seconds. A detection limit of 1.3×10^{-5} absorption units has been demonstrated with this technique.⁵⁰ The fast sweep method requires a fast data acquisition card, fast A/D conversion, a fast computer to perform the averaging, and a good frequency lock to ensure reproducibility of the scan.

In a typical experiment, the diode current is modulated at a rate of 30 mA/ms, which corresponds to nearly $1\text{ cm}^{-1}/\text{ms}$ in the output frequency. At this rate, the full width at half maximum (FWHM) of a Doppler-broadened line is scanned in about $4\ \mu\text{s}$. The laser scan rate is limited by the onset of asymmetric peaks due to frequency limitations of the detection electronics ($\sim 250\text{ kHz}$) and the detector rise time ($\sim 1\text{ MHz}$). The fast scan technique is therefore efficient in removing low-frequency $1/f$ noise and frequency-independent white noise. However, optical fringes are generally amplified in conjunction with the absorption signals, thus limiting the sensitivity of this technique. In molecular beam experiments, the transient nature of the molecular pulses enables the removal of residual fringes by background subtraction.

2.5.2.1 Frequency locking mechanism

For long-term data acquisition, gradual instrument drifts are known to become the limiting source of noise. This is particular true for the fast-scan method, where the

uncontrolled co-addition of repetitive scans can result in significant line broadening. In this instrument, the spectrum of a 10 cm reference cell is acquired simultaneously with the molecular spectrum. A long-term frequency lock is maintained by shifting subsequent spectra relative to the initial reference spectrum before co-addition. The shift by a certain number of data points s is determined using an iterative algorithm designed to find a local minimum to the least-squares error function

$$f(s, os) = \sum_{i=a}^b (x_n(i+s) - x_{ref}(i) + os)^2 \quad (2.7)$$

with respect to both s and os . The term ' os ' corrects for a variable DC offset of the AC-coupled reference channel. The array of data points $x_n(I)$ contains the n^{th} digitized reference spectrum, and the array $x_{ref}(I)$ contains the average of the previous $n-1$ reference spectra.

2.5.3 Frequency modulation method

It has been shown both theoretically^{122,123} and experimentally^{51,124} that high frequency modulation is in principle superior to direct absorption experiments. In typical frequency modulation experiments, the diode laser is modulated at frequencies between the kHz and the GHz region. However, modulating the laser current not only affects the laser output frequency, but also the emitted laser power. In direct absorption experiments, this results only in a positively sloped baseline, which can in principle be corrected in the usual manner by background subtraction. In frequency modulation experiments, however, residual amplitude modulation (RAM) and additional phase noise⁴⁹

significantly lower experimentally obtainable detection limits from their theoretical maximum, especially at high frequencies. Detection limits as low as 10^{-7} absorption units have been reported at a modulation frequency of 10 MHz over a 1 second integration period.¹²⁴ Detection limits of 10^{-7} and below have also been demonstrated by two-tone heterodyne spectroscopy.^{51-53,125}

In this work, frequency modulation experiments were performed on static gas samples (Chapter 3) and molecular beams (Chapter 8). In the frequency modulated experiments, a sinusoidal modulation frequency between 10 and 50 kHz was superimposed on the laser current, and the signals of both main and reference channel are demodulated with the aid of lock-in-amplifiers (Stanford Research Systems 830 and Ithaco Dynatrac 391A, Ithaca, NY). Upper limits to the modulation frequencies were imposed by the lock-in-amplifiers (51 kHz). At these modulation frequencies, $1/f$ noise is known³⁷ to keep the achievable limits of detection orders of magnitude above the shot noise limit. Spectra were recorded by slowly step-scanning through the spectrum, while maintaining the superimposed modulation pattern. The output of the lock-in-amplifier was digitized using the Iotech DaqBoard/2000.

2.5.4 Measurements of molecular expansion spectra

In FM modulation spectroscopy, the S/N ratio of the demodulated signal depends on the time constant, i.e. on how many oscillations at the reference frequency are observed by the lock-in-amplifier. A 50 kHz modulation signal goes at most through 200 cycles in the short lifetime of the molecular beam of <4 ms. Thus, only single frequency point measurements of the molecular beam can be accomplished in FM

modulation mode. In order to record the entire expansion spectrum, the laser output frequency must be slowly stepped through the frequency region of interest between pulses. However, diode laser instability and pulse-to-pulse variations of the amount of gas delivered make frequency stepping between pulses impractical. For the acquisition of molecular expansion spectra, the lead salt diode is therefore operated in rapid scanning mode. In fast-scanning mode, pulse-to-pulse variations are distributed across the entire spectrum and can be averaged out using the signals from many molecular pulses.

In a typical pulsed beam experiment, data from the sample cell and from the reference cell are acquired at sampling rates of 25 MHz. A scan is stored in up to 38000 data points per channel, corresponding to an average lifetime of the molecular expansion in He carrier gas of approximately 1.5 ms. The collected spectra are therefore also a record of the time evolution of the molecular expansion. The frequency sweep can be repeated several times during a single molecular pulse depending on the lifetime of the molecular beam. The end of the coaxial molecular expansion is signaled by the disappearance of characteristic Doppler doublets and by the appearance of thermally populated CO₂ monomer transitions. Since the pulse repetition rate is only 5 Hz - 10 Hz, limited by the pumping speed of the diffusion pump, data processing can take place immediately between pulses.

Because of the transient nature of the pulsed molecular beam, it is important to carefully time the sequence of events such as the beginning and end of the frequency sweep. The triggering scheme for a typical experiment is shown in Fig. 2.5. Upon triggering, the SRS function generator delivers a series of typically several hundred positive 1 ms long linear voltage ramps, separated by short recovery periods. A typical

scan rate is $850 \text{ cm}^{-1} \text{ s}^{-1}$. During data acquisition and subsequent transfer from board to PC memory, the current modulation remains uninterrupted. This has the dual advantage of stabilizing the effect of ohmic heating of the laser diode and allowing the accumulation of several scans within a single gas pulse. It also improves the overall reproducibility of the frequency scan.

A typical experiment begins with the simultaneous acquisition of two spectra (sample cell and reference cell) at time t_1 (Fig. 2.5), which are stored in separate acquisition channels. The background spectrum is taken without injection of a molecular pulse, that is, with the empty sample cell, and is used for background subtraction of the molecular spectrum. The reference spectrum is that of the CO_2 reference cell and is stored in the second channel of the data acquisition card. The pulse nozzle is then triggered at time t_2 , and two new spectra, a molecular spectrum and a reference spectrum, are recorded after a $500 \text{ }\mu\text{s}$ delay (t_3). The delay is necessary because the molecular beam does not instantaneously appear in the sampling region. The earlier recorded background spectrum is subtracted immediately after acquisition of the molecular spectrum. The shift of the new reference spectrum of the CO_2 reference cell with respect to the original reference spectrum is determined and used in the software-locking scheme described in Section 2.5.2.1 to offset any frequency drift. Subsequent scans of the reference spectrum are averaged with previous scans for improved performance. The entire data acquisition cycle is repeated until a satisfactory signal-to-noise ratio is obtained.

Figure 2.5

Timing sequence for single resonance molecular expansion experiments. For an explanation, see Section 2.5.4.

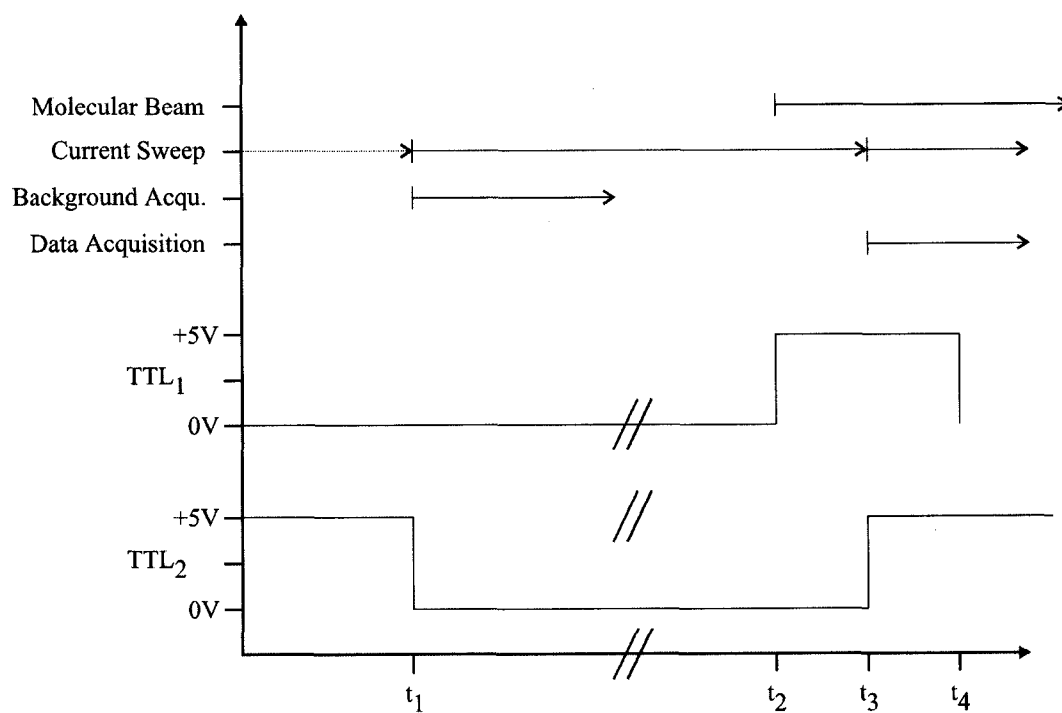
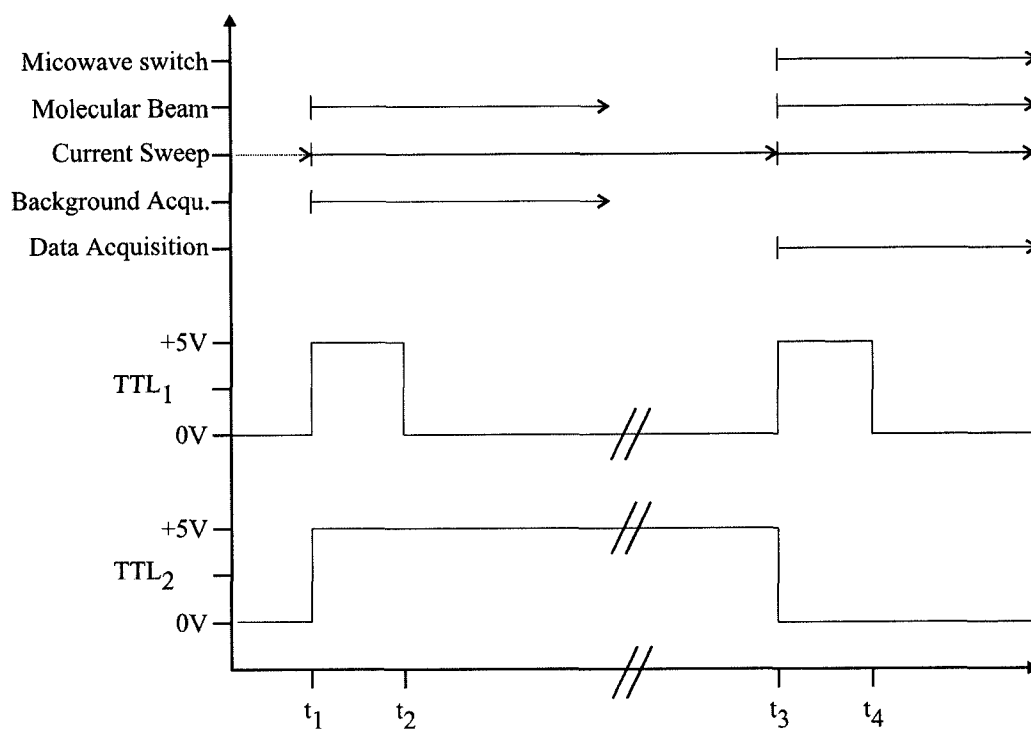


Figure 2.6

Timing sequence for double resonance molecular expansion experiments. At time t_1 , the nozzle driver (TTL₁) is triggered, and the microwave switch is closed. On-board data acquisition is triggered immediately (TTL₂) to capture the background spectrum, but the incoming data is ignored until the molecular beam crosses the laser beam at time t_2 . At time t_3 , the microwave switch is opened and the nozzle driver is triggered again. On-board data capture is triggered simultaneously, but the incoming data are again ignored until time t_4 . The double resonance spectrum is then obtained by subtraction.



2.5.5 Microwave-infrared double resonance experiments

For microwave-infrared double resonance experiments, a molecular pulse is injected into the sample cell for both background and main scan. The microwave switch is closed for the acquisition of background spectra and opened for double resonance spectra. This type of on/off modulation results in spectra showing only double resonance effects. The sequence of events for the double resonance experiment is shown in Fig. 2.6.

2.5.6 Frequency calibration

The need for frequency calibration in high-resolution TDL experiments arises from the nonlinear scaling of the TDL frequency output with the applied current. Lead salt diodes are Fabry-Pérot devices, and the frequency of the produced light depends on resonance conditions within the diode. The ohmic heating associated with the applied current expands the laser medium and changes its refractive index, and the emitted laser frequency changes accordingly. On occasion, the active laser mode may switch, resulting in a gap in the frequency output of the diode. These gaps are commonly referred to as mode hops. An increase in laser current may also activate additional laser modes, which is called multimode lasing.

The transitions in the simultaneously recorded reference spectrum serve as frequency markers for the molecular spectrum. Absolute frequencies are determined by fitting the parameters of Gaussian functions to the known CO₂ transition frequencies listed in the Hitran database.⁷⁸ A 4th order polynomial is then used to describe the tuning behaviour of the laser diode, which serves as a calibration curve relating absolute frequency and data points.

Figure 2.7

Typical frequency calibration curve as a function of channel position in the computer memory. The tuning behaviour of the diode was fitted to a 4th order polynomial, relating frequency entries in the Hitran database⁷⁸ to the acquisition channel. The standard deviation of the fit is 0.00014 cm⁻¹.

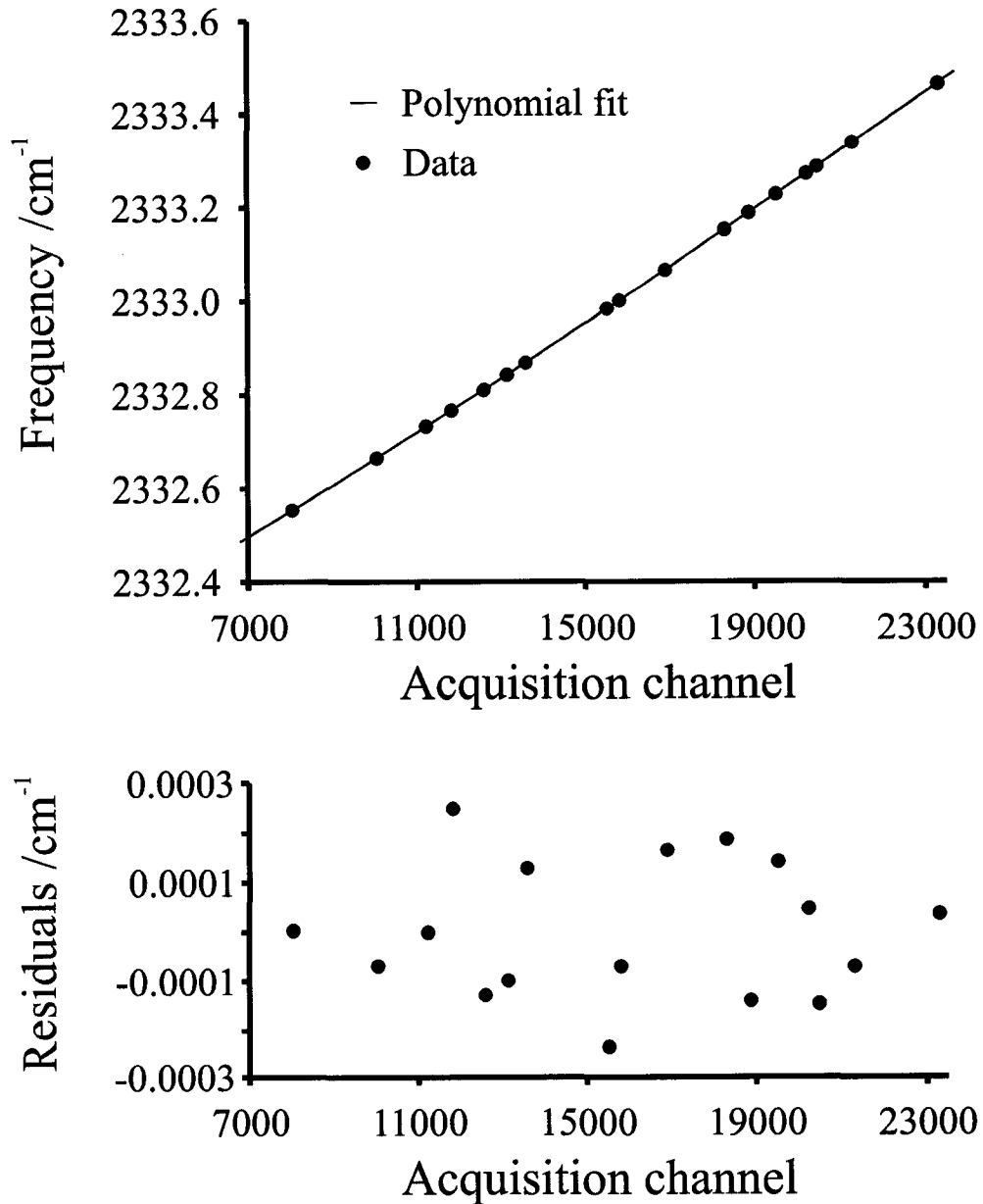


Table 2.2

4th order polynomial parameters relating frequency and position in computer memory

(accompanies Fig. 2.7). The polynomial is of the form $\nu = \nu(0) + \sum_{i=1}^4 (m_i \text{ch}^i)$.

	Value	$\pm\sigma$
$\nu(0) / \text{cm}^{-1}$	2332.1406	0.0059
$m_1 / \text{cm}^{-1} \text{ch}^{-1}$	0.0000470	0.0000017
$m_2 / \text{cm}^{-1} \text{ch}^{-2}$	$6.0 \cdot 10^{-10}$	$1.7 \cdot 10^{-10}$
$m_3 / \text{cm}^{-1} \text{ch}^{-3}$	$-9.1 \cdot 10^{-15}$	$7.6 \cdot 10^{-15}$
$m_4 / \text{cm}^{-1} \text{ch}^{-4}$	$0.7 \cdot 10^{-19}$	$1.2 \cdot 10^{-19}$

CHAPTER 3

SPECTROMETER PERFORMANCE*

* Condensed versions of this Chapter have been published in *Proceedings of SPIE 2002*, 4817, 249 and in *Review of Scientific Instruments 2004*, 75, 46.

3.1 Introduction

In this Chapter, the performance and applicability of the spectrometer towards gas sensing and the acquisition of spectra are evaluated. For this purpose, the so-called rapid-sweep, or fast-scan, method developed by de Piante *et al.*⁵⁰ was employed. Initial experiments were performed on static gas samples (Section 3.2). In these experiments, the lasing characteristics of the diodes, such as output frequencies, mode structure, tuning rate, and operating temperature, were determined. Spectral regions containing low J lines were identified by comparing the observed spectra with simulations based on the Hitran⁷⁸ database (Section 3.2.1). The performance of the fast scan⁵⁰ technique is discussed and compared to conventional frequency modulation spectroscopy in Section 3.2.2.

Section 3.3 deals with the implementation and properties of the molecular beam expansion. Signal enhancement is demonstrated in Section 3.3.1. In Section 3.3.2, the pulse reproducibility is addressed. In Section 3.3.3, the advantages of axial sample introduction compared to perpendicular sample introduction are discussed. In Section 3.3.4, a line shape model for the axial sample introduction is developed. Beam evolution, molecular speeds and lifetimes are described in Section 3.3.5. Line intensities and their

relationship to the beam temperature are discussed in Section 3.3.6. In Section 3.3.7, some sample data on the accuracy and precision of van der Waals spectra are presented.

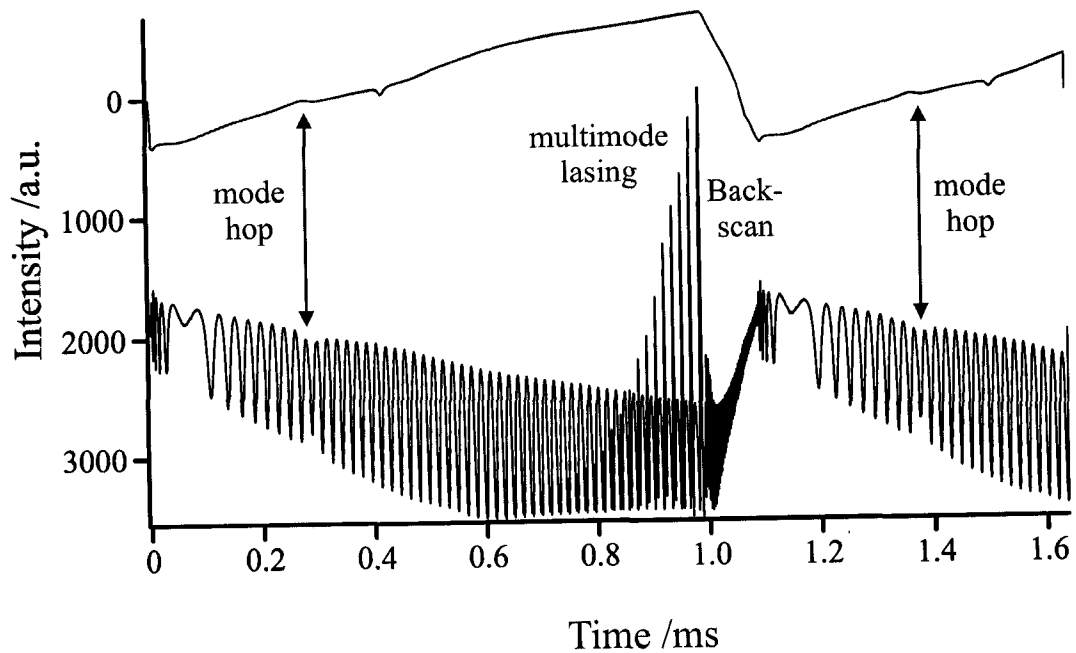
3.2 Experiments using static gas cells

3.2.1 Evaluation of diode laser characteristics

After installation of a new diode, the laser current and temperature are adjusted to produce single mode output of the diode. For this purpose, the rapid-sweep method (Section 2.5.2) is employed. Single mode operation is verified using the étalon scan and by comparison of the observed spectra to simulated spectra using the Hitran⁷⁸ database. Locating a useful laser mode can be a tedious task, especially since the gaps between laser modes frequently exceed several wavenumbers. Multimode lasing action is visible by a second set of fringes superimposed on the main fringing pattern (Fig. 3.1). Mode hops are usually harder to spot, but often cause an abrupt phase shift in the periodic étalon output (Fig 3.1). In general, single mode lasing is more likely when the laser is operated near threshold conditions. Single mode diode operation is advantageous because it eliminates the need for a monochromator, whose insertion would result in a significant reduction of effective laser power. By operating near threshold and avoiding freeze-thaw cycles, the lasing characteristics of the diodes are stable over the period of many months.

Figure 3.1

Example of mode hop and multimode lasing. The absorption spectrum of the empty cell is shown in the trace at the top. The trace at the bottom shows the simultaneously scanned fringe spectrum of a 2.54 cm Ge étalon (FSR=0.048 cm⁻¹). The laser is operated in rapid-scan⁵⁰ mode, in which 1 ms long positive current sweeps are followed by fast (here: 0.1 ms) back scans. Multimode lasing is visible as a second set of interference fringes.



The diode used for the most work presented here (Laser Components F-2462-GMP) is capable of lasing near 2349 cm^{-1} in a several wavenumber wide single mode, which covers the fundamental asymmetric stretching region of CO_2 (Fig. 3.2). The observed CO_2 transitions in this region are listed in Table A3.2 in the appendix. Initially, the mode covered the region between 2349.9 and 2351.1 cm^{-1} . During the experiments, the mode gradually shifted towards lower frequencies (2347.4 to 2350.0 cm^{-1}). By increasing the operating temperature, the output of this laser diode can be tuned up to 2500 cm^{-1} . A second diode (Laser Components F-1887-GMP) provides frequency coverage of the region around 1880 cm^{-1} . However, this diode is prone to multimode lasing and has very irregular modes. In experiments with this diode, several N_2O and NO lines were observed but could not be assigned. A third diode (Laser Components IR-2333) covers the asymmetric stretching fundamental of the 3rd most abundant isotopomer of carbon dioxide, ^{18}OCO , between 2331.6 and 2334.6 cm^{-1} (Fig 3.3). The identified transitions of ^{18}OCO and CO_2 in this region are summarized in Table A3.3 in the appendix. In addition to the laser modes listed above, several other "good" laser modes were identified. However, because these modes did not contain low J transitions (a requirement for molecular beam experiments), they were rarely used in the experiments. The following transitions listed in Tables A3.2 and A3.3 have a sufficiently low rotational quantum number J to be observed in the molecular beam: The P(2) and R(0) lines of CO_2 and the R(0) up to R(3) lines of ^{18}OCO .

Figure 3.2

Rapid-sweep spectrum of CO₂ contained in a 10 cm long cell at a few torr pressure near 2350 cm⁻¹ (Laser: F-2462-GMP). 100 sweeps were averaged. The observed transitions are Doppler-broadened. A simulated spectrum based on the Hitran database is shown at the bottom for comparison.

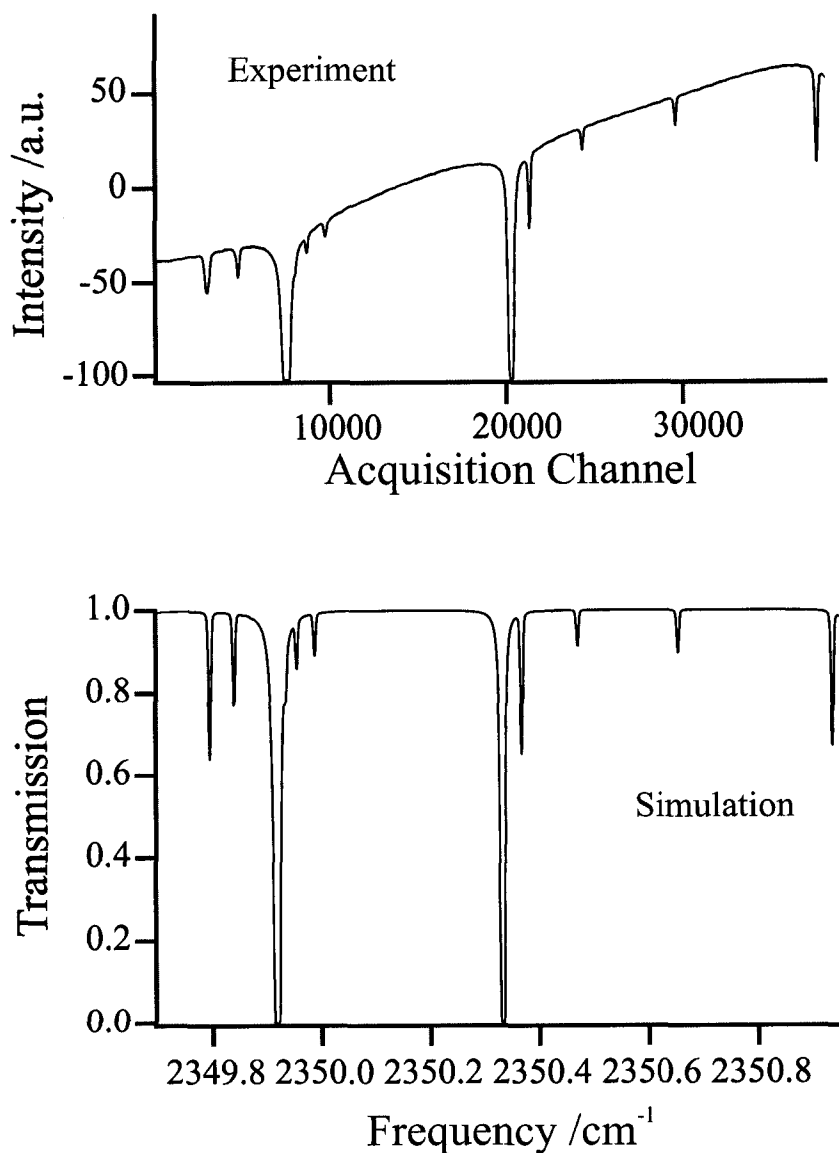
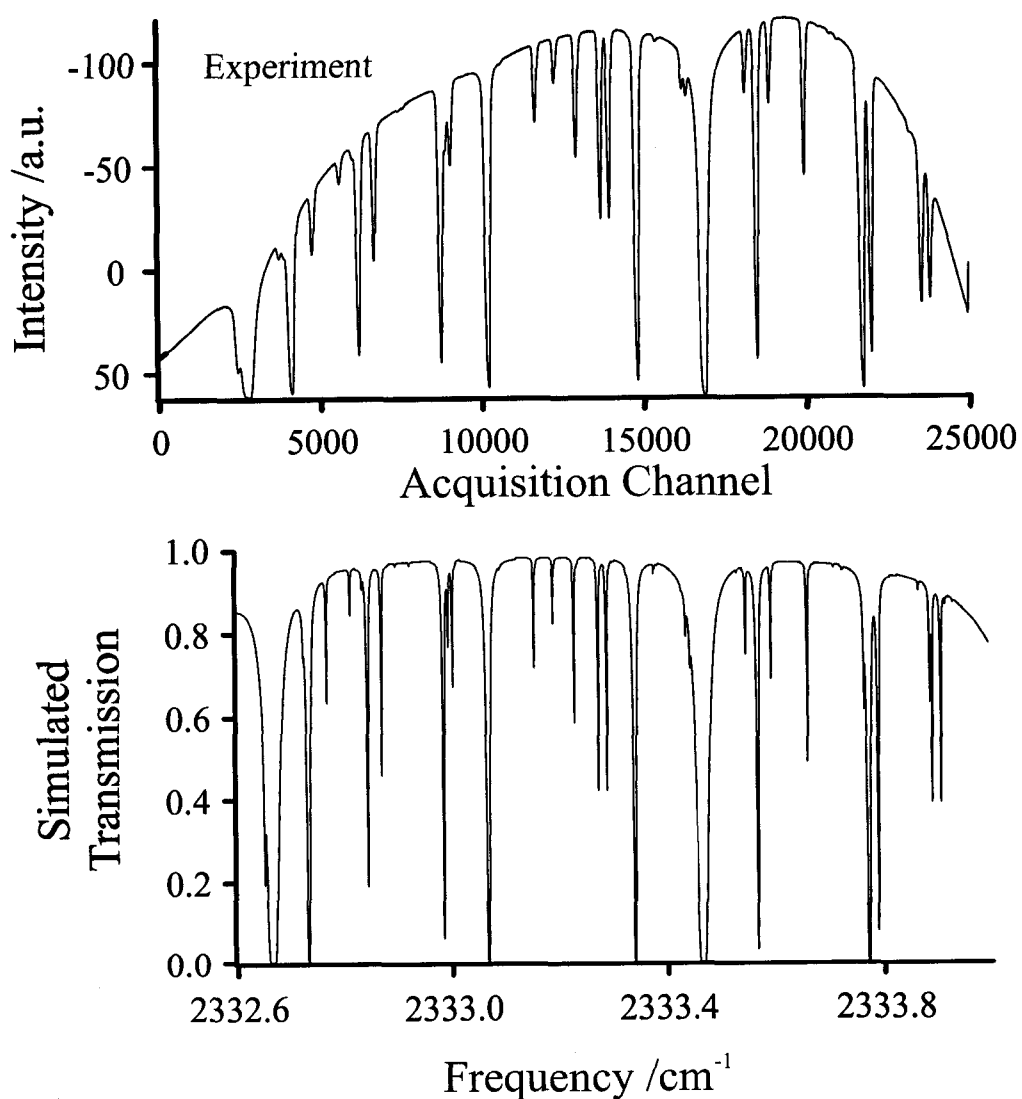


Figure 3.3

Rapid-sweep spectrum of CO₂ contained in 10 cm long cell at a few torr pressure near 2333 cm⁻¹ (Laser: IR-2333). 100 sweeps were averaged. A simulated spectrum based on the Hitran database is shown at the bottom for comparison. Strong and broad atmospheric absorption lines of CO₂ are located at 2332.369 cm⁻¹ and at 2334.156 cm⁻¹, which affect the baseline of the experimental spectrum.



3.2.2 Performance of modulation and detection schemes

3.2.2.1 Sample H₂S spectrum

A representative fast-scan spectrum and a frequency modulation spectrum are shown in Fig 3.4. The gold-coated mirrors had to be replaced soon after these experiments because a thin, non-reflective film had formed on the mirror surfaces due to H₂S exposure. The line positions and intensities in the recorded spectra match those in the simulated spectrum based on the Hitran⁷⁸ database (Table 3.1). The experimental conditions were adjusted so that both modulation techniques yield similar signal-to-noise ratios. The FM spectra are still limited by 1/f noise at the modulation frequency of 10 kHz.³⁷ The smallest identified feature in the spectra (marked by the arrow) has a simulated absorption of ~0.002, which was recorded with a S/N ratio of ~3. Upon close inspection, small étalon fringes are visible in the spectra, which raise the background noise level. Weaker spectral features are present but could not be assigned. The unassigned lines are either due to lines not yet included in Hitran, or appear in the spectra as a result of multimode lasing.

Figure 3.4

Spectra of ~ 1 torr H_2S in a 2 m absorption path. The spectrum shown at the top was acquired in rapid-sweep mode (1200 runs at 250 Hz repetition rate). The spectrum shown in the middle of the page was acquired by frequency modulation at 10 kHz coupled with 1f detection ($\tau=125$ ms). The modulation amplitude was set to twice the average peak width. A simulation based on the Hitran⁷⁸ database is shown at the bottom of the page.

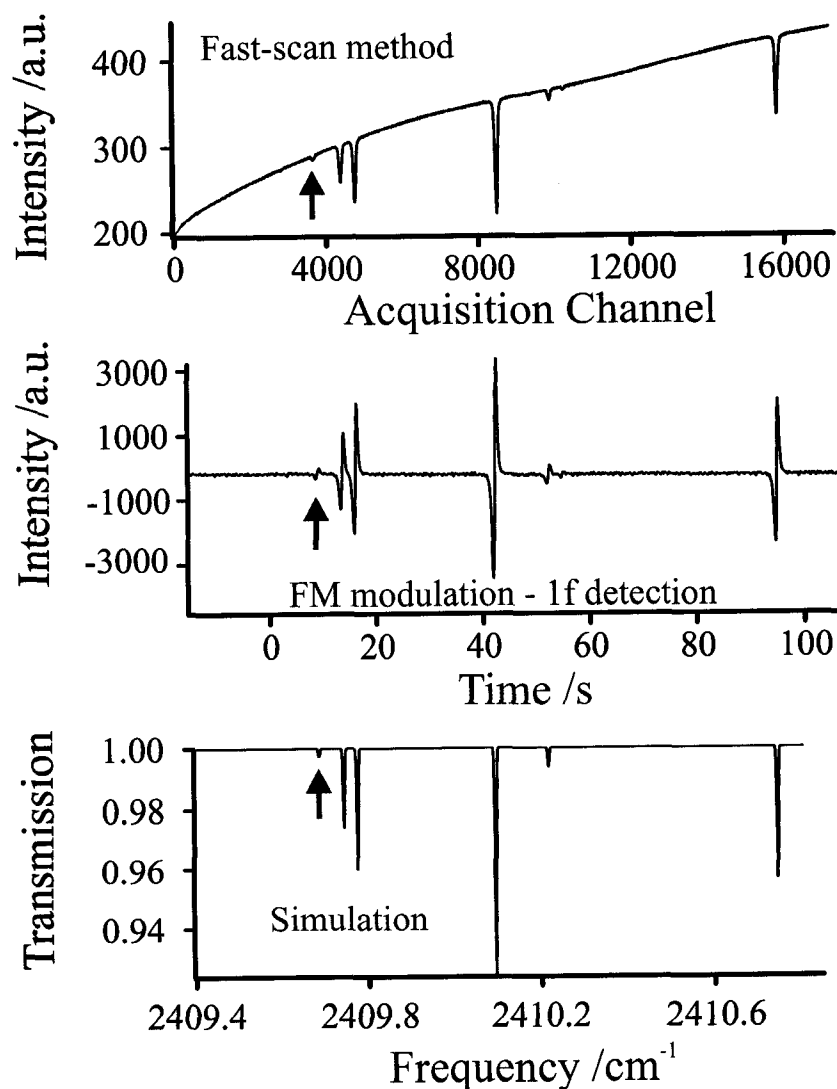


Table 3.1

H₂S transitions observed in Fig. 3.4 (source: Hitran⁷⁸).

Isotope	ν /cm ⁻¹	Intensity @296K /cm molecule ⁻¹	E" /cm ⁻¹	Band	Transition
H ₂ ³² S	2409.68662	2.33E-24	985.3512	ν_3	9 ₅₄ ← 10 ₇₃
H ₂ ³² S	2409.74323	2.12E-23	281.5946	2 ν_2	6 ₂₄ ← 6 ₁₅
H ₂ ³² S	2409.77428	3.24E-23	387.8848	2 ν_2	6 ₆₁ ← 6 ₅₂
H ₂ ³² S	2410.09502	6.38E-23	281.6023	2 ν_2	6 ₃₄ ← 6 ₂₅
H ₂ ³⁴ S	2410.21783	5.21E-24	94.9433	2 ν_2	4 ₂₃ ← 3 ₁₂
H ₂ ³² S	2410.74464	3.57E-23	96.3925	2 ν_2	4 ₁₃ ← 3 ₂₂
H ₂ ³² S	2410.91844	8.93E-24	608.5654	2 ν_2	8 ₅₃ ← 8 ₄₄
H ₂ ³² S	2411.93564	9.43E-24	776.3769	ν_3	8 ₃₅ ← 9 ₅₄

Notes: All observed transitions originate from the vibrational ground state. The accuracy of the lines is in the range of ≥ 0.0001 and < 0.001 cm⁻¹.

3.2.2.2 Performance of fast-scan technique

One of the great advantages of the fast-scan method is its acquisition speed. While it takes only ~ 4.8 s to average 1200 scans, one scan through the spectrum in frequency modulation mode takes over 100 s (Fig 3.4). The fast-scan spectrum shown in Fig. 3.4 has a characteristically sloped background, because the modulation of the diode current not only modulates the output frequency, but also the output power. Strong molecular absorption features outside the sample cell make an additional contribution to the overall shape of the background. The background can in principle be modeled as a polynomial function similar to the polynomials used in the frequency calibration (Section 2.5.5) and can then be subtracted from the observed spectrum. It is much more efficient, however, to record and subtract a blank background spectrum, which is relatively easy to acquire when a pulsed molecular beam is employed (Section 3.3).

The absence of observable broadening in the rapid-sweep spectrum, even though 1200 scans were averaged, is evidence of a functional frequency lock. In follow-up experiments, up to 10^6 spectra were successfully averaged without observable peak broadening. The maximum sweep rate before the line shapes of the Doppler-broadened peaks degrade is about 30 mA/ms, which corresponds to about $1 \text{ cm}^{-1}/\text{ms}$. The sweep rate is limited by the response time of the preamplifier electronics.

Good signal-to-noise ratios S/N are achieved by the fast-scan technique by extensive signal averaging. S/N is defined as the peak intensity divided by the standard deviation of the background noise. In separate experiments with 1, 10, 100 and 1000 averaged scans, it was observed that the S/N ratio increases with the square root of the number of scans. This is indicative of frequency-independent white noise. The fast-scan

technique is very insensitive to low-frequency $1/f$ noise because of the rapid acquisition speed. However, this type of signal averaging has both practical and fundamental limits. An improvement of the S/N ratio by factor of 2 requires 4-fold increase in integration time, which quickly becomes prohibitive. A fundamental limit is posed by systematic noise, for example optical fringing. This kind of noise is amplified in the same manner as the molecular absorption signal. In fact, the spectra shown in Fig 3.4 are limited by fringe noise. Fringe noise can be reduced in a variety of ways, including jitter, digital filtering, and background subtraction.

The sensitivity of the fast-scan method is also limited by the resolution of the data acquisition card. The employed 12-bit card has a maximum resolution of $1/4096$. If the entire spectrum is to be acquired in a single sweep, the sloped background requires that the input voltage range is high. Small signals superimposed on the sloped baseline are then drowned by bit or digitization noise. In applications requiring high sensitivity, one can of course lower the input range to reduce the bit noise. However, the main advantage of the fast-scan method is that the entire spectrum is scanned per sweep. If the input range of the data acquisition is lowered, this fundamental advantage disappears. In frequency modulation spectroscopy, the resolution of the data acquisition card is not as important.

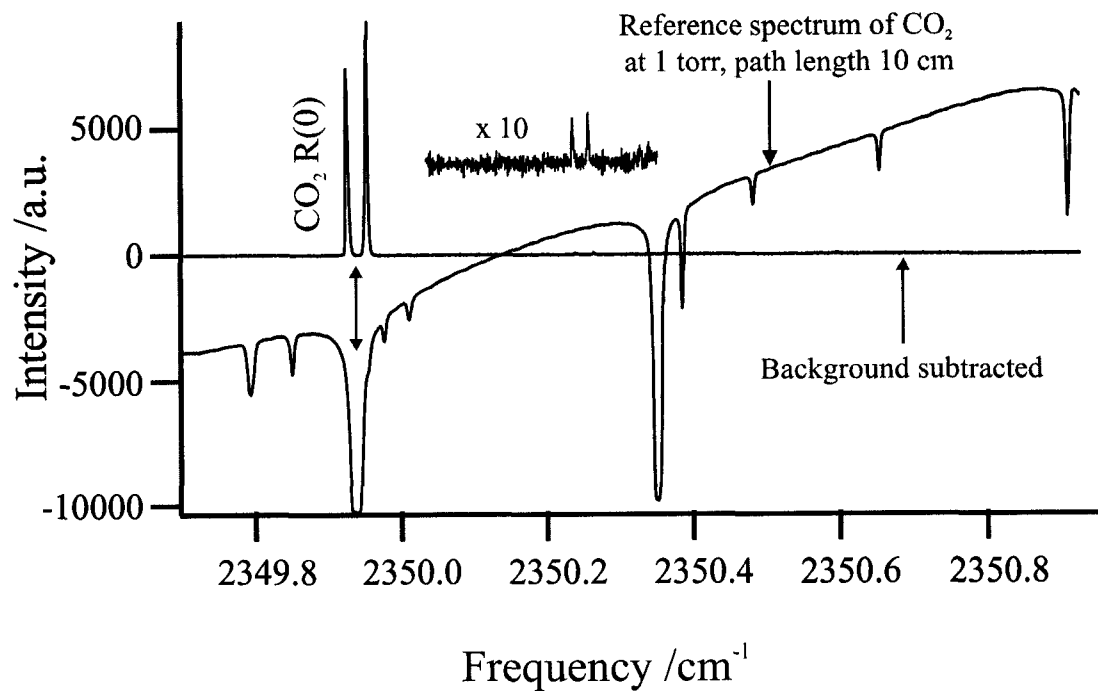
3.3 Experiments with molecular beams

3.3.1 Signal enhancement and selectivity

In the cold environment of the molecular beam, the population distribution of the gas molecules is compressed into the lowest rotational energy levels. As a result, transitions such as the H₂S lines shown in Fig. 3.4, which originate from rotational levels J'' of 3 or greater (Table 3.1), cannot be detected in the expansion spectra even when highly concentrated H₂S gas mixtures are used. In contrast, the intensities of transitions from $J=0$ energy levels are significantly enhanced in the molecular expansion. In the sample spectrum shown in Fig. 3.5, for example, only the R(0) transition of CO₂ appears as a very intense Doppler doublet on an otherwise flat baseline. The R(0) transition appears as a Doppler doublet because of the axial placement of the injection nozzle in the experiment. The flat baseline is a significant advantage over the normally sloped background typical of tunable diode laser spectra. Many additional CO₂ transitions can be seen in the reference spectrum and the Hitran simulation (Fig 3.2), which are not visible in the spectrum of the molecular expansion (Fig 3.4). The energy levels corresponding to these additional lines are effectively depopulated in the molecular expansion by rotational and vibrational cooling.

Figure 3.5

Demonstration of selective signal enhancement. a) Spectrum of a molecular expansion of CO_2 in He carrier gas. The dominant feature is the Doppler doublet of the $R(0)$ transition of CO_2 . The flat baseline is a consequence of the molecular pulse on/off modulation. The transition at 2350.226 cm^{-1} is the ${}^R R_0(1)$ line of the He- CO_2 weakly bound complex. b) The CO_2 reference spectrum (sloped baseline) obtained using a reduced pressure static gas sample. A simulated spectrum of this spectral region is shown in Fig. 3.2.



3.3.2 Pulse reproducibility

One experimental parameter that affects the performance of the spectrometer is the reproducibility of the molecular pulses. We noticed that the intensity of individual transitions varied substantially from pulse to pulse, and compensated by averaging several hundred scans in each experiment, which does not lead to additional line-broadening (Section 3.2.2.2). The large pulse-to-pulse variations in the amount of gas delivered is mainly a result of the nozzle design. In this spectrometer, a commercially available General Valve nozzle is employed. Improved sample delivery has recently been demonstrated with a new flow nozzle designed at the National Institute of Standards and Technology (NIST).¹¹

3.3.3 Axial vs. perpendicular expansion

To assess the merits of the axial nozzle arrangement, the experiments were done with the nozzle in the axial and a perpendicular position, and the resulting signals were compared (Fig. 3.6). When the nozzle is in the axial position, the absorption line is split into a Doppler pair. The line width of each Doppler component is significantly smaller than the Gaussian line shape observed in the perpendicular expansion. The reduced line width is a result of a narrower velocity distribution and decreased residual Doppler broadening (Section 3.3.4). To avoid broadening of the narrow Doppler doublet, the laser sweep rate needs to be reduced from 30 mA/ms (Section 3.2.2.2) to 7 mA/ms. The line widths achieved using the axial sample introduction method at the lower sweep rates are comparable to the line widths obtained in similar work with slit nozzles.¹²⁰

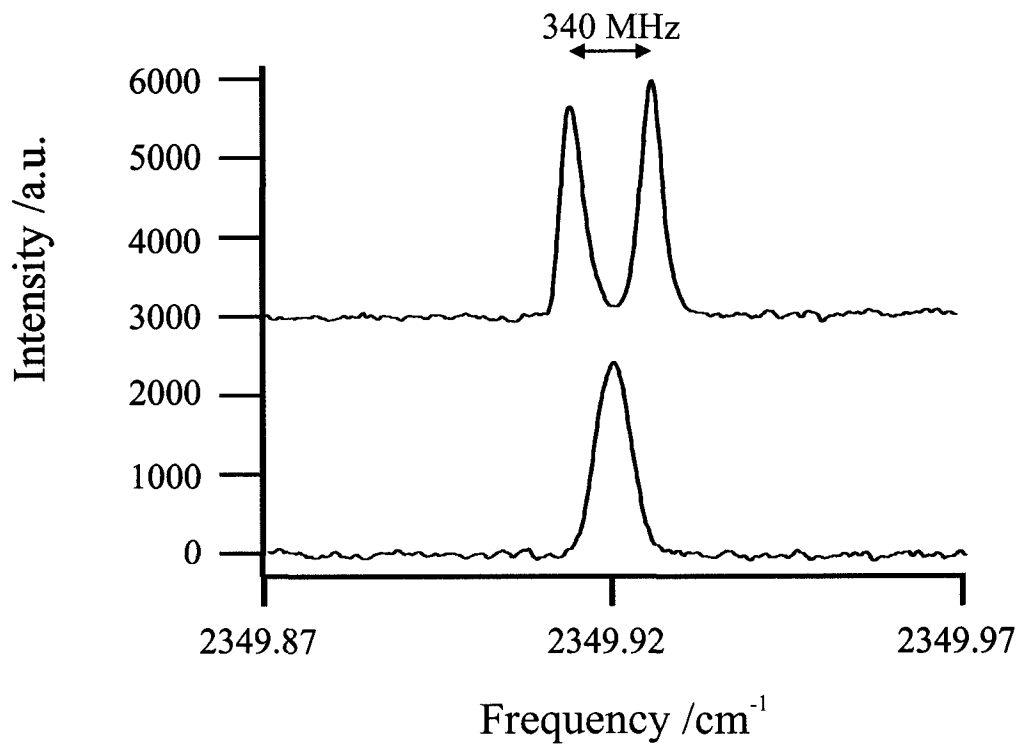
Even though each Doppler component samples only half of the total absorption

path, the intensity of the Doppler pair is approximately equal to the signal from the perpendicularly injected sample. Thus, a signal-to-noise gain of a factor of about 2 is realized by moving to the axial position. This is in accord with results obtained by Walker *et al.* in the mm-wave region.¹²¹ The sensitivity is improved with the axial injection because of the narrower line width, better overlap of the laser beam with the denser portion of the molecular expansion immediately behind the nozzle and because of the longer residence time of the molecular expansion in the laser beam. However, the sensitivity cannot be arbitrarily increased by increasing the sample cell length, mainly because the density of the molecular expansion decreases quadratically along the expansion direction as a result of the expanding molecular beam.

The splitting of each transition into a Doppler doublet has several advantages. In general, the fitting of a line shape equation to two peaks simultaneously yields more precise and accurate results than those obtained from single peak fits. The doublet allows also the application of new modulation schemes (Chapter 8). In addition, the Doppler doublet provides information about the beam velocity. If the beam velocity is known *a priori* or from fitting of nearby more intense transitions, the doublet line shape may lead to lower detection limits. For example, if the signal-to-noise ratio is poor, it is generally hard to discriminate between a single peak and random spikes in the baseline. In contrast, the doublet line shape is more easily distinguished from a noisy background, for example through automated pattern recognition algorithms. One disadvantage of the Doppler splitting is the increased spectral crowding, which complicates the analysis of closely spaced transitions, for example in the spectra of van der Waals complexes.

Figure 3.6

The R(0) transition of CO₂ in air at ambient pressure observed with the nozzle in the axial position (top) and in the perpendicular position (bottom). The blue-shifted Doppler component is slightly more intense because of variation of the laser power with frequency. The Doppler components shown have ~100 MHz full width at half maximum. In subsequent experiments at slower scan speed narrower line widths down to 46 MHz were achieved. The line width of the perpendicular injection signal (~160 MHz) resembles the calculated FWHM of CO₂ in air (mass 28.8) at 300 K based on equation 1.12 (163 MHz).



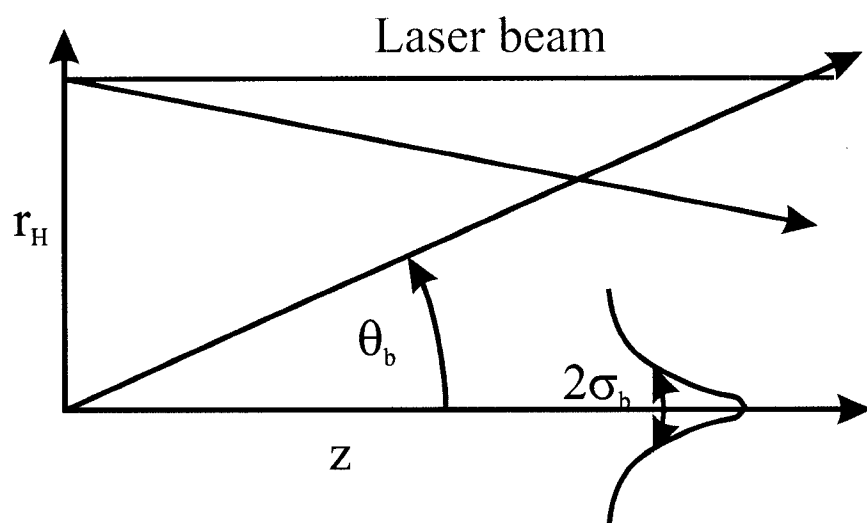
3.3.4 Line shape model

When the pulsed nozzle is placed in the axial position, the Doppler components are observed to have approximate Gaussian envelopes. The lowest observed full width at half maximum (FWHM) in the experiments was 46 MHz (CO₂ in air at 1 atm backing pressure). If He is employed as the carrier gas at backing between 2 and 8 atm, the Doppler components have a FWHM of 60 to 80 MHz. A close inspection of the line shapes reveals that both Doppler components are somewhat broadened towards the center of the pair. This effect is particularly pronounced when light carrier gases such as He or H₂ are used.

The observed line width can be explained by residual Doppler broadening resulting from selective sampling of different velocity components of the molecular expansion by the laser beam. The orientation of the laser beam with respect to the molecular expansion is shown in Fig 3.7. The laser spots on the spherical mirror are radially displaced from the center by a distance $r_H = 1$ cm due to the finite size of the coupling hole. A fraction of the molecules will leave the nozzle at a relative large angle θ_b with respect to the optical axis of the cavity. These molecules have somewhat smaller velocity components along the cavity axis than the majority and their absorptions have therefore smaller Doppler shifts. This leads to a slight broadening of the Doppler components towards the center frequency. The exact angular distribution of trajectories has in the past been described by empirical equations that mostly take the form of cosine functions.⁹ In the model presented here, the velocities are assumed to have a Gaussian distribution of angle θ_b with spread σ_b .

Figure 3.7

Definition of the coordinate system for the axial line shape model. r_H is the radius of the laser spots on the mirror (Fig. 2.3). The molecules leave the nozzle at an angle θ_b with respect to the optical axis. The angular distribution of the velocities is approximated as a Gaussian function of half-width σ_b .



When the molecules leave the pin hole nozzle, a nearly uniform speed distribution is achieved in the direction of the gas flow through a series of inelastic collisions. The molecules then leave the nozzle traveling at the speed $v_b = v_0 \pm \delta v_b$, where δv_b represents a small Gaussian distribution of velocities. The velocity v_{eff} projected onto the laser beam, is given by

$$v_{\text{eff}} \approx v_z = v_b \cos\left(\tan^{-1}\left(\frac{r(z)}{d_m}\right)\right) = \frac{v_b}{\sqrt{1 + \left(\frac{r(z)}{z}\right)^2}} \quad (3.1)$$

where $r(z)$ is the distance of the laser beam from the optical axis, and d is the position on the optical axis relative to the nozzle origin. In the Herriott cell, the laser beam travels both diagonally through the cell and parallel to the optical axis, so that

$$r(z)^{\text{par}} = r_H = 1 \text{ cm} \quad (3.2)$$

and

$$r(z)^{\text{dia}} = r_H - (2r_H/d_m) z \quad (3.3)$$

where d_m is the separation of the two mirrors. The magnitudes of the Doppler shifts are determined from equations 3.1 and 1.9. The relative weights of each Doppler component is given by the gas density observed in the laser path. The gas density ρ is a function of both the (Gaussian) angular distribution θ_b and the distance z from the nozzle:

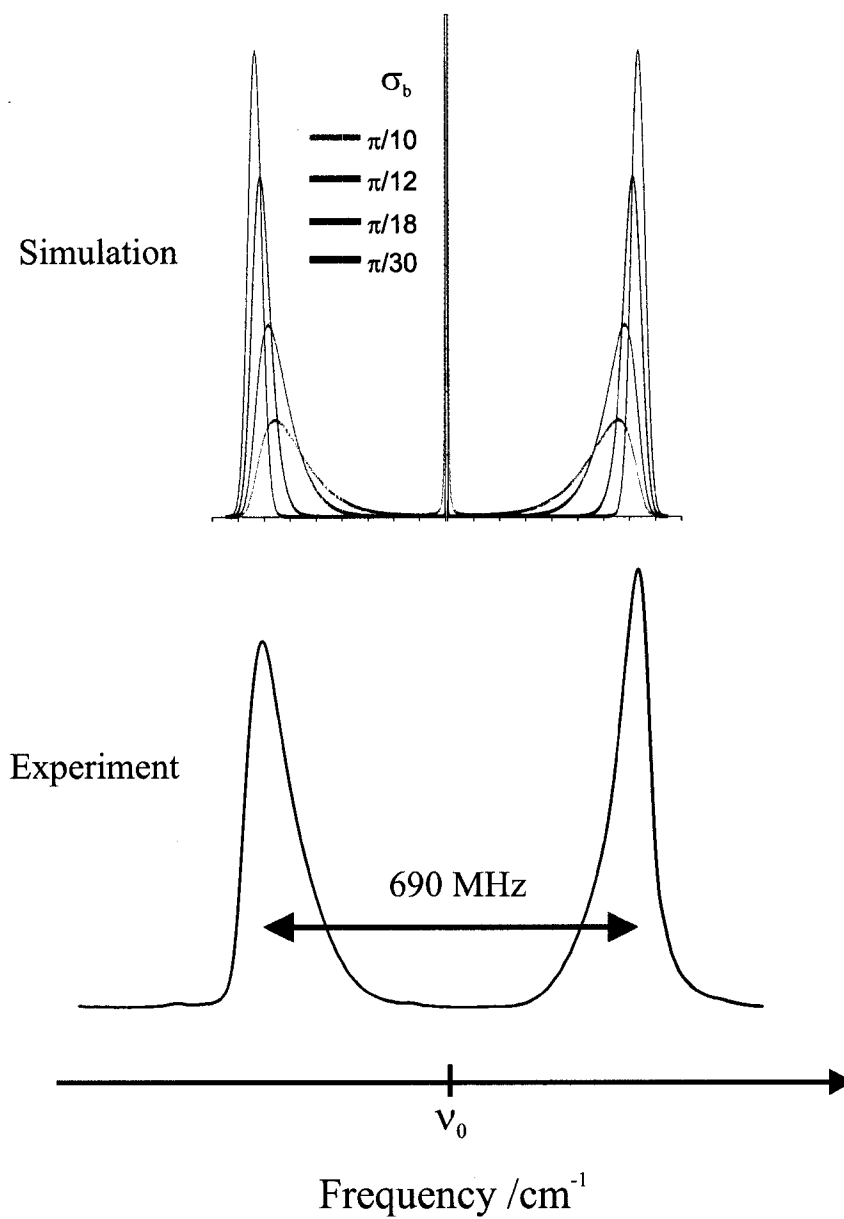
$$\rho \propto \frac{1}{Z^2} e^{-\frac{[\tan^{-1}(\frac{r(z)}{Z})]^2}{\sigma_b^2}} \quad (3.4)$$

Equation 3.4 can be normalized numerically. From equations 3.1-3.4 and the Doppler equation 1.9, the line shape function of the axial molecular expansion signal can be calculated numerically using a Maple spreadsheet (Appendix C). In Fig. 3.8, simulated line shapes are compared to an experimental line shape of the R(1) transition of ^{18}OCO line, generated in the expansion of a trace amount of carbon dioxide in He using a sample backing pressure of 8 atm. Good agreement of simulation and experiment is obtained if the angular spread of the beam σ_b is $\pi/30$ or 6° . If the angular distribution is wide (i.e. $\sigma_b > \pi/12$ or 15°), the model predicts unshifted absorption at the line center frequency. Absorption at peak center was not observed in the early stages of the molecular beam, proving that a significant portion of the molecules travels in a fairly narrow cone toward the far mirror.

In high resolution experiments on weak absorption lines, the broadening of the Doppler doublet towards the peak center is hardly noticeable. In this case, the parameters of the simplified Gaussian expression shown in equation 3.5 are fit to the observed Doppler pair. The fitting parameters are FWHM $\Delta\nu_D$, amplitude $I(\nu_0)$, Doppler splitting $\Delta\nu$, and center frequency ν_0 :

Figure 3.8

Comparison of the calculated Doppler line shape (top) with the line shape of the R(1) transition of ^{18}OCO (bottom) observed during the expansion of a trace amount of carbon dioxide in He carrier gas at 8 atm backing pressure.



$$I(\nu) = I(\nu_0) \left(e^{-\frac{4 \ln(2) \left(\nu - \nu_0 - \frac{\Delta\nu}{2}\right)^2}{\Delta\nu_D^2}} + e^{-\frac{4 \ln(2) \left(\nu - \nu_0 + \frac{\Delta\nu}{2}\right)^2}{\Delta\nu_D^2}} \right) \quad (3.5)$$

Lorentzian expressions were also used for data analysis, giving the same center frequencies and Doppler splittings as the Gaussian expressions.

A lower limit for the line width is set by the laser line width, which the manufacturer specifies as 20 MHz. Since the Airy equation (1.16) is well-reproduced by a Lorentzian function, the experimental line shape should have a 20 MHz wide Lorentzian component. The group led by Nesbitt routinely deconvolves their experimental line shapes obtained with a slit nozzle into a Gaussian and a Lorentzian component.^{100,101,103,126} However, because the lowest achieved Doppler width in the experiments was 46 MHz, this Lorentzian component is sufficiently masked by the Gaussian line shape.

3.3.5 Beam evolution, speed and lifetime

Molecular beam spectra acquired by fast-scan modulation spectroscopy are also a record of the time evolution of the molecular expansion. The time evolution of the molecular beam was followed and characterized using both fast scan and lock-in amplification methods. The results are shown in Fig. 3.9. The fast scan modulation pattern is shown in the top trace; the modulation amplitude was reduced to 6 mA (~0.18 cm⁻¹) and the scan repetition rate increased for this experiment. The laser frequency was modulated near the R(0) transition of CO₂ at 2349.917 cm⁻¹. The position in the

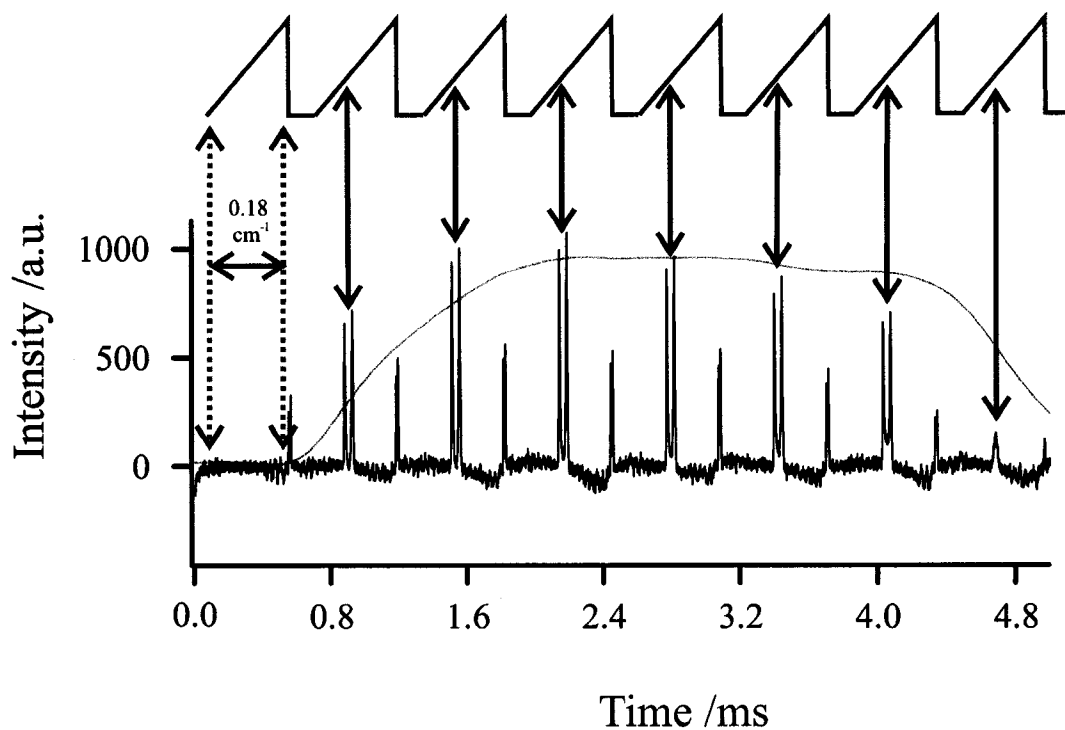
modulation pattern where this frequency is traversed is marked by the solid arrows. 100 scans were accumulated and co-added, and the background subtracted spectrum (bottom trace) was boxcar-averaged (51 points) before presentation. In the fast scan spectrum one can see the Doppler doublet arising from the coaxial expansion. The end of the molecular expansion is signaled by the disappearance of the characteristic Doppler doublets and by the appearance of CO₂ monomer transitions. The increase of the absorption at the center frequency from frame to frame is consistent with CO₂ molecules drifting back into the laser beam after colliding with the chamber walls. This explanation is supported by the occasional observation of intense monomer transitions from higher ro-vibrational states with a diminished Doppler splitting in the expansions spectra. These molecules do not appear to be in equilibrium with the main beam, judging from the unchanged Doppler splitting and relative intensity distribution of nearby transitions. If He is used as carrier gas, molecular beam lifetimes are typically 1.5 ms or shorter. When Ne, Ar or air are used, the beam can be observed for as long as 4 ms. In the last frame of Fig 3.9, only a single Doppler-broadened peak at the center frequency is visible, indicating the end of the molecular beam. The difference in the peak heights of the two Doppler components in Fig. 3.9 is a result of the increase of laser power with frequency. In the frequency modulation experiment, the laser was detuned from the center frequency, slightly beyond one of the Doppler components, and modulated at 50 kHz. The resulting 1f-demodulated signal thus samples only one line of the Doppler pair. However, because of continuous sampling over the absorption line a duty cycle much higher than for the fast scan method is achieved. Note that only one molecular pulse was used to generate the 1f-demodulated signal (middle trace) compared to 100 molecular pulses for the fast-scan signal (bottom

trace).

The magnitude of the Doppler doublet splitting $\Delta\nu$ serves as a temporal snapshot of the speed at which the molecules are traveling. $\Delta\nu$ was often observed to decrease slightly during the duration of the pulse, probably because of selective sampling of slower molecules during the later states of the molecular beam experiment. We found that the beam speed is mainly a function of the carrier gas and is independent of the applied backing pressure. In He, for example, a typical value for $\Delta\nu$ is 0.0246 cm^{-1} . The beam speed is calculated from the linear Doppler shift to $v_z = (0.0123/2349.917) c = 1570\text{ m/s}$. In air, the average Doppler splitting is 0.0109 cm^{-1} , corresponding to a beam speed of 695 m/s . At these speeds, the molecules reach the far end of the multipass cell within the 0.6 and 1.3 ms lifetime of the molecular beam. Collisions with the far mirror apparently do not interfere with the experiment.

Figure 3.9

Time evolution of a pulse of ambient air characterized by fast scan and lock-in amplification methods. Shown in the top trace is the modulation pattern employed in the fast scan method. The transition shown is the R(0) line of CO₂, and the sample is air. The bottom trace shows the series of fast scan spectra, averaged over 100 molecular pulses. The middle trace shows the 1f-demodulated signal of a single Doppler component of a single molecular pulse.



3.3.6 Line intensities in the molecular beam

The intensity of the transitions in the molecular beam depends on the sample concentration, the line shape, the amount of gas injected into the vacuum chamber per pulse, and the beam temperature.

The beam temperature can be estimated from the relative line intensities of transitions from adjacent rotational energy levels. For a linear molecule like CO₂, molecular transitions are separated by $\sim 2B$. Since the B constants of CO₂ and ¹⁸OCO are ~ 11.7 GHz (~ 0.39 cm⁻¹) and ~ 11.0 GHz (~ 0.36 cm⁻¹), respectively,¹²⁷ at most two of the monomer transitions could be observed simultaneously in the scans that typically are ~ 1 cm⁻¹ wide. In contrast, the rotational constants of weakly bound van der Waals complexes are typically small, because of the relative large intermolecular separation of 3 to 4 Å. As a result, the spectra of van der Waals complexes are relative dense. From the intensity distribution of van der Waals spectra, the rotational temperature of the expanding gas can be determined using equation 1.2. An example spectrum of the Ar-CO₂ van der Waals complex is shown in Fig. 3.10. The observed intensities are consistent with a rotational temperature of the expansion of 1-2 K. Expansions in pure He yielded slightly colder beam temperatures (0.7-1 K). Cooling the pipes outside the spectrometer with dry ice did not further lower the beam temperature, but did improve the overall spectral appearance (i.e. higher S/N, smoother baseline), likely because of freeze-trapping of trace impurities like water vapor.

The amount of gas injected per pulse is determined primarily by the pulse nozzle driver settings and the backing pressure. In order to elucidate the dependence of the peak intensity on the backing pressure, a large steel sample reservoir was filled with

0.2% CO₂ in He, and the expansion spectrum of the CO₂ R(0) transition at 2349.917 cm⁻¹, averaged over 100 scans each, was recorded. The parameters $\Delta\nu$, $\Delta\nu_D$, and $I(\nu_0)$ of equation 3.5 were fit to the observed spectra. The line shape parameters $\Delta\nu$ and $\Delta\nu_D$ and therefore the speed of the beam were independent of the applied backing pressure. The line intensity $I(\nu_0)$ was found to follow the Beer-Lambert law (Fig. 3.11).

To avoid line saturation, the much weaker line intensities of (CO₂)₂ dimer transitions⁸⁵ were studied in a separate experiment (Fig 3.12). The observed line widths and Doppler splittings of the complex were again independent of the backing pressure. The line intensities clearly correlate with the quantum number assignment of the ground state, favoring lower J transitions at higher backing pressures (Fig 3.12). The preferential increase of the intensity of low J transitions indicates that the beam temperature drops as the backing pressure is increased.

Figure 3.10

Molecular expansion spectrum of the Ar-CO₂ van der Waals complex near 2349 cm⁻¹.

The sample consisted of 0.2% CO₂, 20% Ar and 80 % He at 7 atm. 1000 scans were averaged. The observed intensities are consistent with a rotational temperature of the expansion of 1-2 K.

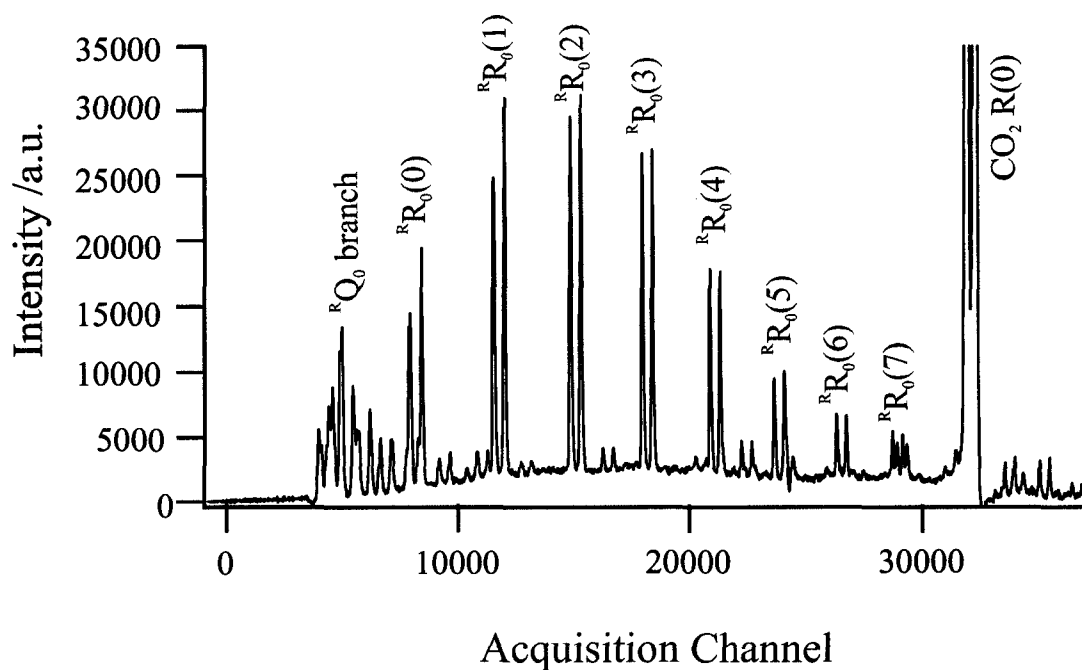


Figure 3.11

Intensity of the CO_2 R(0) transition as a function of backing pressure. The sample is 0.2% CO_2 in He carrier gas. The current sweep is 30 mA in 1 ms. 100 scans were averaged per point. The absorption line saturates at high backing pressure.

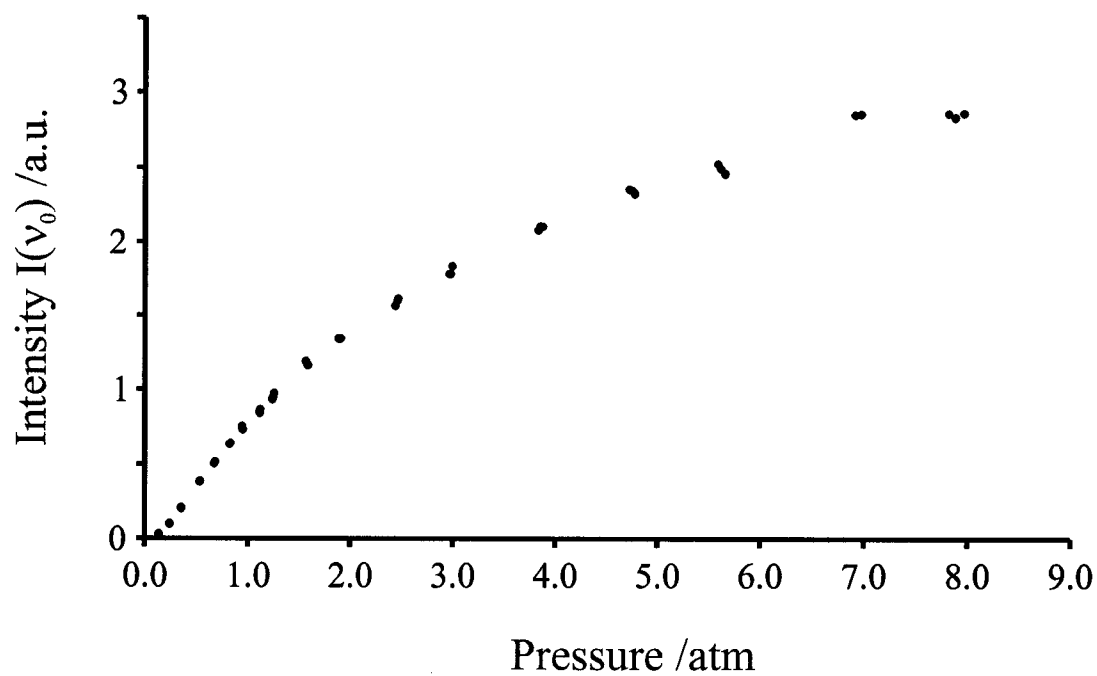
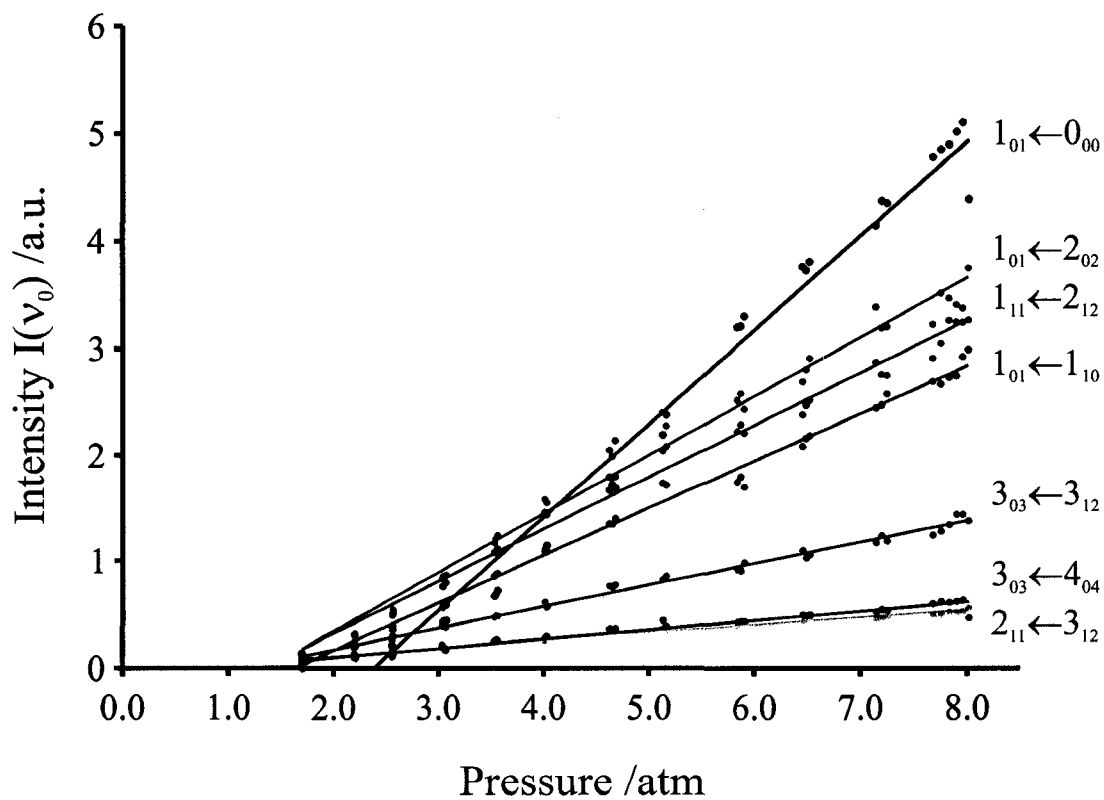


Figure 3.12

Intensities of selected $(\text{CO}_2)_2$ dimer lines as a function of backing pressure. The beam temperature reduces with applied backing pressure, as judged from the intensity ratios of adjacent energy levels. The sample consisted of 0.5% CO_2 in He carrier gas. 100 scans were averaged per data point.



3.3.7 Spectra of van der Waals complexes

We recorded the mid-infrared spectra of several van der Waals complexes, including Ar-CO₂,⁸⁶ (CO₂)₂⁸⁵ and He-CO₂.¹⁰³ These were chosen because their mid-infrared spectra are known and could serve to optimize sample conditions and evaluate the performance of the spectrometer. An example spectrum of Ar-CO₂ is shown in Fig. 3.13. The P, Q, and R branches of the K_a = 1←0 stack are shown. This spectrum illustrates several aspects of the axial molecular beam diode laser spectrometer, among them a properly functioning frequency lock, baseline subtraction, and increased spectral congestion due to Doppler doubling. The broad baseline features visible in the spectrum in Fig. 3.13 are mainly due to formation of higher order clusters, and are not a result of a failing background subtraction. The broad absorption features of atmospheric carbon dioxide and the steeply sloped background typical of diode lasers have been effectively removed by background subtraction. One must keep in mind, though, that the transition intensities shown in the spectrum are dependent on the incident laser power, which is not constant in a regular frequency scan.

To assess accuracy and precision of the instrument, transitions of the weakly bound dimers (CO₂)₂⁸⁵ and He-CO₂¹⁰³ were recorded repeatedly over a period of several days and analyzed. Frequencies of (CO₂)₂ were reproduced within 0.0004 cm⁻¹ of the predictions based on the previously⁸⁵ reported spectroscopic constants (Table 3.2). Precise results were obtained because the line shape of the entire Doppler doublet was used in the numerical fit. The He-CO₂ frequencies were reproduced to within 0.0008 cm⁻¹ of the previously¹⁰³ measured values. In this case, the experimental results reproduce

more poorly because both measured and literature frequencies are experimental values and not as accurate as the model for $(\text{CO}_2)_2$.

In general, the measurement accuracy of the spectrometer is limited by the nonlinear tuning rate of the lead salt diode, which cannot be exactly expressed by a polynomial function. Higher uncertainty exists especially in the relative large gaps between known CO_2 transitions. In addition to polynomial functions, several different equation types, such as polynomials with variable non-integer exponents, were tested with mixed success. Ultimately, a high-finesse and low free spectral range temperature- and pressure-stabilized étalon would lead to better frequency calibration.

The line widths of different transitions of the complexes (Table 3.3) varied substantially but reproducibly between 55 and 109 MHz FWHM for $(\text{CO}_2)_2$, and between 84 and 94 MHz FWHM for He-CO_2 . CO_2 monomer lines were narrower, down to 46 MHz FWHM. The different line widths for monomer and complexes may be a result of predissociation broadening. Vibrational predissociation of the CO_2 dimer in particular has been investigated by Pine and Fraser.¹²⁸ In the original work on He-CO_2 , lifetime broadening was masked by what was thought to be excess laser jitter¹⁰³; however, lifetime broadening has been demonstrated recently by the same group for the similar complex $\text{H}_2\text{-H}_2\text{O}$.¹²⁶

In addition to dimer interactions, higher order clusters can also be investigated with this spectrometer. In Fig. 3.14, the $R(0)$ transitions of $\text{He}_N\text{-CO}_2$ are shown for $N=1$ to 4. This assignment was recently confirmed by Tang and McKellar.¹²⁹

Figure 3.13

A portion of the Ar-CO₂ spectrum near 2349 cm⁻¹. The sample was 8% CO₂ in Ar carrier gas at a pressure of 2 atm. 2000 cycles were averaged. The ^RP₀, ^RQ₀, ^RR₀ branches (from left to right) are clearly visible. The elevated background is due to the formation of higher order clusters. The negative spike at 2349.0 cm⁻¹ is due to a CO₂ monomer line. Such lines are due to residual static gas present in the sampling region and were recorded during the background scan. Their presence could have been avoided by a lower molecular pulse repetition rate.

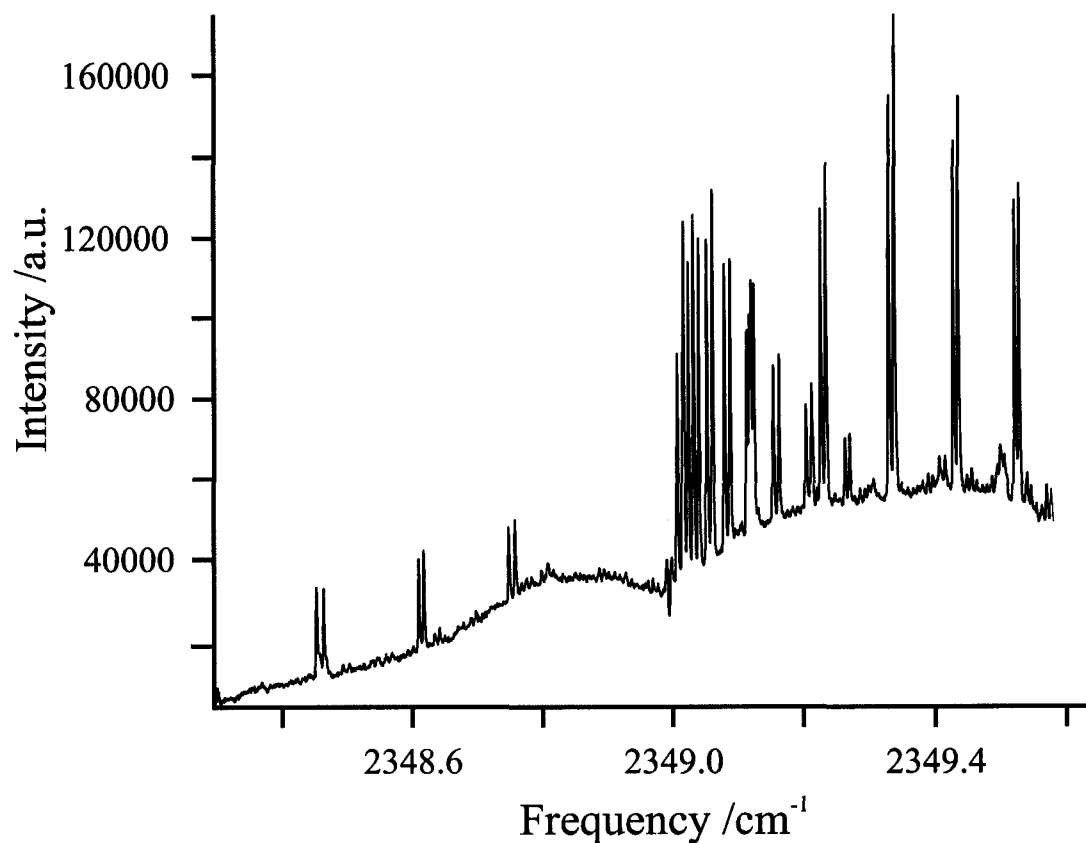


Table 3.2

Comparison of measured frequencies of selected CO₂, (CO₂)₂ and He-CO₂ transitions to literature values.

Molecule	Transition	ν_{obs} /cm ⁻¹	σ_{obs} /cm ⁻¹	n_{obs}	ν_{Lit} /cm ⁻¹	$\Delta(\nu_{\text{obs}} - \nu_{\text{Lit}})$ /cm ⁻¹
CO ₂	R(0)	2349.91710	± 0.00044	10	2349.91723 ¹²⁷	- 0.00013
(CO ₂) ₂	1 ₀₁ ← 0 ₀₀	2350.86965	± 0.00008	33	2350.87056 ⁸⁵	- 0.00091
(CO ₂) ₂	1 ₀₁ ← 2 ₀₂	2350.57413	± 0.00005	33	2350.57401 ⁸⁵	+ 0.00012
(CO ₂) ₂	1 ₀₁ ← 1 ₁₀	2350.51685	± 0.00006	33	2350.51670 ⁸⁵	+ 0.00015
(CO ₂) ₂	3 ₀₃ ← 3 ₁₂	2350.49320	± 0.00008	33	2350.49282 ⁸⁵	+ 0.00037
(CO ₂) ₂	2 ₁₁ ← 3 ₁₂	2350.46188	± 0.00006	33	2350.46206 ⁸⁵	- 0.00019
(CO ₂) ₂	3 ₀₃ ← 4 ₀₄	2350.37532	± 0.00010	33	2350.37566 ⁸⁵	- 0.00035
He-CO ₂	1 ₁₀ ← 1 ₀₁	2349.48653	± 0.00036	13	2349.4874 ¹⁰³	- 0.00087
He-CO ₂	1 ₁₁ ← 0 ₀₀	2349.86497	± 0.00013	13	2349.8646 ¹⁰³	+ 0.00037
He-CO ₂	2 ₁₂ ← 1 ₀₁	2350.22755	± 0.00028	13	2350.2264 ¹⁰³	+0.00115

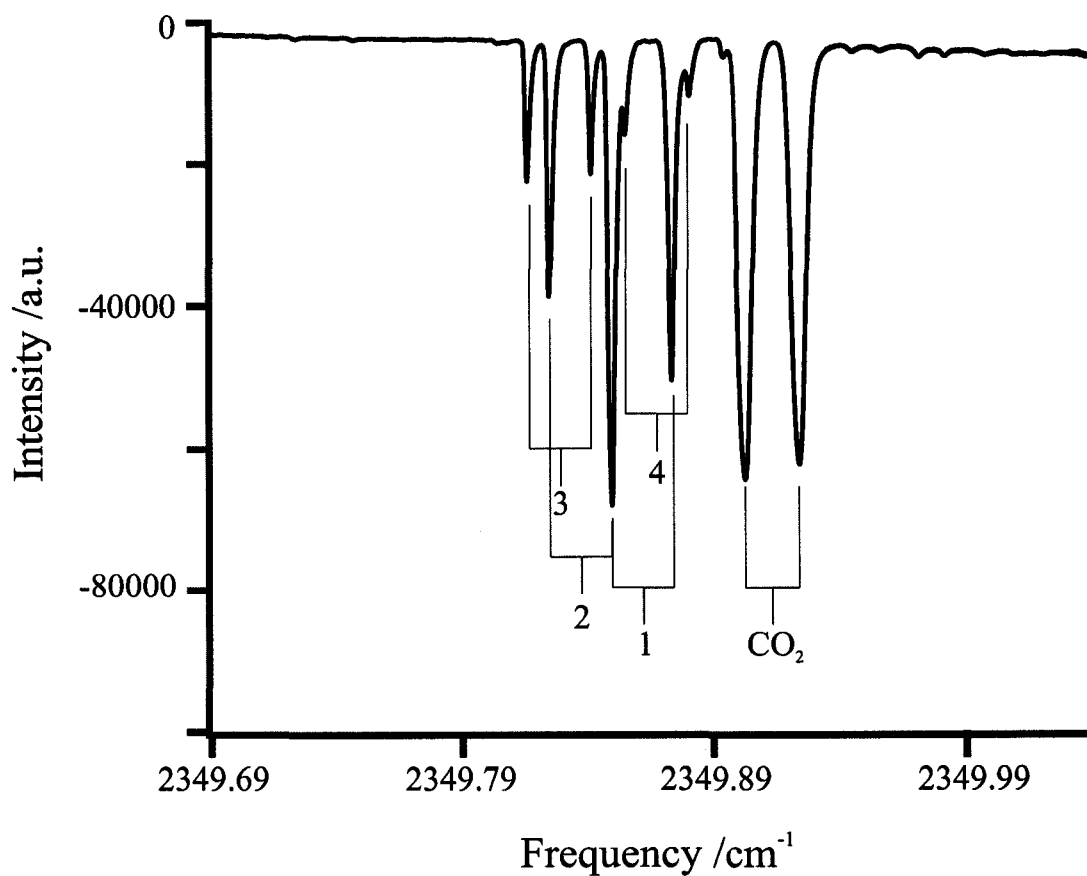
Table 3.3

Summary of observed line widths of selected CO₂, (CO₂)₂ and He-CO₂ transitions.

Molecule	Transition	FWHM /cm ⁻¹	σ_{obs} /cm ⁻¹	FWHM /MHz	σ_{obs} /MHz
CO ₂	R(0)	0.00131	± 0.00002	46.3	± 0.6
(CO ₂) ₂	1 ₀₁ ← 0 ₀₀	0.00364	± 0.00028	109	± 8.4
(CO ₂) ₂	1 ₀₁ ← 2 ₀₂	0.00234	± 0.00006	70.2	± 1.8
(CO ₂) ₂	1 ₀₁ ← 1 ₁₀	0.00232	± 0.00016	69.6	± 4.8
(CO ₂) ₂	3 ₀₃ ← 3 ₁₂	0.00282	± 0.00030	84.6	± 9.0
(CO ₂) ₂	2 ₁₁ ← 3 ₁₂	0.00184	± 0.00014	55.2	± 4.2
(CO ₂) ₂	3 ₀₃ ← 4 ₀₄	0.00294	± 0.00028	88.2	± 8.4
He-CO ₂	1 ₁₀ ← 1 ₀₁	0.00310	± 0.00018	93.0	± 5.4
He-CO ₂	1 ₁₁ ← 0 ₀₀	0.00280	± 0.00008	84.0	± 2.4
He-CO ₂	2 ₁₂ ← 1 ₀₁	0.00312	± 0.00014	93.6	± 4.2

Figure 3.14

Spectrum of He_NCO_2 showing the R(0) transitions of $N=1$ to $N=4$. The sample consisted of 0.3% CO_2 in 21 atm He. 100 scans were acquired over 20 minutes.



3.4 Summary

The spectrometer's adaptability towards recording spectra of van der Waals complexes has been evaluated. The fast-scan technique was found to outperform traditional frequency modulation techniques with regards to acquisition of spectra of samples in a molecular beam. The lead salt diodes were found to cover several frequency regions in single mode output, in particular near the asymmetric stretching fundamental of CO₂ and ¹⁸OCO. Selective signal enhancement in a molecular beam was demonstrated for the R(0) line of CO₂. The novel axial sample introduction results in sensitivity enhancement due to narrower line widths and longer residence time of the molecular beam in the sampling region. The observed doublet line shape is reproduced by Doppler broadening model. Line intensities in the molecular beam were observed to follow the Beer-Lambert law. The lifetime of the supersonic molecular expansion was determined to be on a ms scale. The suitability of the spectrometer to study van der Waals complexes in the IR has been demonstrated. In the following chapters, the spectra of several novel van der Waals complexes containing the CO₂ subunit are presented and analyzed.

CHAPTER 4

THE MID-INFRARED SPECTRUM OF CO₂-SO₂

4.1 Introduction

In this Chapter, the mid-infrared spectrum of the weakly bound complex CO₂-SO₂ near the asymmetric stretch of CO₂ at 2349 cm⁻¹ is presented and analyzed. The spectral assignment is directly confirmed by microwave-infrared double resonance experiments. This work follows up on a previous Fourier transform microwave study¹⁰⁵ of CO₂-SO₂ and several of its isotopomers. The microwave spectrum of CO₂-SO₂ consists purely of *a*-type transitions (Table 4.1). Transitions to and from energy levels with odd K_a value are absent for symmetrically substituted isotopomers as a result of nuclear spin statistics. A full set of *a*-type transitions can be observed when the symmetry is broken through unsymmetric substitution. Due to the restrictive selection rules for symmetrically substituted versions of this complex, there is not enough information in the microwave spectrum of the main isotopomer to independently determine a complete set of spectroscopic constants. A fit using Watson's S-reduction Hamiltonian in the I' representation¹³⁰ was only possible after constraining the molecular *A* constant to a value of 5500 MHz, extrapolated from the molecular constants of nonsymmetrically substituted isotopomers and the proposed equilibrium structure.¹⁰⁵ In contrast to the situation in the microwave range, the mid-infrared spectrum is predicted to consist of *c*-type transitions, since the asymmetric stretching mode of CO₂ is parallel to the molecular *c*-axis. One of the goals of this study is therefore to achieve a much more precise determination of the

molecular constants of CO₂-SO₂ through a combined fit of *a*-type microwave and *c*-type infrared transitions.

4.2 Molecular symmetry (MS) group analysis

4.2.1 Choice of MS group

Molecular symmetry group (MS) theory¹³¹ is widely used in the spectral analysis of weakly bound systems such as CO₂-SO₂ because of possible internal motions. In an MS analysis, it is important to decide which symmetry operations are feasible, and often this can only be decided upon after investigating the observed spectra. For example, labeling the oxygen nuclei on the CO₂ moiety 1 and 2, and the oxygen nuclei on SO₂ 3 and 4, chemical intuition suggests that feasible molecular symmetry group operations for this molecule might include the elements of the G₈(M) group¹³¹ E, (12), (34), E*, (12)(34), (12)*, (34)*, and (12)(34)*. However, the operations (12), (34), E*, and (12)(34)* involve an internal rotation-contortion motion of the complex, and the feasibility of these operations depends on the barrier height for internal rotation.

Figure 4.1

Proposed¹⁰⁵ equilibrium structure of the CO₂-SO₂ van der Waals complex.

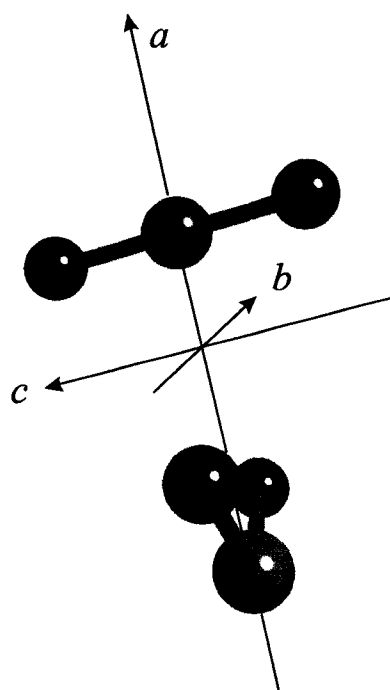


Table 4.1

Previously¹⁰⁵ observed microwave transitions of CO₂-SO₂.

J_{KaKc}'	J_{KaKc}''	Frequency /MHz
2 ₀₂	1 ₀₁	5998.642
3 ₂₂	2 ₂₁	8993.168
3 ₂₁	2 ₂₀	8993.534
3 ₀₃	2 ₀₂	8997.498
4 ₂₃	3 ₂₂	11990.289
4 ₂₂	3 ₂₁	11991.206
4 ₀₄	3 ₀₃	11995.780
5 ₂₄	4 ₂₃	14986.892
5 ₂₃	4 ₂₂	14988.720
5 ₀₅	4 ₀₄	14993.306

Table 4.2

The molecular symmetry group $G_4(M)$.¹³¹

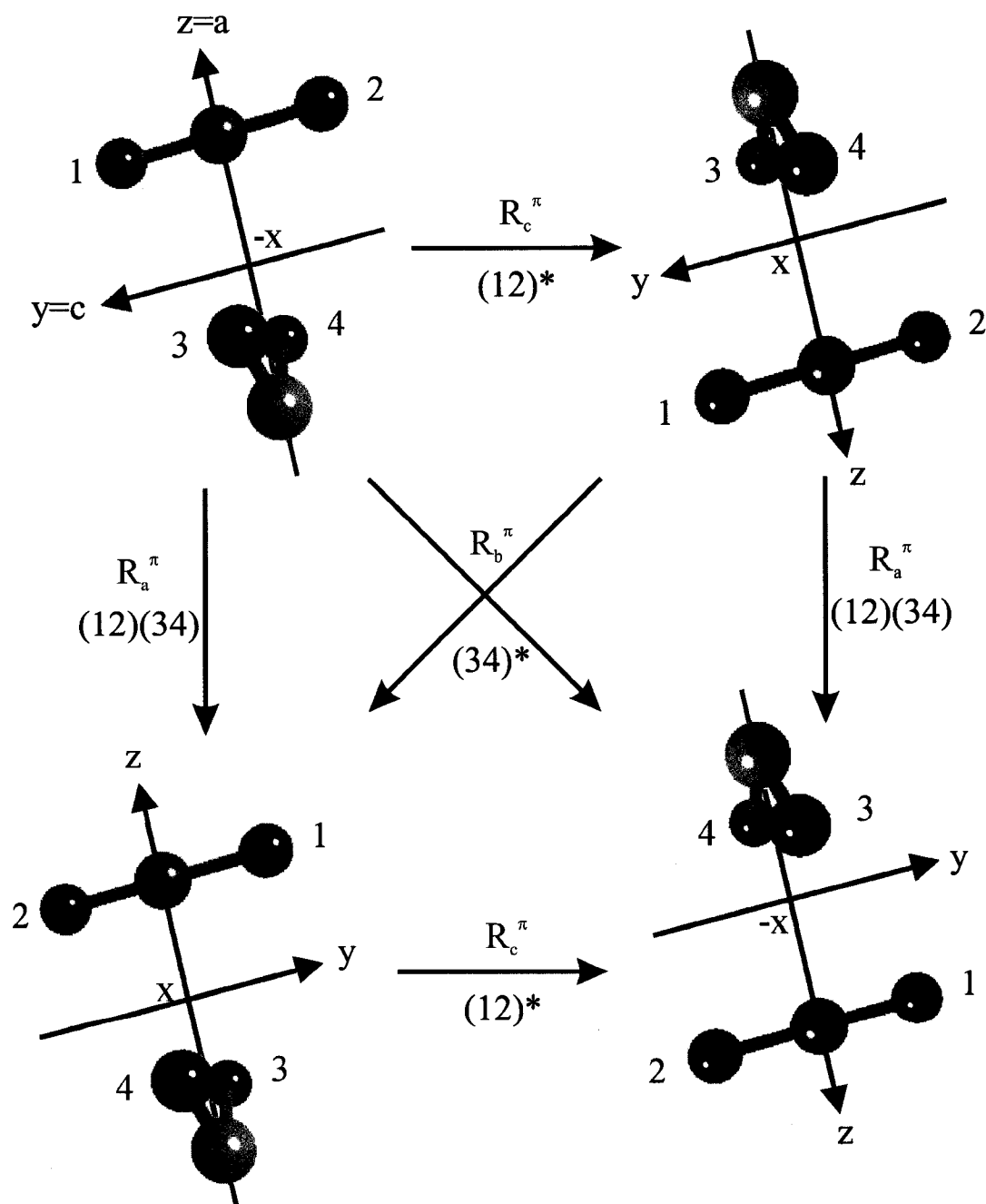
$G_4(M)$: Equiv. Rot.: Γ :	E R^0	(12)(34) R_a^*	(12)* R_c^*	(34)* R_b^*	$\Gamma(G_8)$
A ₁ :	1	1	1	1	A ₁ ', A ₂ ''
A ₂ :	1	1	-1	-1	A ₁ '', A ₂ '
B ₁ :	1	-1	1	-1	B ₁ '', B ₂ '
B ₂ :	1	-1	-1	1	B ₁ ', B ₂ ''

If the internal rotation is unhindered, all operations of the molecular symmetry group $G_8(M)$ are feasible. In the intermediate case, where internal rotation occurs over a finite potential energy barrier, the $G_8(M)$ group can still be used, as it was done by Columberg *et al.* in their analysis of the $\text{CO}_2\text{-H}_2\text{O}$ system.¹³² However, Soldán¹³³⁻¹³⁵ has shown that in the general case of a pair of coaxial internal rotors the molecular symmetry group should be extended with the symmetry operation E' to remove the double-valuedness when classifying the wavefunctions Ψ_{tor} , Ψ_{vib} and Ψ_{rot} separately. The resulting group is commonly referred to as an extended molecular symmetry (EMS) group.¹³¹

If the barriers to internal rotation are high, or in the absence of experimental evidence for tunneling, the operations (12), (34), E^* and (12)(34)* are deemed unfeasible. The system can then be treated as a rigid rotor and described using the smaller MS group $G_4(M) = \{E, (12)(34), (12)^*, (34)^*\}$ (Table 4.2). For $\text{CO}_2\text{-SO}_2$, there has been no conclusive evidence for internal rotation - contortion motions within the complex. Therefore, the MS group $G_4(M)$ is used in the analysis. The symmetry operations of the $G_4(M)$ group are depicted graphically in Fig. 4.2.

Figure 4.2

Feasible symmetry operations of $\text{CO}_2\text{-SO}_2$. The equivalent rotations¹³¹ are identified in the figure.



4.2.2 Nuclear spin statistics

Because CO_2 - SO_2 contains two sets of equivalent oxygen nuclei, which are bosons, the overall wavefunction must remain unchanged upon their exchange:²⁸

$$(12) \Psi_{\text{tot}} = + \Psi_{\text{tot}} \quad (4.1)$$

$$(34) \Psi_{\text{tot}} = + \Psi_{\text{tot}} \quad (4.2)$$

From equations 4.1 and 4.2 it follows that

$$(12) (34) \Psi_{\text{tot}} = + \Psi_{\text{tot}} \quad (4.3)$$

As a result of equation 4.3, the only spin-allowed total wavefunctions Ψ_{tot} are those that transform as A_1 or A_2 :

$$\Psi_{\text{tot}} \in \{A_1, A_2\} \quad (4.4)$$

The total wavefunction Ψ_{tot} is assumed¹³¹ to be separable into vibrational, rotational, electronic, nuclear, and internal rotation parts:

$$\Psi_{\text{tot}} = \Psi_{\text{rot}} \otimes \Psi_{\text{vib}} \otimes \Psi_{\text{elec}} \otimes \Psi_{\text{nucl}} \otimes \Psi_{\text{tor}} \quad (4.5)$$

Ψ_{elec} and Ψ_{nucl} and Ψ_{tor} are completely symmetric, due to the absence of any

electronic or nuclear spin and higher internal rotation-contortional states, and therefore transform as A_1 . This leaves only the characters of the vibrational (Ψ_{vib}) and rotational (Ψ_{rot}) wavefunctions to be determined.

4.2.3. Classification of the vibrational wavefunctions Ψ_{vib} in $G_4(M)$

The vibrational ground state transforms as the completely symmetric representation A_1 . The symmetry species of the asymmetric stretching mode of CO_2 can be deduced by determining the transformation properties of the (cartesian) internal displacement coordinates Δr_1 and Δr_2 under the effects of the symmetry operations in $G_4(M)$.¹³¹ Δr_1 is the displacement (parallel to the molecular c -axis) of oxygen atom 1 from its equilibrium position, and Δr_2 is the displacement of oxygen atom 2 from its equilibrium position. Because the stretching motion can be either symmetric or asymmetric, representations of both modes are generated by the Cartesian displacement coordinates.¹³¹ The character $\chi[E]$ (the sum of the diagonal matrix elements) under the identity operation E is +2. The operation (12)(34) exchanges Δr_1 and Δr_2 , so that the character is $\chi[(12)(34)]$ is 0. The operation (34)* inverts the signs of Δr_1 and Δr_2 . However, under the (34)* operation, the y -axis also changes sign, so that the signs of Δr_1 and Δr_2 are not changed overall (see Fig 4.2). The character $\chi[(23)*]$ under the (23)* operation is therefore +2. The characters of the representation Γ_{car} can be expressed in terms of the irreducible representations as $A_1 \oplus B_2$. The asymmetric stretching mode therefore transforms as B_2 .

4.2.4 Classification of the rotational wavefunctions Ψ_{rot} in $G_4(M)$

For an asymmetric top molecule like the near-prolate CO_2 - SO_2 the rotational eigenfunctions are linear combinations of the symmetric top functions. The transformation properties of the rotational wavefunctions can be deduced from the asymmetric top symmetry rule¹³¹ and knowledge of the equivalent rotations (Table 4.2). The asymmetric top symmetry rule states that rotational wavefunctions with $K_a = K_c =$ even transform as the totally symmetric representation, the eo functions ($K_a =$ even, $K_c =$ odd) as the representation having +1 for R_a^n and -1 for R_b^n and R_c^n , the oe functions as +1 for R_c^n and the oo function as +1 under R_b^n . The resulting labels of the rovibrational wavefunctions of the vibrational ground and excited state are summarized in Table 4.3.

4.2.5 Energy levels and selection rules

From the results in Sections 4.2.3 and 4.2.4, the symmetry labels of rovibrational molecular energy levels with non-zero spin statistical weight can be derived. Only those energy levels whose total wavefunction transforms as per equation 4.4 need to be considered. For example, the symmetry of the total wavefunction of the 1_{10} rotational energy level in the vibrational excited state is calculated from equation 4.5 as $B_1 \otimes B_2 = A_2$ and is therefore populated following equation 4.4. The symmetry labels of a few low energy levels are shown in the energy level diagram shown in Fig. 4.3.

Table 4.3a

Symmetries of the rotational wavefunctions of CO₂-SO₂ in the vibrational ground state.

Equiv. Rot.: $ K_a K_c\rangle$	E R^0	(12)(34) R_a^π	(12)* R_c^π	(34)* R_b^π	Γ_{rot}
$ ee\rangle$	+1	+1	+1	+1	A ₁
$ eo\rangle$	+1	+1	-1	-1	A ₂
$ oe\rangle$	+1	-1	+1	-1	B ₁
$ oo\rangle$	+1	-1	-1	+1	B ₂

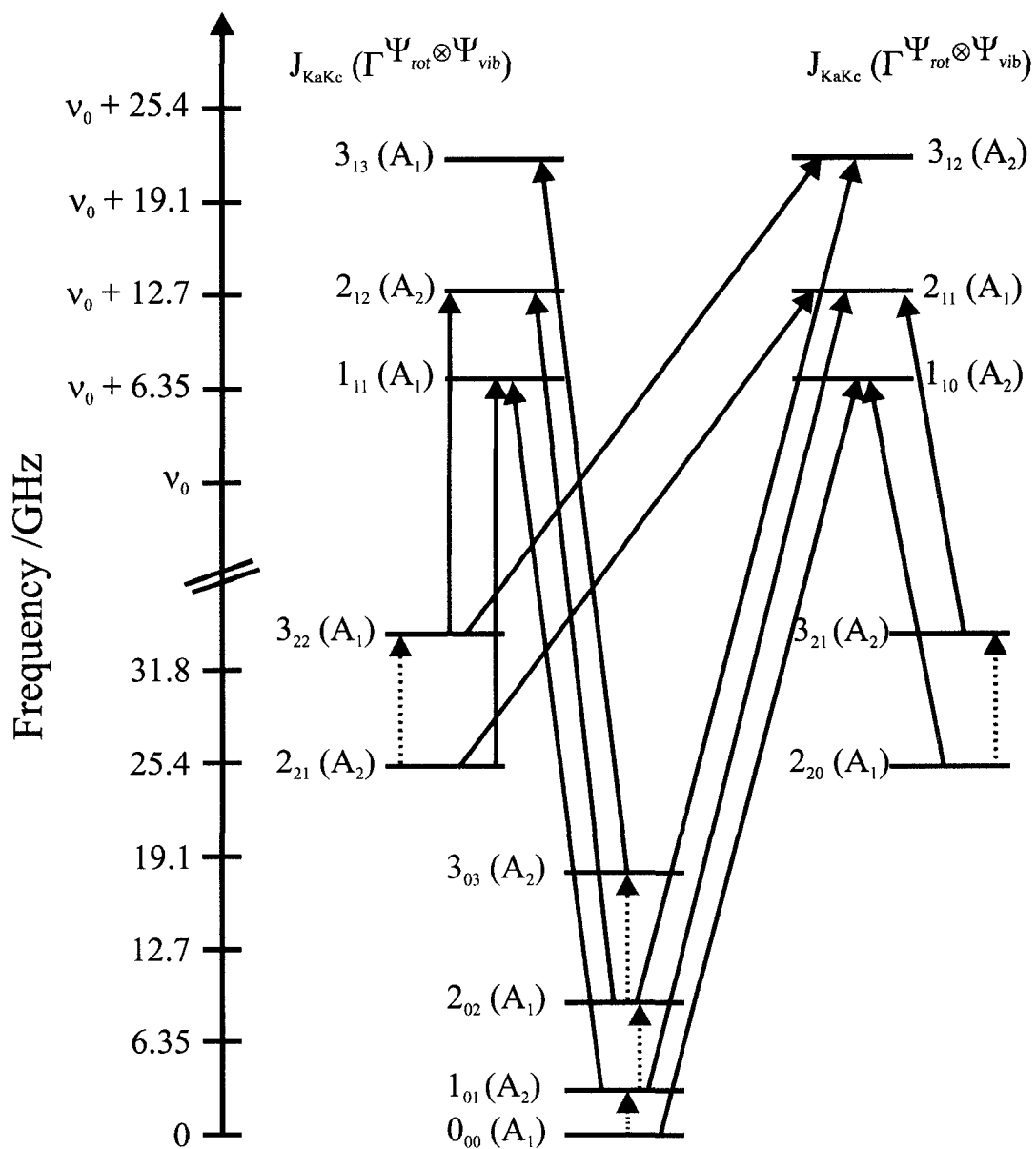
Table 4.3b

Symmetries of the ro-vibrational wavefunctions of CO₂-SO₂ in the B₂ excited vibrational state.

Equiv. Rot.: $ K_a K_c\rangle$	E R^0	(12)(34) R_a^π	(12)* R_c^π	(34)* R_b^π	$\Gamma_{\text{ro-vib}}$
$ ee\rangle$	+1	-1	-1	+1	B ₂
$ eo\rangle$	+1	-1	+1	-1	B ₁
$ oe\rangle$	+1	+1	-1	-1	A ₂
$ oo\rangle$	+1	+1	+1	+1	A ₁

Figure 4.3

Energy level diagram of CO₂-SO₂ (to scale) and representative transitions. Microwave *a*-type transitions are shown in dashed green, and infrared *c*-type ro-vibrational transitions are shown in solid red. The symmetry of the total wavefunction is given next to the energy level.



For a transition to be spin-allowed, the parity selection rule must be obeyed.¹³¹ Again, only the A symmetries need to be considered, since B₁ and B₂ levels have zero spin weight. The selection rule for the ro-vibrational transitions of the CO₂-SO₂ complex is therefore

$$A_1 \leftrightarrow A_2 \quad (4.6)$$

4.3 Experimental

Experiments were performed as described in Section 2.5.4. In the previous microwave experiments¹⁰⁵ a mixture of He and Ne (80% Ne and 20% He) was used as a carrier gas. We initially tried similar sample mixtures, but found that formation of Ne-CO₂ van der Waals complex⁸⁶ was competitive under these conditions. Due to the lower absolute resolution in the infrared, formation of secondary species leads to spectral overlap and should be avoided. Best results were obtained with a gas mixture consisting of 0.25% SO₂ and 0.75% CO₂ in 2-3 atm He carrier gas. From the observed Doppler shift of $\sim 0.012 \text{ cm}^{-1}$, the average molecular velocity was deduced to be $\sim 1500 \text{ m s}^{-1}$.

In the IR spectrum of CO₂-SO₂ many transitions of the (CO₂)₂ dimer⁸⁵ as well as He-CO₂¹⁰³ were observed. These transitions were identified by recording spectra of (CO₂)₂ and He-CO₂. The remaining lines could only be observed when both CO₂ and SO₂ were present in the sample reservoir. A portion of the infrared spectrum is reproduced in Fig. 4.4 (a-c).

Double resonance experiments were performed as described in Section 2.5.5. The microwave excitation frequencies were known from previous¹⁰⁵ work and are listed in Table 4.1. The concentrations of SO₂ and CO₂ in the sample gas could be increased relative to the single resonance experiments, because the background subtraction removes all absorption features that are not affected by double resonance. Formation of higher order clusters in the molecular beam is acceptable as long as the concentration of the dimer species also increases.

Because of the large dipole moment of SO₂ (1.634 D)¹³⁶, the microwave power (max. 500 mW) could be attenuated by 40 dB before reduction of the double resonance signal was observed. Similarly, the microwave radiation could be detuned by ~0.5 MHz at maximum power before the double resonance signal degraded. The double resonance experiment could therefore still be performed in the absence of the power amplifier.

4.4 Results

4.4.1 Spectral analysis and assignment

On the basis of the previous microwave work¹⁰⁵ and group theoretical analysis a *c*-type spectrum (with missing transitions as determined in Section 4.2.5) was anticipated. At first glance, the infrared spectrum of the CO₂-SO₂ complex consists of a series of approximately equally (~0.10 cm⁻¹) spaced lines, corresponding to the ^RP₀ and ^RR₀ branches of the complex. Sun *et al.*¹⁰⁵ used an Watson's S-reduction Hamiltonian¹³⁰ in the *I* representation, which was also used in this analysis. Initially, it was attempted to predict the experimental spectrum by constraining the upper state constants to the known¹⁰⁵ lower state constants. With exception of the main P and R branches, the

experimental spectrum could not be predicted in that manner, largely a result of the poorly known A constant.

At this point, a MW-IR double resonance experiment was performed, utilizing the known¹⁰⁵ microwave transition frequencies. In the double resonance experiment, the ground state quantum number assignments of the vibrational transitions are determined. An example is shown in Fig. 4.5. The transition intensity of the ${}^R R_0(3)$ or $4_{13} \leftarrow 3_{03}$ infrared transition is increased by pumping molecules from the 2_{02} to the 3_{03} rotational level in the vibrational ground state (bottom trace), and it is decreased by pumping molecules from the 3_{03} to the 4_{04} rotational level (middle trace). Because of its high selectivity, the MW-IR double resonance experiment showed improved spectral resolution compared to the single resonance infrared experiment. The resolution of the double resonance experiment is ultimately limited by the laser line width and scan reproducibility. The high resolution of the double resonance experiment enabled us to resolve and assign the narrowly spaced ${}^R Q_0$ branch of $\text{CO}_2\text{-SO}_2$, which could not be resolved in the single resonance infrared spectrum (Fig. 4.6). In the case of closely spaced Q branches, transitions from adjacent J levels are easily differentiated in a double resonance experiment because of the opposite effect of pumping on the absorption at each rotational level. In total, 17 transitions belonging to R, P, and Q branches were identified and assigned by double resonance.

The double resonance experiment greatly simplified the assignment of the remaining transitions in the infrared spectrum. More than 62 c -type infrared transitions were assigned (Table 4.4), but about a dozen transitions could not be identified (Table

4.5). The spectral parameters, which are summarized in Table 4.6, were obtained with Pickett's SPFIT program.¹³⁷ A stick spectrum comparing spectral data with the model is shown in Fig. 4.7. The rms error of the fit was 0.0006 cm^{-1} , approximately on the order of the experimental measurement uncertainty. The quality of fit did not significantly improve when additional parameters were added.

Figure 4.4 (a)

Mid-infrared expansion spectrum of the $\text{CO}_2\text{-SO}_2$ van der Waals complex. The simultaneously recorded spectrum of the reference cell containing CO_2 at a few torr pressure is superimposed on top. The sample consisted of 0.15% SO_2 , 0.45% CO_2 in He carrier gas at a backing pressure of 2 atm. 200 cycles were averaged per experiment.

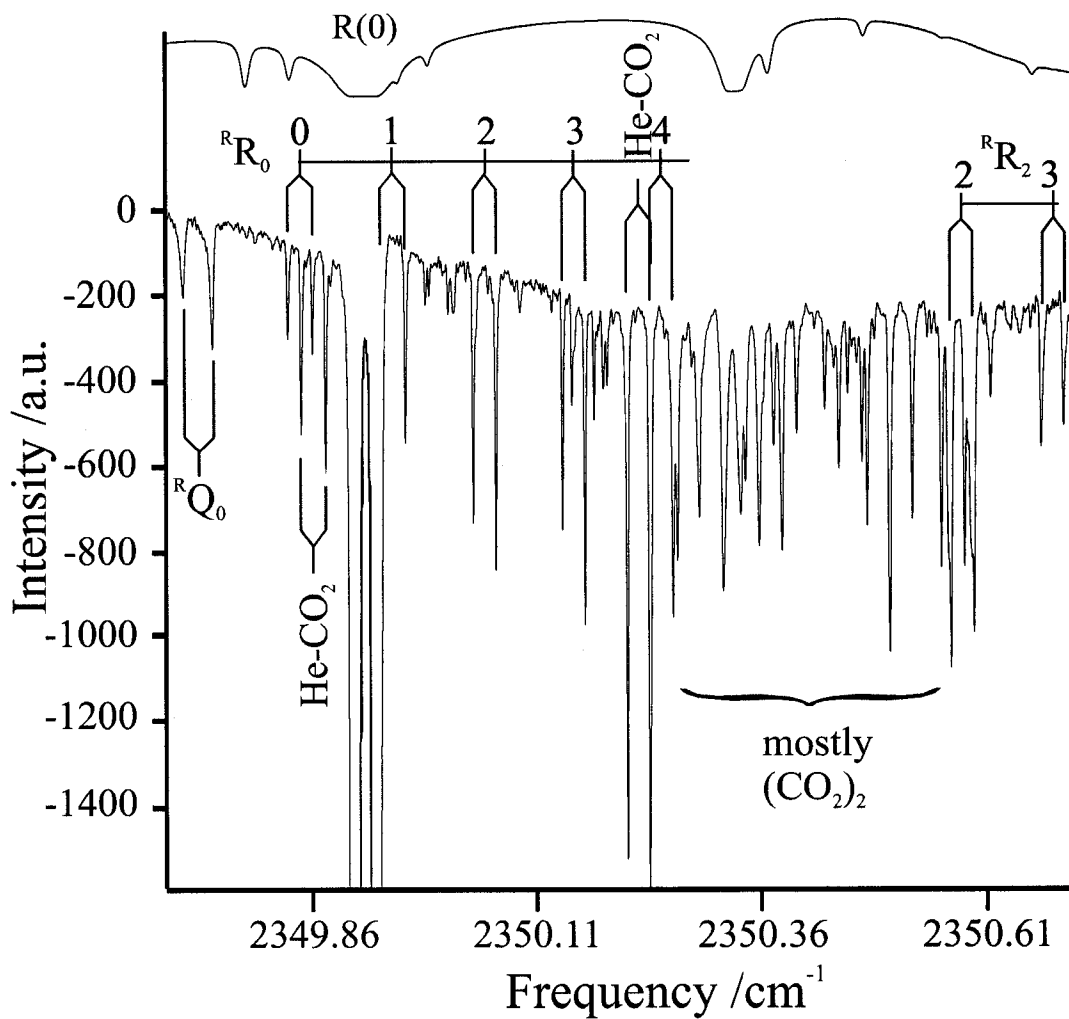


Figure 4.4 (b)

Mid-infrared expansion spectrum of the CO₂-SO₂ van der Waals complex (cont'd).

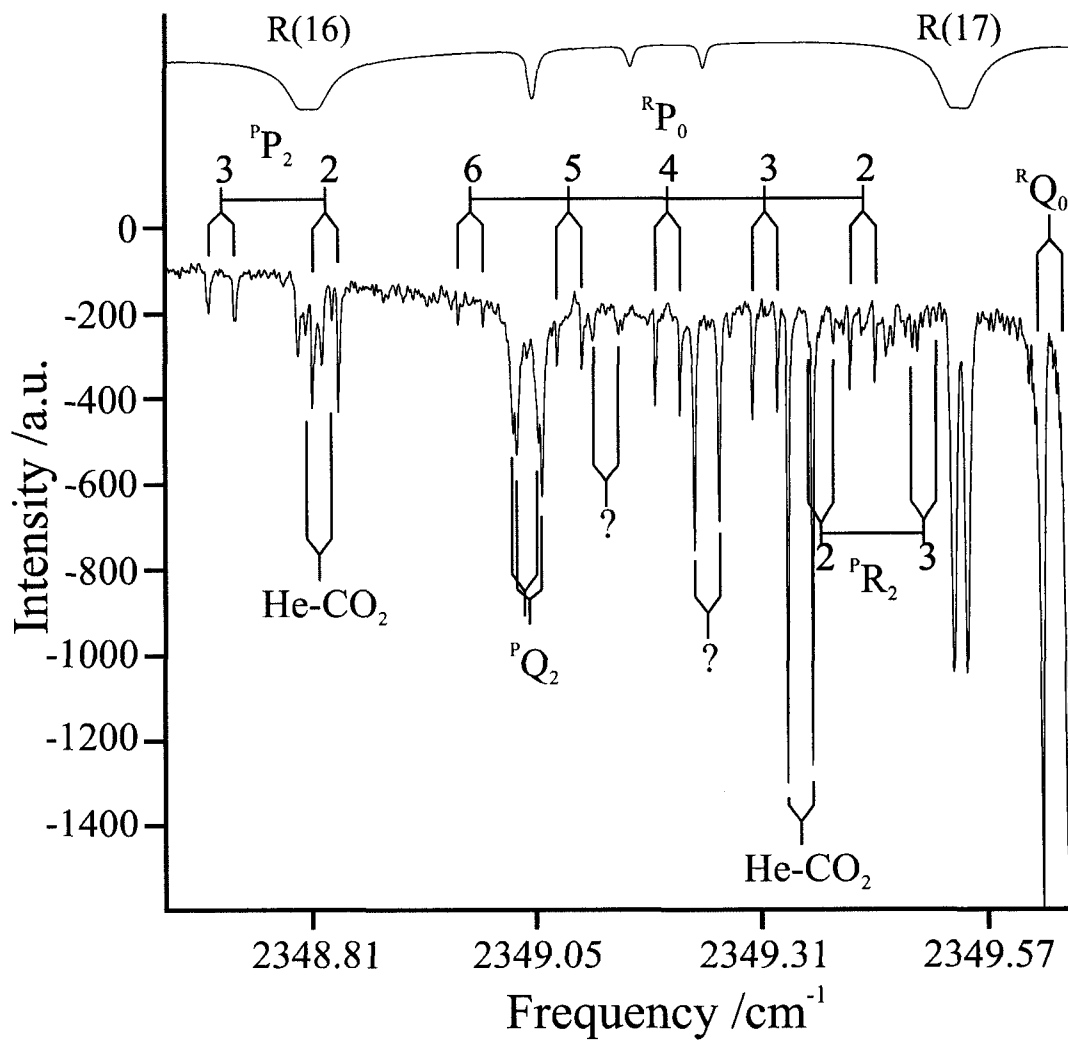


Figure 4.4 (c)

Mid-infrared expansion spectrum of the $\text{CO}_2\text{-SO}_2$ van der Waals complex (cont'd).

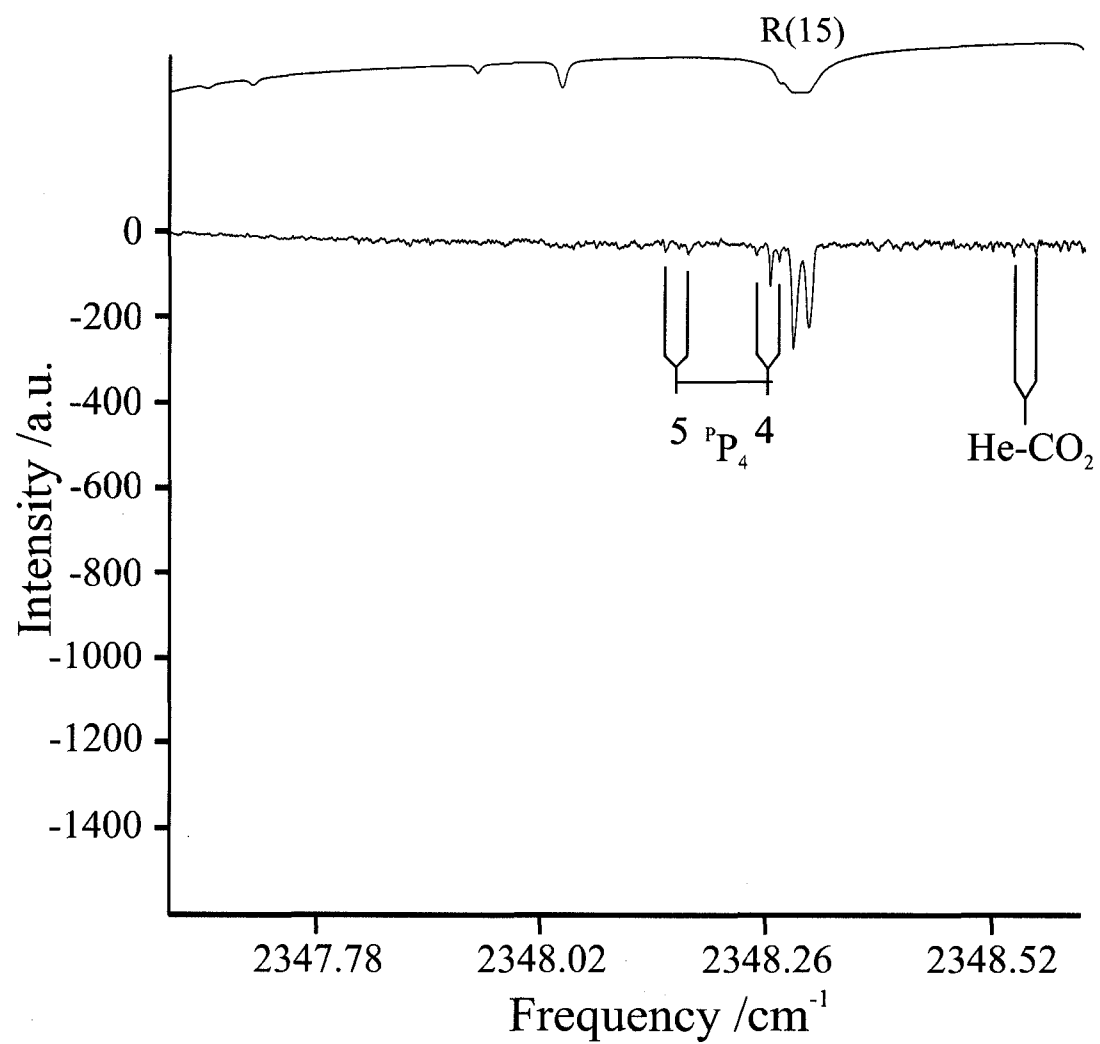


Figure 4.5

The ${}^R R_0$ branch of $\text{CO}_2\text{-SO}_2$ observed by MW-IR double resonance. Each trace is an average of 200 scans. The sample consisted of 1.0% CO_2 , 0.3% SO_2 in He carrier gas at a backing pressure of 3 atm. The samples were irradiated at the frequencies of the microwave transitions indicated on the right hand side. Positive intensity indicates an increase in population of a rotational energy level, negative intensity a decrease.

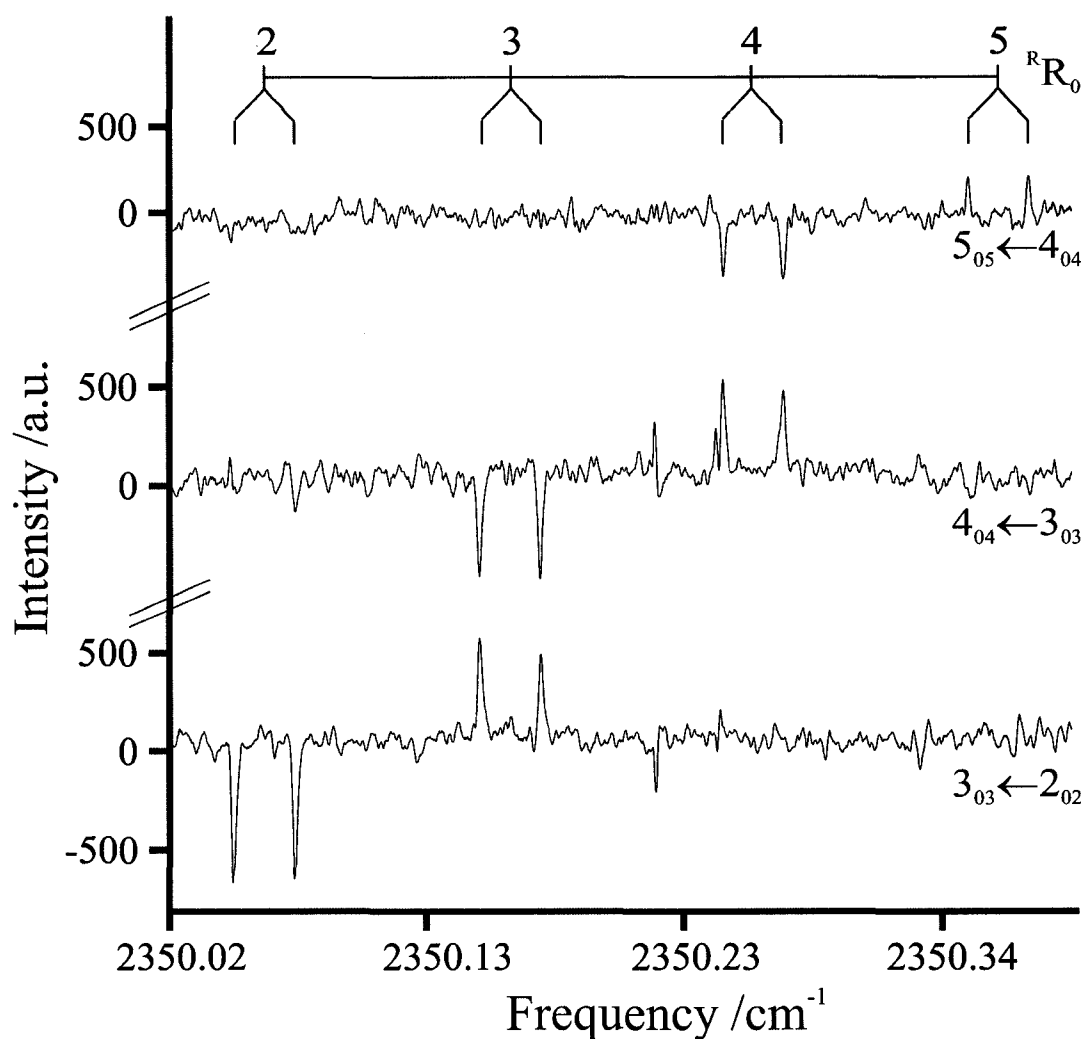


Figure 4.6

The RQ_0 branch of $\text{CO}_2\text{-SO}_2$, observed by single resonance IR (trace a, top) and MW-IR double resonance (traces b-d). Only the higher J transitions of the RQ_0 are resolved in the single resonance experiment. The lower J transitions are resolved in the double resonance experiment.

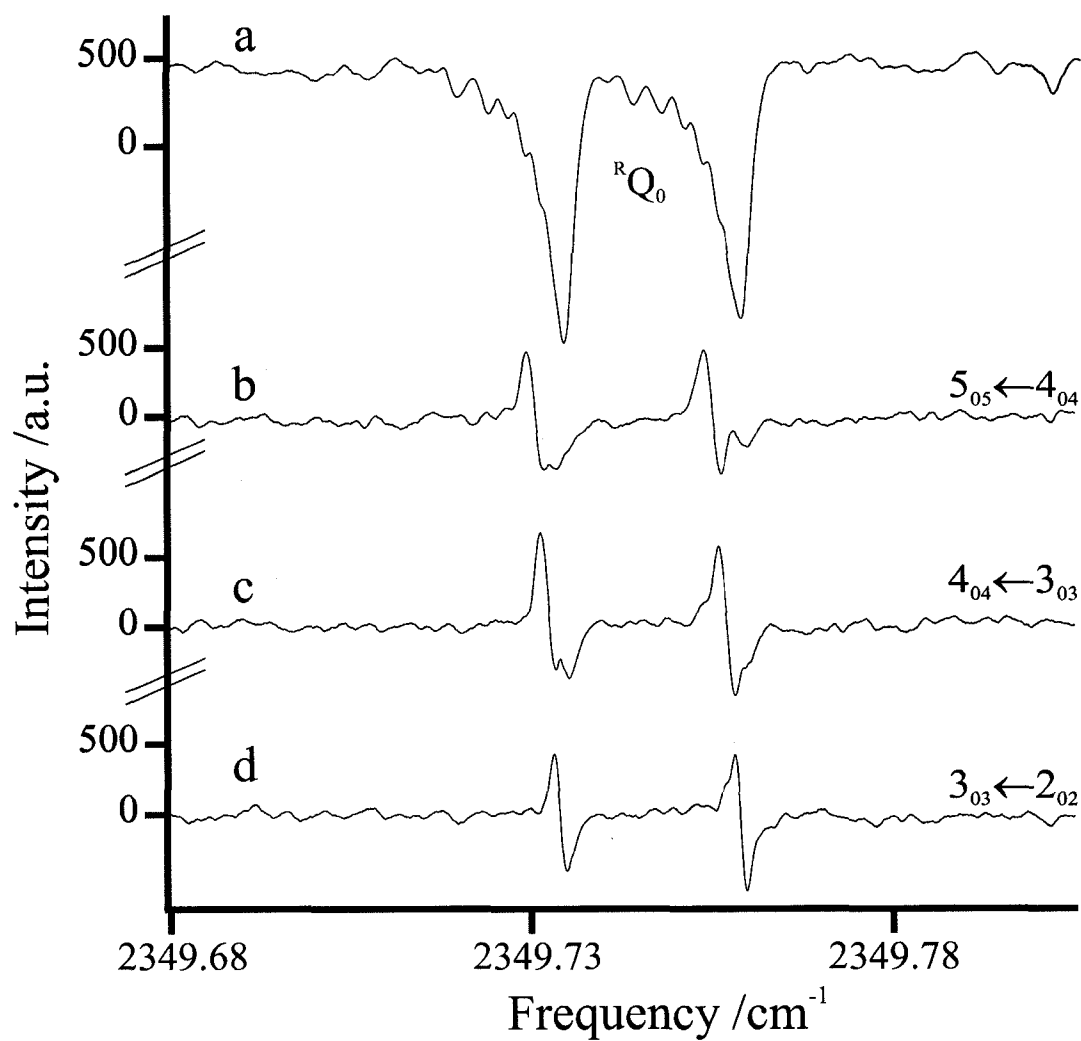


Table 4.4

Observed and assigned infrared transition frequencies of the CO₂-SO₂ van der Waals complex, double resonance (DR) confirmation indicated. The frequencies have an experimental uncertainty of ± 0.0004 cm⁻¹.

J_{KaKc}' $\leftarrow J_{KaKc}''$	ν_{obs} /cm ⁻¹	$\nu_{\text{obs}}-\nu_{\text{calc}}$ /cm ⁻¹	DR	J_{KaKc}' $\leftarrow J_{KaKc}''$	ν_{obs} /cm ⁻¹	$\nu_{\text{obs}}-\nu_{\text{calc}}$ /cm ⁻¹	DR
^R R ₀ :				^R Q ₀ :			
1 ₁₀ ← 0 ₀₀	2349.8505	0.0000		1 ₁₁ ← 1 ₀₁	2349.7504	0.0006	
2 ₁₁ ← 1 ₀₁	2349.9507	-0.0003		2 ₁₂ ← 2 ₀₂	2349.7493	0.0004	Y
3 ₁₂ ← 2 ₀₂	2350.0525	0.0009	Y	3 ₁₃ ← 3 ₀₃	2349.7473	-0.0003	Y
4 ₁₃ ← 3 ₀₃	2350.1535	0.0009	Y	4 ₁₄ ← 4 ₀₄	2349.7455	-0.0004	Y
5 ₁₄ ← 4 ₀₄	2350.2537	0.0001	Y	5 ₁₅ ← 5 ₀₅	2349.7440	0.0003	Y
6 ₁₅ ← 5 ₀₅	2350.3552	0.0003	Y	6 ₁₆ ← 6 ₀₆	2349.7414	0.0003	
7 ₁₆ ← 6 ₀₆	2350.4561	-0.0004		7 ₁₇ ← 7 ₀₇	2349.7383	0.0001	
9 ₁₈ ← 8 ₀₈	2350.6619	0.0017*		8 ₁₈ ← 8 ₀₈	2349.7344	-0.0004*	
^R P ₀ :				9 ₁₉ ← 9 ₀₉ 2349.7304 -0.0007*			
1 ₁₀ ← 2 ₀₂	2349.5502	-0.0002		^P Q ₂ :			
2 ₁₁ ← 3 ₀₃	2349.4507	0.0000		2 ₁₁ ← 2 ₂₁	2349.2126	0.0012	
3 ₁₂ ← 4 ₀₄	2349.3516	0.0002		3 ₁₂ ← 3 ₂₂	2349.2126	0.0005	
4 ₁₃ ← 5 ₀₅	2349.2525	0.0002		2 ₁₂ ← 2 ₂₀	2349.2087	-0.0006	
5 ₁₄ ← 6 ₀₆	2349.1528	-0.0006		3 ₁₃ ← 3 ₂₁	2349.2087	0.0005	
6 ₁₅ ← 7 ₀₇	2349.0531	-0.0018		4 ₁₄ ← 4 ₂₂	2349.2057	-0.0009	
7 ₁₆ ← 8 ₀₈	2348.9563	-0.0003					

* = not included in fit because transitions are very weak.

Table 4.4 (cont'd)

$J_{KaKc}' \leftarrow$ J_{KaKc}''	ν_{obs} /cm ⁻¹	$\nu_{\text{obs}} - \nu_{\text{calc}}$ /cm ⁻¹	DR	$J_{KaKc}' \leftarrow$ J_{KaKc}''	ν_{obs} /cm ⁻¹	$\nu_{\text{obs}} - \nu_{\text{calc}}$ /cm ⁻¹	DR
^P P ₂ :				^R R ₂ :			
1 ₁₀ ← 2 ₂₀	2349.0097	-0.0011	Y	3 ₃₀ ← 2 ₂₀	2350.5840	0.0001	Y
1 ₁₁ ← 2 ₂₁	2349.0097	-0.0005		3 ₃₁ ← 2 ₂₁	2350.5840	0.0001	Y
2 ₁₁ ← 3 ₂₁	2348.9107	-0.0006	Y	4 ₃₁ ← 3 ₂₁	2350.6846	0.0014	Y
2 ₁₂ ← 3 ₂₂	2348.9086	-0.0008		4 ₃₂ ← 3 ₂₂	2350.6846	0.0014	Y
3 ₁₂ ← 4 ₂₂	2348.8121	0.0000	Y	5 ₃₂ ← 4 ₂₂	2350.7827	0.0004	
3 ₁₃ ← 4 ₂₃	2348.8085	0.0002	Y	5 ₃₃ ← 4 ₂₃	2350.7827	0.0003	
4 ₁₃ ← 5 ₂₃	2348.7140	0.0008	Y	6 ₃₃ ← 5 ₂₃	2350.8816	0.0004	
4 ₁₄ ← 5 ₂₄	2348.7075	0.0008		6 ₃₄ ← 5 ₂₄	2350.8816	0.0002	
5 ₁₄ ← 6 ₂₄	2348.6139	-0.0005		^R P ₄ :			
5 ₁₅ ← 6 ₂₅	2348.6047	-0.0001		5 ₅₀ ← 6 ₄₂	2350.2120	-0.0003	
7 ₁₆ ← 8 ₂₆	2348.4174	-0.0002		5 ₅₁ ← 6 ₄₃	2350.2120	-0.0003	
9 ₁₈ ← 10 ₂₈	2348.2226	0.0010*		^P Q ₄ :			
^R Q ₂ :				4 ₃₁ ← 4 ₄₁	2348.6644	-0.0013	
3 ₃₁ ← 3 ₂₁	2350.2832	-0.0007		5 ₃₂ ← 5 ₄₂	2348.6644	-0.0012	
4 ₃₂ ← 4 ₂₂	2350.2832	0.0000		^P R ₄ :			
^P R ₂ :				5 ₃₂ ← 4 ₄₀	2349.1654	0.0006	
3 ₁₃ ← 2 ₂₁	2349.5074	-0.0008		5 ₃₃ ← 4 ₄₁	2349.1654	0.0006	
4 ₁₄ ← 3 ₂₂	2349.6069	0.0003		6 ₃₃ ← 5 ₄₁	2349.2644	-0.0001	
4 ₁₃ ← 3 ₂₁	2349.6137	0.0006		6 ₃₄ ← 5 ₄₂	2349.2644	-0.0001	
^P P ₄ :				^N R ₄ :			
3 ₃₀ ← 4 ₄₀	2348.2661	-0.0003		6 ₁₆ ← 5 ₄₂	2348.1850	-0.0003	
4 ₃₁ ← 5 ₄₁	2348.1667	0.0002		7 ₁₆ ← 6 ₄₂	2348.3030	0.0013	

Table 4.5

Unassigned transitions in the expansion spectra of the CO₂-SO₂ van der Waals complex.

Frequency /cm⁻¹	Frequency /cm⁻¹	Frequency /cm⁻¹
2348.6318	2349.3911	2349.8095
2348.6492	2349.4265	2349.9987
2349.1022	2349.4860	2350.0437
2349.1576	2349.5597	2350.0794
2349.2625	2349.5884	2350.2014
2349.2884	2349.5912	2350.2034

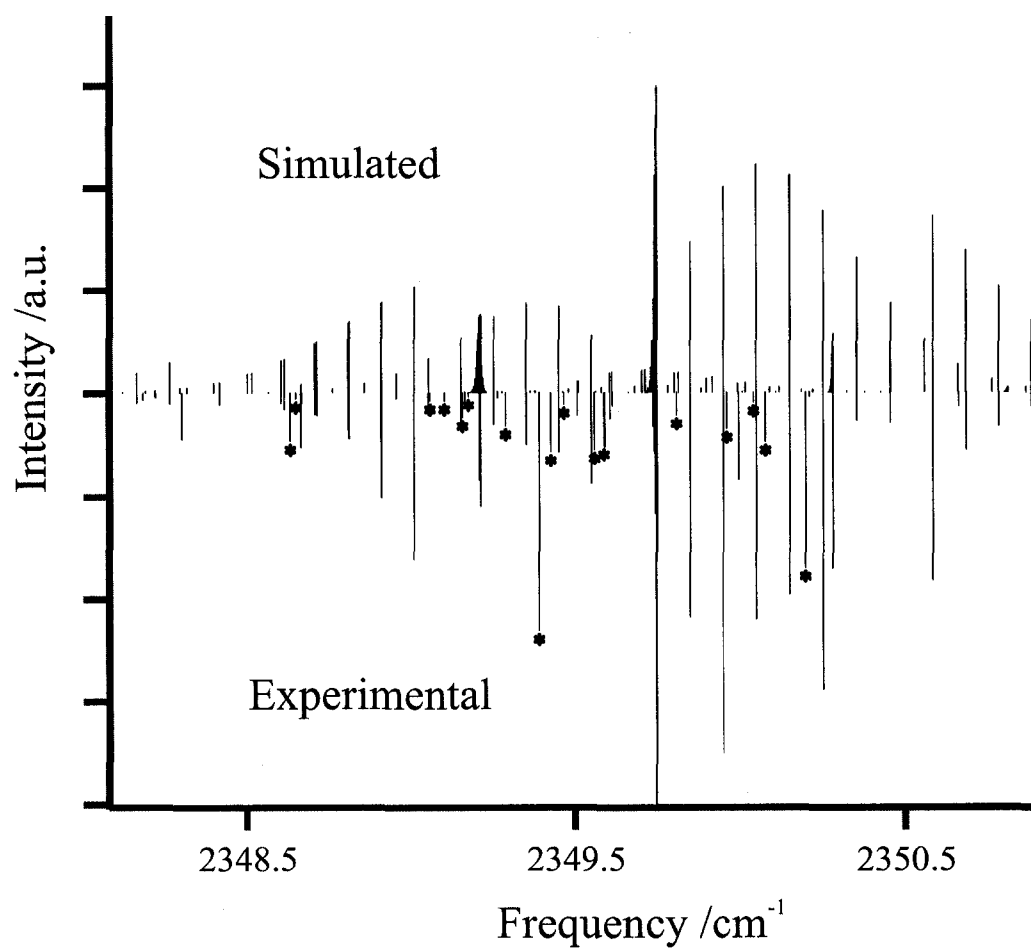
Table 4.6

Spectral parameters of CO₂-SO₂ (in MHz unless otherwise noted).

Parameter	This work	Previous ¹⁰⁵
ν_0 / cm^{-1}	2349.6160 (11)	-
A''	5544.81 (40)	5500 (500)
A'	5524.34 (63)	-
B''	1510.034 (37)	1509.976 (300)
B'	1507.99 (16)	-
C''	1489.402 (36)	1489.459 (300)
C'	1488.40 (21)	-
D_J'' / kHz	4.578 (16)	4.58 (0.8)
D_J' / kHz	4.63 (80)	-
D_{JK}'' / kHz	192.40 (31)	192.40 (14)
D_{JK}' / kHz	192 (13)	-
d_2'' / kHz	0.259 (13)	0.259 (6)
d_2' / kHz	0.4 (60)	-

Figure 4.7

Comparison between experimental and model stick spectra of CO₂-SO₂.



4.4.2 *ab initio* calculations

A number of single-point calculations on the potential energy surface of the CO₂-SO₂ complex were carried out at the CCSD(T) level of theory using the software package MOLPRO, version 2002.¹³⁸ The interaction energy of the complex was calculated using the supermolecule approach,¹³⁹ in which the energy of the monomer units is subtracted from the total energy of the complex. Dunning's aug-cc-pVTZ basis set,¹⁴⁰ supplemented by bond functions¹⁴¹ with exponents $\alpha_s = \alpha_p = 0.9, 0.3, 0.1$, $\alpha_d = 0.6, 0.2$, $\alpha_f = \alpha_g = 0.3$, was used. Since there was no reason to doubt the C_{2v} symmetry of the complex, and calculations at a lower level of theory had already been carried out in the original microwave work,¹⁰⁵ a complete potential energy surface was not calculated. Instead, several cuts through the potential energy surface were calculated to determine the equilibrium intermolecular separation. The OC and SO bond lengths as well as the OSO bond angle were held at their respective monomer values.¹²⁷ In the first cut through the potential energy surface, the sulfur atom points away from the CO₂ unit (Fig. 4.1). In the second cut, the SO₂ moiety is inverted with the sulfur atom pointing towards CO₂. For the structure shown in Fig 4.1, a potential minimum was found at an intermolecular separation r_e of 3.24 Å with an interaction energy of 744 cm⁻¹ (Table A4.1 in the appendix and Fig. 4.8). The minimum in the second cut (inverted SO₂) has a much lower binding energy of only 136 cm⁻¹ at a much higher intermolecular separation r_e^* of 3.96 Å (Fig. 4.8).

Attempts were also made to calculate the barrier height to internal rotation. This ideally requires finding a minimum energy path, which is computationally expensive.

The barrier height to internal rotation was estimated by keeping the center of mass separation of the two subunits at the potential minimum value found in the previous calculation, and rotating two of the oxygen nuclei along the internal rotation coordinate τ_{tor} , keeping both the C and S nuclei fixed at their respective positions in space. The results presented here (Table A4.3 and Fig. 4.9) are useful in that estimates for (the upper limit of) the potential energy barrier are obtained, which aids in the spectral analysis. It was found that the maximum barrier to internal rotation is approximately 982 cm^{-1} . At that energy, the transition state for internal rotation is positive, indicating that some radial movement is associated with the internal rotation.

Figure 4.8

Cuts through the potential energy surface of CO₂-SO₂ as a function of intermolecular separation (see Tables A4.1 and A4.2 in the appendix).

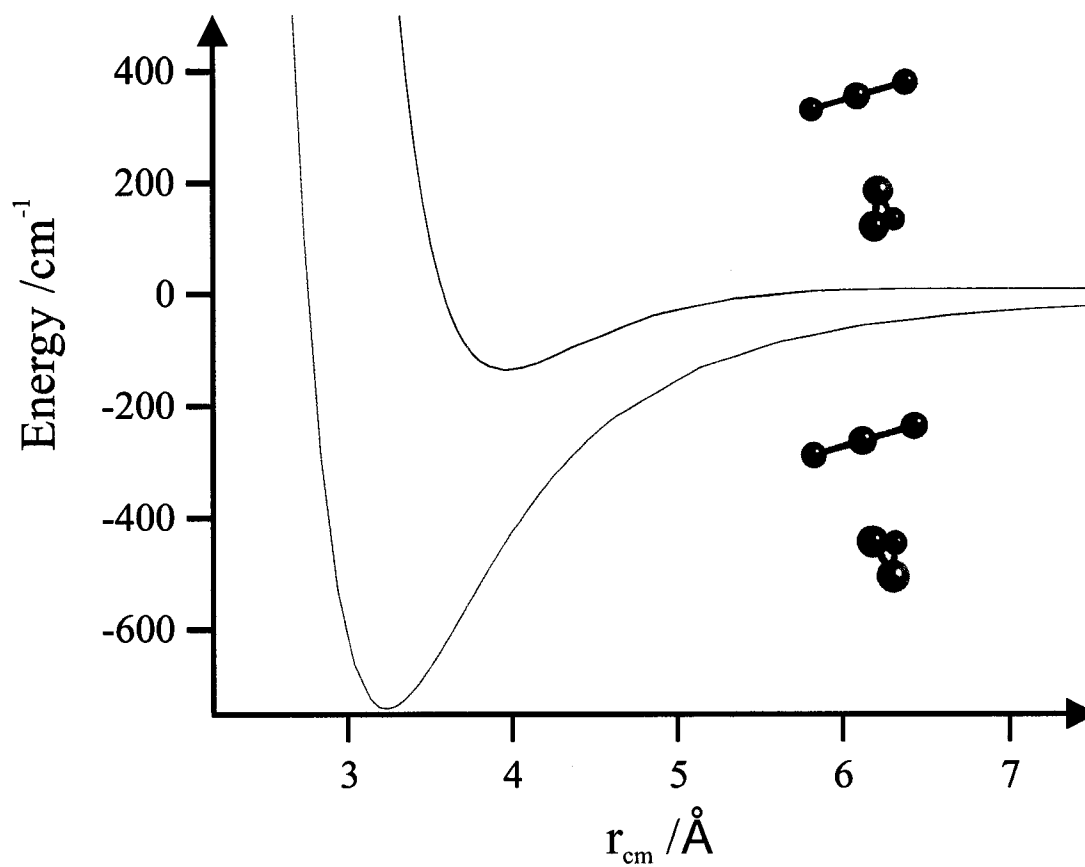
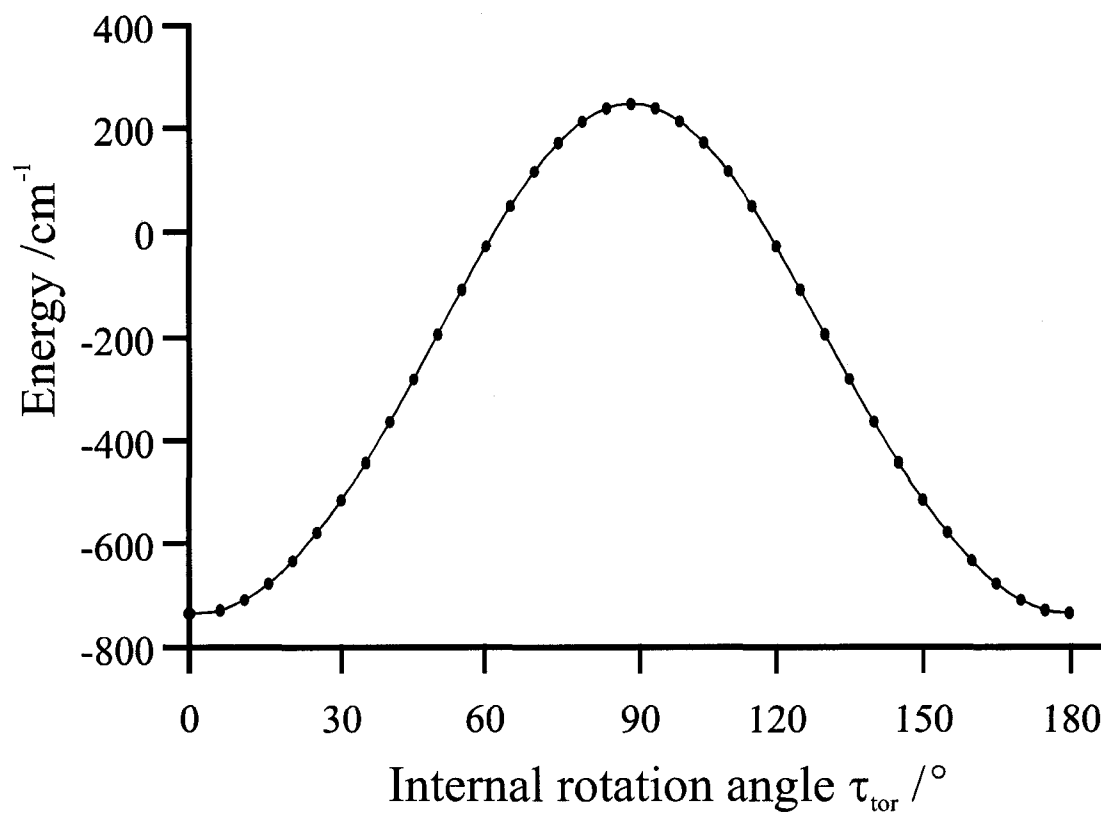


Figure 4.9

Cuts through the intermolecular potential energy surface $\text{CO}_2\text{-SO}_2$ along the internal rotation coordinate τ_{tor} (see table A4.3 in the appendix).



4.5 Discussion

4.5.1 Structural Analysis

The spectral parameters obtained from the combined fit of microwave and infrared transitions (Table 4.6) complete the set of rotational constants of CO₂-SO₂ in the vibrational ground state. The good fit to the semi-rigid Hamiltonian indicates that the internal motions of the system are of moderate amplitude and that therefore meaningful structural parameters may be derived from the effective rotational constants. Since CO₂-SO₂ is a six-atom system, and there are only three rotational constants, assumptions need to be made to reduce the number of fitting parameters. A common approach is to assume that the bond lengths and bond angles of the monomer units do not change upon complex formation. A further reduction of the number of structural parameters results from the C_{2v} point group symmetry of the molecule,¹⁰⁵ which constrains the relative orientation of the two subunits to a crossed geometry. However, the symmetry does not preclude the theoretical possibility of an equilibrium geometry with inverted SO₂ unit. The *ab initio* calculations presented in this Chapter clarify this point by showing that the S atom prefers to be in a position away from the C atom in the complex (Fig. 4.8). Thus, the only "free" parameter is the effective intermolecular distance, expressed as the center of mass separation r_{cm} .

Effective structural parameters were calculated in the following manner: The experimental moments of inertia of the complex were calculated from the molecular constants using equation 1.21. These values were compared to calculated moments of inertia based on the assumed geometry using equation 1.22, and the differences were minimized by the least-squares error method. The results are shown in Table 4.7. The

effective intermolecular separation r_0 was determined to be 3.29 Å, which is identical to the value that Sun *et al.*¹⁰⁵ calculated by extrapolation from the other isotopomers.

Upon closer inspection of Table 4.7, small differences between the calculated and measured moments of inertia are noticeable. These are most likely a result of approximating the bond lengths and distances in the complex with their monomer values. If more parameters are allowed to “float” in the fit, these differences vanish (Table 4.8). The two additional variables used in the later fit are the bond distance r_{CO} and the bond angle α_{OSO} . The first was chosen because of its obvious sensitivity to the vibrational excitation. Variation of the bond angle α_{OSO} was chosen because Sun *et al.*¹⁰⁵ had measured an increase in dipole moment upon complex formation. This could be attributed to a decrease of the angle α_{OSO} . Because the increase in the CO₂ monomer bond length upon vibrational excitation is known (Table 1.3) but was not utilized in the calculations in Table 4.8, these calculations serve as a test of the least squares method.

Fitting the three parameters α_{OSO} , r_{CO} and r_{cm} to three molecular constants A , B and C reproduces the experimental moments of inertia (Table 4.8). The calculated bond lengths r_{CO}' and r_{CO}'' in the complex are identical to the monomer¹⁴² values. Also, the angle α_{OSO} decreases by -1.8° with respect the free monomer value of 119.329° , which is consistent with the dipole measurements. This demonstrates that the least-squares error structure determination method used here yields correct results.

Upon excitation of the asymmetric stretching mode of CO₂, all three rotational constants decrease slightly in value (Table 4.6). The decrease of all three rotational constants indicates an overall weakening of the complex upon vibrational excitation. The

derived structural parameters for the excited state are listed in Table 4.8. The A constant is most affected by the vibrational excitation, because rotation around the a -axis “captures” most of the additional moment of inertia associated with the increase of r_{CO} . The moment of inertia calculations indicate that the bond distance r_{CO} increases upon vibrational excitation by the same amount as observed for the free monomer, which is consistent with a (nearly) unperturbed CO_2 asymmetric stretching motion in the complex. The band origin ν_0 of the complex is slightly blue-shifted relative to the band origin of the free monomer, similar to the T-shaped $\text{CO}_2\text{-CO}$,⁸⁹ which also has a dipole moment perpendicular to the asymmetric stretch (Table 4.9).

Table 4.7

Calculation of structural parameters of CO₂-SO₂. Chemical bond lengths and angles were restricted to their respective ground state monomer values.

Parameter	g.s. (exp)	g.s. (model)	e.s. (exp)	e.s. (model)
I _{aa} /amu Å ²	91.12 (1)	92.01	91.45 (1)	92.30
I _{bb} /amu Å ²	334.58 (1)	334.10	335.03 (4)	334.59
I _{cc} /amu Å ²	339.21 (1)	339.69	339.44 (5)	339.88
r ₀ /Å		3.292		3.293
r _{CO} /Å		1.1620 (fixed) ¹²⁷		1.1660 (fixed) ¹²⁷
r _{SO} /Å		1.4308 (fixed) ¹²⁷		1.4308 (fixed) ¹²⁷
α _{OSO} /°		119.329 (fixed) ¹²⁷		119.329 (fixed) ¹²⁷

Note: The numerical precision of the model is larger than the number of digits shown in the table. Uncertainty is introduced by the simplicity of the model.

Table 4.8

Revised calculation of structural parameters of CO₂-SO₂. The only parameter constrained to the monomer value was the bond distance r_{SO}.

Parameter	g.s. (exp)	g.s. (model)	e.s. (exp)	e.s. (model)
I _{aa} /amu Å ²	91.12 (1)	91.12	91.45 (1)	91.45
I _{bb} /amu Å ²	334.58 (1)	334.58	335.03 (4)	335.03
I _{cc} /amu Å ²	339.21 (1)	339.21	339.44 (5)	339.44
r ₀ /Å		3.292		3.293
r _{CO} (complex) /Å		1.162		1.166
r _{CO} (monomer) /Å		1.162 ¹²⁷		1.166 ¹²⁷
r _{SO} /Å		1.4308 (fixed) ¹²⁷		1.4308 (fixed) ¹²⁷
α _{OSO} (complex) /°		117.49		117.60
α _{OSO} (monomer) /°		119.329 ¹²⁷		119.329 ¹²⁷

Table 4.9

Comparison of asymmetric stretching band origins of CO₂ complexes. The highest order electrostatic interaction is also indicated (disp = dispersion, q-q = quadrupole - quadrupole, H = Hydrogen bonding, q-d = quadrupole - dipole).

Molecule	ν_0 /cm ⁻¹	$\Delta\nu_0$ /cm ⁻¹	Complex Geometry	Highest order electrostatic Interaction	Ref.
CO ₂	2349.14326	-			142
CO ₂ -He	2349.238	+0.095	T-shaped	disp	103
CO ₂ -Ne	2349.2795	+0.1362	T-shaped	disp	86
CO ₂ -Ar	2348.67315	-0.47011	T-shaped	disp	86
CO ₂ -Kr	2348.25921	-0.88405	T-shaped	disp	86
CO ₂ -Xe	2347.67194	-1.47132	T-shaped	disp	86
CO ₂ -CH ₄	2348.278	+0.135	T-shaped	disp	Chapter 5
CO ₂ -N ₂	2349.62785	+0.48459	T-shaped	q-q	87
CO ₂ -Br ₂	2349.7758	+0.6325	linear	q-q	94
CO ₂ -HF	2359.1239	+9.9806	linear	H	92
CO ₂ -H ³⁵ Cl	2353.0171	+3.8738	linear	H	92
CO ₂ -HBr	2348.2018	-0.9415	T-shaped	H	92
CO ₂ -CO ₂	2350.77212	+1.62886	slipped parallel	q-q, resonant dipole	85
CO ₂ -CS ₂	2346.5448	-2.5985	X-shaped	q-q	95
CO ₂ -N ₂ O	2348.86	-0.28326	slipped parallel	q-q	93
CO ₂ -CO	2349.35479	+0.21153	T-shaped	q-d	88
CO ₂ -SO ₂	2349.6160	+0.4668	X-shaped	q-d	This Chapter

4.5.2 Unassigned lines

In addition to the >62 assigned transitions in the mid-infrared expansion spectra, there were other transitions present in the expansions spectra. Most of those could be identified as belonging to either CO₂, (CO₂)₂ or He-CO₂. Formation of (CO₂)₂ and He-CO₂ was competitive because relative low concentrations of SO₂ and CO₂ were employed to avoid formation of higher order clusters. Still, there were 18 observed lines which could not be assigned (Table 4.5). These lines were observed in fresh sample batches, as well as over a wide range of backing pressures. We considered that these transitions might arise from impurities introduced from the sample bottle(s). However, the observed transitions did not fit those of CO₂ complexes with the most common impurities, H₂O or N₂. A possible explanation is that these transitions belong to isotopomeric lines, for example the isotopomer ³⁴SO₂-CO₂. The natural abundance of ³⁴SO₂ is approximately 4%. We did not have ³⁴S enriched samples to further examine this possibility.

Some of the unassigned fall in the proximity of formally forbidden transitions of odd symmetry; however, this assignment did not hold up under scrutiny because the branches were incomplete and because the intensity pattern was inconsistent. The observation of additional transitions was considered because of possible tunneling motions. It is unfortunately still not quite clear if there are additional lines in the spectra due to internal rotor states. The good fit of the rigid rotor model seems to suggest otherwise.

4.6 Summary

The mid-infrared spectrum of CO₂-SO₂ has been recorded and analyzed. The spectrum is *c*-type, and transitions to and from odd K_a levels are absent, consistent with spin statistical analysis. The spectral analysis was confirmed by MW-IR double resonance experiments and is in good agreement with a previous microwave study.¹⁰⁵ Effective structural parameters were derived for both the vibrational ground and excited state. Overall, the CO₂-SO₂ complex is fairly rigidly bound as judged from the good fit to the rigid asymmetric rotor Hamiltonian and small structural changes upon vibrational excitation.

CHAPTER 5

MICROWAVE, INFRARED AND MICROWAVE-INFRARED DOUBLE RESONANCE SPECTRA OF THE WEAKLY BOUND COMPLEX $\text{CO}_2\text{-CH}_4$

5.1 Introduction

Even though numerous weakly bound complexes have been studied by molecular beam spectroscopy in the last 15 years, only a small number of weakly bound complexes containing a spherical top have been reported. In the microwave region, the rotational spectra of methane - hydrogen halides $\text{CH}_4\text{-HF}$,¹⁴³ $\text{CH}_4\text{-HBr}$,¹⁴⁴ $\text{CH}_4\text{-HCl}$,¹⁴⁵ and $\text{CH}_4\text{-HCN}$ ¹⁴⁶ were reported in the early 1990s. In the infrared region, the ro-vibrational spectra of the weakly bound methane complexes $\text{CH}_4\text{-Ne}$,¹¹¹ $\text{CH}_4\text{-Ar}$,¹⁴⁷ $\text{CH}_4\text{-Kr}$,¹⁴⁸ $\text{CH}_4\text{-H}_2$ ¹⁰⁸ and the analog silane complexes $\text{SiH}_4\text{-Ne}$ ^{149,150} and $\text{SiH}_4\text{-Ar}$ ¹⁵¹ have been investigated. In all of these investigations, the complexes have been treated as pseudo-diatomics. Pseudo-diatomic models were also successfully applied to simulate the microwave spectra of $\text{CH}_4\text{-H}_2\text{O}$ and $\text{CH}_4\text{-O}_3$.^{152,153} $\text{CH}_4\text{-H}_2\text{O}$ was found to undergo double internal rotation of both subunits, and the appearance of its microwave spectrum was explained after the vibration-rotation tunneling bands had been observed in the far-infrared.¹⁵⁴ A pseudo-diatomic model was also used to reproduce the infrared and millimeter wave spectra of $\text{CH}_4\text{-CO}$ in the ground internal rotation state, but the observed spectra of higher order internal rotation states of this system have so far not been successfully modeled.¹¹²

The presence of multidimensional internal motions in addition to the degrees of

freedom for the overall rotation of the complex makes the features appearing in the spectra of these weakly bound complexes difficult to interpret.¹⁴⁵ Transitions of weakly bound complexes containing a spherical top are usually split into at least three sub-bands, which are associated with internal rotation states of the spherical top. Nuclear spin statistics preserves the populations of these states, which would otherwise collapse into the lowest torsional level(s) in the cold environment of a molecular expansion. The study of methane containing weakly bound complexes in molecular beams offers therefore the unique opportunity to gain insight into the nature of the weak interactions of a van der Waals complex containing an internally rotating binding partner.

For rare gas - spherical top molecules, models were developed in papers by Randall *et al.*¹⁵⁵ and by Hutson and Thornley.¹⁵⁶ In a recent publication, Hearn *et al.*¹⁵⁷ investigated the CH₄-OCS weakly bound complex in both the infrared and microwave regions and were able to apply the pseudo-diatomic model developed by Randall *et al.*¹⁵⁵ to an asymmetric rotor containing a spherical top. From this result, it can be anticipated that the same model can also be used for the asymmetric rotor CO₂-CH₄.

In this chapter, the spectra of CO₂-CH₄ in the microwave region of 4-28 GHz and in the mid-infrared near the CO₂ asymmetric stretching fundamental at 2349 cm⁻¹ are presented and analyzed. The CO₂-CH₄ complex was chosen because its spectra had not been seen previously in either the infrared or microwave regions, nor had a theoretical study been done on this system. The spectral assignment is confirmed by microwave-infrared double resonance experiments. The combined spectral data are modeled using Watson's A-reduction Hamiltonian¹³⁰ and the results are compared to CH₄-OCS.¹⁵⁷ The derived structural parameters and the effects of internal rotation are discussed.

5.2 *ab initio* Theoretical Predictions

In first approximation, the coarse appearance of the molecular spectrum may be inferred from the underlying effective molecular structure of the complex. Because the CO₂-CH₄ complex had not been studied prior to this work, a theoretical study was undertaken to locate the minimum on the potential energy surface, from which in turn the effective molecular structure can be estimated. Single-point calculations on the potential energy surface of CO₂-CH₄ were carried out at the CCSD(T) level of theory using the software package MOLPRO, version 2002.¹³⁸ The interaction energy of the complex was calculated using a supermolecule approach,¹³⁹ in which the energy of the monomer units is subtracted from the total energy of the complex. The basis set used in the calculations was Dunning's aug-cc-pVTZ basis set,¹⁴⁰ supplemented by bond functions¹⁴¹ with exponents $\alpha_s = \alpha_p = 0.9, 0.3, 0.1$, $\alpha_d = 0.6, 0.2$, and $\alpha_f = \alpha_g = 0.3$. The input geometries are defined in terms of the intermolecular separation $r_{cm} = r_{CC}$, the in-plane rotation angles θ_H and $\alpha = \alpha_{OCC}$, and the out-of-plane angle ϕ_H (Fig. 5.1). r_{cm} and α define the orientation of the methane unit within the complex, and the angles θ_H and ϕ_H define the orientation of a proton. Chemical bond lengths and angles were assumed to be unaffected by complex formation and were thus held fixed at the respective monomer values. Calculations were carried out on four different cuts through the potential energy surface (Fig. 5.2). The calculated interaction energies are listed in Tables A5.1-A5.4 in the appendix. The global minimum on the potential energy surface was found at angle $\alpha = 90^\circ$ and intermolecular distance $r_{cm} = 3.4 \text{ \AA}$ of cut B (Fig. 5.3).

Figure 5.1

Definition of structural parameters of the $\text{CO}_2\text{-CH}_4$ complex. The oxygen nuclei are assumed to be in the xz -plane. α is the angle of the CO_2 molecule with respect to the z -axis. θ_{H} is the angle of the hydrogen nucleus in the xz -plane with respect to the z -axis, and ϕ_{H} is the corresponding angle in the yz -plane.

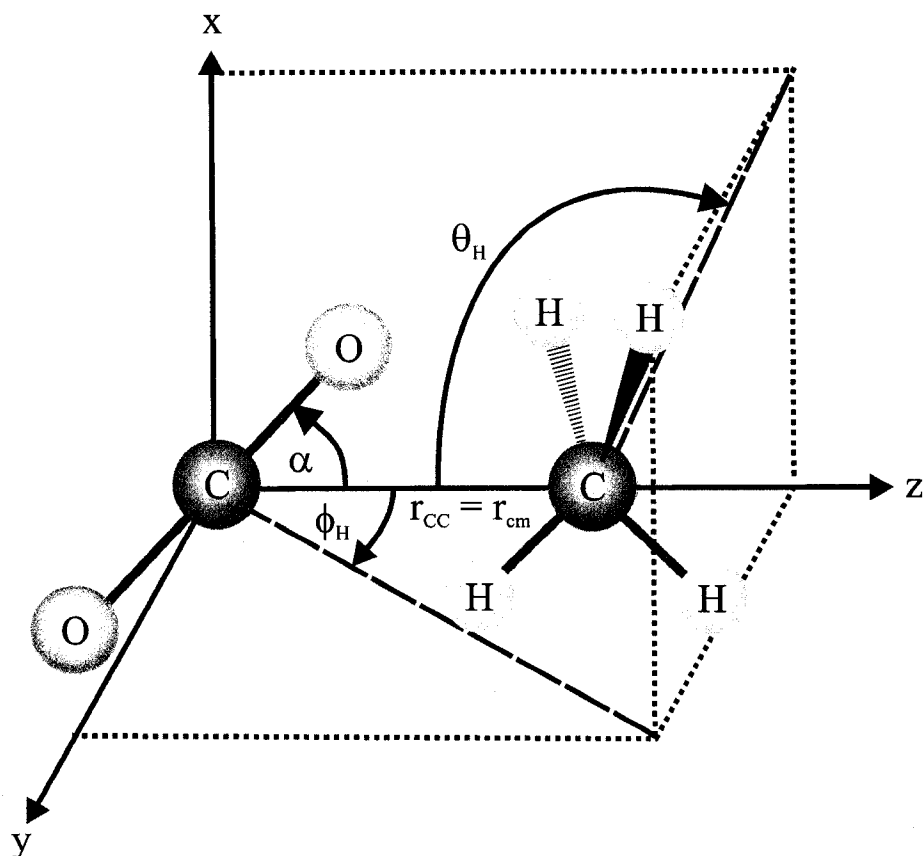


Figure 5.2

Input structures for the *ab initio* calculations of the potential energy surface of the CO₂-CH₄ van der Waals complex. Single point energy calculations were performed on four cuts of the multidimensional surface. The cuts are defined by keeping both ϕ_H and θ_H constant for 2 protons and by varying r_{cm} and α . Cut A corresponds to an H-bonded version of the complex. In cuts C and D, two of the hydrogen nuclei are either parallel (doubly H-bonded) or perpendicular to the oxygen nuclei. In cut B, three hydrogen nuclei point towards the CO₂ unit. Each surface was scanned over r_{cm} from 3.5Å to 10Å and $\alpha = 0^\circ$ to 90°.

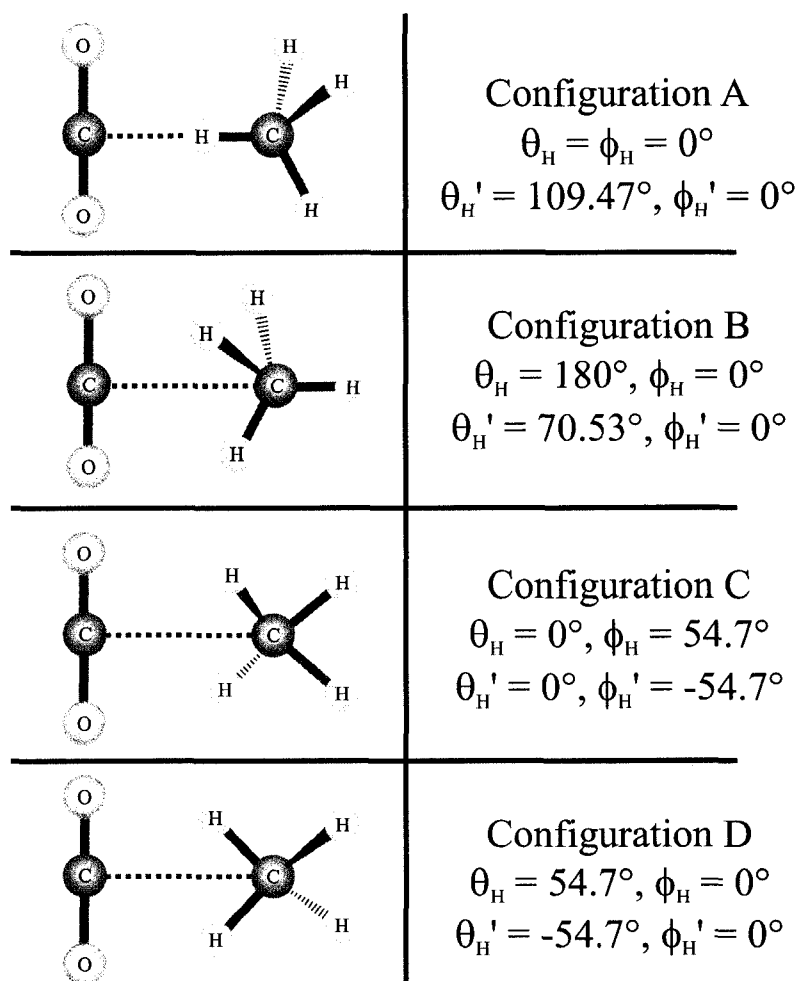
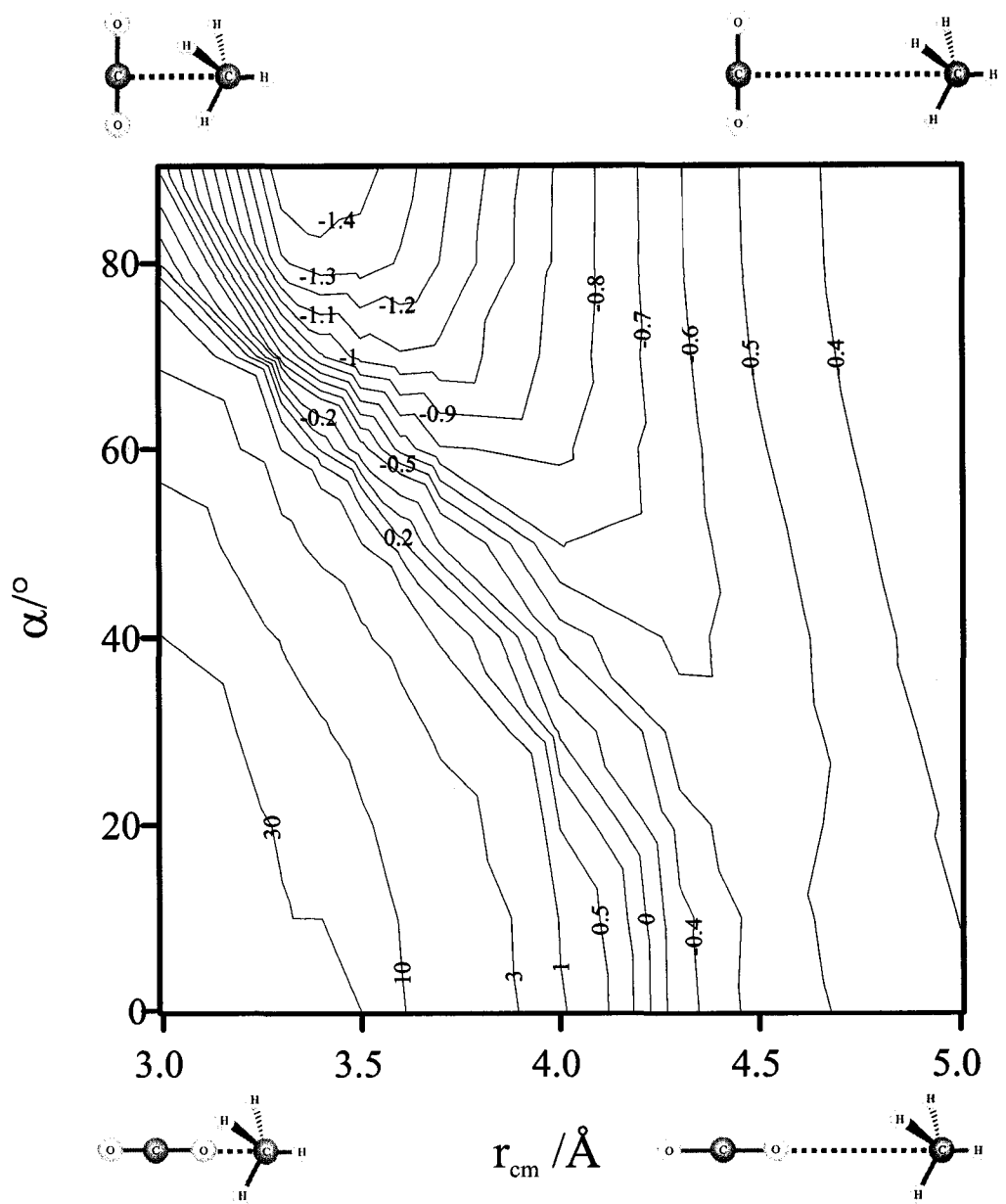


Figure 5.3

Cut B through the potential energy surface of the $\text{CO}_2\text{-CH}_4$ van der Waals complex. The potential energy is given in mH. The global minimum is located at $r_{\text{cm}} = 3.4\text{\AA}$ and $\alpha = 90^\circ$.



5.3 Symmetry considerations

The spin weights of energy levels and selection rules of weakly bound systems that undergo large amplitude internal motions can be derived from a molecular symmetry (MS) group analysis.¹³¹ The complete nuclear permutation inversion (CNPI) group of CO₂-CH₄ contains all operators that permute the four protons (labeled 1, 2, 3, and 4) and the two oxygen nuclei (labeled 5 and 6). The CNPI group of the complex can be constructed by forming the direct product of three groups, the nuclear permutation groups of the two monomers and a group consisting of the identity and inversion operator of the overall complex.¹³¹ In the case of CO₂-CH₄, this group is the direct product of $C_{2v}(\mathbf{M}) = \{E, E^*\} \otimes \{E, (56)\}$ and $T_d(\mathbf{M})$. Since $C_{2v}(\mathbf{M})$ contains 4 and $T_d(\mathbf{M})$ contains 5 classes, the direct product contains $4 \times 5 = 20$ classes. The MS group of CO₂-CH₄ can be constructed from its CNPI group by removing unfeasible operations.¹³¹ If methane and carbon dioxide are assumed to be nearly free internal rotors, all exchange operations except those that change the handedness of methane are feasible. In Fig. 5.4 representative operations of each class and their effect on the CO₂-CH₄ geometry are illustrated. The resulting molecular symmetry group of CO₂-CH₄ contains 10 classes (Table 5.1) and is isomorphic to the G_{48} group which was applied previously^{152,154} to CH₄-H₂O. The group symmetry labels in G_{48} can be rationalized as follows: The labels A, F and E correlate to those of the **T** group of methane (Table 5.2). The superscripts + and - refer to the symmetry with respect to the exchange of the oxygen nuclei (56). The subscripts 1 and 2 are symmetry labels with respect to the parity operator.

Table 5.1

Molecular symmetry group used for CO₂-CH₄. This group is isomorphic to the G₄₈ group used in the analysis of CO₂-H₂O.^{152,154}

G ₄₈	E	(123)	(13)(24)	(56)	(123) (56)	(13)(24) (56)	(1432)*	(24)*	(1432) (56)*	(24) (56)*
	1	8	3	1	8	3	6	6	6	6
A ₁ ⁺	1	1	1	1	1	1	1	1	1	1
A ₂ ⁺	1	1	1	1	1	1	-1	-1	-1	-1
E ⁺	2	-1	2	2	-1	2	0	0	0	0
F ₁ ⁺	3	0	-1	3	0	-1	1	-1	1	-1
F ₂ ⁺	3	0	-1	3	0	-1	-1	1	-1	1
A ₁ ⁻	1	1	1	-1	-1	-1	1	1	-1	-1
A ₂ ⁻	1	1	1	-1	-1	-1	-1	-1	1	1
E ⁻	2	-1	2	-2	1	-2	0	0	0	0
F ₁ ⁻	3	0	-1	-3	0	1	1	-1	-1	1
F ₂ ⁻	3	0	-1	-3	0	1	-1	1	1	-1

Note: Hydrogen nuclei are labeled 1-4, and oxygen nuclei are labeled 5 and 6.

Table 5.2

The $T(M)$, and $T_d(M)$ molecular symmetry groups¹³¹ of CH_4 .

$T(M)$	$T_d(M):$	E	(123)	(14)(23)	(1423)*	(23)*
A	A_1	1	1	1	1	1
A	A_2	1	1	1	-1	-1
E	E	2	-1	2	0	0
F	F_1	3	0	-1	1	-1
F	F_2	3	0	-1	-1	1

Table 5.3

Nuclear spin statistics of CH_4 using labels of the $T(M)$ molecular symmetry group.¹⁴⁵

	A	F	E
I_{CH_4}	2	1	0
$j_{CH_4} (j \leq 3)$	0, 3	1, 2, 3	2
Spin weight	5	3	2
Statistical weight	1	3	1
Relative population	5	9	2

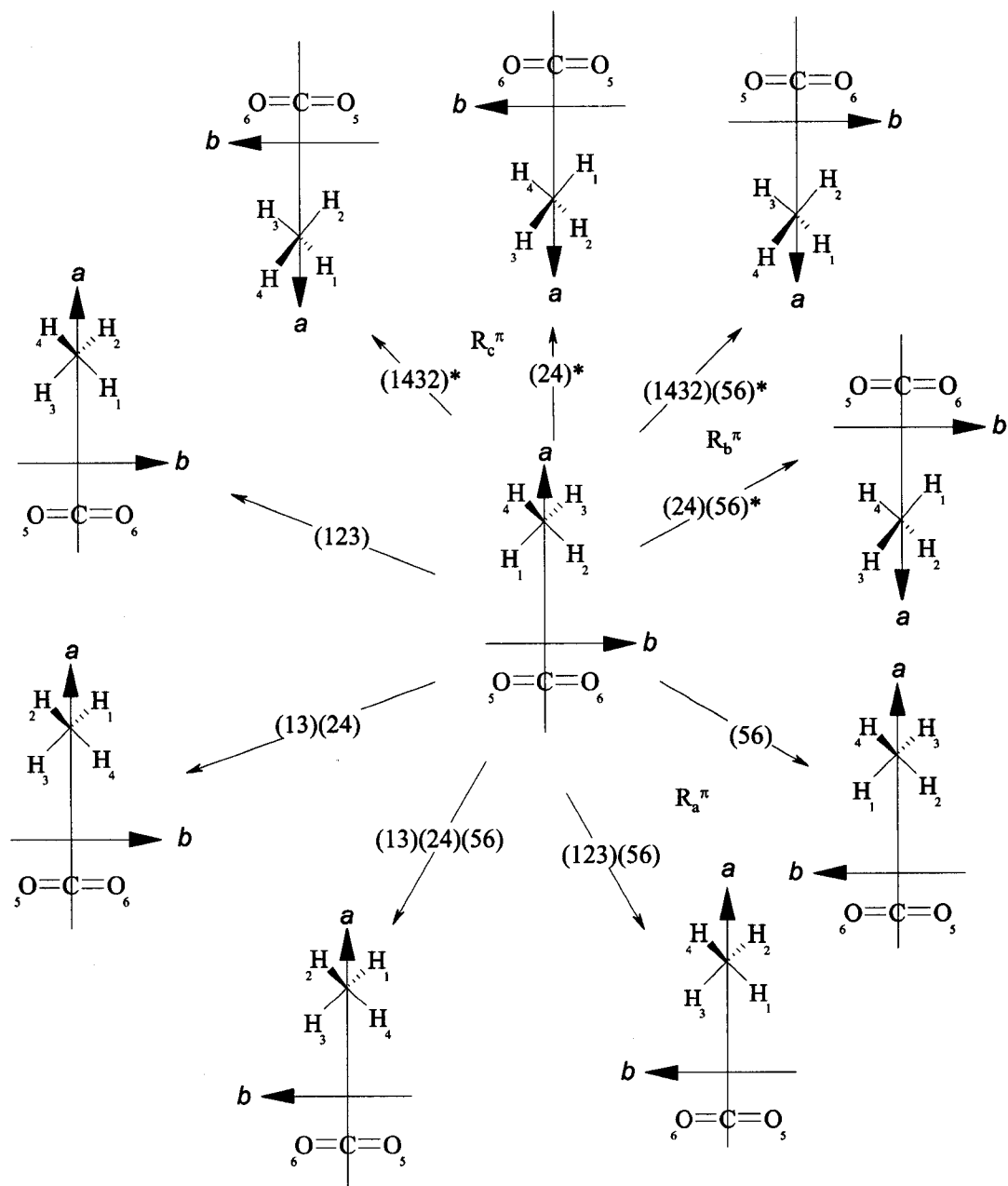
Spin statistics demands that the total wavefunction is antisymmetric with respect to the exchange of any two protons, which are spin $\frac{1}{2}$ fermions, and symmetric with respect to the exchange of the oxygen nuclei, which are spin zero bosons. Only those energy levels whose total wavefunctions are symmetric with respect to the permutation of the two oxygen nuclei will have nonzero spin statistical weight, and all other ro-vibrational energy levels will have spin weight zero. In terms of the labels of the G_{48} group, this implies that the only spin-allowed states must transform as the A_1^+ , A_2^+ , F_1^+ , F_2^+ or E^+ representation.

It is common practice to assume that the overall wavefunction is separable into electronic, rotational, vibrational, internal rotation, and nuclear spin wavefunctions. The electronic wavefunction is completely symmetric and need not be considered.

To determine the symmetry labels of the overall rotations, the equivalent rotations¹³¹ need to be identified. Using Fig. 5.4 as a guide, the equivalent rotations work out to be $R_a^{180^\circ}$ for (56) and (123)(56), $R_b^{180^\circ}$ for (24)(56)* and (1432)(56)*, and $R_c^{180^\circ}$ for (24)* and (1432)*, respectively. From the asymmetric top symmetry rule,¹³¹ it follows that energy levels with $|K_a K_c\rangle = |ee\rangle$ transform as the totally symmetric representation A_1^+ , those with $|eo\rangle$ as A_2^+ , those with $|oe\rangle$ as A_1^- and those with $|oo\rangle$ as A_2^- . The overall rotation of the complex does not permute the protons. The independence of the overall rotation from proton spin statistics is supported by the observed intensity distribution of adjacent J level within branches, which follows simple Boltzmann statistics. If the hydrogen nuclei were permuted somehow, these levels should have different spin statistical weights, but this was not observed.

Figure 5.4

The effects of the MS group operations on $\text{CO}_2\text{-CH}_4$. Each operation shown is a representative member of its class. Motions that change the handedness of methane are unfeasible and are not shown.



The vibrational wavefunction in the ground state is totally symmetric (A_1^+). The symmetry of the vibrational wavefunction in the excited state can be deduced from the cartesian displacement coordinates Δr_1 and Δr_2 . Δr_1 is the displacement (parallel to the molecular b -axis) of oxygen atom 1 from its equilibrium position, and Δr_2 is the displacement of oxygen atom 2 from its equilibrium position. The representation Γ_{car} of the vibrational wavefunction can be expressed in terms of the irreducible representations $A_1^+ \oplus A_1^-$, corresponding to the symmetric (A_1^+) and asymmetric (A_1^-) stretching modes, respectively.

Since internal rotation involves permutation of the protons, the symmetries and spin statistical weights of the internal rotation wavefunctions need to be determined. Proton exchange occurs independently from the overall rotation and vibration (which is located on CO_2) of the complex. Because of the unfeasibility of CH_4 inversion, it is sufficient to derive the spin statistical weights of the methane internal rotation states using the $\mathbf{T}(\mathbf{M})$ group (Table 5.2).^{145,153,157} The $\mathbf{T}_d(\mathbf{M})$ group is not used because methane inversion changes its handedness. Methane has four spin $\frac{1}{2}$ nuclei, i.e. $(2 I_{\text{H}} + 1)^4 = 16$ nuclear spin wavefunctions. These wavefunctions transform as:¹³¹

$$\Gamma_{\text{ns}} = 5A \oplus E \oplus 3F \quad (5.1)$$

in the notation of the applicable $\mathbf{T}(\mathbf{M})$ group (Table 5.2). Different internal rotation states of methane are associated with the three nuclear spin states (Table 5.3). In the cold environment of a molecular expansion, practically all freely rotating methane molecules

in the A nuclear spin state (spin 2) relax to $j=0$, molecules in the F state (spin 1) relax to $j=1$ and the remaining E spin state (spin 0) molecules relax to $j=2$ (Table 5.3).

The selection rules of methane complexes have been shown¹⁴⁵ to be

$$A \leftrightarrow A, E \leftrightarrow E, F \leftrightarrow F \quad (5.2)$$

In the cold environment of the molecular beam a triplicate set of weakly bound complexes is therefore generated and observed, with relative intensities corresponding to the spin statistical weights of the methane subunit. The spin statistical weights for the ro-vibrational wavefunctions in each nuclear spin state are determined in Table 5.4. All odd K_a levels in the totally symmetric vibrational ground state and all even K_a levels in the vibrational excited state are absent. For an infrared transition to be active, a parity change has to occur, i.e. the subscripts must change:

$$A_1^+ \leftrightarrow A_2^+ \quad (5.3a)$$

$$F_1^+ \leftrightarrow F_2^+ \quad (5.3b)$$

$$E^+ \leftrightarrow E^+ \quad (5.3c)$$

Table 5.4a

Symmetries and spin statistical weights of rotational energy levels of CO₂-CH₄ in the vibrational ground state.

Γ_{nucl}	Ψ_{rot}	Γ_{rot}	Γ_{vib}	Γ_{tot}	Weight	Intensity
A	ee>	A ₁ ⁺	A ₁ ⁺	A ₁ ⁺	5	5
A	eo>	A ₂ ⁺	A ₁ ⁺	A ₂ ⁺	5	5
A	oe>	A ₁ ⁻	A ₁ ⁺	A ₁ ⁻	0	0
A	oo>	A ₂ ⁻	A ₁ ⁺	A ₂ ⁻	0	0
F	ee>	A ₁ ⁺	A ₁ ⁺	F ₁ ⁺	3	9
F	eo>	A ₂ ⁺	A ₁ ⁺	F ₂ ⁺	3	9
F	oe>	A ₁ ⁻	A ₁ ⁺	F ₁ ⁻	0	0
F	oo>	A ₂ ⁻	A ₁ ⁺	F ₂ ⁻	0	0
E	ee>	A ₁ ⁺	A ₁ ⁺	E ⁺	2	2
E	eo>	A ₂ ⁺	A ₁ ⁺	E ⁺	2	2
E	oe>	A ₁ ⁻	A ₁ ⁺	E ⁻	0	0
E	oo>	A ₂ ⁻	A ₁ ⁺	E ⁻	0	0

Table 5.4b

Symmetries and spin statistical weights of rotational energy levels of CO₂-CH₄ in the vibrationally excited state.

Γ_{nucl}	Ψ_{rot}	Γ_{rot}	Γ_{vib}	Γ_{tot}	Weight	Intensity
A	ee>	A ₁ ⁺	A ₁ ⁻	A ₁ ⁻	0	0
A	eo>	A ₂ ⁺	A ₁ ⁻	A ₂ ⁻	0	0
A	oe>	A ₁ ⁻	A ₁ ⁻	A ₁ ⁺	5	5
A	oo>	A ₂ ⁻	A ₁ ⁻	A ₂ ⁺	5	5
F	ee>	A ₁ ⁺	A ₁ ⁻	F ₁ ⁻	0	0
F	eo>	A ₂ ⁺	A ₁ ⁻	F ₂ ⁻	0	0
F	oe>	A ₁ ⁻	A ₁ ⁻	F ₁ ⁺	3	9
F	oo>	A ₂ ⁻	A ₁ ⁻	F ₂ ⁺	3	9
E	ee>	A ₁ ⁺	A ₁ ⁻	E ⁻	0	0
E	eo>	A ₂ ⁺	A ₁ ⁻	E ⁻	0	0
E	oe>	A ₁ ⁻	A ₁ ⁻	E ⁺	2	2
E	oo>	A ₂ ⁻	A ₁ ⁻	E ⁺	2	2

The parity selection rule predicts *b*-type infrared and *a*-type microwave transitions. This analysis is supported by the close resemblance of the observed CO₂-CH₄ spectra to those of T-shaped weakly bound carbon dioxide - rare gas complexes⁸⁶ (*b*-type transitions in the IR and *a*-type transitions in the MW), and is consistent with the absence of transitions involving energy levels with odd K_a'' and even K_a' .

5.4 Results

5.4.1 Infrared spectrum

Mid-infrared spectra of the CO₂-CH₄ complex were recorded in the region between 2347.8 and 2350.0 cm⁻¹. The complex was generated by expanding a mixture of typically 0.4% CO₂ and 0.4% CH₄ in He carrier gas containing up to 25% Ne at backing pressures of 2-5 atm. Higher concentrations of Ne led to competitive formation of Ne-CO₂ van der Waals complex,⁸⁶ whose transitions partially overlap with those of CO₂-CH₄. In a typical experiment, the signals from 200 molecular pulses were averaged.

The assignment of the infrared spectrum of CO₂-CH₄ on its own is made difficult by spectral crowding. Since microwave-infrared double resonance experiments were of great use in the assignment of the infrared spectrum of CO₂-SO₂ (Chapter 4), a search was undertaken for the microwave transitions of CO₂-CH₄, so that double resonance experiments could be performed.

5.4.2 Microwave spectrum

Microwave transitions were recorded on a Fourier transform microwave (FTMW) spectrometer described earlier.^{15,18} Sample conditions were identical to those used in the infrared experiments. Initial spectral searches were guided by a preliminary assignment of the infrared spectrum. Two transitions were found near the predicted position of the $1_{01} \leftarrow 0_{00}$ line in the 6 GHz region and assigned to the A and F nuclear spin states on the basis of their relative intensity. During the search for the corresponding $2_{02} \leftarrow 1_{01}$ transitions in the 12 GHz region, a third line was located, which was assigned to the E nuclear spin state. Higher J transitions of each of the three internal rotation states were subsequently found by iterative refinement of the spectral predictions.

Both carbon dioxide and methane lack permanent dipole moments, and only the intermolecular dipole moment can give rise to microwave transitions. Accordingly, the intensity of microwave transitions was relative low, in particular in the E nuclear spin state. A total of three self-consistent sets of *a*-type transitions within the $K_a=0$ and $K_a=2$ stacks were found and assigned to the corresponding nuclear spin states on the basis of their relative intensity distributions (Table 5.5). Nuclear hyperfine splittings were not observed. A search for formally forbidden transitions within the $K_a=1$ stack yielded three transitions slightly red-shifted relative to the predicted $2_{12} \leftarrow 1_{11}$ transition of the F state. Higher order J transitions in the $K_a=1$ stack were not found, and MW-IR double resonance signals were not observed at these frequencies. These transitions are therefore tentatively assigned to higher order internal rotation states of the complex.

Table 5.5

Observed microwave transitions of the CO₂-CH₄ complex.

$J_{KaKc}' \leftarrow J_{KaKc}''$	A	F	E
$1_{01} \leftarrow 0_{00}$	6024.671	5933.715	-
$2_{02} \leftarrow 1_{01}$	11994.679	11822.017	11872.282
$3_{03} \leftarrow 2_{02}$	17857.010	17620.514	17683.564
$4_{04} \leftarrow 3_{03}$	23566.456	23290.044	23352.970
$3_{21} \leftarrow 2_{20}$	18270.435	17953.844	-
$3_{22} \leftarrow 2_{21}$	18057.155	17776.167	17872.073
$4_{22} \leftarrow 3_{21}$	24554.174	24103.504	-
$4_{23} \leftarrow 3_{22}$	24031.339	23666.130	23782.887

Note: Additional transitions were observed at 11141.834, 11097.648 and 11109.888

MHz. The tentative assignment of the E state transitions is based on nearby A and F state transitions.

The $3_{21} \leftarrow 2_{20}$ and $4_{22} \leftarrow 3_{21}$ transitions of the E state were not observed (Table 5.5), most likely because of their low intensity. The corresponding transitions of the F and A states are extremely weak, and required in excess of several hundred cycles to be observed. The search of the predicted much less intense E state transitions was therefore abandoned after repeated trials to locate them.

5.4.3 Microwave-infrared double resonance spectra

Higher concentrations of CH_4 and CO_2 than in the single resonance experiments were employed in the sample gas to generate more of the dimer species. The generation of higher order clusters did not interfere with the double resonance experiment because of background subtraction. The microwave power (max. 500 mW) could be attenuated by up to 6 dB before a reduction of the double resonance signal was observed. Similarly, the microwave radiation could be detuned by ~ 0.1 MHz at maximum power before the double resonance signal degraded.

Due to the lack of a permanent monomer dipole moment, only the relatively small intermolecular dipole moment of the complex gives rise to microwave transitions. The observation of double resonance spectra was therefore more difficult than it had been for the experiments on $\text{CO}_2\text{-SO}_2$ (Chapter 4). As a result, the double resonance signal is more strongly affected by power attenuation of the microwave radiation and more sensitive to frequency detuning. Substantial interference resulted from incomplete subtraction of transitions involving spin states other than the ones probed by double resonance, likely due to small frequency drifts, irreproducibility of the gas pulse delivery,

and perhaps collisional energy transfer in the early stages of the molecular expansion. The strongest transitions, and therefore the strongest double resonance signals, belong to the F nuclear spin state. Since the resolution of the MW-IR double resonance experiment is higher than the single resonance IR experiment, infrared transitions of the weaker A nuclear spin state transitions could be resolved (Fig. 5.5) from the stronger F state peaks in the double resonance experiment. In total, the ground rotational levels of 20 infrared transitions could be identified by double resonance (Tables 5.6 and 5.7), including transitions of the ${}^R R_0$, ${}^R Q_0$ and ${}^R P_0$ branches of the A and F nuclear spin states (Fig. 5.6 and Fig. 5.7). Attempts to locate infrared transitions belonging to the $K_a=2$ stacks or the unassigned microwave transitions near 11 GHz were unsuccessful.

Double resonance probing of the E state transitions revealed a spectral pattern radically different from the A and F state transitions: The R branch is red-shifted by 0.15 cm^{-1} , a Q branch was not apparent, and the P branch is blue-shifted by $\sim 0.20\text{ cm}^{-1}$ and appears as a doublet (Fig. 5.8). The different appearance of the E state spectrum is consistent with observations on other molecular systems of CH_4 . It is believed that the E state converges on an excited librational state of the complex, in that therefore the rotational constants are significantly different in the vibrationally excited state.¹⁵⁷

Figure 5.5

High resolution MW-IR double resonance experiment on $\text{CO}_2\text{-CH}_4$. The sample was irradiated at the $2_{02} \leftarrow 1_{01}$ MW transition frequencies of the A and F nuclear spin states. The ${}^R\text{Q}_0(1)$ and ${}^R\text{Q}_0(2)$ infrared transitions of the A and F nuclear spin states are resolved and identified in the double resonance experiment (bottom trace) but not in the single resonance infrared spectrum (top trace). States with enhanced (depleted) vibrational ground state population have positive (negative) intensity. The data from 200 cycles were averaged.

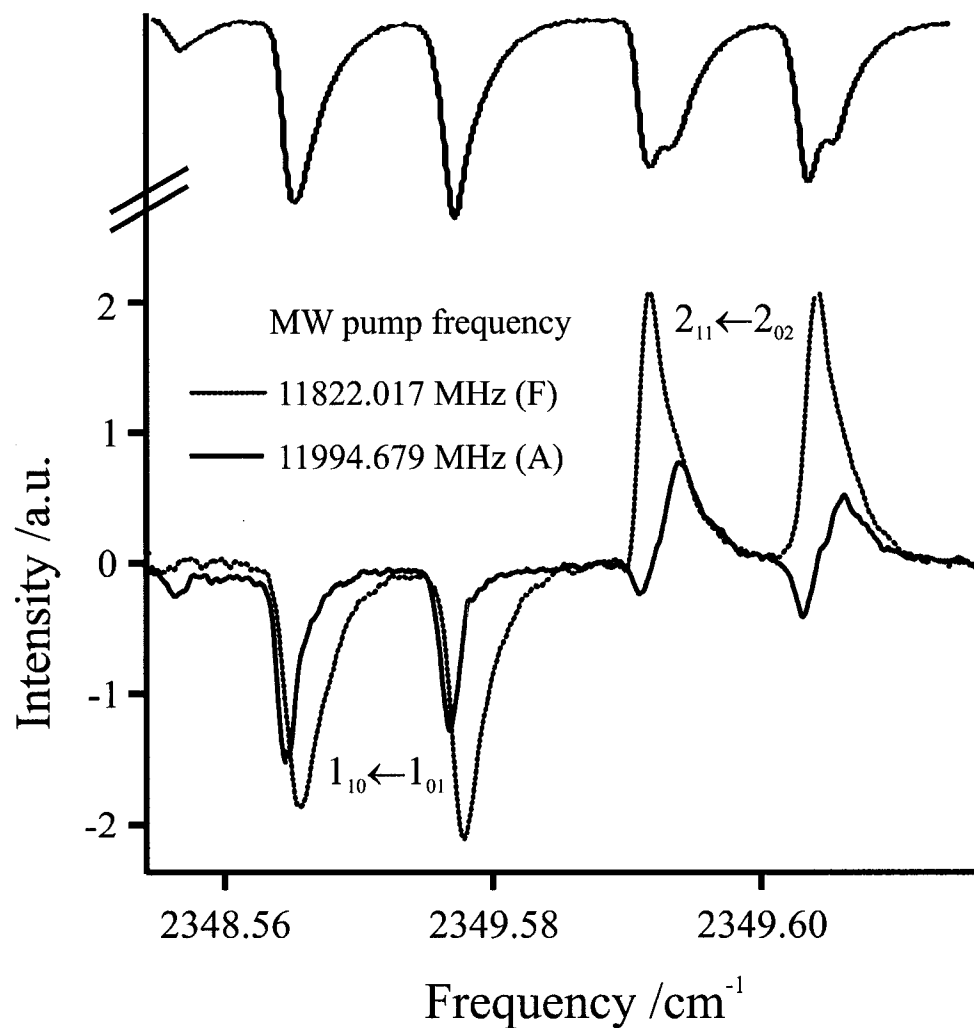


Figure 5.6

MW-IR double resonance experiments on $\text{CO}_2\text{-CH}_4$ in the A state. The MW excitation frequency and energy levels are indicated next to each trace. Each trace is offset for clarity. Assigned P, Q and R branch transitions are circled. Additional features are most likely due to incomplete subtraction.

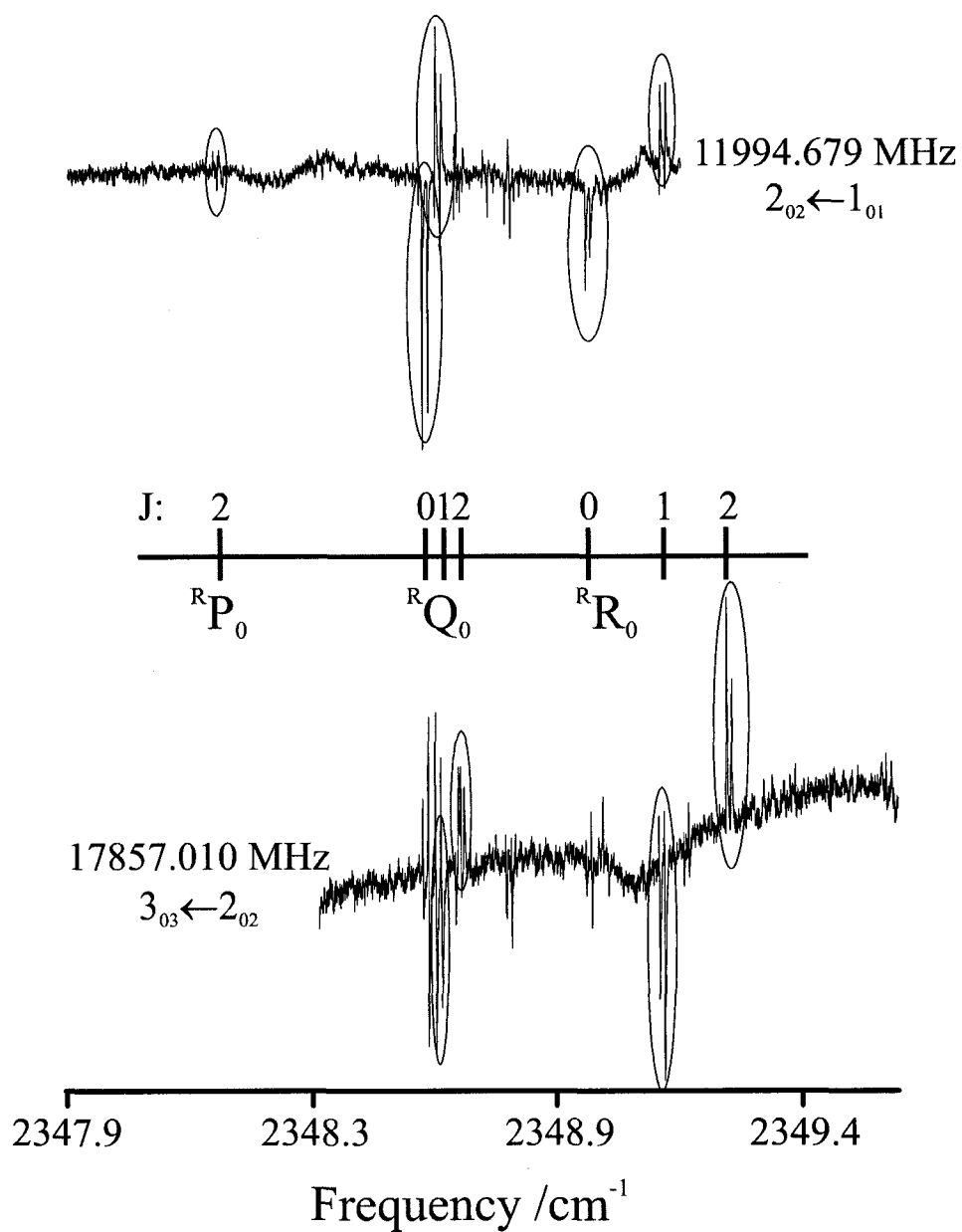


Figure 5.7

MW-IR double resonance experiments on $\text{CO}_2\text{-CH}_4$ in the F state. A higher signal-to-noise ratio was achieved for the F state transitions because of their greater intensity.

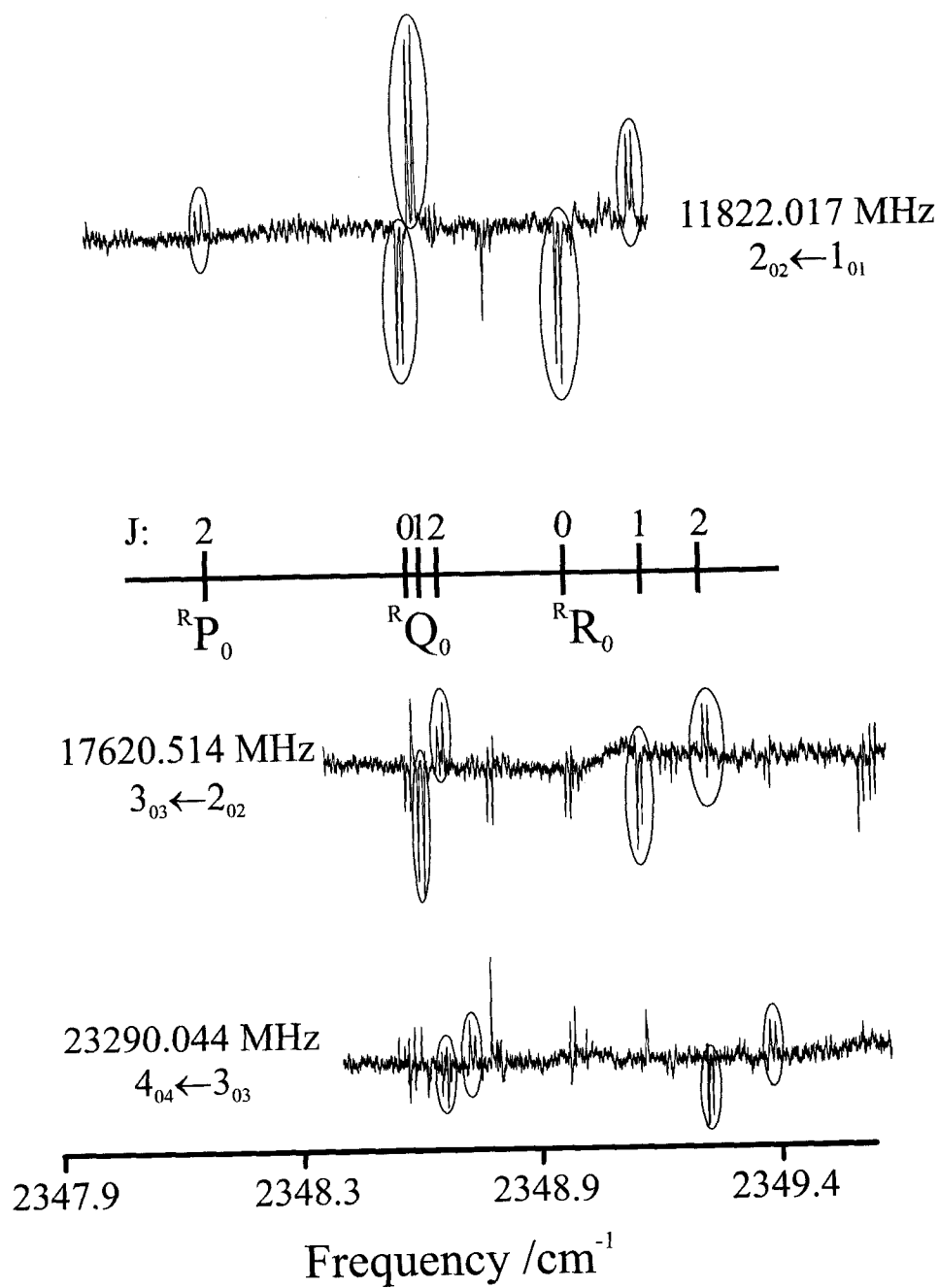


Figure 5.8

MW-IR double resonance experiments on $\text{CO}_2\text{-CH}_4$ in the E state. The noise level was highest in the experiments on the E state transitions because their intensity was lowest. The circled transitions were unambiguously identified as belonging to the E nuclear spin state.

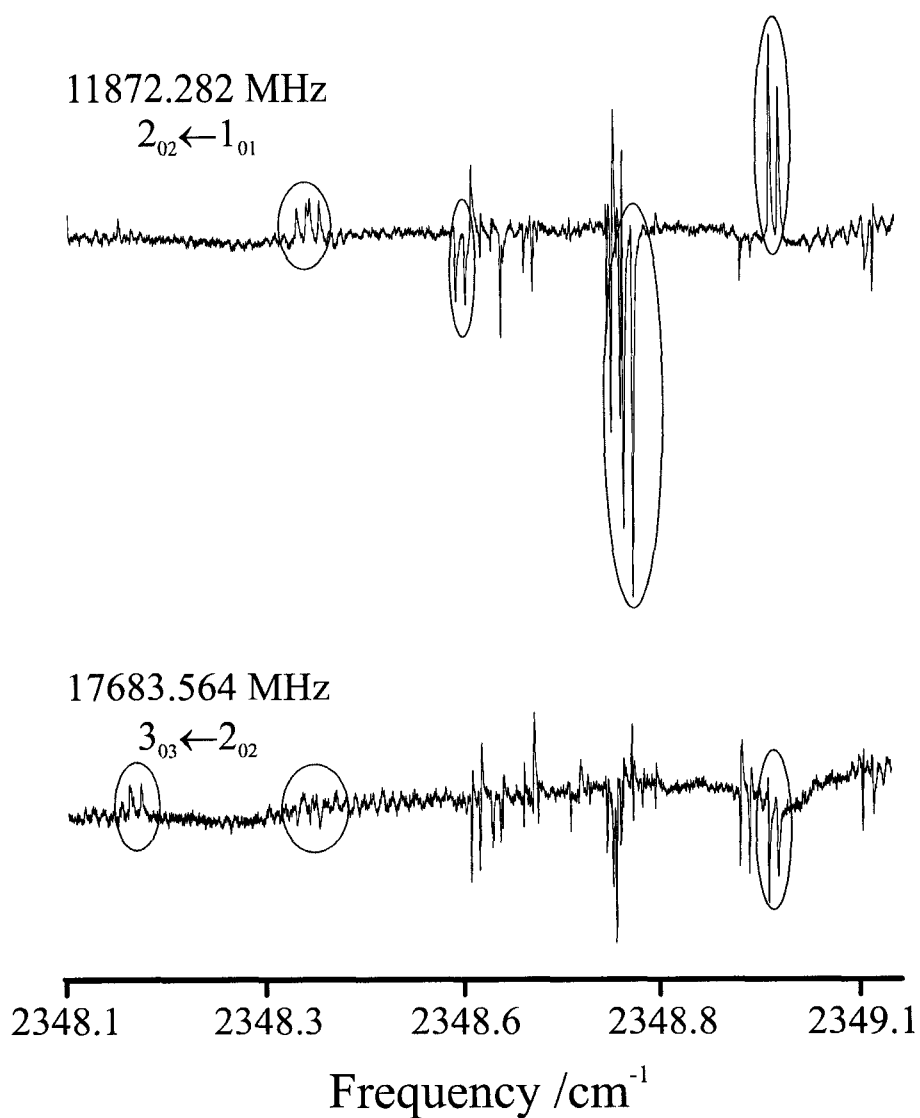


Table 5.6

Observed microwave-infrared double resonance transitions of CO₂-CH₄ in the A and F nuclear spin states.

$J_{KaKc}' \leftarrow J_{KaKc}''$	A /cm ⁻¹	F /cm ⁻¹
2 ₁₂ ← 1 ₀₁	2348.9182	2348.9176
3 ₁₃ ← 2 ₀₂	2349.0800	2349.0791
4 ₁₄ ← 3 ₀₃	2349.2296	2349.2305
5 ₁₅ ← 4 ₀₄		2349.3733
1 ₁₀ ← 1 ₀₁	2348.5695	2348.5708
2 ₁₁ ← 2 ₀₂	2358.5983	2358.5964
3 ₁₂ ← 3 ₀₃	2348.6443	2348.6384
4 ₁₃ ← 4 ₀₄		2348.6972
1 ₁₁ ← 2 ₀₂	2348.1445	2348.1529

Note: A blank entry indicates the double resonance signal was either too weak to be observed and/or masked by incomplete subtraction of stronger nearby transitions.

Table 5.7

Observed microwave-infrared double resonance transitions of CO₂-CH₄ in the E nuclear spin state. The quantum number assignment in the vibrationally excited state is uncertain, and therefore only the vibrational ground state assignment is shown (bold font).

MW frequency /MHz	MW transition $J_{K_a K_c}' \leftarrow J_{K_a K_c}''$	IR increased Intensity /cm ⁻¹	IR reduced Intensity /cm ⁻¹
11872.282	$2_{02} \leftarrow 1_{01}$		2348.7658
11872.282	$2_{02} \leftarrow 1_{01}$	2348.9547	
17683.564	$3_{03} \leftarrow 2_{02}$		2348.9547
17683.564	$3_{03} \leftarrow 2_{02}$	2349.1341	
11872.282	$2_{02} \leftarrow 1_{01}$	2348.5507	
11872.282	$2_{02} \leftarrow 1_{01}$	2348.3688	
17683.564	$3_{03} \leftarrow 2_{02}$		2348.3688
11872.282	$2_{02} \leftarrow 1_{01}$	2348.3531	
17683.564	$3_{03} \leftarrow 2_{02}$		2348.3531
17683.564	$3_{03} \leftarrow 2_{02}$	2348.1668	
17683.564	$3_{03} \leftarrow 2_{02}$	2348.1585	

5.4.4 Analysis of the infrared spectrum and spectral fit

The mid-infrared expansion spectrum of CO₂-CH₄ (Fig. 5.9a-c) resembles a triplicate version of a perpendicular band of a near-prolate asymmetric top, similar to that of the Ar-CO₂ complex.⁸⁶ The assigned infrared transitions are entirely *b*-type. After several low *J* transitions of the ^RP₀, ^RQ₀ and ^RR₀ branches of the A and F states as well as an R branch of the E state had been identified by double resonance, the assignments of higher *J* transitions within those branches was straightforward. In addition to the assigned CO₂-CH₄ transitions listed in Table 5.8, CO₂ monomer, CO₂ dimer, and Ne-CO₂ dimer peaks were present in the spectrum. The clearly visible elevation of the background is most likely due to formation of higher order clusters in the molecular beam and the presence of higher order internal rotation states.

Watson's A-reduction Hamiltonian in the I' representation¹³⁰ was used to model the microwave (Table 5.10) and combined microwave-infrared data (Table 5.11) with the aid of Pickett's SPFIT program.¹³⁷ Each nuclear spin state was fitted separately. The inclusion of quartic distortion constants Δ_{JK} and Δ_K in the fit to the microwave transitions leads to a significant reduction in σ_{rms} and improves the prediction of the $K_a=2$ stack microwave frequencies. In the combined microwave-infrared fit of the A and F nuclear spin states (Table 5.11), the upper state quartic distortion constants were constrained in the fit to the same values as the ground state constants because higher *J* and K_a stack transitions in the vibrationally excited state were not observed. The microwave transitions were given higher weights in the fit consistent with their relative experimental accuracies. The σ_{rms} values obtained in the fits were on the order of the experimental

uncertainty. Inclusion of the infrared transition frequencies in the spectral fit did not result in a noticeable change of the ground state constants. A fit of the same model to the E state transitions was attempted but could not be accomplished. The E state infrared transitions are therefore listed separately in Table 5.9.

The intensity ratio of the closely spaced F and A branches is in agreement with spin statistical analysis (9:5), both in the double resonance and in the single resonance experiments. Each branch appears to have a regular Boltzmann intensity distribution. The intensity of the R branch transitions of the E state, which are red-shifted by 0.15 cm^{-1} relative to the A and F transitions, is slightly larger than predicted by spin statistical analysis. This might in part be caused by the lack of a $J=0$ level, which also increases the relative intensity of the $2_{02} \leftarrow 1_{01}$ microwave transition of the E state.

Figure 5.9a

Mid-infrared expansion spectrum of the $\text{CO}_2\text{-CH}_4$ van der Waals complex. The simultaneously recorded reference spectrum of 10 cm long cell containing CO_2 at a few torr pressure is shown on top. The background is elevated as a result of higher order cluster formation. Transitions marked with a question mark are unassigned and may belong to excited states of the complex. The sample consisted of 0.4% CO_2 and 1.9% CH_4 in 2.5 atm Ne. Data from 200 cycles were averaged.

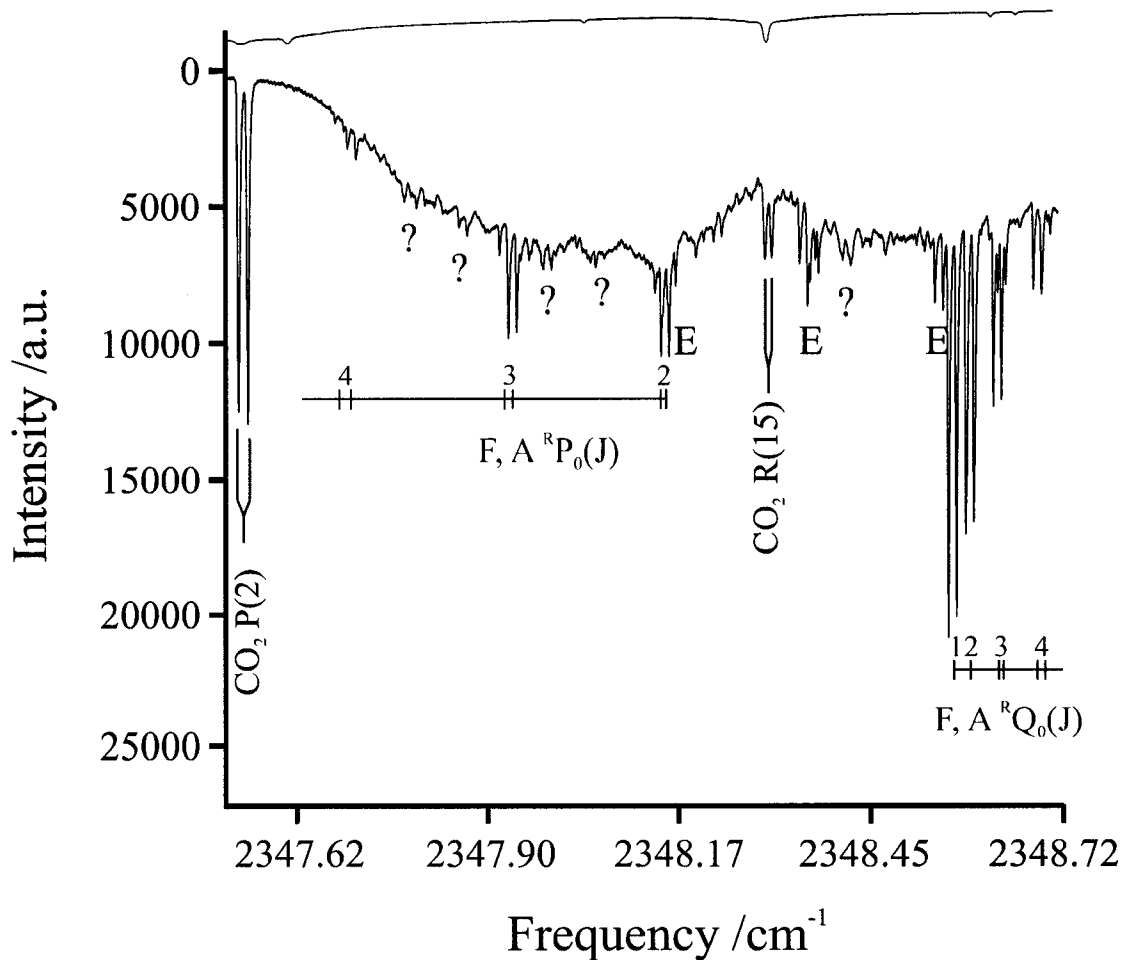


Figure 5.9b

Mid-infrared expansion spectrum of the $\text{CO}_2\text{-CH}_4$ van der Waals complex (cont'd).

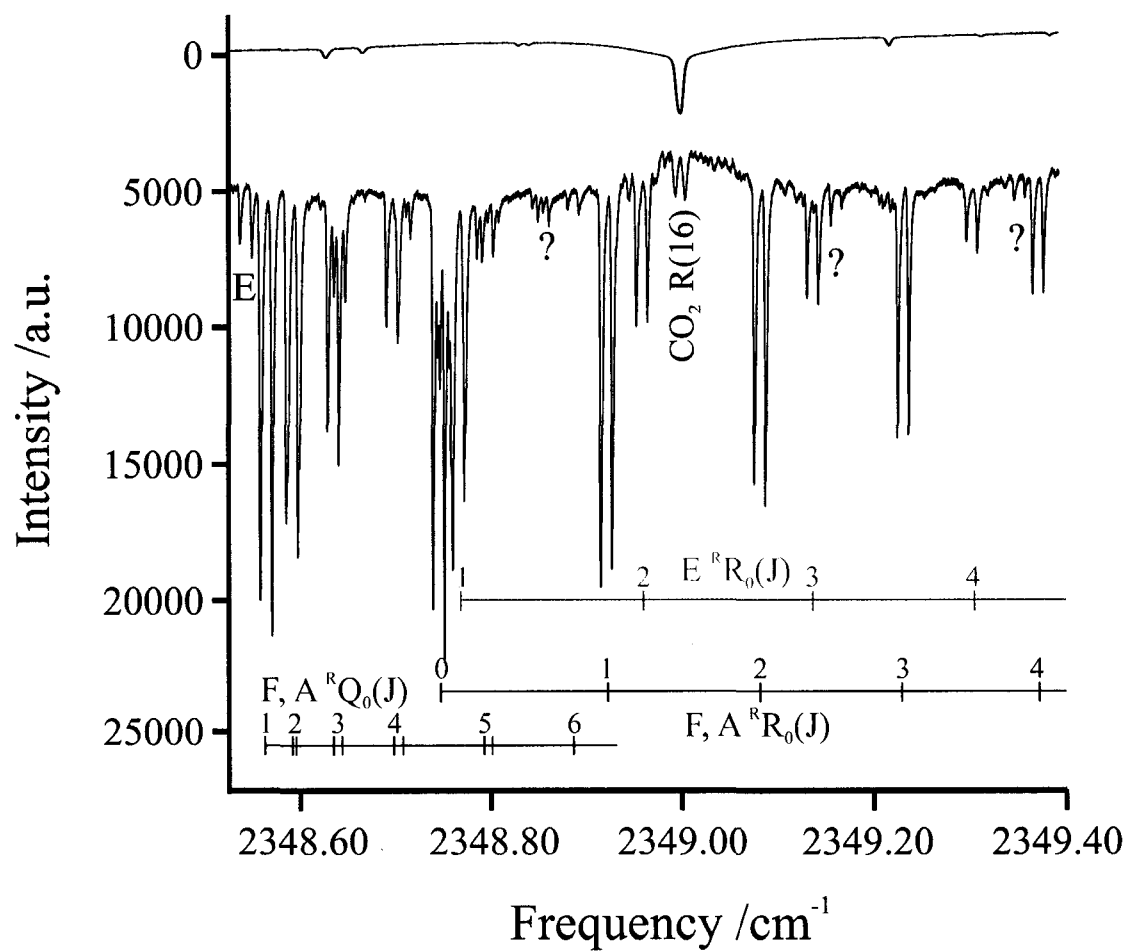


Figure 5.9c

Mid-infrared expansion spectrum of the CO₂-CH₄ van der Waals complex. The sample consisted of 0.4% CO₂ and 1.9% CH₄ in 3.7 atm Ne. Data from 100 cycles were averaged.

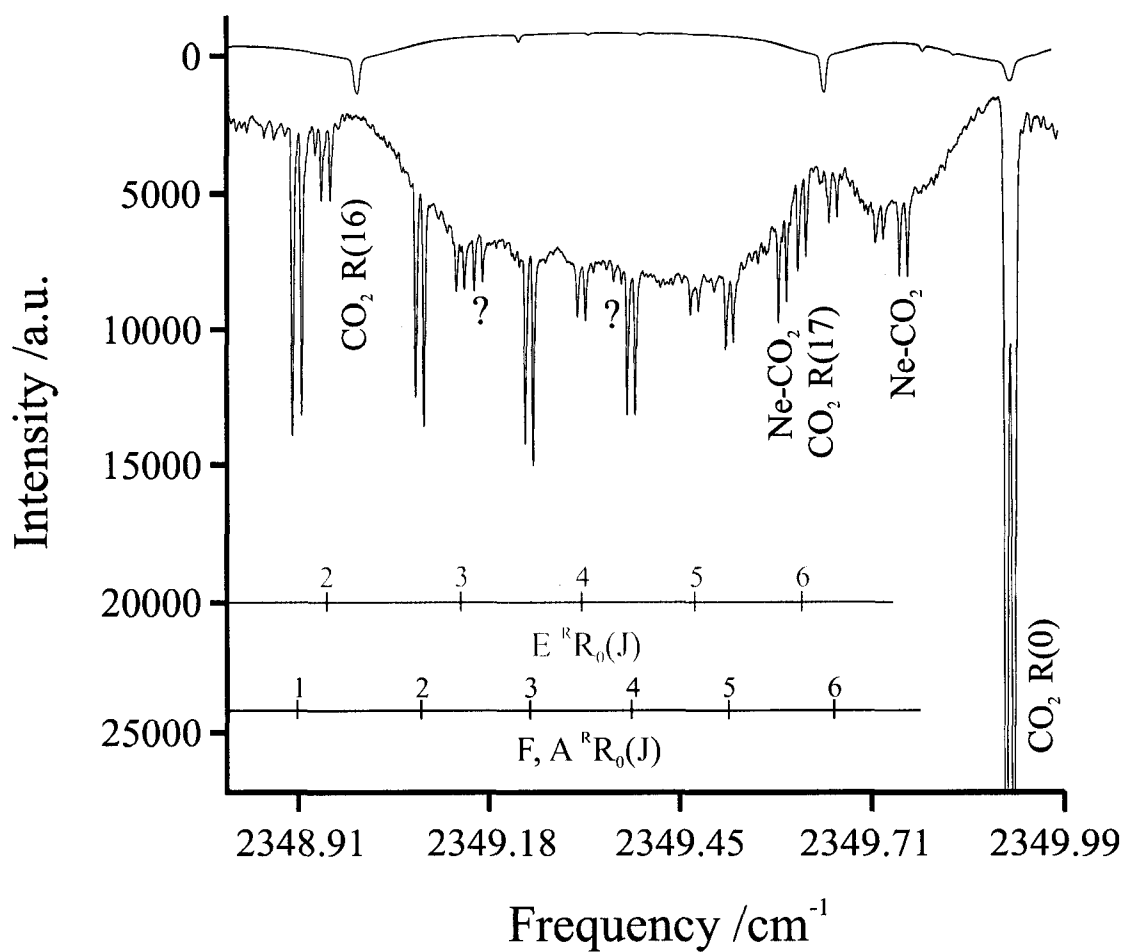


Table 5.8

Assigned infrared transitions of CO₂-CH₄ in the A and F nuclear spin states.

$J_{KaKc}' \leftarrow J_{KaKc}''$	ν_{obs} (A state) /cm ⁻¹	$\nu_{\text{obs}} - \nu_{\text{calc}}$ (A state) /cm ⁻¹	ν_{obs} (F state) /cm ⁻¹	$\nu_{\text{obs}} - \nu_{\text{calc}}$ (F state) /cm ⁻¹
1 ₁₁ ← 0 ₀₀	2348.7458	+0.0010	2348.7458	+0.0008
2 ₁₂ ← 1 ₀₁	2348.9182	-0.0005	2348.9176	-0.0003
3 ₁₃ ← 2 ₀₂	2349.0800	+0.0003	2349.0791	+0.0002
4 ₁₄ ← 3 ₀₃	2349.2296	-0.0004	2349.2305	+0.0007
5 ₁₅ ← 4 ₀₄	2349.3733	+0.0005	2349.3733	-0.0004
6 ₁₅ ← 5 ₀₅	2349.5120	-0.0002	2349.5141	-0.0002
7 ₁₆ ← 6 ₀₆	-	-	2349.6550	-0.0002
8 ₁₇ ← 7 ₀₇	-	-	2349.7995	+0.0002
1 ₁₀ ← 1 ₀₁	2348.5695	-0.0010	2348.5708	-0.0008
2 ₁₁ ← 2 ₀₂	2358.5983	-0.0005	2358.5964	-0.0007
3 ₁₂ ← 3 ₀₃	2348.6443	-0.0001	2348.6384	0.0004
4 ₁₃ ← 4 ₀₄	2348.7113	+0.0007	2348.6972	-0.0003
5 ₁₄ ← 5 ₀₅	2348.8006	-0.0002	2348.7785	-0.0001
6 ₁₅ ← 6 ₀₆	-	-	2348.8840	-0.0001
7 ₁₆ ← 7 ₀₇	-	-	2349.0150	+0.0005
8 ₁₇ ← 8 ₀₈	-	-	2349.1681	-0.0002
1 ₁₁ ← 2 ₀₂	2348.1445	+0.0008	2348.1529	+0.0001
2 ₁₂ ← 3 ₀₃	2347.9229	-0.0001	2347.9361	+0.0003
3 ₁₃ ← 4 ₀₄	2347.6976	-0.0004	2347.7144	+0.0002

Table 5.9

Observed infrared transitions of CO₂-CH₄ in the E state nuclear spin state.

Frequency /cm⁻¹
2348.1585
2348.1668
2348.3531
2348.3688
2348.5507
2348.7658
2348.9547
2349.1341
2349.3032
2349.4641

Table 5.10

Molecular constants derived from a fit of Watson's A-reduction Hamiltonian in the F representation¹³⁰ to the assigned FTMW transitions.

Parameter	A	F	E
n	8	8	5
<i>A</i> /MHz	11357 (12)	11409 (18)	11079 (22)
<i>B</i> /MHz	3400.78 (25)	3325.56 (36)	3343.49 (47)
<i>C</i> /MHz	2624.04 (26)	2608.27 (36)	2618.21 (47)
Δ_J /kHz	38.715 (64)	30.552 (64)	77.20 (10)
Δ_{JK} /kHz	546.79 (32)	918.14 (32)	195.82 (94)
Δ_K /MHz	-17.25 (16)	-47.66 (18)	-
σ_{rms} /kHz	4.0	2.5	-

Table 5.11

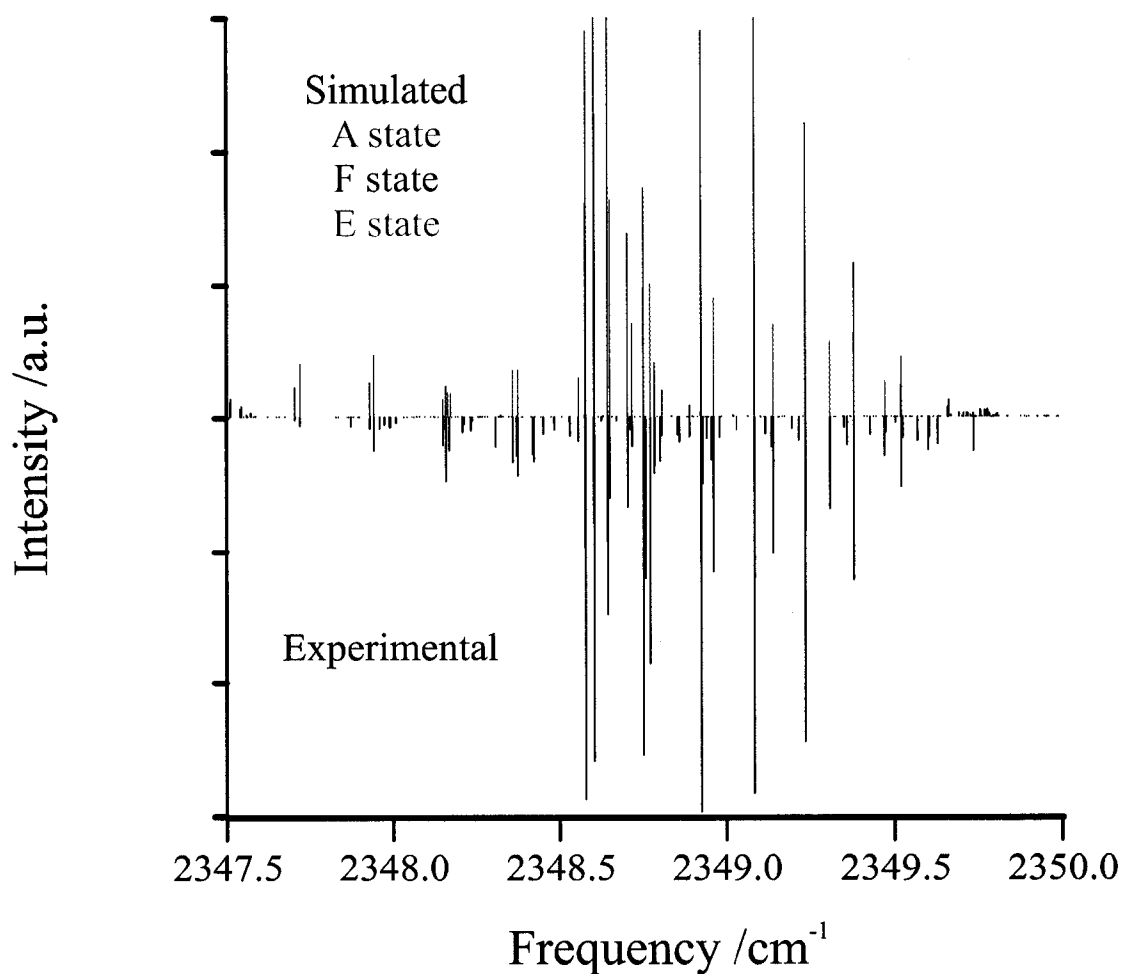
Molecular constants derived from a fit of Watson's A-reduction Hamiltonian in the F representation¹³⁰ to the assigned FTMW and IR transitions.

Parameter	A	F
n	22	27
ν_0 /cm ⁻¹	2348.2782 (158)	2348.2785 (62)
A'' /MHz	11357 (12)	11408 (18)
A' /MHz	11361 (474)	11343 (187)
B'' /MHz	3400.78 (25)	3325.55 (36)
B' /MHz	3412.28 (97)	3331.03 (52)
C'' /MHz	2624.04 (26)	2608.28 (36)
C' /MHz	2610.8 (11)	2596.59 (64)
Δ_J'' /kHz	38.715 (64)	30.556 (64)
Δ_J' /kHz	72 (36)	12 (13)
Δ_{JK} /kHz ^a	546.79 (32)	918.15 (32)
Δ_K /MHz ^a	-17.25 (0.16)	-47.68 (18)
σ_{rms} /cm ⁻¹	0.00057	0.00042

^a Upper and lower state constants were constrained to identical values.

Figure 5.10

Stick spectrum comparison between experimental and simulated spectra of the CO₂-CH₄ van der Waals complex. The major spectral features are assigned. Transitions identified as belonging to the E state are substantially shifted relative to the A and F state transitions.



5.4.5 Structural parameters and moment of inertia defects

The resemblance of both infrared and microwave spectra to those of rare gas - carbon dioxide systems suggests treatment of CO₂-CH₄ as a ball-rod system, where CH₄ is viewed as a pseudo-atom of mass 16. The effects of zero-point vibrations in so-called ball-stick systems are usually quantified in terms of the inertial defect $\Delta = I_c - I_b - I_a$.²⁸ For a rigid and planar molecule, Δ is exactly zero. Positive contributions to the inertial defect arise from in-plane motions, negative deviations from out-of-plane motions.

For a ball-rod analysis to be valid, the moment of inertia of the methane hydrogens I_{CH_4} (3.17 amu Å²)¹²⁷ must be subtracted from the experimental moment of inertia of the complex I_{aa} , I_{bb} , and I_{cc} .¹⁵⁷

$$I_{aa}' = I_{aa} - I_{\text{CH}_4} \quad (5.4a)$$

$$I_{bb}' = I_{bb} - I_{\text{CH}_4} \quad (5.4b)$$

$$I_{cc}' = I_{cc} - I_{\text{CH}_4} \quad (5.4c)$$

Effective structural parameters were calculated as in Section 4.5.1 by least-squares fitting of calculated moments of inertia of the complex to the experimental values, keeping the CO₂ bond length and angle r_{CO} and α_{CO} fixed at their respective monomer values¹⁴² and allowing the intermolecular bond angle and distance to float in the fit. Structural parameters were also calculated using Howard's method for Rg-CO₂.⁸⁶ The results are summarized in Table 5.14.

Table 5.12

Experimental moments of inertia and inertial defects of CO₂-CH₄ (uncorrected).

	A /amu Å ²	F /amu Å ²	E /amu Å ²
I _{aa} "	44.49 (4)	44.28 (6)	45.60 (8)
I _{bb} "	148.56 (1)	151.92 (2)	151.11 (2)
I _{cc} "	192.54 (2)	193.70 (3)	192.96 (3)
Δ"	-0.51	-2.51	-3.74
ΔΔ"	0.00	-1.99	-3.23
I _{aa} '	44.47 (186)	44.54 (73)	-
I _{bb} '	148.06 (4)	148.50 (2)	-
I _{cc} '	193.51 (8)	191.40 (5)	-
Δ'	+0.98	-1.64	-
ΔΔ'	0.00	-2.62	-

Notes: $\Delta = I_c - I_a - I_b$. $\Delta\Delta$ is the change of the inertial defect with respect to $\Delta_{j=0}$.

Table 5.13

Experimental moments of inertia and inertial defects of CO₂-CH₄ (revised using equation 5.4).

	A (exp.) /amu Å ²	A (calc.) ^a /amu Å ²	F (exp.) /amu Å ²	F (calc.) ^a /amu Å ²	E (exp.) /amu Å ²	E (calc.) ^a /amu Å ²
I _{aa} "	41.32 (4)	42.20	41.11 (6)	41.33	42.43 (8)	42.24
I _{bb} "	145.39 (1)	146.28	148.75 (2)	148.97	147.94 (2)	147.74
I _{cc} "	189.37 (2)	188.48	190.53 (3)	190.31	189.79 (3)	189.99
Δ"	+2.66	0	+0.66	0	-0.57	0
ΔΔ"	0.00		-1.99		-3.23	
I _{aa} '	41.30 (186)	42.68	41.37 (73)	41.88	-	-
I _{bb} '	144.89 (4)	146.27	148.50 (2)	149.01	-	-
I _{cc} '	190.34 (8)	188.96	191.40 (5)	190.89	-	-
Δ'	+4.15	0	+1.53	0	-	-
ΔΔ'	0.00		-2.62		-	-

^a Calculated using equation 1.22.

Table 5.14a

Effective structural parameters of the CO₂-CH₄ weakly bound complex calculated by a least-squares error fit to the observed moments of inertia.

	A	F	E
$r_{\text{cm}}'' / \text{\AA}$	3.519	3.541	3.537
$r_{\text{cm}}' / \text{\AA}$	3.521	3.544	-
$\alpha'' / ^\circ$	81.2	78.0	81.4
$\alpha' / ^\circ$	82.1	78.9	-

Table 5.14b

Effective structural parameters of the CO₂-CH₄ weakly bound complex calculated using Howard's method for Rg-CO₂ complexes.⁸⁶ In Howard's method, only two of the three rotational constants, which are believed to be least affected by the internal motions, are used to estimate the effective structure.

	A	F	E
$r_{\text{cm}}'' / \text{\AA}$	3.530	3.544	3.535
$r_{\text{cm}}' / \text{\AA}$	3.542	3.555	-
$\alpha'' / ^\circ$	79.84	79.28	83.60
$\alpha' / ^\circ$	79.79	79.97	-

Table 5.15

Comparison of structural parameters of T-shaped complexes containing CO₂.

Molecule	Δv_0 /cm ⁻¹	Δ'' /amuÅ ²	Δ' /amuÅ ²	r_{cm}'' /Å	α'' /°	r_{cm}' /Å	α' /°
CO ₂ -He ¹⁰³	+0.095	+8.54	+10.98	3.581	83.9	3.614	81.4
CO ₂ -Ne ⁸⁶	+0.1362	+3.88	+3.91	3.290	81.4	3.293	81.2
CO ₂ -Ar ⁸⁶	-0.47011	+2.44	+2.39	3.504	83.1	3.504	83.0
CO ₂ -Kr ⁸⁶	-0.88405	+2.22	+2.41	3.624	83.3	3.625	83.2
CO ₂ -Xe ⁸⁶	-1.47132	+3.16	+2.29	3.815	83.3	3.815	83.4
CO ₂ -CH ₄ (A) ^a	-0.865	+2.66	+4.15	3.530	79.8	3.542	79.8
CO ₂ -CH ₄ (F) ^a	-0.865	+0.66	+1.53	3.544	79.3	3.555	80.0
CO ₂ -CH ₄ (E) ^a	?	-0.57	?	3.535	83.6	?	?

^a Structural parameters based on Howard's equations⁸⁶ (Table 5.14b).

5.5 Discussion

Because $\text{CO}_2\text{-CH}_4$ had not been studied prior to this work, the equilibrium geometry and selection rules had to be determined. The *ab initio* calculations on several cuts of the potential energy surface (Section 5.2) indicate that the equilibrium configuration of $\text{CO}_2\text{-CH}_4$ is T-shaped. Consistent with a T-shaped equilibrium structure, the observed infrared spectrum consists of *b*-type transitions belonging to a perpendicular band of a near-prolate asymmetric top. The observed transitions are further split into three components belonging to the three internal rotation states of $\text{CO}_2\text{-CH}_4$, which leads to significant spectral crowding. Different internal rotation states are associated with the three nuclear spin states in the cold environment of the molecular beam (Section 5.3). In order to achieve an assignment of the IR spectrum, it was essential to locate and assign the microwave transitions of the different internal rotation states and to perform microwave-infrared double resonance experiments. In agreement with spin statistical analysis, the microwave transitions are purely *a*-type, and transitions to and from odd K_a levels are absent as anticipated from the equivalency of the two oxygen nuclei. In both the microwave and infrared regions, the relative intensities of transitions within the internal rotor states correspond to their nuclear spin statistical weights, and the intensity distribution within each nuclear spin state follows Boltzmann statistics.

While the double resonance experiments were essential in identifying the branch origins of two of the three internal rotor states (which are unresolved in the single resonance experiment), the ground rotational states of weaker, high *J* ro-vibrational transitions could not be confirmed in that manner. This is especially unfortunate because infrared transitions linked to the $K_a''=2$ stacks were not identified. As a result, the

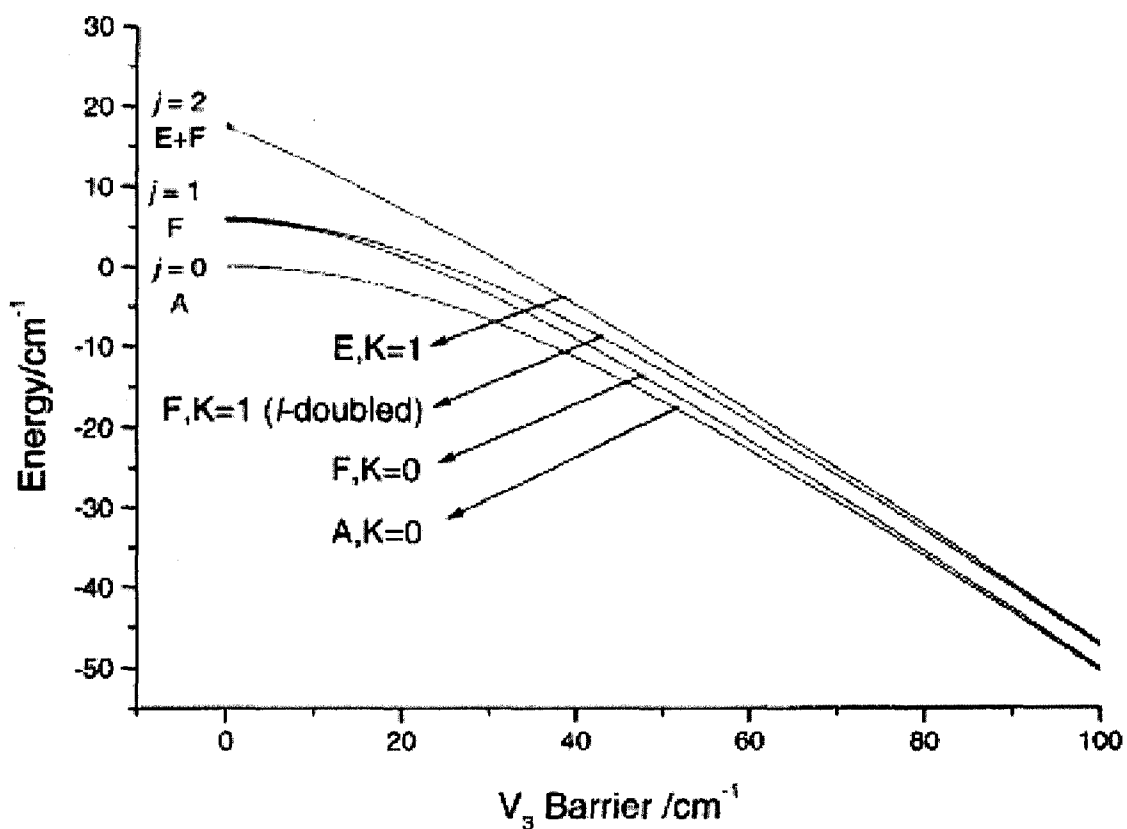
predictive power of the molecular constants is limited. Weak transitions were observed at frequencies above 2350 cm^{-1} but could not be assigned due to absence of double resonance data and overlap with $(\text{CO}_2)_2$ or Ne- CO_2 transitions. Similarly, double resonance experiment failed to identify infrared transitions linked to the unassigned microwave transitions at 11 GHz and $J''=3$ or $J''=4$ transitions of the E state. Lack of microwave excitation power may have been part of the problem, but a higher power amplifier was not available in the laboratory.

The *ab initio* calculations (Section 5.2) predict an equilibrium intermolecular separation r_e of 3.4 \AA , which is in good agreement with the observed effective value r_0 of $\sim 3.5\text{ \AA}$. While dispersion forces dominate intermolecular forces in the complex, residual electrostatic interaction through the protons also appears to be a factor in the interactions of carbon dioxide with methane. This explains why particular geometric arrangements of the methane unit are preferred in the complex. For example, the intermolecular interaction for surface D (Figure A5.3), in which two hydrogen atoms point towards carbon dioxide, is significantly stronger than for surface C (Figure A5.2) for identical r_{cm} and α .

Insight into the rigidity, effective structure and internal dynamics of the CO_2 - CH_4 complex can be gained from the comparison of the molecular constants of the three CO_2 - CH_4 internal rotation states. CO_2 - CH_4 complex is as rigidly bound as a rare gas - carbon dioxide system, judged from the good fit to the rigid rotor Hamiltonian model (Tables 5.10 and 5.11) and magnitude of the inertial defect (Table 5.13) and the distortion constants.

Figure 5.11

Energy level diagram showing the hindered-rotor state energies of Ar-SiH₄ as a function of barrier height to internal rotation V_3 (adapted from Kawashima *et al.*¹⁵⁸). Very similar energy level diagrams were derived for other rare gas- spherical top systems.¹⁵⁵ At high barrier to internal rotation, the lowest energy levels of the A and F nuclear spin states converge to a ground torsional state, but the lowest energy level of the E nuclear spin state converges onto an excited torsional state (right hand side). This energy level diagram has been applied to OCS-CH₄,¹⁵⁷ and therefore is also expected to be applicable to CO₂-CH₄.

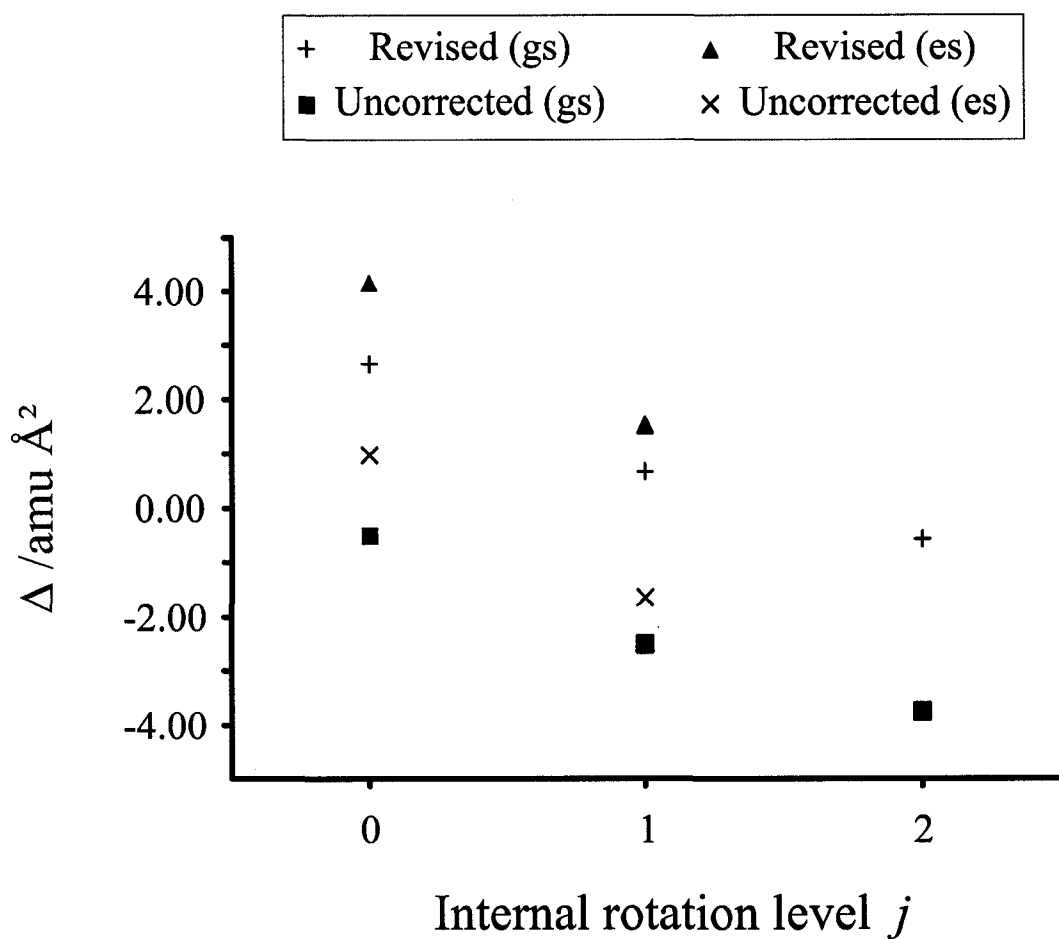


The differences between the nuclear spin states can be used as an indirect measure of the anisotropy of the intermolecular potential.¹⁵⁵ If the anisotropy of the potential is large, the A and F nuclear spin states converge onto the lowest torsional state and have therefore similar molecular constants, while the E state converges onto an excited librational state, with very different molecular constants. An example of this effect for the Ar-SiH₄ complex is shown in Fig. 5.11. For OCS-CH₄, the splittings between A and F state microwave transitions are 10 kHz or less.¹⁵⁷ The splittings between microwave transitions belonging to the A and F nuclear spin states of CO₂-CH₄ are several orders of magnitude larger, about 100 MHz (Table 5.5). On the basis of the work by Randall *et al.*,¹⁵⁵ one can argue that the barrier to internal rotation is smaller for CO₂-CH₄ than for OCS-CH₄. The barrier height can be calculated theoretically, if the minimum energy path is known. If the internal rotation motion is assumed to be connected through configurations B (Table A5.2) and D (Table A5.4), the barrier to internal rotation is estimated from the *ab initio* calculations to be between 0.037 mH (8.1 cm⁻¹) and 0.181 mH (40 cm⁻¹).

The effective structure of the complex is slightly different for each internal rotation state (Table 5.14). For example, r_{cm} increases from 3.519 Å in the totally symmetric A state to 3.541 Å in the F state, and decreases slightly to 3.537 Å in the E state. This can in part be attributed to a larger effective van der Waals radius of an internally rotating methane unit. The shorter van der Waals bond length of the E state may be an artifact as a result of fitting only 5 microwave transitions.

Figure 5.12

Inertial defect as a function of internal rotational level j . The increase of the inertial defect with the level of internal rotation can be explained by an increase of out-of-plane motions.



The effective intermolecular bond angle α of the revised moments of inertia is calculated using Howard's method as 79.8° in the A state, 79.3° in the F state and 83.6° in the E state. Compared to values of 81.4° and 83.1° for Ne-CO₂ and Ar-CO₂ (Table 5.15), the computed values indicate that the magnitude of the in-plane motions in CO₂-CH₄ is slightly larger than those in the rare gas - carbon dioxide systems. This conclusion is corroborated by the positive revised inertial defect ($\Delta = +2.66$ amu Å²) of the A nuclear spin state, which is comparable to the inertial defects of Ne-CO₂ and Ar-CO₂ of 3.88 amu Å² and 2.44 amu Å².⁸⁶ For the E and F nuclear spin states of CO₂-CH₄, the inertial defect decreases with increasing internal rotation quantum number j (Fig. 5.12), consistent with an increase of out-of-plane motions. The internal rotation in the F state most likely resembles the motion of the main propeller blades of a helicopter. The internal motions of the complex in the E state are more complicated to assess.

In the vibrational excited state of the assigned A and F nuclear spin states, the effective intermolecular separation and the intermolecular bond angle increase, suggesting overall weakening of the van der Waals bond upon vibrational excitation. However, the moment of inertia defects Δ become significantly more positive ($+2.66 \rightarrow +4.15$ for the A state, and $+0.66 \rightarrow +1.53$ for the F state). This indicates that the amplitude of in-plane internal motions is increasing upon vibrational excitation. Such an increase was not observed for rare gas - carbon dioxide.⁸⁶ The sensitivity of the inertial defect to the level of the internal rotation also increases in the vibrational excited state ($\Delta\Delta''_{F-A} = -1.99$, $\Delta\Delta'_{F-A} = -2.62$), indicating that the increase in amplitude of in-plane motion is less severe for the internally rotating CO₂-CH₄. Another important aspect of the

vibrational upper state is the band origin shift of the asymmetric stretching frequency relative to the free monomer (Table 5.15). Because the interaction of methane with carbon dioxide is dominated by van der Waals dispersion forces, and the complex is T-shaped, the band origin should be comparable to those of the rare gas - carbon dioxide dimers. The red-shift of the CO₂-CH₄ band origin is similar to that of Kr-CO₂ (Table 5.15) and too large to be explained by dispersion interactions alone. The relative placement of the band origin is consistent with what was previously observed for OCS-CH₄.¹⁵⁷

The observed E state transitions cannot be modeled by the same Hamiltonian as the A and F state transitions. In addition, the line intensities of the E state transitions are slightly greater than predicted by nuclear spin statistics. In the infrared spectrum, for example, the relative intensities of the overlapping A and F state R branches to the E state R branch are expected to be 14:2, but an intensity ratio of between 4:1 and 3:1 is observed (Fig. 5.9). As pointed out by Hearn *et al.* for OCS-CH₄,¹⁵⁷ the E state rotational constants may be significantly different between the ground and vibrationally excited states, and this may also be the case for CO₂-CH₄. In addition, the intensity of the E state transitions may be enhanced by the lack of a J=0 level and corresponding increased relative population.

5.6 Summary and future work

$\text{CO}_2\text{-CH}_4$ has been investigated by microwave, infrared and microwave-infrared double resonance spectroscopy. The *b*-type infrared and *a*-type microwave spectra and *ab initio* calculations are consistent with a T-shaped equilibrium structure. The transitions are split into three sub-bands, which were assigned to different internal rotation states associated with different nuclear spin states of methane. The magnitude of this splitting is orders of magnitude larger than observed for OCS-CH_4 , indicating a reduced barrier height to internal rotation. Observed transitions in the A and F nuclear spin states within the $K_a''=0$ and $K_a'=1$ stacks were fitted to Watson's A-reduction Hamiltonian in the F representation, while only the $K_a''=0$ stack of the E state MW transitions could be fit by this model. Inertial defect calculations indicate an increase of out-of-plane motions with internal rotation.

In order to gain additional insight into the internal dynamics of $\text{CO}_2\text{-CH}_4$, a comprehensive microwave study of isotopically substituted versions of the complex should be undertaken. For example, an investigation of the unsymmetrically substituted $^{18}\text{OCO-CH}_4$ or $^{17}\text{OCO-CH}_4$ would be particularly useful because the presence of combination differences are not only an additional confirmation of the assignment but allow in principle a much more precise determination of spectroscopic constants. In addition, observation of vibration-rotation tunneling spectra in the near-infrared would provide additional insight into the various internal motions of this complex.

CHAPTER 6

MID-INFRARED SPECTRA OF THE WEAKLY BOUND COMPLEXES $^{18}\text{OCO-Ne}$, $^{18}\text{OCO-N}_2$ AND $^{18}\text{OCO-He}$

6.1 Introduction

In many mid-infrared spectra of van der Waals complexes containing the CO_2 unit, entire branches are absent as a result of nuclear spin statistics due to the presence of two equivalent oxygen nuclei. It is therefore often difficult to test the predictive power and self-consistency of a model on the basis of the infrared spectra alone. One such example is the case of the He-CO_2 complex.¹⁰³ The mid-infrared spectrum of He-CO_2 is entirely *b*-type, and the spectrum is complicated by large amplitude internal motions.¹⁰³ Consequently, the quality of the spectroscopic constants, their predictive power, and match to theory¹⁵⁹ is lower than usual, and more experimental data would be useful to fully characterize this system.

In contrast to CO_2 containing complexes, infrared spectra of complexes that lack symmetry such as OCS-He are not restricted by nuclear spin statistics, so that good spectral fits can be obtained even in the absence of microwave data.¹⁰⁹ The symmetry of CO_2 can be broken by unsymmetric isotopic substitution of the oxygen nuclei, which then lights up the formerly dark transitions. One suitable isotopomer is ^{18}OCO . However, the entire ro-vibrational spectrum of ^{18}OCO is red-shifted by 17 cm^{-1} relative to the main isotopomer. The only known weakly bound complex of ^{18}OCO prior to this work is $\text{Ar-}^{18}\text{OCO}$, which has been studied both in the infrared¹⁰⁴ and the microwave region.¹⁹

In this Chapter, the mid-infrared spectra of $\text{N}_2\text{-}^{18}\text{OCO}$, $\text{Ne-}^{18}\text{OCO}$ and $\text{He-}^{18}\text{OCO}$ are presented and analyzed. The deduced molecular constants and derived effective structures are compared to those of the main isotopomers $\text{N}_2\text{-CO}_2$,⁸⁷ Ne-CO_2 ⁸⁶ and He-CO_2 .¹⁰³

6.2 Experimental

^{18}OCO was synthesized by exchanging CO_2 over ^{18}O labeled water (99% H_2^{18}O , Cambridge Isotopes, Andover, MA) in a 1L sealed glass tube. Initially, a 3-year old batch was used in the experiments. Subsequent samples of ^{18}OCO were prepared over seven day periods. To extract the ^{18}OCO , the glass tube was submerged in a liquid nitrogen bath and cooled to -196°C . The supernatant gases were pumped off, and the liquid nitrogen bath was removed. The condensed dry ice was allowed to evaporate and flood a 10 L steel reservoir up to pressures of 0.05 atm. Care was taken that the temperature of the glass bottle stayed well below the freezing point of water. Pressurized samples were then prepared in the steel container. Spectra of static sample gas in the multipass cell revealed the presence of $^{12}\text{C}^{18}\text{O}_2$, $^{12}\text{C}^{16}\text{O}^{18}\text{O}$ and $^{12}\text{C}^{16}\text{O}_2$, indicating satisfactory conversion to ^{18}OCO . ^{18}OCO could be recycled from unused sample portions by freezing the steel cylinder with liquid nitrogen and pumping off the carrier gas. The molecular spectra were often accompanied by additional lines, which were tentatively assigned to mixed CO_2 dimers and $(^{18}\text{OCO})_2$. At the end of the experiments, left-over ^{18}OCO was used to locate several microwave transitions of the $^{18}\text{OCO-Ne}$ complex using the Fourier transform microwave spectrometer described earlier.^{15,18}

Samples of $\text{N}_2\text{-}^{18}\text{OCO}$ (or $\text{Ne-}^{18}\text{OCO}$) were prepared by adding up to 5% N_2 (or Ne) to He carrier gas at backing pressures of up to 8 atm. Spectra of $\text{He-}^{18}\text{OCO}$ were recorded at backing pressures of up to 12 atm. In a typical experiment, 200 cycles were averaged.

6.3 Results and Discussion

6.3.1 $\text{N}_2\text{-}^{18}\text{OCO}$

A portion of the mid-infrared expansion spectrum of $\text{N}_2\text{-}^{18}\text{OCO}$ is shown in Fig. 6.1. The mid-infrared spectrum of $\text{N}_2\text{-}^{18}\text{OCO}$ is that of a perpendicular band of a near-prolate asymmetric top and is very similar to the known⁸⁷ spectrum of $\text{N}_2\text{-CO}_2$. 49 rovibrational transitions of $\text{N}_2\text{-}^{18}\text{OCO}$ were assigned (Table 6.1). The observed intensity distribution is consistent with a Boltzmann temperature of 0.8 K. Watson's S-reduction Hamiltonian in the Γ representation¹³⁰ was used to fit the experimental data with the aid of Pickett's SPFIT program.¹³⁷ The rms error of the fit was on the order of the experimental uncertainty. The derived molecular constants of $\text{N}_2\text{-}^{18}\text{OCO}$ are consistent with a T-shaped equilibrium structure (Table 6.2).

Table 6.1

Frequencies and assignments of observed infrared transitions of the N₂-¹⁸OCO complex.

	$\begin{matrix} J_{KaKc}' \\ \leftarrow J_{KaKc}'' \end{matrix}$	ν_{obs} /cm ⁻¹	$\nu_{\text{obs}} - \nu_{\text{calc}}$ /cm ⁻¹		$\begin{matrix} J_{KaKc}' \\ \leftarrow J_{KaKc}'' \end{matrix}$	ν_{obs} /cm ⁻¹	$\nu_{\text{obs}} - \nu_{\text{calc}}$ /cm ⁻¹
^R R ₀	1 ₁₁ ← 0 ₀₀	2333.0454	+0.0002		4 ₁₃ ← 4 ₀₄	2332.9818	-0.0004
	2 ₁₂ ← 1 ₀₁	2333.1585	0.0000		5 ₁₄ ← 5 ₀₅	2333.0129	+0.0002
	3 ₁₃ ← 2 ₀₂	2333.2664	+0.0001		6 ₁₅ ← 6 ₀₆	2333.0512	-0.0003
	4 ₁₄ ← 3 ₀₃	2333.3689	+0.0001	^R Q ₁	2 ₂₀ ← 2 ₁₁	2333.5243	-0.0004
	5 ₁₅ ← 4 ₀₄	2333.4662	-0.0006		3 ₂₁ ← 3 ₁₂	2333.5083	-0.0006
	7 ₁₇ ← 6 ₀₆	2333.6519	-0.0001		5 ₂₄ ← 5 ₁₅	2333.6194	-0.0003
	8 ₁₈ ← 7 ₀₇	2333.7418	+0.0003	^P Q ₁	1 ₀₁ ← 1 ₁₀	2332.2991	-0.0012
	9 ₁₉ ← 8 ₀₈	2333.8302	0.0000		2 ₀₂ ← 2 ₁₁	2332.2892	+0.0003
^R R ₁	2 ₂₁ ← 1 ₁₀	2333.7845	+0.0002		3 ₀₃ ← 3 ₁₂	2332.2724	+0.0011
	2 ₂₀ ← 1 ₁₁	2333.7954	-0.0001		4 ₀₄ ← 4 ₁₃	2332.2476	+0.0008
	3 ₂₂ ← 2 ₁₁	2333.8973	+0.0001		5 ₀₅ ← 5 ₁₄	2332.2144	-0.0004
	3 ₂₁ ← 2 ₁₂	2333.9316	+0.0005		6 ₀₆ ← 6 ₁₅	2332.1745	+0.0004
	4 ₂₃ ← 3 ₁₂	2334.0054	+0.0011		7 ₀₇ ← 7 ₁₆	2332.1233	-0.0006
^P R ₁	2 ₀₂ ← 1 ₁₁	2332.5597	0.0000	^P Q ₂	2 ₁₁ ← 2 ₂₀	2331.6956	-0.0003
	3 ₀₃ ← 2 ₁₂	2332.6931	-0.0004		2 ₁₂ ← 2 ₂₁	2331.6643	+0.0008
	5 ₀₅ ← 4 ₁₄	2332.9712	-0.0003		3 ₁₂ ← 3 ₂₁	2331.7104	-0.0004
	6 ₀₆ ← 5 ₁₅	2333.1131	-0.0005		3 ₁₃ ← 3 ₂₂	2331.6466	-0.0003
	7 ₀₇ ← 6 ₁₆	2333.2565	+0.0003		4 ₁₃ ← 4 ₂₂	2331.7285	-0.0007
^R Q ₀	1 ₁₀ ← 1 ₀₁	2332.9318	-0.0002		4 ₁₄ ← 4 ₂₃	2331.6245	-0.0001
	2 ₁₁ ← 2 ₀₂	2332.9424	+0.0001		6 ₁₅ ← 6 ₂₄	2331.7719	+0.0005
	3 ₁₂ ← 3 ₀₃	2332.9593	+0.0003				

Table 6.1 (cont'd).

	$\begin{matrix} \mathbf{J}_{K_a K_c} ' \\ \leftarrow \mathbf{J}_{K_a K_c} '' \end{matrix}$	ν_{obs} /cm ⁻¹	$\nu_{\text{obs}} - \nu_{\text{calc}}$ /cm ⁻¹
^R P ₀	1 ₁₁ ← 2 ₀₂	2332.6712	-0.0005
	2 ₁₂ ← 3 ₀₃	2332.5361	-0.0009
	5 ₁₅ ← 6 ₀₆	2332.1121	0.0000
^P P ₁	0 ₀₀ ← 1 ₁₁	2332.1868	+0.0001
	1 ₀₁ ← 2 ₁₂	2332.0731	+0.0003
	2 ₀₂ ← 3 ₁₃	2331.9645	+0.0003
	3 ₀₃ ← 4 ₁₄	2331.8605	+0.0001
	4 ₀₄ ← 5 ₁₅	2331.7615	+0.0007

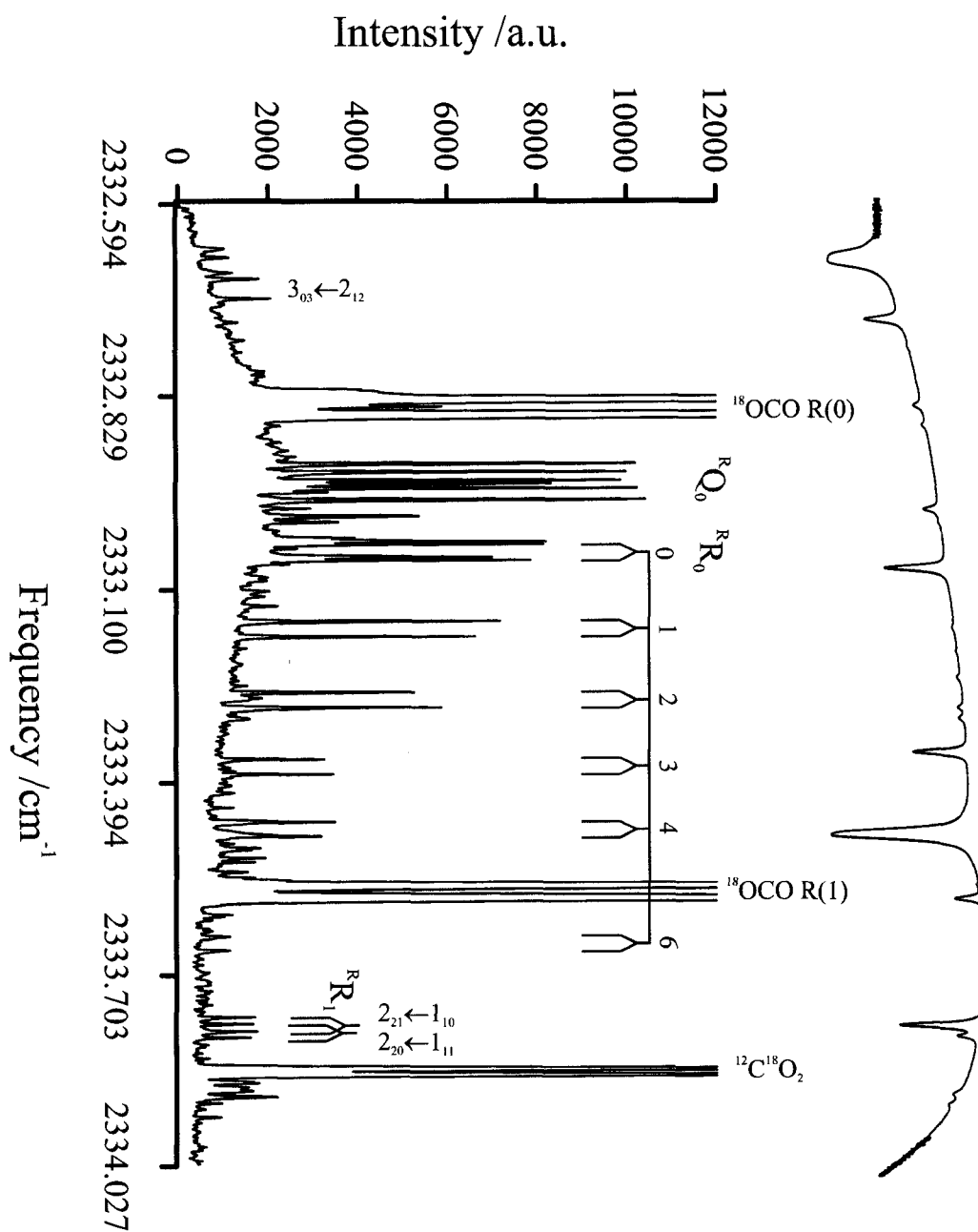
Table 6.2

Spectroscopic constants of $\text{N}_2\text{-}^{18}\text{OCO}$ and $\text{N}_2\text{-CO}_2$ (in MHz unless specified otherwise).

	$\text{N}_2\text{-}^{18}\text{OCO}$	$\text{N}_2\text{-CO}_2$ ⁸⁷
Model	Watson S	Watson S
ν_0 / cm^{-1}	2332.61737 (14)	2349.627846 (94)
$\Delta\nu_0 / \text{cm}^{-1}$	+0.5047	+0.4845
A''	11208.3 (18)	11885.3 (11)
A'	11126.3 (17)	11793.06 (91)
B''	2030.16 (97)	2063.18 (34)
B'	2028.46 (69)	2061.13 (26)
C''	1705.37 (78)	1743.21 (43)
C'	1702.11 (74)	1740.27 (29)
D_J''	0.014 (15)	0.0042 (24)
D_J'	0.011 (10)	0.0042 (24)
D_{JK}	0.556 (67)	0.557 (32)
$\sigma_{\text{IR}} / \text{cm}^{-1}$	0.00047	0.00030

Figure 6.1

Portion of the mid-infrared expansion spectrum of $\text{N}_2\text{-}^{18}\text{OCO}$. The data from 400 molecular pulses were averaged.



Compared to the main isotopomer $\text{N}_2\text{-CO}_2$, the rotational constants of $\text{N}_2\text{-}^{18}\text{OCO}$ are somewhat smaller due to the increased mass. Upon vibrational excitation, the decrease of the molecular constants of both systems is consistent with the expected weakening of the intermolecular bond. The band shifts $\Delta\nu_0$ relative to the monomer asymmetric stretching fundamentals are similar in both complexes. The slight increase in the distortional constants of $\text{N}_2\text{-}^{18}\text{OCO}$ compared to $\text{N}_2\text{-CO}_2$ is consistent with the increase in mass and has been observed in similar systems.¹⁶

6.3.2 Ne-¹⁸OCO

A portion of the mid-infrared expansion spectrum of $\text{Ne-}^{18}\text{OCO}$ is shown in Fig. 6.2. The spectrum is that of a perpendicular band of a near-prolate asymmetric top and is similar to those of $\text{N}_2\text{-}^{18}\text{OCO}$ and Ne-CO_2 .⁸⁶ All the assigned infrared transitions are *b*-type (Table 6.3). The intensity distribution was reproduced by a Boltzmann temperature of 0.7 K. Additional transitions, presumably due to $^{22}\text{Ne-}^{18}\text{OCO}$, were observed but were too few to assign. In addition, three microwave transitions were located and included in the fit (Table 6.4). Watson's A-reduction Hamiltonian in the I' representation¹³⁰ was used to fit a total of 24 ro-vibrational and 3 rotational transitions with the aid of Pickett's SPFIT program.¹³⁷ The Δ_{JK} distortion constant was constrained to a value of 2 MHz, consistent with the other isotopomers of the Ne-CO_2 series.¹⁶

Table 6.3

Assigned infrared transitions of the Ne-¹⁸OCO complex.

	$\begin{matrix} J_{KaKc}' \\ \leftarrow J_{KaKc}'' \end{matrix}$	ν_{obs} /cm ⁻¹	$\nu_{\text{obs}} - \nu_{\text{calc}}$ /cm ⁻¹		$\begin{matrix} J_{KaKc}' \\ \leftarrow J_{KaKc}'' \end{matrix}$	ν_{obs} /cm ⁻¹	$\nu_{\text{obs}} - \nu_{\text{calc}}$ /cm ⁻¹
^R R ₀	1 ₁₁ ← 0 ₀₀	2332.7130	-0.0001	^R Q ₁	2 ₂₁ ← 2 ₁₂	2333.1193	+0.0003
	2 ₁₂ ← 1 ₀₁	2332.8833	-0.0002	^P Q ₁	1 ₀₁ ← 1 ₁₀	2331.9572	+0.0003
	3 ₁₃ ← 2 ₀₂	2333.0396	-0.0003		2 ₀₂ ← 2 ₁₁	2331.9257	-0.0004
	4 ₁₄ ← 3 ₀₃	2333.1854	+0.0004		3 ₀₃ ← 3 ₁₂	2331.8764	+0.0003
^R R ₁	2 ₂₁ ← 1 ₁₀	2333.4616	-0.0004	^R P ₀	1 ₁₁ ← 2 ₀₂	2332.1164	+0.0001
	2 ₂₀ ← 1 ₁₁	2333.4921	0.0000		2 ₁₂ ← 3 ₀₃	2331.8951	-0.0009
	3 ₂₂ ← 2 ₁₁	2333.6308	+0.0001	^P P ₁	0 ₀₀ ← 1 ₁₁	2331.7860	+0.0003
	3 ₂₁ ← 2 ₁₂	2333.7252	+0.0002		1 ₀₁ ← 2 ₁₂	2331.6144	+0.0006
^P R ₁	3 ₀₃ ← 2 ₁₂	2332.5985	-0.0002	^P R ₂	3 ₁₃ ← 2 ₂₀	2331.9188	+0.0001
^R Q ₀	1 ₁₀ ← 1 ₀₁	2332.5412	-0.0002		3 ₁₂ ← 2 ₂₁	2332.0879	-0.0003
	2 ₁₁ ← 2 ₀₂	2332.5702	+0.0001				
	3 ₁₂ ← 3 ₀₃	2332.6172	+0.0002				
	4 ₁₃ ← 4 ₀₄	2332.6862	+0.0001				
	5 ₁₄ ← 5 ₀₅	2332.7811	-0.0001				

Table 6.4

Assigned microwave transitions of the Ne-¹⁸OCO complex.

	$\begin{matrix} \mathbf{J_{KaKc}'} \\ \leftarrow \mathbf{J_{KaKc}''} \end{matrix}$	$\begin{matrix} \mathbf{v_{obs}} \\ \text{/MHz} \end{matrix}$	$\begin{matrix} \mathbf{v_{obs}-v_{calc}} \\ \text{/MHz} \end{matrix}$
^R R ₀	1 ₀₁ ← 0 ₀₀	5985.4367	0.0000
	2 ₀₂ ← 1 ₀₁	11905.7750	0.0000
^R R ₁	2 ₁₁ ← 1 ₁₀	12798.2889	0.0000

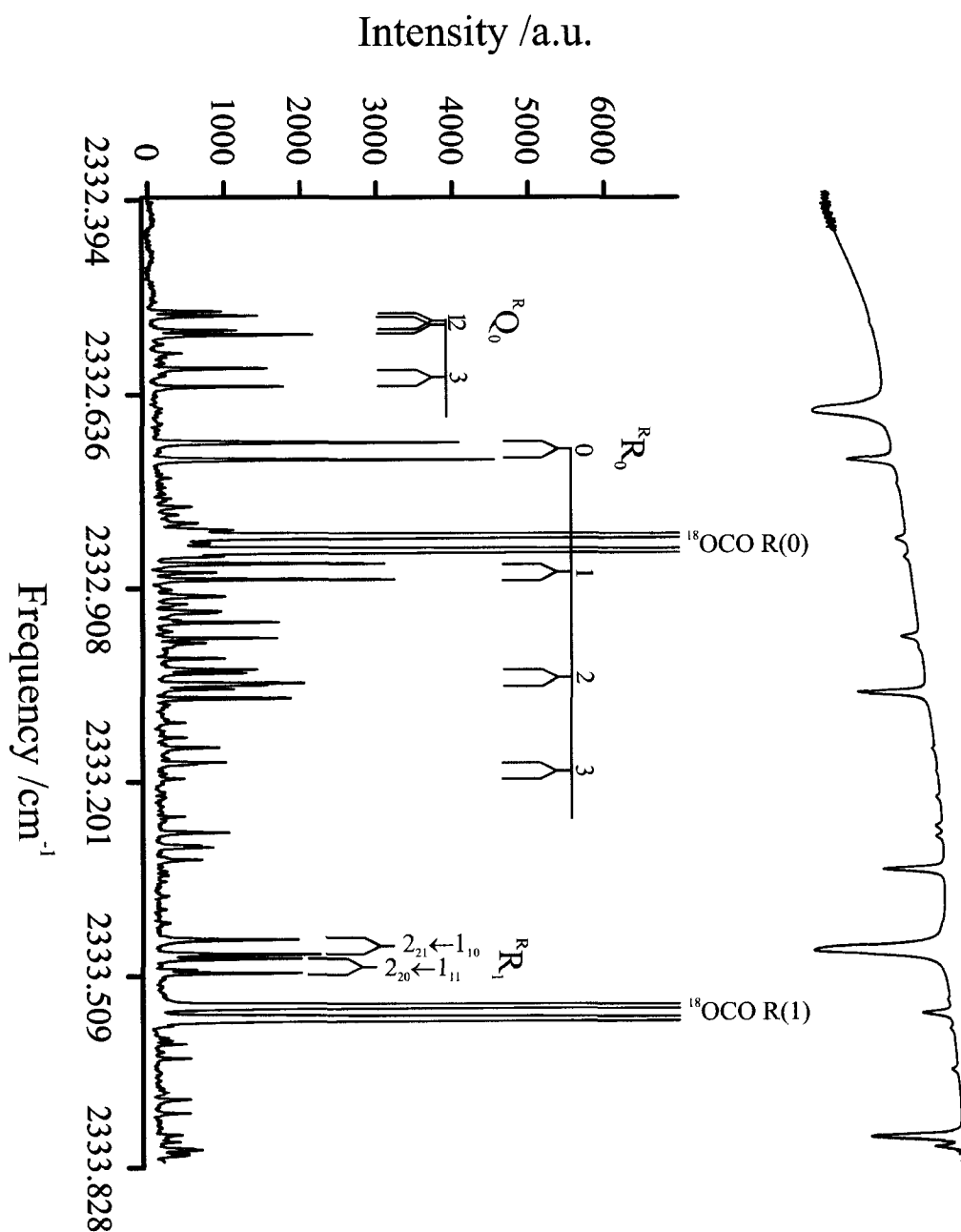
Table 6.5

Spectroscopic constants of Ne-¹⁸OCO and selected Ne-CO₂ isotopomers (in MHz unless specified otherwise). The two columns in the middle of the table contain molecular constants from fits to microwave transitions.

	Ne- ¹⁸ OCO	Ne-CO ₂ ¹⁶⁰	Ne- ¹⁸ O ¹³ CO ¹⁶	Ne-CO ₂ ⁸⁶
Model	Watson A	Watson A	Watson A	Watson S
ν_0 / cm^{-1}	2332.25091 (17)	-	-	2349.27953 (31)
$\Delta\nu_0 / \text{cm}^{-1}$	+0.1382	-	-	+0.1363
A''	11376.6 (23)	12074.2 (17)	11387.724 (29)	12072.7 (27)
A'	11293.4 (18)	-	-	11992.7 (31)
B''	3411.791 (20)	3457.34 (54)	3394.83591 (95)	3455.1 (13)
B'	3403.86 (63)	-	-	3448.66 (77)
C''	2574.036 (19)	2631.19 (57)	2557.9033 (10)	2631.96 (67)
C'	2566.83 (78)	-	-	2624.05 (71)
Δ_j'' / D_j''	0.09751 (79)	0.0755 (63)	0.128761 (20)	0.0589 (96)
Δ_j' / D_j'	0.0991 (97)	-	-	0.0589 (96)
Δ_{JK}	2.00 (fixed)	2.84 (15)	2.08068 (21)	2.631 (168)
σ_{MW}	0.0000	-	0.0005	-
$\sigma_{\text{IR}} / \text{cm}^{-1}$	0.00032	-	-	0.00031

Figure 6.2

Portion of the mid-infrared expansion spectrum of Ne- ^{18}OCO . The spectrum also contains many transitions of the N_2 - ^{18}OCO complex. Some of the unassigned lines may belong to the ^{22}Ne isotopomer, $(^{18}\text{OCO})_2$ or mixed CO_2 dimers.



The ground state molecular constants obtained in this work fit the pattern established by Xu and Jäger for other Ne-CO₂ isotopomers.¹⁶ For example, Δ_J'' and Δ_J' of ¹⁸OCO are slightly larger than for the main isotopomer, but less than for ¹⁸O¹³CO (Table 6.5). Upon vibrational excitation, all three rotational constants decrease as expected. The band shift $\Delta\nu_0$ of Ne-¹⁸OCO is very similar to that of the main isotopomer, Ne-CO₂.

6.3.3 He-¹⁸OCO

A portion of the mid-infrared expansion spectrum of He-¹⁸OCO is shown in Fig. 6.3. On first inspection, the infrared spectrum of He-¹⁸OCO is very different from those of Ne-¹⁸OCO and N₂-¹⁸OCO. There are several pairs of transitions with approximate relative intensity of 1:2 separated by about ~ 0.010 cm⁻¹ (300 MHz) in the infrared spectrum of He-¹⁸OCO. The pairs consist of *a*- and *b*-type transitions, with the *a*-type transitions being the more intense. In total, a self-consistent set of 9 *a*-type and 8 *b*-type transitions up to $J''=2$ was assigned (Table 6.6). Higher *J* lines were not observed. Watson's A-reduction Hamiltonian in the I' representation¹⁶¹ was used to fit the observed transitions plus the two microwave transitions measured by Xu and Jäger¹⁷ (with the correct quantum number assignments) with the aid of Pickett's SPFIT program¹³⁷ (Table 6.7). The intensities were reproduced by a Boltzmann temperature of 0.7K. Additional lines can be seen in the spectrum (Fig. 6.3), which may be due to a low-lying intermolecular bending mode¹⁰³ of the complex, higher order clusters, or dimer species like (¹⁸OCO)₂. Unassigned transitions are not uncommon in the mid-infrared spectra of He complexes. For example, 27 unassigned transitions were observed in the mid-infrared

spectrum of He-CO₂.¹⁰³

He containing dimers are prone to large amplitude internal motions, due to the shallowness of the intermolecular potentials. As a result, the rigid rotor Hamiltonian may reproduce the experimental spectrum only poorly, and many distortion constants may be required to get a satisfactory fit of the data. In this work, 13 parameters were fitted to 19 observed transitions. The signs and magnitudes of the distortion constants by and large follow those of the main isotopomer, with one notable exception: In this work, the rotational constants of the vibrationally excited state A' , B' , and C' are much closer to their ground state counterparts than in the fit of the He-CO₂ transitions, in which the A constant increased by 500 MHz (!) upon vibrational excitation. The physical interpretation of such an increase is that the complex is somehow more tightly bound in the excited state. Such an increase was neither seen for He-OCS¹⁰⁹ nor in this work, which makes the constants given by Weida *et al.*¹⁰³ a bit questionable, in particular since theory still cannot reproduce the experimental lines and quantum number assignment.¹⁵⁹ Even though the observed lines were fitted within experimental uncertainty in this fit, the model may be inappropriate for this type of system, because the predictive power is poor.

Table 6.6

Assigned mid-infrared transitions of the He-¹⁸OCO complex.*a*-type:*b*-type:

	J_{KaKc}' $\leftarrow J_{KaKc}''$	ν_{obs} /cm ⁻¹	$\nu_{\text{obs}}-\nu_{\text{calc}}$ /cm ⁻¹		J_{KaKc}' $\leftarrow J_{KaKc}''$	ν_{obs} /cm ⁻¹	$\nu_{\text{obs}}-\nu_{\text{calc}}$ /cm ⁻¹
^Q R ₀	1 ₀₁ ← 0 ₀₀	2332.8008	-0.0002	^R R ₀	1 ₁₁ ← 0 ₀₀	2332.8117	-0.0003
	2 ₀₂ ← 1 ₀₁	2333.1765	-0.0002		2 ₁₂ ← 1 ₀₁	2333.1620	+0.0004
	3 ₀₃ ← 2 ₀₂	2333.5121	-0.0010	^R R ₁	2 ₂₁ ← 1 ₁₀	2333.5975	+0.0002
^Q R ₁	2 ₁₂ ← 1 ₁₁	2333.1519	+0.0006		2 ₂₀ ← 1 ₁₁	2333.9991	+0.0002
	3 ₁₃ ← 2 ₁₂	2333.5293	+0.0009	^P R ₁	2 ₀₂ ← 1 ₁₁	2333.1661	-0.0004
^Q Q ₁	1 ₁₀ ← 1 ₁₁	2332.4330	+0.0002	^R Q ₀	1 ₁₀ ← 1 ₀₁	2332.4433	+0.0002
	1 ₁₁ ← 1 ₁₀	2332.0122	-0.0004	^P Q ₁	1 ₀₁ ← 1 ₁₀	2332.0015	+0.0000
^Q P ₀	0 ₀₀ ← 1 ₀₁	2331.6483	+0.0002	^P P ₁	0 ₀₀ ← 1 ₁₁	2331.6379	+0.0001
^S P ₀	2 ₂₀ ← 1 ₀₁	2334.0088	-0.0004				

Table 6.7

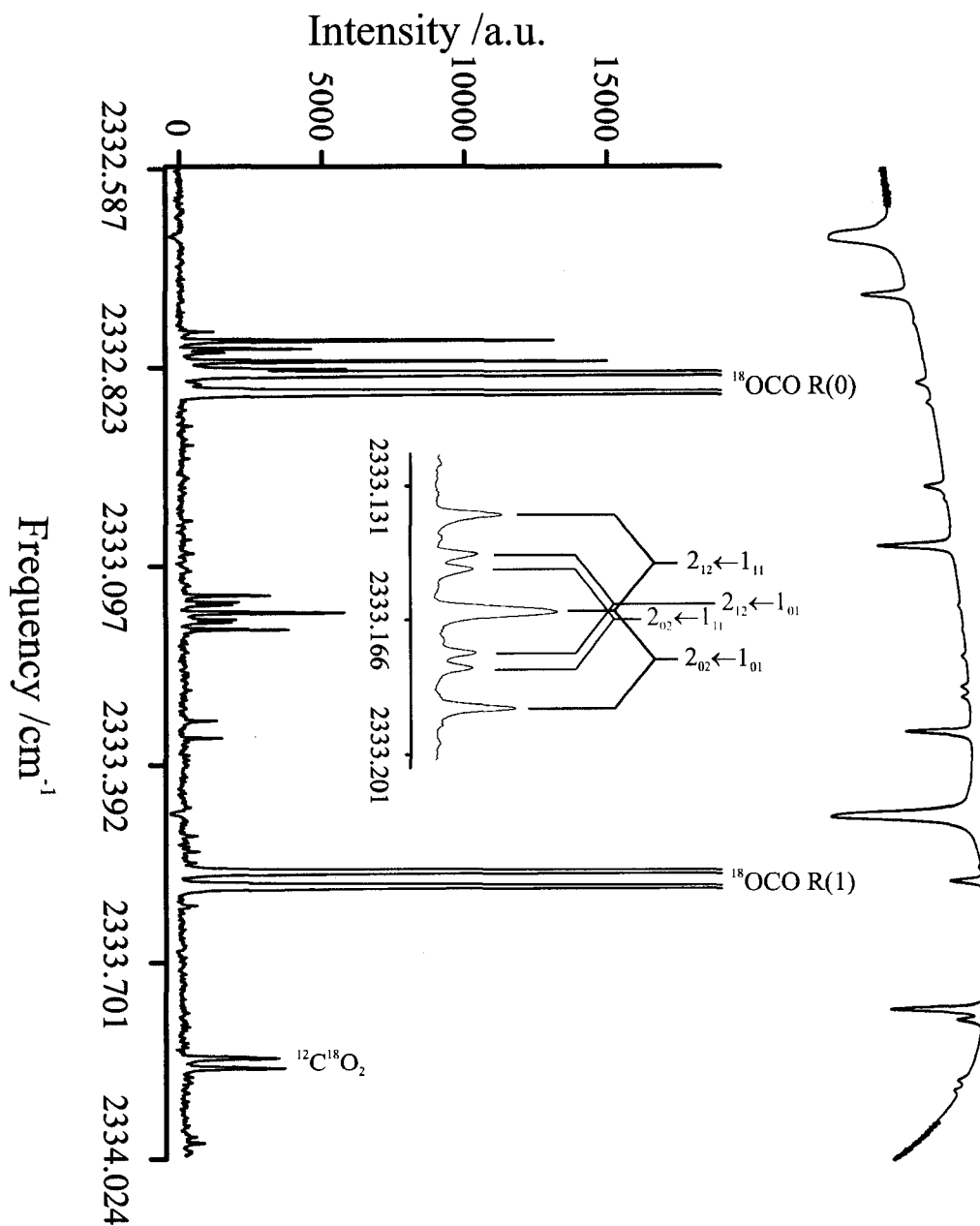
Spectroscopic constants of He-¹⁸OCO and He-CO₂ (in MHz).

	He- ¹⁸ OCO	He-CO ₂ ¹⁰³
n	17+2	49
Model	Watson A	Watson A
ν_0 /cm ⁻¹	2332.22616 (26)	2349.2379 (13)
$\Delta\nu_0$ /cm ⁻¹	+0.1135	+0.0947
A''	12244.2 (83)	12650 (16)
A'	12187.9 (135)	13166 (22)
B''	11952.5 (102)	12101 (24)
B'	11846.2 (126)	12097 (17)
C''	5405.1 (99)	5599.8 (60)
C'	5411.7 (125)	5545.0 (63)
Δ_J''	7.14 (97)	7.55 (66)
Δ_J'	6.53 (72)	6.12 (48)
Δ_{JK}''	95.8 (85)	32.1 (15)
Δ_{JK}'	95.8 (85)*	42.5 (1.6)
Δ_K''	-99.8 (113)	-33.3 (14)
Δ_K'	-99.8 (113)*	18.5 (21)
δ_J''	8.6 (16)	3.30 (33)
δ_J'	8.6 (16)*	2.50 (26)
δ_K''	37.2 (69)	34.7 (11)
δ_K'	37.2 (69)*	41.55 (42)
σ_{IR} /cm ⁻¹	0.00042	0.0024

* upper state constant constrained to lower state constant.

Figure 6.3

A portion of the mid-infrared expansion spectrum of He- ^{18}OCO . The sample was a trace amount of ^{18}OCO in 8 atm He. 200 scans were averaged. Additional lines may belong to $\text{He}_2\text{-}^{18}\text{OCO}$, $(^{18}\text{OCO})_2$ or other mixed dimers of CO_2 , or a ν_5 band of He- ^{18}OCO .



6.3.4 Derivation of molecular structures

For a complex formed between a linear molecule like CO₂ and a rare-gas atom in the absence of distortion, the only possible structure is planar. If the bond length of CO₂ is constrained to its monomer value, the structure of the complex can be defined by just two parameters, $r_{\text{cm}}(\text{H})$ and α , which can be calculated from the equations originally derived by Howard:⁸⁶

$$r_{\text{cm}}(\text{H}) = \left[\frac{\Theta}{\mu} \left(\frac{1}{C} - \frac{1}{B_{\text{mon}}} \right) \right]^{\frac{1}{2}} \quad (6.1)$$

$$\sin \alpha = \frac{B_{\text{mon}}}{A} \left[\frac{C - A}{C - B_{\text{mon}}} \right]^{\frac{1}{2}} \quad (6.2)$$

where B_{mon} is the rotational constant of the monomer, μ is the reduced mass of the complex, and Θ is a conversion constant (505376 MHz / amu Å²). Only two of the three rotational constants are used in this approach.⁸⁶ The results are listed in Table 6.8. The data (with the exception of N₂-CO₂ and He-CO₂) are consistent with zero point effects in that the intermolecular bond distances are slightly less in the heavier complexes. The rotational constants of neither N₂-CO₂ nor He-CO₂ are known to high enough precision to observe this subtle effect.

Kraitchman has developed a convenient method for calculation of the principal axis coordinates of a substituted atom, using the resulting change of the moments of inertia.¹⁶² For a planar molecule like Rg-CO₂, Kraitchman has derived the following equations for the coordinates of the substituted atom:²⁸

Table 6.8

Comparison of structural constants calculated using Howard's equations.⁸⁶

Molecule	r_{cm}'' (H) / Å	r_{cm}' (H) / Å	α'' / °	α' / °
N ₂ -CO ₂ ⁸⁷	3.731	3.733	83	83
N ₂ - ¹⁸ OCO	3.7941	3.7984	83.6	85.4
Ar-CO ₂ ⁸⁶	3.5039	3.5044	83.1	83.0
Ar- ¹⁸ OCO ¹⁰⁴	3.5022	3.5040	83.1	84.6
Ne-CO ₂ ⁸⁶	3.2904	3.2930	81.4	81.3
Ne- ¹⁸ OCO	3.2864	3.2924	81.7	82.8
He-CO ₂ ¹⁰³	3.581	3.614	83.9	81.4
He- ¹⁸ OCO	3.601	3.597	83.4	83.6

Table 6.9

Location of the oxygen atom in the complexes derived from Kraitchman equations, specified in terms of its coordinates in the x,y plane. For the T-shaped complexes, x is anticipated to be equal to the monomer bond length ($r_{CO}'' = 1.162$ Å and $r_{CO}' = 1.166$ Å).

	$ x ''$ / Å	$ y ''$ / Å	$ x '$ / Å	$ y '$ / Å	r_{cm}'' (K) / Å	r_{cm}' (K) / Å
N ₂ -CO ₂ N ₂ - ¹⁸ OCO	1.160	1.422	1.160	1.415	3.66	3.73
Ar-CO ₂ Ar- ¹⁸ OCO	1.180	1.632	1.155	1.825	3.43	3.83
Ne-CO ₂ Ne- ¹⁸ OCO	1.161	0.991	1.171	0.985	3.17	3.15
He-CO ₂ He- ¹⁸ OCO	0.942	0.270	1.423	0.205	3.24	2.46

$$|x| = \left[\frac{(I_y' - I_y)(I_x' - I_x)}{\mu(I_x - I_y)} \right]^{\frac{1}{2}} \quad (6.3)$$

$$|y| = \left[\frac{(I_x' - I_x)(I_y' - I_y)}{\mu(I_x - I_y)} \right]^{\frac{1}{2}} \quad (6.4)$$

In this model, the z-axis is located out-of-plane and $|z|=0$. μ is the reduced mass given by:

$$\mu = \frac{M\Delta m}{M + \Delta m} \quad (6.5)$$

where M is the total mass of the parent molecule and Δm is the change in mass upon isotopic substitution.

The results of the Kraitchman calculations are summarized in Table 6.9. The data of Ne and N₂ complexes predict the monomer carbon-oxygen bond length ($|x|$) of the complex to be similar to the monomer bond length, but the data of the Ar and He complexes does not. The deviation of Ar may be a result of the high correlation of the B and C constants¹⁹ and consequential poor knowledge of either. The model completely breaks down for He-CO₂ because of the effects of large amplitude internal motions. The Kraitchman calculations can also be used to estimate the distance to the center of mass ($|y|$). From this value, the intermolecular separation $r_{cm}(K)$ may be calculated using the known reduced masses. Much larger uncertainty is expected in this type of calculation because of the floppy nature of the van der Waals bond.

Table 6.10

Comparison of inertial defects of CO₂ and ¹⁸OCO weakly bound complexes. The term $\Delta\Delta$ is the change of the inertial defect upon isotopic substitution.

Molecule	CO ₂	¹⁸ OCO	$\Delta\Delta''$	CO ₂	¹⁸ OCO	$\Delta\Delta'$
	Δ'' /amuÅ ²	Δ'' /amuÅ ²		Δ' /amuÅ ²	Δ' /amuÅ ²	
N ₂ -CO ₂ ⁸⁷ / N ₂ - ¹⁸ OCO	2.44	2.32	-0.12	2.35	2.35	0
Ar-CO ₂ ⁸⁶ / Ar- ¹⁸ OCO ¹⁰⁴	2.44	2.69	+0.25	2.39	1.07	-1.32
Ne-CO ₂ ⁸⁶ / Ne- ¹⁸ OCO	3.88	3.79	-0.09	3.91	3.66	-0.25
He-CO ₂ ¹⁰³ / He- ¹⁸ OCO	8.54	9.94	+1.40	10.98	9.26	-1.72

6.3.5 Internal motions

The inertial defect Δ can be regarded as a measure of the magnitude of the internal motions. Δ is defined as:

$$\Delta = I_C - I_B - I_A \quad (6.6)$$

Positive values of Δ are associated with in-plane; negative values with out-of-plane motions.²⁸ The inertial defects in the ground and excited state are summarized in Table 6.10. The moments of inertia and therefore the inertial defect of He-CO₂ are not as accurately known as for the other molecules, and are listed solely for completeness. All the molecules studied here have positive inertial defect. This suggests that the internal motions are generally in-plane, which can be rationalized by zero-point van der Waals bending and stretching vibrations.⁸⁶ As pointed out by Ozaki and coworkers,¹⁰⁴ the amplitudes of these van der Waals vibrational modes and therefore Δ should decrease slightly if a heavier atom is substituted. Δ decreases slightly for Ne and N₂ upon isotopic substitution as expected, but not for Ar. The structural parameter $90^\circ - \alpha$ is a direct measure of the rms amplitude of the van der Waals bending motion. α is only known well for Ne-CO₂, where it is observed to increase upon isotopic substitution as predicted (Table 6.8). The relative low inertial defect of Ar-¹⁸OCO in the excited state (Table 6.10) suggests that the constants reported by Ozaki et al.¹⁰⁴ may be somewhat in error.

6.4 Summary

The mid-infrared spectra of $\text{N}_2\text{-}^{18}\text{OCO}$, $\text{Ne-}^{18}\text{OCO}$, and $\text{He-}^{18}\text{OCO}$ near the ν_3 asymmetric stretching fundamental of ^{18}OCO were observed and assigned. The derived structural parameters and inertial defects of $\text{N}_2\text{-}^{18}\text{OCO}$ and $\text{Ne-}^{18}\text{OCO}$ are very similar to those of their respective main isotopomers, and only shifted by small amounts consistent with isotope effects. The derived structural parameters and inertial defects of $\text{He-}^{18}\text{OCO}$ are inconsistent with those He-CO_2 , likely due to breakdown of the rigid rotor Hamiltonian model as a result of large amplitude internal motions.

CHAPTER 7

POST-DATA ACQUISITION DIGITAL FILTERING

7.1 Introduction

In tunable diode laser absorption spectroscopy (TDLAS), there are many sources of noise that can potentially become sensitivity-limiting (Chapter 1.3.4). Noise can be identified by its properties in the frequency domain as either white, $1/f$, shot, or periodic fringe noise. The signal-to-noise ratio (S/N) increases by the square root of the number of measurements for all types of noise, with the exception of systematic noise like periodic fringes. Frequency independent white noise is characterized by a Gaussian distribution. $1/f$ noise is the sum of random and systematic noise, whose amplitude decreases at higher detection frequencies. Digitization or shot noise results from repeated measurements of a variable that can only take up discrete values (e.g. 0, 1, 2, 3, ...). This type of measurement obeys Poisson statistics.¹⁶³ Periodic fringe noise is caused, for example, by unwanted étalons. Because fringe noise is systematic, it is not removed by averaging.

With the rapid and dramatic improvement in computing power and processing speed, post-data acquisition digital filtering is becoming increasingly popular in single-line monitoring applications.¹⁶⁴⁻¹⁶⁷ In this Chapter, several algorithms, including the Kalman¹⁶⁸ and Wiener¹⁶⁹ filters, are described and their performance is evaluated using rapid-sweep spectra of the Ar-CO₂ van der Waals complex.

7.2 Description of algorithms

7.2.1 Boxcar integration

In this algorithm, each data point is replaced by the average of it and its nearest n (for example $n=50$) neighbours.

7.2.2 Bandpass filter

In this algorithm, the data is converted to the frequency domain *via* a fast Fourier transformation (FFT). For low-pass (or high-pass) filtering, all frequencies above (below) a specified threshold are set to zero, and the inverse FFT is calculated.

7.2.3 Wiener filter

The Wiener algorithm has been described in detail elsewhere.¹⁶⁶ It was originally designed to filter out periodic noise.¹⁶⁹ The corrupted signal $cor(t)$ can be thought of as superposition of “true” signal $sig(t)$ and noise $noi(t)$:

$$cor(t) = sig(t) + noi(t) \tag{7.1}$$

In our experiments we obtained a representative noise spectrum $noi(t)$ by subtracting the sum of all even background scans from the sum of all odd background scans.

After a Fourier transform the power spectra of the corrupted signal $COR(f)$ are related to those of the “true” signal $SIG(F)$ and noise $NOI(F)$ by:

$$|\text{COR}(f)|^2 = |\text{SIG}(f)|^2 + |\text{NOI}(f)|^2 \quad (7.2)$$

It can be shown by least-squares error minimization that the best estimate of the signal in the frequency domain $\text{SIG}'(f)$ can be calculated by

$$\text{SIG}'(f) = H(f) * \text{COR}(f) \quad (7.3)$$

where $H(f)$ is the Wiener filter response function. $H(f)$ is given by

$$H(f) = \frac{|\text{SIG}(f)|^2}{|\text{SIG}(f)|^2 + |\text{NOI}(f)|^2} = \frac{|\text{COR}(f)|^2 - |\text{NOI}(f)|^2}{|\text{COR}(f)|^2} \quad (7.4)$$

The Wiener algorithm consists of the following steps:

1. FFT $\text{noi}(t) \rightarrow \text{NOI}(f)$ and $\text{cor}(t) \rightarrow \text{COR}(f)$
2. Calculate $H(f)$ using equation 7.4
3. Calculate $\text{SIG}'(f)$ using equation 7.3
4. Inverse FFT $\text{SIG}'(f) \rightarrow \text{sig}(t)$

7.2.4 Low-pass Wiener filter

As implied by its name, this filter is a combination of the previous two. After calculating the best estimate $\text{SIG}'(f)$ using equation (7.3) and before the inverse FFT step, all values above a specified threshold frequency are set to zero.

7.2.5 Kalman filter

The Kalman filter consists of a recursive algorithm applied to a series of discrete measurements. The filter response of the Kalman algorithm takes advantage of either some *a priori* knowledge and/or past behaviour of an observable. For the algorithm to work, it is necessary that consecutive measurements are autocorrelated to a certain degree. The “true” value $\text{sig}(I)$ of the system at a point in time can be modeled as

$$\text{sig}(I) = \phi_i \text{sig}(I-1) + \omega_i \quad (7.5)$$

where ϕ_i is a recursive parameter and ω_i is superimposed noise with variance Q' and average $\langle \omega \rangle = 0$. For example, actual peaks on an otherwise flat baseline fall under this type of noise. In contrast, the actually observed value consists of the “true” signal, to which some observational noise $\text{noi}(I)$ (for example random spikes on the baseline) is added:

$$\text{cor}(I) = \text{sig}(I) + \text{noi}(I) \quad (7.6)$$

The observation noise $\text{noi}(I)$ has variance R' and mean $\langle \omega_i \rangle = 0$ (no bias). It is important to assume that $\text{noi}(I)$ and ω_i are uncorrelated. It is also implicitly assumed that $R' > Q'$, i.e. that fluctuations in the observed signal are instrumental artifacts and not due to (real) fluctuations in the “true” signal itself.

The Kalman algorithm is performed as follows:

1. A first observation $\text{cor}(I)$ is made.
2. The estimate of the “true value” (because of lack of other knowledge) is $\text{sig}_e(I) = \text{cor}(I)$.
3. The error of this best estimate in terms of its variance P'_i is given by

$$P'_i = (\text{sig}_e(I) - \text{sig}(I))^2 \quad (7.7)$$

Since we do not know the “true” value $\text{sig}(I)$, P'_i is initially set to zero.

4. The best possible estimate of the next value $\text{sig}_e(I+1)$ follows from equation 7.5:

$$\text{sig}_e(I+1) = \phi_i \text{sig}_e(I) + \omega_{i+1} = \phi_i \text{sig}_e(I) \quad (7.8)$$

ω_{i+1} is not known, but it can be assumed to be equal to $\langle \omega \rangle = 0$.

5. The variance P'_{i+1} is then

$$\begin{aligned} P'_{i+1} &= (\text{sig}_e(I+1) - \text{sig}(I+1))^2 \\ &= ((\phi_i \text{sig}_e(I) + \omega_{i+1}) - \phi_i \text{sig}_e(I))^2 \\ &= \phi_i^2 (\text{sig}_e(I) - \text{sig}_e(I))^2 + \omega_{i+1}^2 + 2\phi_i (\text{sig}_e(I) - \text{sig}_e(I))\omega_{i+1} \\ &= \phi_i^2 P'_i + Q' \end{aligned} \quad (7.9)$$

given that on average ω_{i+1} is zero.

6. It can be shown that the Kalman gain K' is calculated by

$$K'_{i+1} = \frac{P'_{i+1}}{P'_{i+1} + R'} \quad (7.10)$$

7. The next observation $\text{cor}(i+1)$ is made.

8. The best estimate $\text{sig}'(i+1)$ is then calculated by

$$\text{sig}'(i+1) = \text{sig}_e(i+1) + K'_{i+1} (\text{cor}(i+1) - \text{sig}_e(i+1)) \quad (7.11)$$

Equations (7.8) through (7.11) represent the Kalman algorithm. At the beginning of an experiment, the parameters K' , ϕ , R' and Q' need to be initialized. K' is initially set to 0.75, ϕ is set to 1, R' is estimated from the variance of the "noise spectrum", if available, and Q' is set to $R'/1000$ or whatever ratio is appropriate.

7.3 Filter performance in rapid-sweep mode

The spectrum shown in Fig. 7.1 - 7.3 contains many different regions of interest: Strong peaks, for example around channel 10410, partially resolved peaks, for example near channel 9950, weak peaks near channel 1938 (not shown in the Figures), and seemingly peak-free areas, for example around channel 7500. The "performance" of each individual filter is judged in terms of achieved improvements in S/N ratio as well as loss of resolution and peak shape. S/N is taken as the peak center intensity divided by the standard deviation of background noise. In general, non-linearity effects of digital filtering are neglected; for analytical applications new concentration calibration curves should be constructed.

Figure 7.1

Effect of digital filtering on a sample rapid-sweep spectrum: Boxcar averaging and low-pass filtering. The spectrum is that of Ar-CO₂ van der Waals complex near 2349 cm⁻¹. The sample consisted of 0.2% CO₂, 20% Ar and 80% He at a backing pressure of 7 atm. 100 scans were averaged and background subtracted.

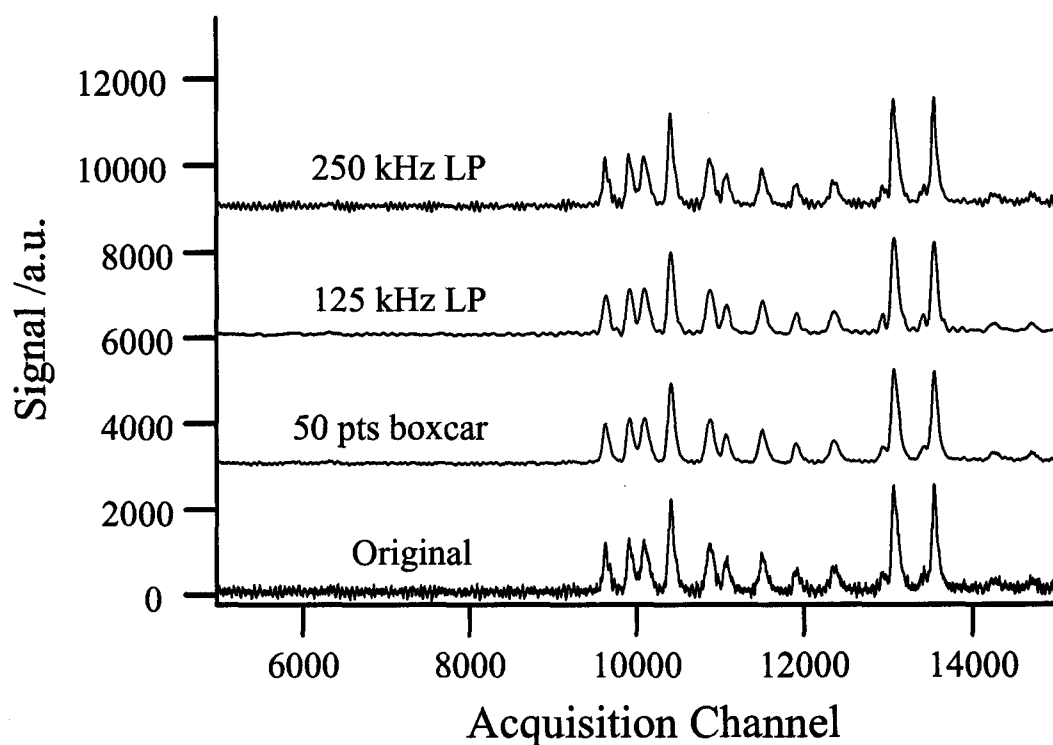


Figure 7.2

Effect of digital filtering on a sample rapid-sweep spectrum: Wiener and low-pass

Wiener filters. The spectrum shown is the same as in Fig. 7.1.

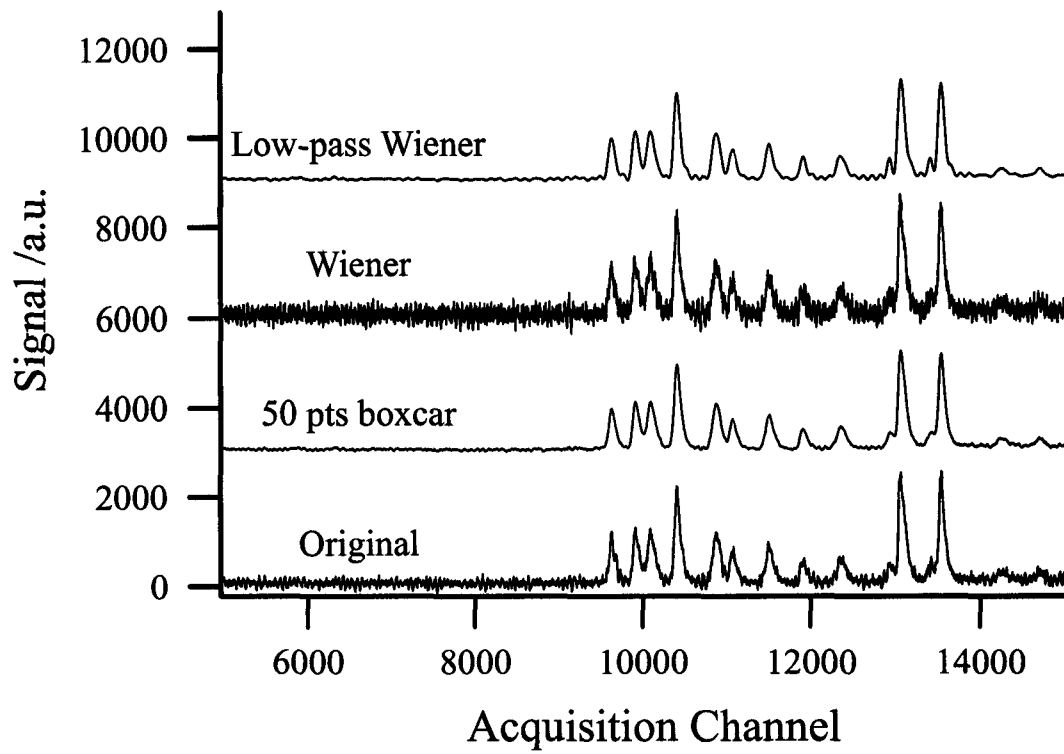


Figure 7.3

Effect of Kalman digital filtering on a sample rapid-sweep spectrum. The spectrum shown is the same as in Fig. 7.1.

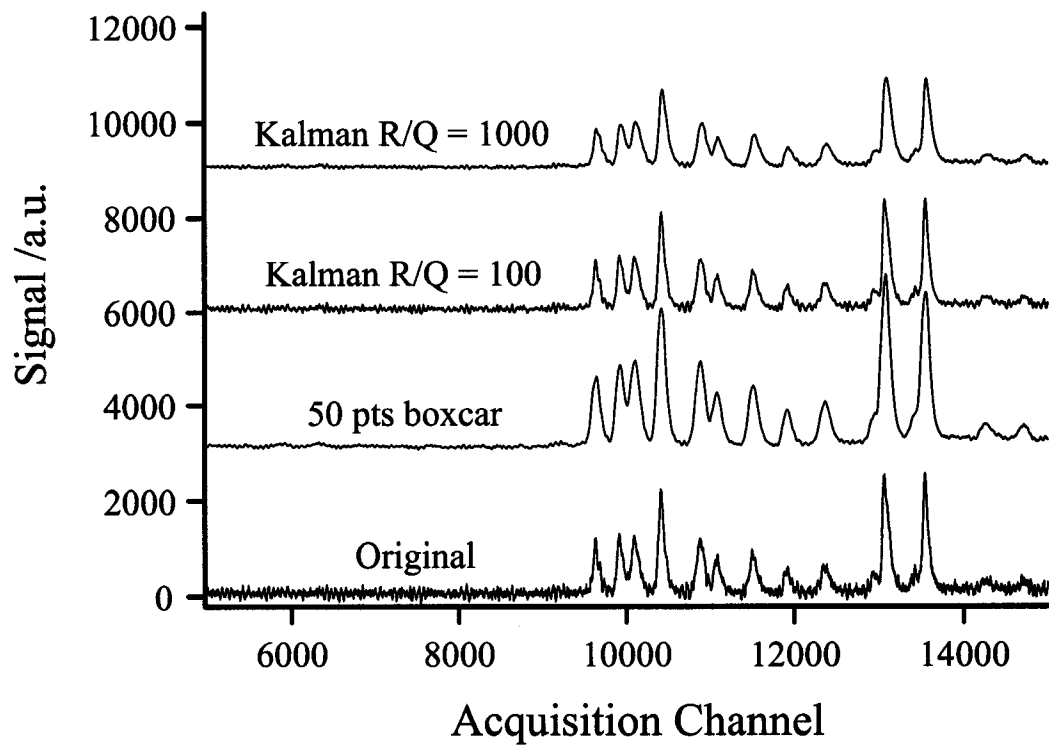


Table 7.1

Comparison of digital filter performance. For a discussion, see text.

Filter	Background Intensity (6600-8780)	S/N at weak peak (1938)	S/N at strong peak (10411)	Resolution ^a of 9916 -10090
No filter	67.7±61.5	3.3	35.2	1.55
Boxcar 50 pts	67.8±15.1	8.8	123	1.44
Boxcar 80 pts	67.8± 12.1	8.9	133	1.07
Boxcar 100 pts	67.7±10.3	10.8	142	0.96
250 kHz LP	67.5±41.1	3.9	51.3	1.58
125 kHz LP	67.9±13.9	7.6	139	1.38
Wiener	72±115	2.5	19.1	1.58
LP Wiener	71.4±12.7	8.9	152	1.41
Kalman Q'=R'/100	67.7±35.5	4.0	57.2	1.53
Kalman Q'=R'/1000	67.6±16.3	7.3	99.2	1.41
Kalman Q'=R'/10000	67.8±7.4	10.8	137	1.01

^a Resolution is defined as peak separation divided by the average full-width-at-half-maximum.

7.3.1 Boxcar integration

At the employed modulation rate, an absorption peak is scanned in 4 μs , which corresponds to a 250 kHz modulation. The data acquisition card is operated at 25 MHz and therefore the absorption line is oversampled in the experiment. Boxcar averaging should obtain an improvement of the S/N ratio by a factor of approximately \sqrt{n} . Boxcar averaging over $n=50$ points (Table 7.1) resulted in an increase in S/N of about 2.6 (weak peak) and 3.5 (strong peak), which is significantly less than the predicted value of ~ 7 . The poor performance is due to the low intensity of the peak shoulders, and may have been avoided by using a weighted boxcar averaging algorithm.¹⁷⁰

7.3.2 Lowpass filter

A lowpass filter is used to eliminate high-frequency noise. Because of the frequency response limit of the detector preamplifier, it was assumed that anything detected in excess of ~ 250 kHz can be rejected as noise. Correspondingly, highpass filtered data above 250 kHz was found to contain only noise (not shown). Lowpass filtering achieves similar S/N and resolution to the boxcar algorithm (Figure 7.1). However, lowpass filtering adds a "ringing" near stronger peaks (for example near channel 13000). We also tried various other cutoff frequencies without seeing any improvements. Because of the observed artifacts, we concluded that a straight lowpass filter is not an ideal method to smooth our data.

7.3.3 Wiener filter

The Wiener filter clearly worsened the S/N compared to the original trace (Fig. 7.2). There are two reasons for this: (a) We have insufficient or inaccurate knowledge of the noise spectrum, and (b) Periodic signals like optical fringes do not dominate the spectra. Apparently, inserting optical elements at slight angles and background subtraction is effective in removing fringe noise. In a separate experiment, we re-aligned the optics to create broad interference fringes. In this case, the Wiener filter outperformed simple boxcar averaging (because the boxcar averaging also *amplified* the fringing pattern, whereas the Wiener filter *reduced* the fringing).

7.3.4 Lowpass Wiener filter

The performance of the lowpass Wiener filter is similar to that of the simple boxcar and slightly better than the performance of a lowpass filter by itself. This result shows that the degradation of the Wiener filtered signal is due to insufficient knowledge of high-frequency noise. Because of its simplicity and similar performance, boxcar averaging is preferable.

7.3.5 Kalman filter

Several groups, for example Riris¹⁶⁵ and recently Leleux¹⁶⁷ and coworkers have reported remarkable gains in their S/N when applying a Kalman filter to their single-line monitoring measurements. Among the (potential) advantages of the Kalman algorithm is that it can be applied in real-time. In Chapter 8, the effectiveness of the Kalman filter for single line monitoring is demonstrated. Here, it is tested if similar improvements can be

made if the Kalman filter is applied in post-data acquisition digital filtering of van der Waals spectra.

The S/N gains observed in the above mentioned papers were made possible largely because of *a priori* knowledge of the noise level associated with the measurement (R') relative to the intrinsic variance of the signal (Q'). In addition, the respective experiments were designed such that relative long periods of constant signals were *expected*. Such a situation, in terms of the equations defined above, would correspond to a low value of Q' (with respect to R') and $\phi=1$, i.e. an absorption-feature free and essentially flat signal.

We examined the effect that the value of Q' (as a function of the fixed measurement noise R) has on the performance of the filter when ϕ is kept constant. Clearly, the smaller the Q' , the more smoothed the data appears (Figure 7.3). At a value of $Q'=R'/10$, i.e. when the variance of the noise R' is comparable to the variance of the noise of the “true” signal Q' , the Kalman output essentially equals the original data (not shown). On the other hand, when the noise is assumed to be larger relative to the “true” signal (small Q') the filter effectively removes background spikes from the spectrum (not shown). However, as Q' is increased, the peaks become more and more asymmetric. This is due to the fact that the algorithm’s model of the data is a flat line ($\phi=1$) without absorption features. We therefore implemented other versions of the Kalman algorithm with variable ϕ , and observed sharp and smoothly filtered absorption lines. However, we only gained a marginal performance increase relative to simple boxcar averaging.

7.4 Conclusions

The signal-to-noise ratio (S/N) of van der Waals spectra can be improved by post data-acquisition digital filtering. In addition to simple boxcar averaging, we explored several other digital filters, including modifications of the Wiener and Kalman algorithms. While the performance of the Kalman filter was on occasion impressive, we found that optimization of sample conditions, elimination of optical fringing, accumulation of more frequency scans and simple box car averaging were generally more effective in improving the signal-to-noise ratio of van der Waals spectra.

CHAPTER 8

GAS SENSING WITH A FREE JET EXPANSION IR SPECTROMETER*

* Portions of this Chapter have been accepted for publication in the journals *Proceedings of SPIE* **2002**, 4817, 249 and *Reviews of Scientific Instruments* **2004**, 75, 46.

8.1 Introduction

In the preceding Chapters, the spectra of several previously unknown van der Waals complex containing the CO₂ unit were presented. This Chapter represents a break from this theme and focuses solely on how the spectrometer can be used for gas sensing of CO₂ monomer and its third most abundant isotopomer, ¹⁸OCO. CO₂ plays a central role in such diverse fields as atmospheric chemistry,⁴ geochemistry¹⁷¹ and biochemistry.¹⁷² Isotope specific measurements of atmospheric gases are emerging as a new method to trace biological and geochemical events. The great selectivity and sensitivity of laser based instruments have enabled measurements of minor isotopomers, for example ¹H²DO and H₂¹⁸O in water vapours.¹⁷³ For carbon dioxide, the most commonly studied isotopomer is ¹³CO₂.¹⁷⁴ The oxygen isotope ratios of carbon dioxide are less frequently studied. However, δ¹⁸O has recently been identified as an indicator for photosynthetic activity.⁷⁶

Many analytical techniques exist for accurate and precise CO₂ gas phase measurements. Laser-based spectroscopic methods are often superior because of their multiplexing capability and higher selectivity, sensitivity, and speed. In the last five years

alone, nearly a dozen new laser-based CO₂ sensors have been reported.¹⁷⁴⁻¹⁸⁴ The recent boom in the telecommunication and related industries has significantly improved the availability of diodes in the near-infrared. Not surprisingly, the majority of instruments developed for CO₂ sensing utilize absorption bands in the near-infrared at or below 2.0 μm.¹⁷⁶⁻¹⁸⁰ However, these near-infrared instruments utilize only relatively weak overtone and combination bands of CO₂. Much more sensitive fundamental absorption lines are located in the mid-infrared (Chapter 1). Several instruments that exploit the higher sensitivity in the mid-IR with new laser sources have recently been reported.^{181,182,184}

In this Chapter, the application of a mid-infrared molecular beam tunable lead salt diode laser spectrometer towards sensing of ¹⁸OCO and CO₂ is described. The spectrometer performance is evaluated and compared with conventional spectroscopic methods.

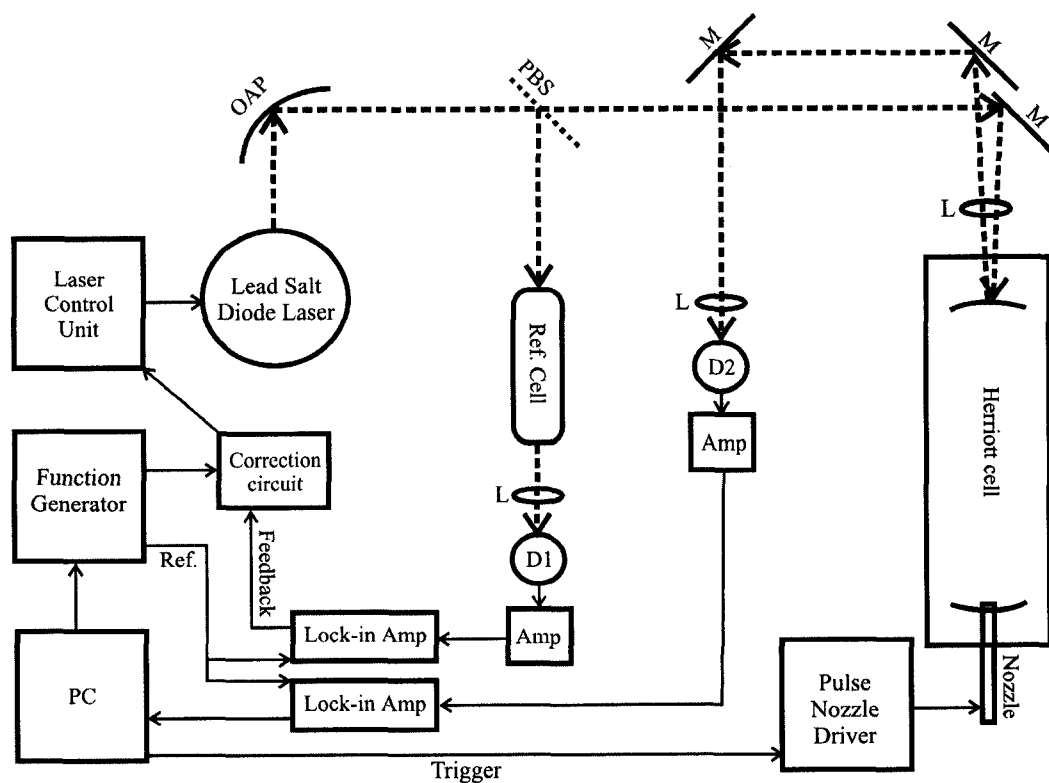
8.2 Experimental

8.2.1 General

The instrument is only slightly changed from the version described in Chapter 2 by the implementation of different frequency locking and modulation schemes. The output of the reference detector is demodulated with a lock-in amplifier (SRS 830) operated in 1 f mode. The demodulated reference signal is then used in a feedback loop to stabilize the frequency of the laser diode. The main signal is demodulated with a second Stanford Research Systems 830 phase sensitive detector before it is processed in the data acquisition board. A layout of the modified instrument is shown in Fig. 8.1.

Figure 8.1

Sketch of the spectrometer modified for gas measurements. M = gold coated mirror; D = InSb detector; L = lens; Amp = Preamplifier; PBS = pellicle beam splitter; OAP = off-axis parabolic mirror.



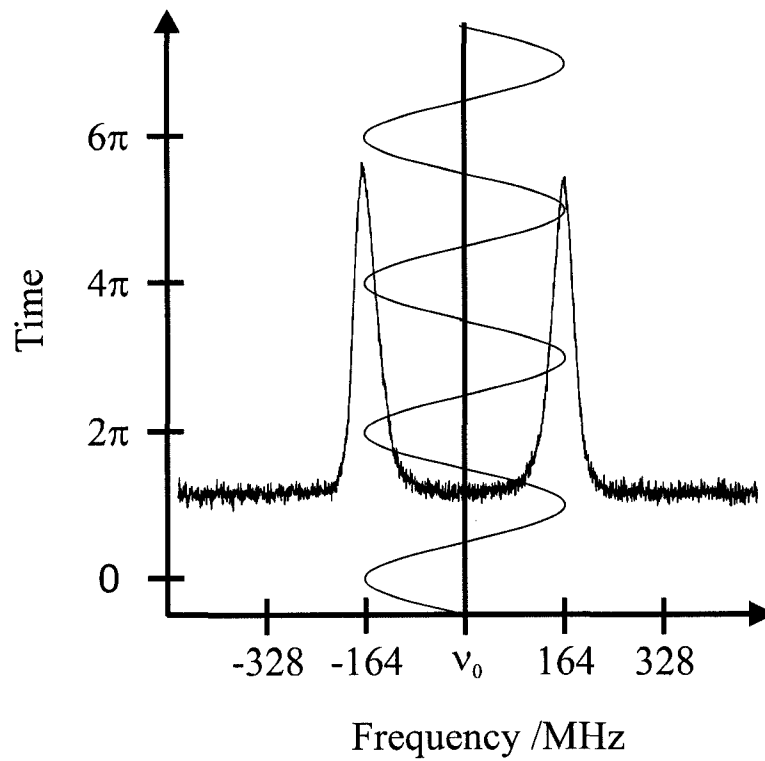
8.2.2 Laser modulation and detection

For single line monitoring, the laser diode needs to be locked to a low J transition of the analyte gas. For this work, the diode was locked to the R(0) transition of CO₂ at 2349.9172 cm⁻¹ or the R(1) transition of ¹⁸OCO at 2333.5677 cm⁻¹. A 51 kHz sinusoidal signal is used to modulate the output of the laser diode. The modulation depth is set such that it reaches both Doppler components of the monitored transition for a specific sample backing pressure and sample composition (Fig. 8.2). The absorption signal is thus observed at twice the input frequency. The lock-in amplifier is operated in 2f-demodulation mode, using time constants of either 300 μs or 1 ms. In contrast, the reference signal is demodulated at the input frequency (1f), and the laser was locked to the zero crossing of the 1f-demodulated reference signal. Since the reference signal is usually much stronger than the analyte signal, the lock-in amplifier can be operated with a smaller time constant (125 μs). In addition, the reference signal was also demodulated in 2f-mode using an Ithaco Dynatrac 391A lock-in-amplifier to obtain a signal proportional to the laser power. The molecular signal is observed for the entire lifetime of the molecular expansion, and the output of the lock-in amplifiers is digitized at a (oversampled) rate of 25 MHz. Each trace is integrated immediately after acquisition. In a typical experiment, data from 200 gas pulses are averaged. Absolute sample concentrations were derived from calibration curves using gas standards. The spectrometer was calibrated by measuring the signals obtained with pure N₂ and a series of standard gas samples in the range of 99 to 605 ppm CO₂ in air, and averaging the

Figure 8.2

The modulation of the laser represented as laser output frequency ν as a function of time.

The units of time are expressed in terms of complete periods of the laser modulation frequency f . The Doppler line shape of the CO_2 R(0) transition is superimposed.



resulting signals over 200 pulses. Gas samples were either purchased from Praxair (CO₂ in air, certified), or prepared by diluting air with nitrogen.

8.2.2.1 Response function of the 2f-detection scheme

The detector response to the frequency modulation - 2f-demodulation experiment on a Doppler doublet was modeled numerically. If the laser is locked to the line center frequency and the modulation amplitude equals the Doppler splitting (Fig. 8.2), the detector "sees" a periodic signal as shown in Fig 8.3 (top trace). In 1f-demodulation, the detector signal is multiplied by the reference signal $\sin(f+\xi)$ shown in the middle trace of Fig. 8.3. From Fig. 8.3, one can see that the 1f-demodulated signal will be zero at any ξ . In 2f-demodulation mode, the detector signal is multiplied by the reference signal $\sin(2f+\xi')$. This reference signal is shown in the bottom trace of Fig. 8.3, with a phase shift $\xi' = \pi/2$. Under those demodulation conditions, the molecular absorption signal from both Doppler components is recovered.

Fig 8.3 is a simulation of the best-case scenario. In reality, the output of the laser diode will fluctuate somewhat around the line center. We investigated the effects of laser drifts by monitoring the signal as the laser is detuned from the line center frequency and compared the experimental signals with a numerical simulation. The results are shown in Fig. 8.4. The top row are experimental data, and the bottom row are calculated data. The left hand side shows the fast-scan spectrum of the Doppler doublet, and the modeled line shape based on equation 3.5. In the frames on right hand side the modulation amplitude equals the Doppler splitting. The experimental frame on the top right hand corner

demonstrates that a 51 kHz frequency-modulated signal, 2f-demodulated, samples the absorption of both Doppler peaks, because the intensity of the sidebands is only half of the peak center frequency. It also shows that the signal is strongly affected if the laser drifts only slightly off the line center. The instrument response is reduced by up to 2% per MHz of laser drift. An unstabilized diode has frequency output fluctuations of ~60 MHz¹⁸⁵ which occur on the time scale of the applied modulation frequency. Strong signals would therefore fluctuate significantly if the diode is not properly locked.

The effects of applying a modulation amplitude that is less than the Doppler splitting is shown in the center frames. An intensity dip at the line center is observed in this case. The same result was obtained if the laser modulation amplitude is slightly larger than the Doppler splitting.

8.2.3 Laser stabilization

In principle, TDLs can exhibit two types of frequency drift. Long-term frequency drifts are caused by small and often systematic operating temperature or pressure changes, and are corrected by adding a DC offset to the diode modulation current. More serious and short-term (sub-ms range) laser fluctuations is caused either by noise superimposed on the laser current, shot noise within the laser junction, or competition between active laser modes. It has been shown that the laser line width observed on a millisecond time scale is determined by a temporal average of many narrow (less than 500 kHz) emission modes.²⁷ Minute structural and thermal fluctuations in the active junction chaotically activate and quench these instantaneous modes on a time scale of microseconds or less.

Figure 8.3

Theoretical detector response (top trace) and the 1f- (middle trace) and 2f- (bottom trace) demodulation reference signals. For an explanation see Section 8.2.2.1.

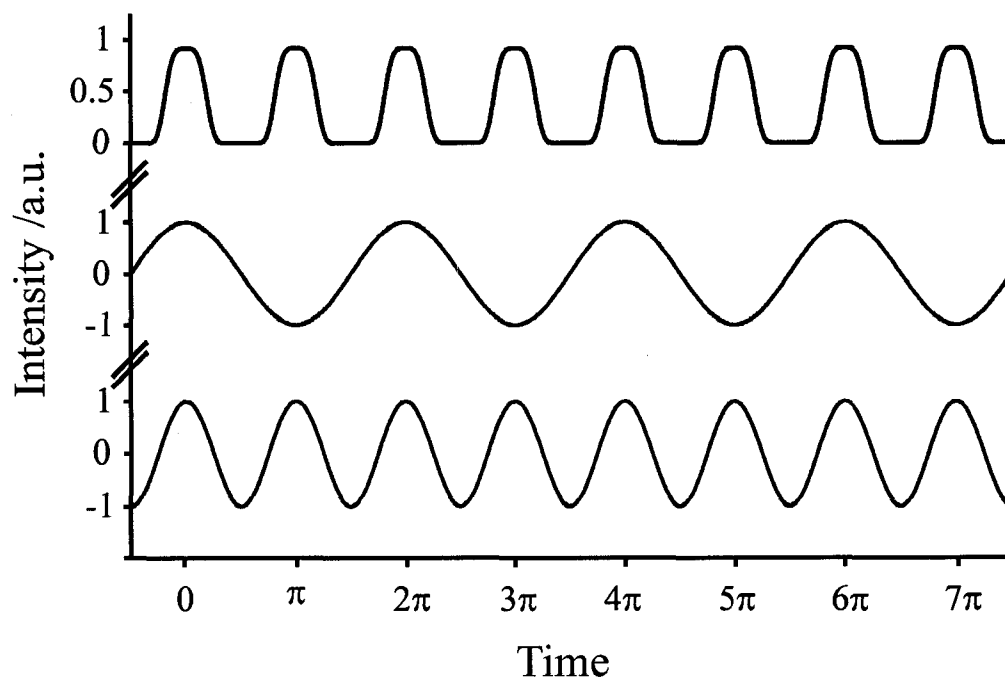
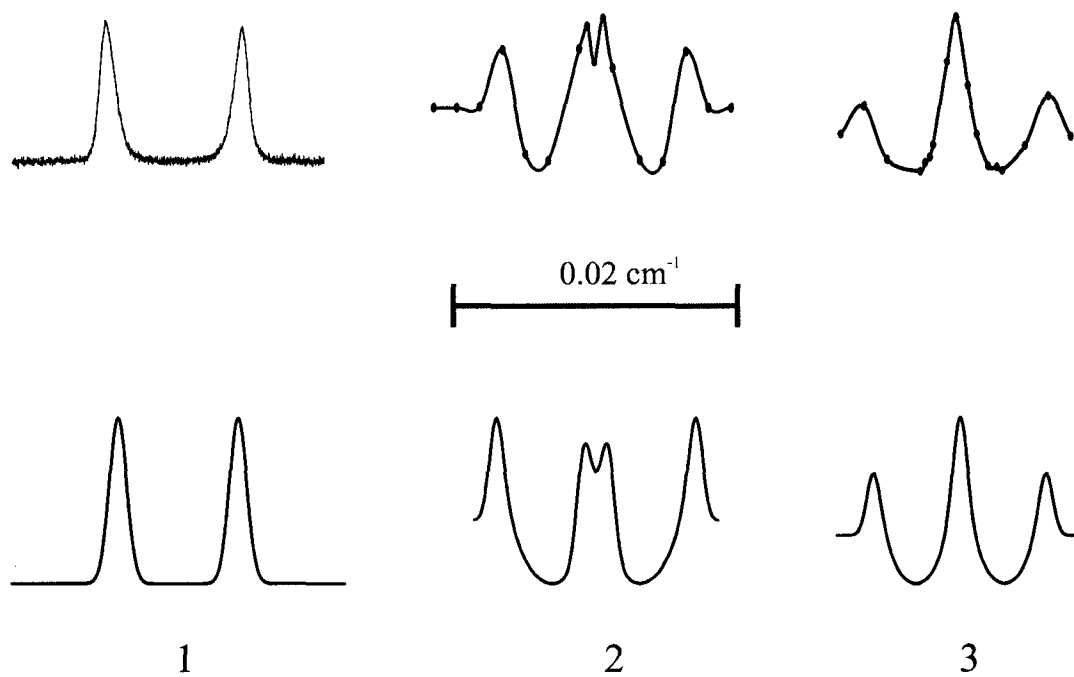


Figure 8.4

Actual (top) and simulated (bottom) spectra using 2f-demodulation detection. The experimental modulation spectra (top) were assembled from a series of individual experiments. In the numerical simulation, a phase angle of $\pi/4$ between modulation and demodulation signal was used. (1) Two Gaussian absorption peaks identical to those shown in Fig. 8.2. (2) 2f-demodulated signal. The modulation amplitude is slightly smaller than the Doppler splitting. (3) 2f-demodulated signal. The modulation depth equals the Doppler splitting.



Many laser locking schemes have been reported in the literature. We constructed a lock-in circuit (Fig. 8.5) using Chapter 2 of Skoog and Leary³⁰ and other introductory electronic texts as a guide. We found that it was necessary to operate this circuit on battery power to prevent high frequency noise from entering through the power supply. In our low noise feedback circuit design, the output of the demodulated reference signal is fed to the input terminal of the feedback circuit (V_{in}). The negative output of the lock-in amplifier is integrated with a variable time constant (selected by SW_1) between 0.47 ms and 3.9 ms. If the laser is locked, the output of the lock-in amplifier and the integrated signal are close to zero. The integration time constant must be set large enough to avoid overcompensation, which results in rapidly increasing oscillations of the correction signal. We typically observed such oscillating feedback at time constants below ~ 0.5 ms. After integration, the correction signal is attenuated by at least a factor of 1000 and added as an offset to the 51 kHz sine modulation signal. Additional attenuation of the circuit output voltage with a 12 dB Attenuator (Mini-Circuits Model Cat-12, DC to 1500 MHz) reduces the electronic noise level (rms ± 5 mV).

In a typical experiment, the laser current is manually set close to the absorption feature, and then the circuit is activated using SW_2 . The output of the correction circuit is monitored with a digital display. If the correction drifts too much off zero Volt, the current is manually adjusted on the dial of the TDL control unit until the correction voltage is close to zero again.

Overcompensation can in principle be avoided if an occasional proportional feedback controller is used.¹⁸⁵ In such a system, the lock-in amplifier control signal is

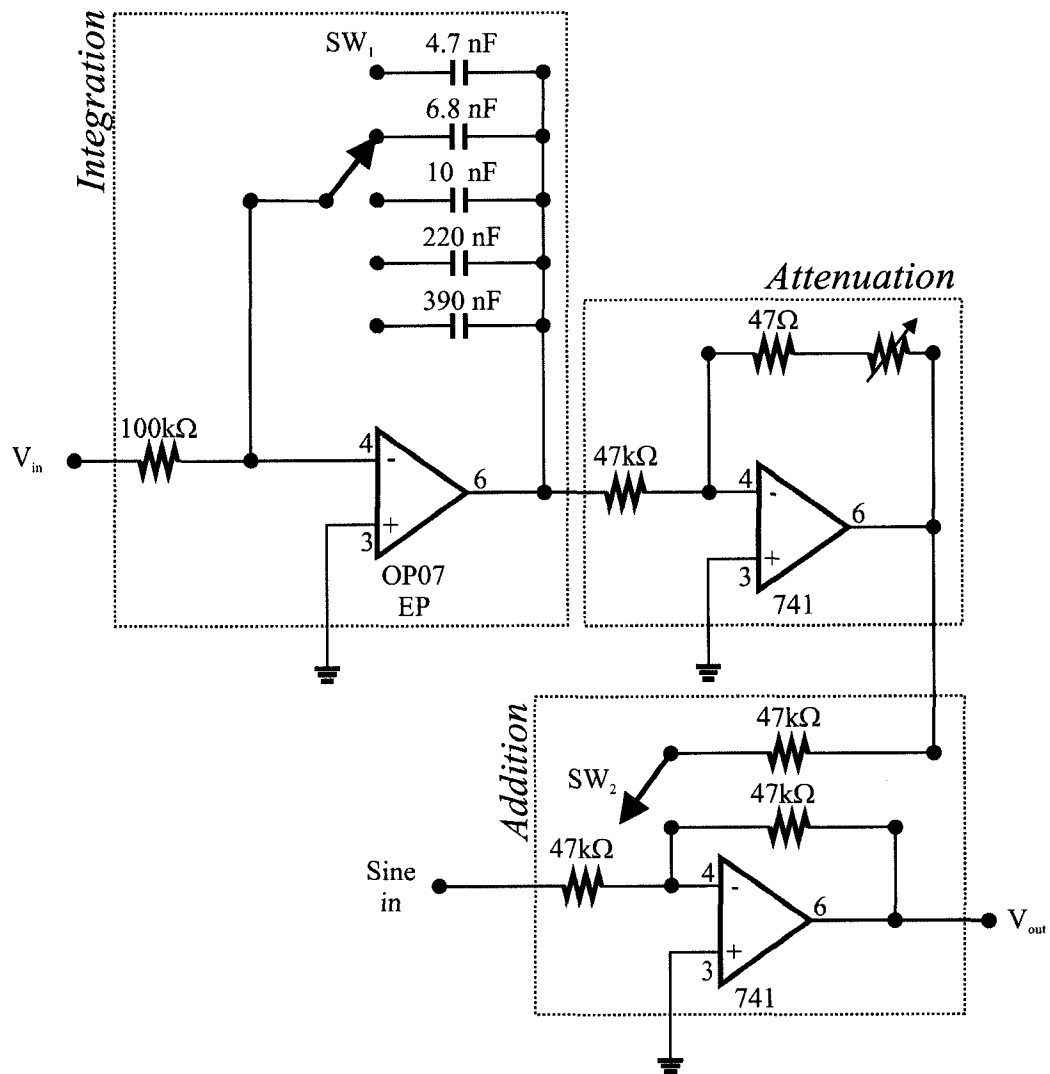
only probed during short selected periods, and the correction signal is sent only "occasionally" to avoid overcompensation. Tunable diode lasers can be stabilized to very narrow emission line widths in that manner.^{27,185} We tested such a device, with mixed success. This circuit did not cope well with persistent frequency drifts, and was therefore not used in the experiments.

8.2.4 Post-data acquisition digital filtering

Noise due to fluctuations in sample delivery and laser output frequency occurs on a much shorter time scale than the time intervals between consecutive measurements, and therefore appear as uncorrelated white noise. On the other hand, sample concentration fluctuations occur on a much larger time scale than the pulse repetition rate. Repeated measurements have therefore a high degree of self-correlation. Digital filtering techniques such as the Kalman filter^{168,186} have been developed to extract self-correlated signals buried in white noise. Kalman filtering in particular is routinely applied in trace gas sensing measurements by tunable diode laser spectroscopy.^{165-167,187} The Kalman filter algorithm is described in detail in Chapter 7. In this spectrometer, the integrated signal is immediately Kalman-filtered between pulses.

Figure 8.5

Diagram of feedback circuit. The circuit consists of a variable time constant integration stage followed by a variable attenuator. In the final stage, the correction signal is added to the sinusoidal modulation.



8.3 Quantitative measurements

8.3.1 Calibration and typical signals

Detection of CO₂ in ambient air with the molecular beam spectrometer is relatively effortless (Fig. 8.6) because of the high natural abundance of CO₂ in air of approximately 370 ppm.² The observed pulse-to-pulse signal fluctuations can be attributed to gas delivery variations and temporary laser frequency drifts. Averages of 100 scans were reproducible within ~6% standard deviation (Table 8.1). Absolute detection limits were difficult to determine with the main isotopomer of CO₂ because of its large ambient concentration. At concentrations near the instrumental detection limit, contamination from leaks and outgassing within the sample pipes become an issue, and low concentration gas standards are very expensive. It was therefore more practical to determine the limit of detection using calibration curves of a less abundant isotopomer of CO₂. ¹⁸OCO has a natural abundance of 0.39%, so that its ambient concentration is ~1.4 ppm. (Table 1.1). Representative data for the R(1) line of ¹⁸OCO are shown in Fig. 8.7. As can be seen in Fig 8.7, acquisition of a sufficient number of data points for construction of a calibration curve takes approximately ½ hour.

Figure 8.6

Representative response curves of the spectrometer operated in frequency – 2f- demodulation mode, averaged over 100 molecular pulses. The laser was locked to the R(0) transition of CO₂ at 2349.917 cm⁻¹. The samples were (top to bottom) 150, 61, and 25 ppb CO₂ in He carrier gas at pressures of 1 atm. The pulse nozzle was triggered at time zero. The response curve corresponds to the appearance of the molecular expansion in the sampling area.

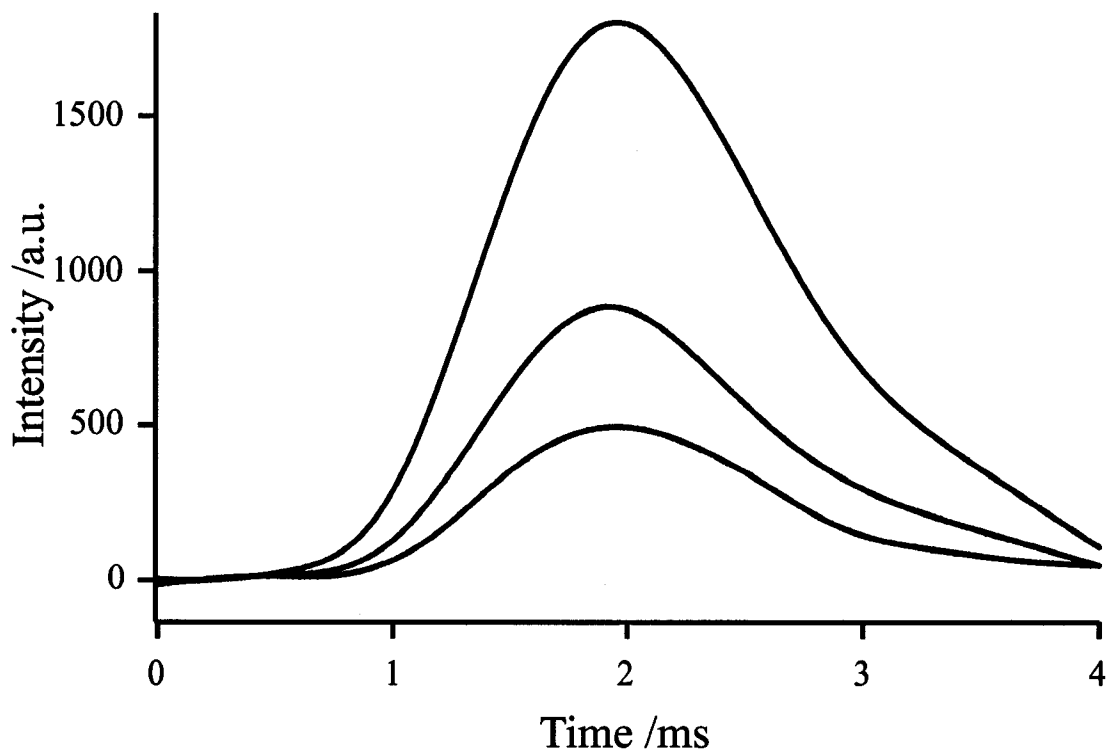


Table 8.1

Signal intensity of the CO₂ R(0) line in Fig. 8.6, averaged over 100 pulses. The samples were prepared by diluting an air sample. σ_{avg} is the standard deviation of repeated runs.

The relative standard deviation (RSD) is given by $\sigma_{\text{avg}}/V_{\text{avg}}$.

[CO ₂] /ppb	Integrated Signal V_{avg}	σ_{avg}	RSD _{avg}
3600	64.6	1.7	2.6%
1600	49.0	2.7	5.4%
770	25.0	1.3	5.0%
360	16.1	1.0	6.0%
150	8.91	0.59	6.7%
61	4.30	0.24	5.6%
25	2.56	0.25	9.7%

Figure 8.7

Instrument response to a series of gas standards. The spectrometer was calibrated by running a series of standard gas samples in the range of 99 to 605 ppm CO₂ plus pure N₂, and averaging the resulting signals over 200 scans. The data shown are those of the R(1) line of ¹⁸OCO, which has a natural abundance of 0.39%. Each dot represents the signal of a single pulse integrated over 2.8 ms. The contents of the sample lines were pumped off between standards. Because the gas standards were all purchased from the same source, it was assumed that the ¹⁸OCO abundance was equal to the natural abundance in each sample. The solid line represents data filtered with a Kalman algorithm ($R'/Q' = 250$).

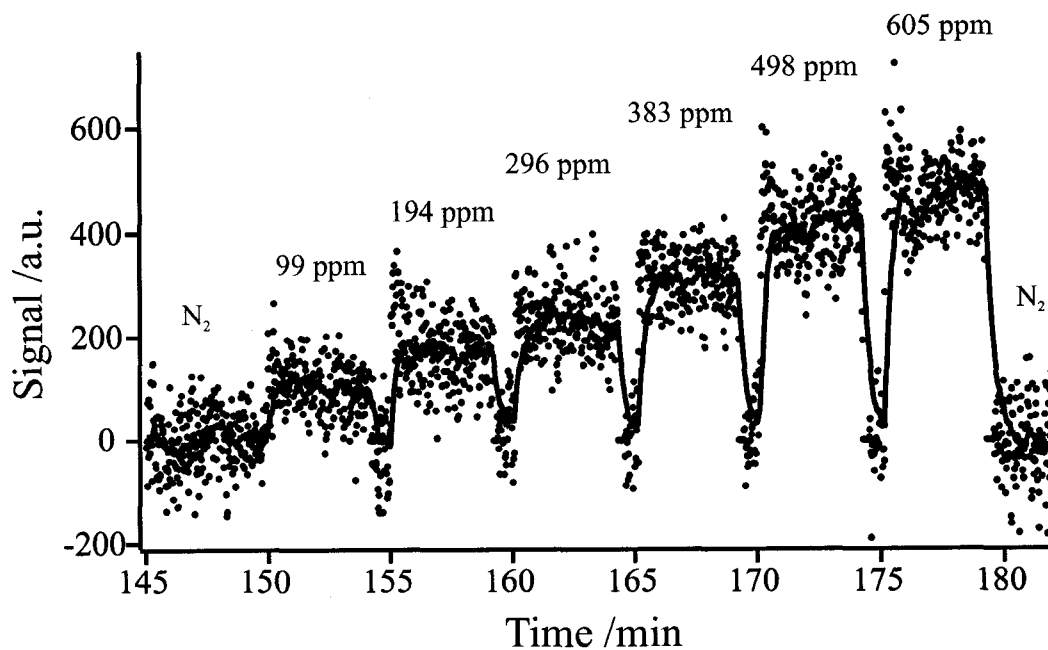


Table 8.2

Signal intensity of the ^{18}OCO R(1) line in Fig. 8.7, averaged over n molecular pulses. σ_{shot} is the pulse-to-pulse standard deviation. The pulse-to-pulse relative standard deviation RSD_{shot} is given by $\sigma_{\text{shot}}/V_{\text{avg}}$. σ_{avg} is the standard deviation of the mean ($= \sigma_{\text{shot}} n^{-1/2}$).

$[\text{CO}_2]$ /ppm	^{18}OCO /ppm	n	V_{avg}	σ_{shot}	RSD_{shot}	σ_{avg}	RSD_{avg}
0	0	200	2.6	59.2	-	4.2	-
99	0.39	200	104.9	49.1	47%	3.5	3.5%
194	0.756	200	177.4	64.6	36%	4.6	2.4%
296	1.15	200	232.2	55.9	24%	4.0	1.4%
383	1.49	200	316.3	51.1	16%	3.6	0.94%
498	1.94	200	422.0	64.8	15%	4.6	0.92%
605	2.36	200	478.8	62.0	13%	4.4	0.73%
0	0	200	-2.6	67.9	-	4.8	-

Note: V_{avg} and σ are in units of bits-seconds, which correspond to 2^{-12} Volt-seconds.

Table 8.3

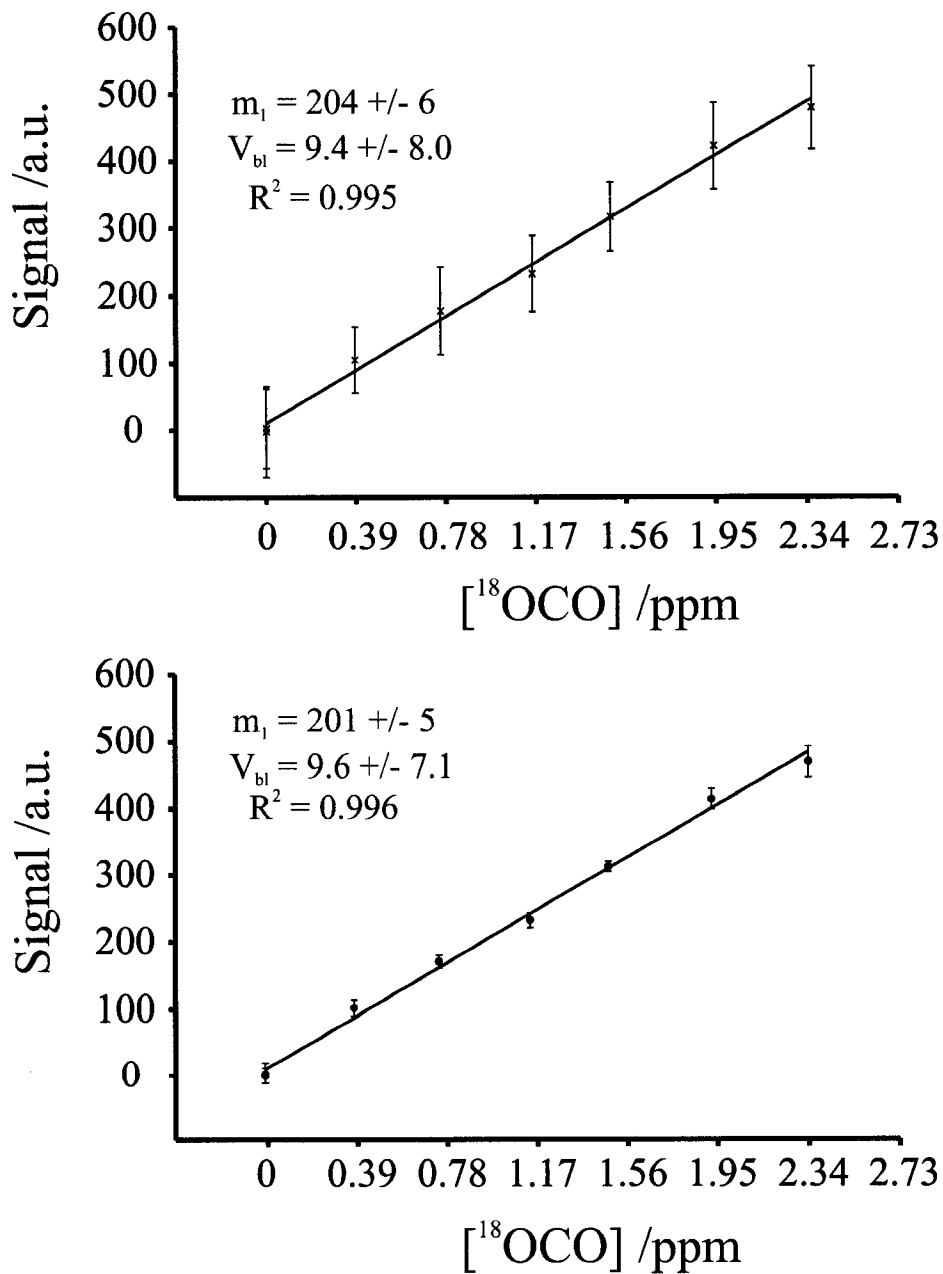
Kalman filtered ($R'/Q' = 250$) signal intensity of the ^{18}OCO R(1) data shown in Fig. 8.7.

The first 50 Kalman filtered points were ignored.

$[\text{CO}_2]$ /ppm	$[\text{}^{18}\text{OCO}]$ /ppm	n	V_{avg}	σ_{shot}	RSD	σ_{avg}
0	0	150	2.6	16.8	-	1.4
99	0.39	150	102.1	11.8	12%	1.0
194	0.756	150	171.2	9.3	5%	0.8
296	1.15	150	232.1	11.3	5%	0.9
383	1.49	150	313.0	7.4	2%	0.6
498	1.94	150	414.0	15.3	4%	1.2
605	2.36	150	469.5	23.1	5%	1.9
0	0	150	-1.0	12.5	-	1.0

Figure 8.8

Calibration curves from data in Tables 8.2 and 8.3. Top: Single-pulse data. Error bars correspond to 1 standard deviation. Bottom: Kalman filtered data averaged over 150 pulses. The slightly elevated intensity at low concentration may be a result of outgassing.



8.3.2 Limit of detection (LOD)

The instrumental limit of detection (LOD) can be derived from calibration curves as shown in Fig. 8.8. The LOD is defined by the equation

$$\text{LOD} = \frac{3\sigma_{bl}}{m_1} \quad (8.1)$$

where σ_{bl} is the standard deviation of the blank signal and m_1 is the slope of the calibration curve.³⁰ The LODs for pulse-to-pulse measurements, data averaged over 200 pulses, and Kalman filtered data averaged over 150 pulses are shown in Table 8.4. It was observed that averaging improves the LOD by the expected factor of \sqrt{n} ; for 200 pulses, $\sqrt{200} \approx 14.1 \approx 995/70.2$, and for 150 pulses $\sqrt{150} \approx 12.2 \approx 250.8/20.9$. Post-data acquisition Kalman filtering improves the LOD up to 21 ppb.

σ_{avg} of weak signals (Tables 8.2 and 8.3) is independent of the sample concentration, whereas for stronger signals σ_{avg} increases with signal strength (Table 8.1). The noise at high sample concentration can be attributed to pulse-to-pulse sample delivery variations and laser frequency fluctuations. The constant noise level at lower concentrations is instrumental, i.e. caused by fluctuating laser power and varying laser frequency. Thus, the LOD of this spectrometer is set by excess laser noise.

Table 8.4

Detection limits for the R(1) transition of ^{18}OCO in standard air.

	Per pulse	200 pulses	Per pulse + Kalman	150 pulses + Kalman
σ_{bl}	67.9	4.8	16.8	1.4
$m_l / (\text{ppm } ^{18}\text{OCO})^{-1}$	204 ± 6	204 ± 6	201 ± 5	201 ± 5
LOD /ppb ^{18}OCO	995 ± 31	70.2 ± 2.0	250.8 ± 6.6	20.9 ± 0.5
LOD /pmol ^a	50 ± 2	700 ± 20	12.5 ± 0.3	210 ± 5

^a Per pulse, approximately 0.05 mmol of gas is delivered.

8.3.3 Concentration monitoring

Ambient CO₂ concentrations were monitored over the period of several hours. Occasionally, the instrument was re-calibrated by running the six standard gas mixtures and a blank. A representative scan over a 3½ hour period is shown in Fig. 8.9 (top trace). The instrument response function is clearly changing within the observed time frame. The reason for this is a change of the emitted laser power. The 2f-demodulated signal of the reference channel (bottom trace) can be used as a direct measure of the laser power incident on the detector. The drifts of both signals is highly correlated, $r > 0.9$ on a pulse-per-pulse basis. Since the detector signal is proportional to the incident laser power I_0 , the signal can be corrected by calculating the ratio I/I_0 . The results are shown in Fig. 8.10. The concentration of ¹⁸OCO in the ambient air during the observation time was determined to be 1.38 ± 0.08 ppm.

8.4 Discussion

8.4.1 TDL stability

Even though the instrumental sensitivity can be pushed into the low ppb range by averaging and post-data acquisition digital filtering, the instrument itself is not yet suitable for routine analytical measurements. Problems arise mainly because the diode laser cannot be simultaneously frequency- and power-stabilized. The instrumental detection limit is set by excess laser noise, and continuous measurements are spoiled by laser power drifts. The instrument is tolerant to small and random fluctuations of the laser power around a fixed average; such behaviour would be similar to pulse-to-pulse sample

Figure 8.9

Concentration measurements during a 3.5 hr period (top trace). The data shown was Kalman filtered before presentation ($R'/Q' = 250$). The 2f-demodulated signal of the reference cell (bottom trace) is a measure of the emitted laser power.

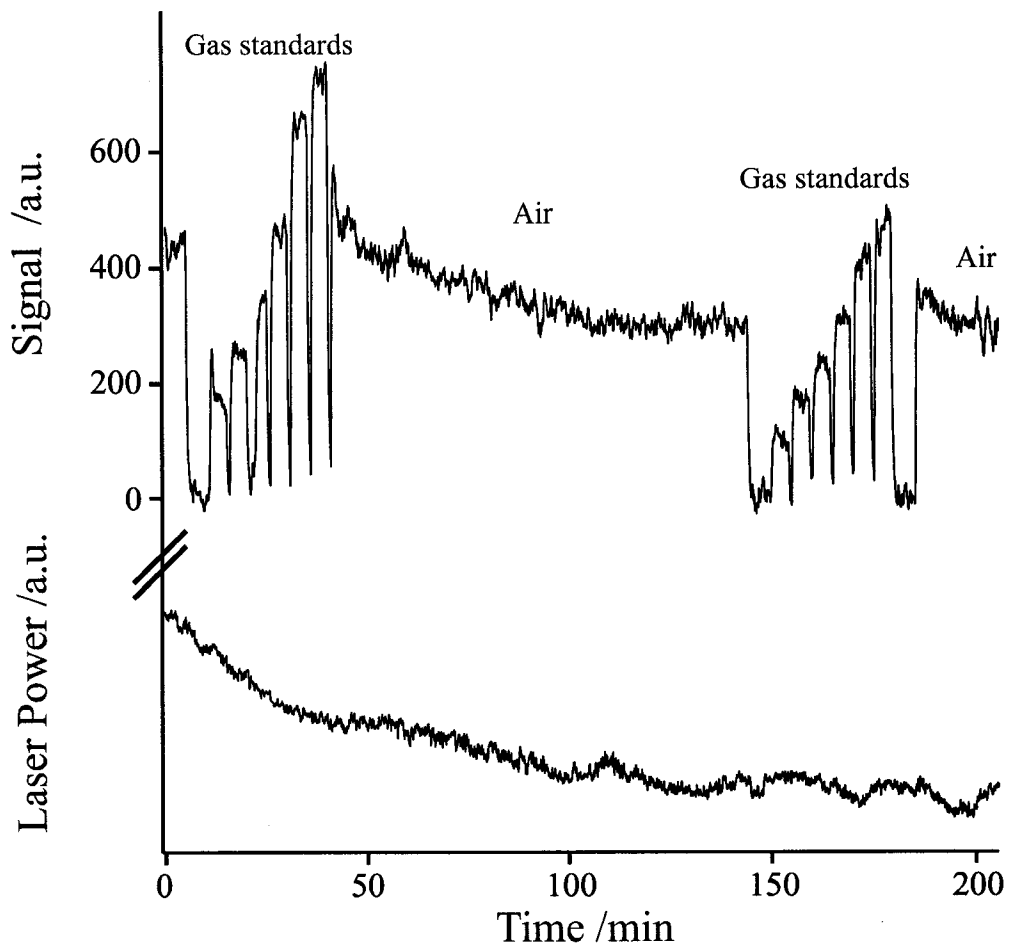


Figure 8.10

Concentration measurements during a 3.5 hr period, corrected for laser power fluctuations. The crude signal and the 2f-demodulated reference signal (bottom trace of Fig. 8.9) were boxcar-averaged over 37 points, and the ratio was calculated. Concentrations were derived by averaging the results from the two calibration curves. The average concentration of the air signal (t = 45 min to 140 min) is 1.38 ± 0.08 ppm.

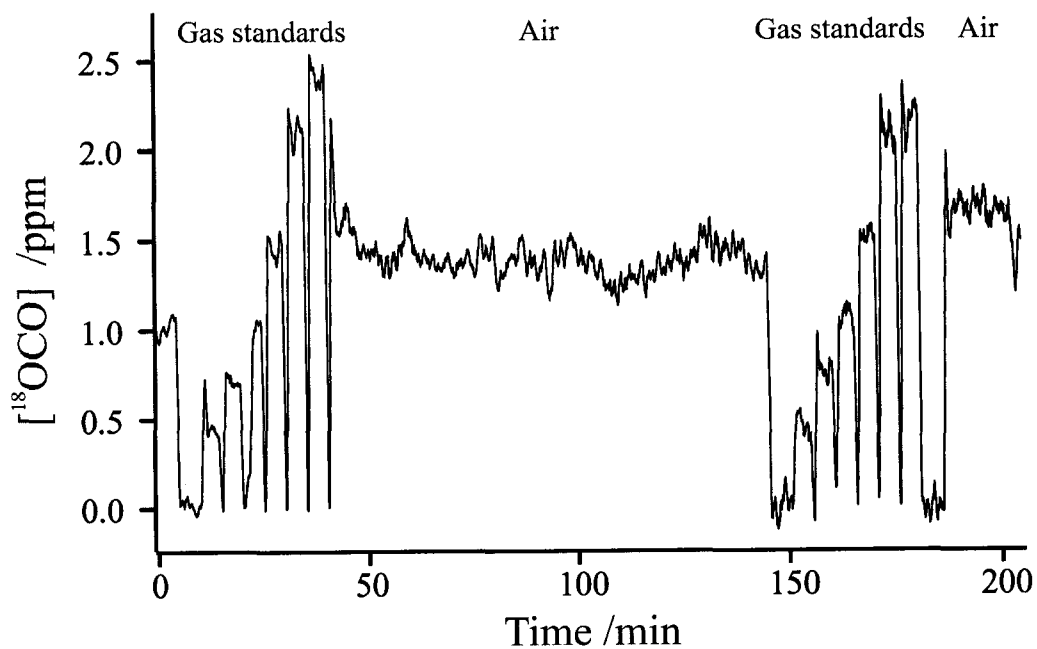
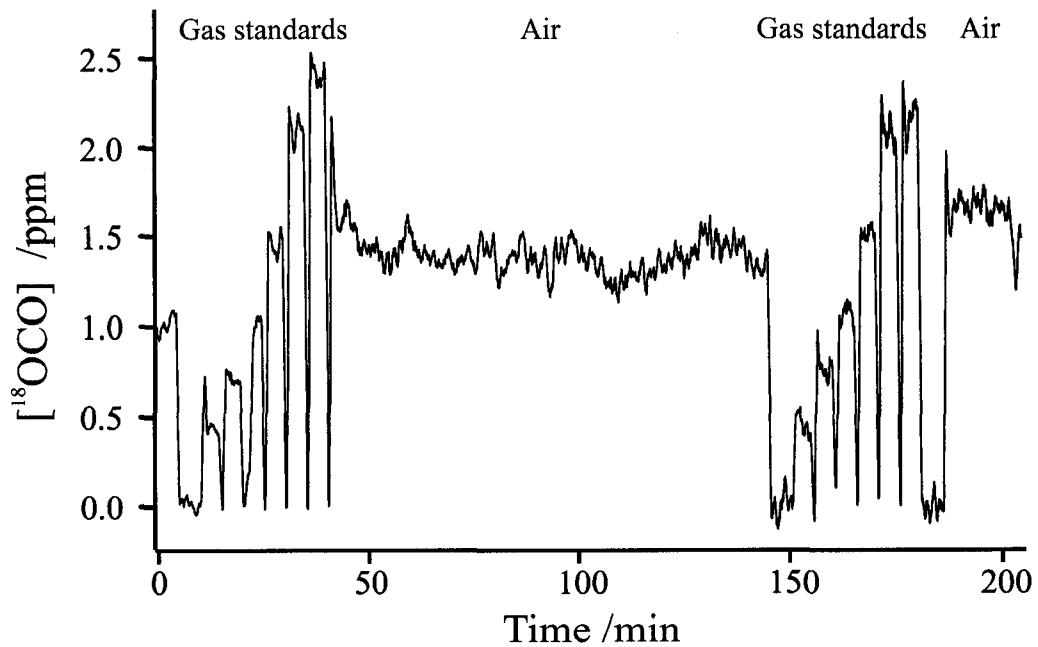


Figure 8.10

Concentration measurements during a 3.5 hr period, corrected for laser power fluctuations. The crude signal and the 2f-demodulated reference signal (bottom trace of Fig. 8.9) were boxcar-averaged over 37 points, and the ratio was calculated. Concentrations were derived by averaging the results from the two calibration curves. The average concentration of the air signal ($t = 45 \text{ min to } 140 \text{ min}$) is $1.38 \pm 0.08 \text{ ppm}$.



delivery fluctuations and averages out over many measurements. The instrument is not tolerant of systematic laser power drifts, as demonstrated in Fig. 8.9. The signal obtained by 2f-demodulation of the reference channel with a 3rd lock-in amplifier is proportional to the laser power I_0 , and can be used to compensate for laser power fluctuations (Fig. 8.10). However, this also increases the overall noise of the measurement.

A possible solution to this problem could be a higher modulation frequency in the 10-100 MHz range. This would require faster lock-in amplifiers capable of handling such modulation frequencies. An alternative solution would be to use a different laser source altogether, in which the output frequency is not a function of the laser pumping rate.

Long-term drifts on the time scale of minutes are known to be a common problem in TDLAS. Werle has advocated the use of Allan-plots to characterize long-term drift.^{37,164,188} The Allan variance $\langle \sigma_A^2 \rangle$ can be calculated from:³⁰

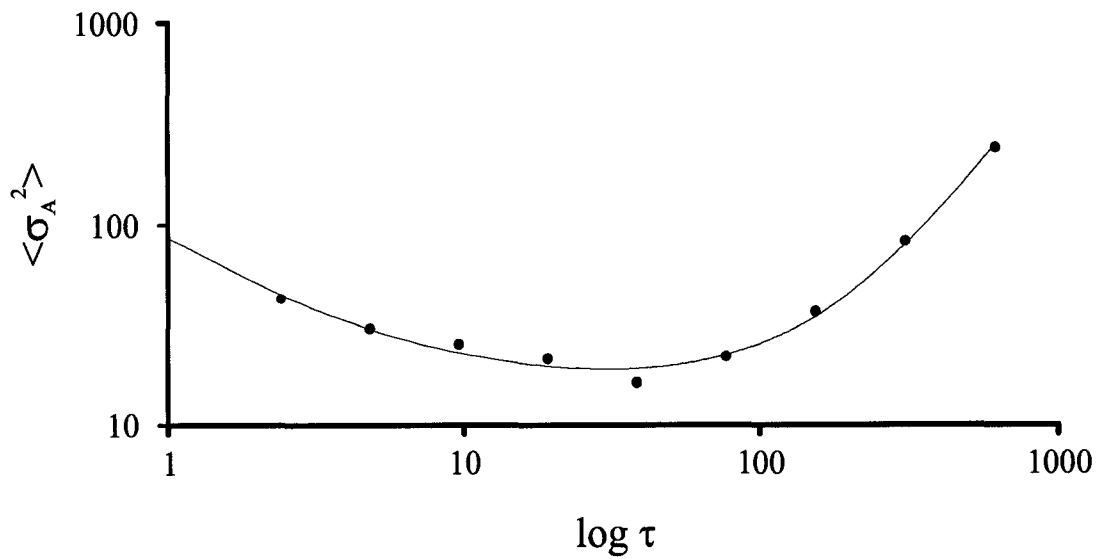
$$\langle \sigma_A^2 \rangle = \frac{1}{2 \text{bar}} \sum_{\text{foo}=1}^{\text{bar}} (A_{\text{foo}+1}(\tau) - A_{\text{foo}}(\tau))^2 \quad (8.2)$$

A_s is the averaged signal in bin foo of size bar, and τ is the integration time constant. In TDLAS, the Allan variance is related to the fundamental noise sources using the following empirical equation:^{37,164,188}

$$\langle \sigma_A^2 \rangle = c_{\text{white noise}} \left(\frac{1}{\tau} \right) + c_{1/f} + \sum_{\alpha} c_{\text{drift}} \tau^{\alpha} \quad (8.3)$$

Figure 8.11

Allan plot¹⁸⁹ of the 2f-demodulated signal of the reference cell during a 3.5 hour measurement. A fitted line based on equation 8.3 is superimposed. The integration time τ is given in units of seconds.



$c_{1/f}$ and $c_{\text{white noise}}$ and c_{drift} are empirical constants. The Allan plot ($\langle \sigma_A^2 \rangle$ vs. $\log \tau$) has a minimum at the optimum integration time.¹⁸⁹ In TDLAS measurements, a maximum S/N is often found at $\tau \approx 100$ s. After this point, S/N decreases nearly linear with integration time because of laser drifts.^{37,164,188}

An Allan plot of the observed power signal (bottom trace of Fig. 8.9) is shown in Fig. 8.11. The lead salt diode output power is stable for about ~ 38 s. Thus, in order to use the instrument in long-term measurements, it needs to be recalibrated often, for example by spiking the sample with a known amount of CO_2 every few minutes.

8.4.2 Gas sampling with a molecular beam

The achieved detection limits obtained with this spectrometer (Table 8.4) are more than three orders of magnitude worse than the calculated detection limit of a traditional TDLAS spectrometer operated in the $4.2 \mu\text{m}$ region.^{25,47} For example, Sigrist has estimated the limit of detection of CO_2 with a lead salt TDLAS system modulated at 10 kHz at the ν_3 fundamental and one second integration over a 132 m optical path as 0.002 ppb.²⁵ However, the achieved detection limits are similar to those of near-infrared instruments, because of the reduced line-strength of overtone and combination bands (Chapter 1).

The poor performance of the molecular beam compared to a static gas cell spectrometer can be explained by the low observation duty cycle, molecular beam divergence resulting in poor overlap of the sample gas with the laser beam, and reduced absolute amount of gas sampled.

The pulsed operation of the nozzle introduces the pulse repetition rate as a variable. In a typical experiment, the sample gas can be observed for ~ 3 ms per pulse (Fig. 3.6). At a pulse repetition rate between 1 and 10 Hz, the sample gas is only observed for 1/333 to 1/33 s in a one second interval. Ideally, experiments would be performed on a nearly continuous molecular beam; in practice, the duty cycle depends on the size of the pump.

The sensitivity is also limited by the divergence of the molecular beam. Even though it was shown that the molecular sample exits the nozzle in a fairly narrow cone (Section 3.3.4), the divergence of the molecular beam is demonstrated by the small sensitivity gain from implementing a longer Herriott cell.

The detection limit is also raised because a smaller amount of gas is present in the multipass chamber. The apparent lower sample consumption might be a potential advantage of using a pulsed nozzle. In a typical pulse at 1 atm backing pressure, about 0.05 mmol of gas is delivered, judged from the amount of gas collected in an inverted graduated cylinder held under water. It then takes about 1800 pulses to fill the sampling volume (~ 2 L) to atmospheric pressure. A typical reduced-pressure static gas experiment is performed at about 100 torr, and this amount of gas would be delivered in about 240 pulses. While only a relative small amount of gas is used in a single pulse, averaging over several hundred pulses actually uses up more sample than filling the entire sample volume, so that employing a pulsed nozzle does not result in reduced sample consumption.

The pulsed operation of the nozzle also introduces additional sources of noise such as sample delivery fluctuations and matrix effects, which are not observed with

static gas samples. Since the signal is very sensitive to the beam temperature, it is therefore very sensitive to the reproducibility of the pulse, the presence of impurities in the sample, the identity of the carrier gas, and complex formation. The signal intensity may, however, be enhanced by compressing the sample with He carrier gas to higher backing pressure.

Sensitivity enhancement is expected from the redistribution of the molecules into the lowest ro-vibrational levels. The signal enhancement due to the cold molecular beam temperature can be calculated from equations 1.2 and 1.3. The lowest observed beam temperature with the spectrometer was 0.7 K. At this temperature, the (calculated) maximum gain from the ro-vibrational cooling is a signal strength enhancement of the R(0) transition of CO₂ by a factor of ~255, and of the R(0) transition of ¹⁸OCO by a factor of ~328. The beam temperature is slightly higher when air is used as carrier gas, so that the R(1) transition of ¹⁸OCO is slightly more intense than its R(0) line.

However, in static gas experiments, one usually selects the strongest possible ro-vibrational transition, for example the R(16) line of CO₂. Comparing the ground state populations of the R(16) lines of either CO₂ or ¹⁸OCO with the population of the R(0) line at 0.7 K only yields a maximum improvement by a factor of 12.9 and 16.1, respectively. Thus, the gain from the cold sampling environment is not as large as perhaps anticipated.

8.5 Summary and future work

In this chapter, the suitability of a molecular beam TDLAS spectrometer towards trace gas sensing was tested at the ppm level. For this purpose, a novel modulation technique was successfully implemented. The main advantage of employing a molecular beam is the highly selective signal enhancement, which was already demonstrated in Chapter 3.

The instrument's response function was found to be linear in the concentration range studied. The detection limit was estimated to be at 21 ppb, which is several orders of magnitude above the theoretical limit. The spectrometer performance is limited by laser power drifts. The maximum useful integration time was estimated at 38 s on the basis of an Allan plot. Compared to traditional TDLAS with a flow-through cell, the present design suffers from additional noise sources, including pulse-to-pulse sample delivery fluctuations and matrix effects, and is dependent on external calibration.

Remaining challenges include reduction of pulse-to-pulse sample delivery fluctuations, further improvement in laser frequency stability, improvements in sample overlap with the laser beam and construction of a mobile version of the spectrometer.

CHAPTER 9

GENERAL CONCLUSIONS AND FUTURE WORK

A functional mid-infrared molecular beam tunable diode laser spectrometer was constructed (Chapter 2) and tested (Chapter 3). Selective signal enhancement of low J lines of CO₂ and ¹⁸OCO and signal reduction of high J lines of H₂S and CO₂ was demonstrated. A twofold sensitivity improvement resulted from mounting the injection nozzle in the axial position. Several post-data acquisition digital filtering techniques, including the Kalman and Wiener algorithms, were implemented and tested (Chapter 7).

The suitability of the spectrometer as a tool to study weak interactions in the gas phase was demonstrated (Chapter 3). The spectrometer was used to record the infrared spectra of several previously unknown weakly bound complexes (Chapters 4-6). The studies of the molecular systems contribute to the understanding of the nature of weakly bound complexes of CO₂. The mid-infrared spectrum of CO₂-SO₂ (Chapter 4) is consistent with the conclusions of the earlier microwave study,¹⁰⁵ for example the structural analysis. Microwave-infrared double resonance was successfully used as an assignment tool and for resolution enhancement. In the study of CO₂-CH₄ by mid-infrared and FTMW spectroscopy (Chapter 5) the effective structure of the complex was determined to be T-shaped. The identification and assignment of the transitions of the three internal rotation states of CO₂-CH₄ allowed the determination of molecular constants for each nuclear spin state. This contributes to the understanding of the internal motions of a weakly bound complex containing a spherical top.

In the studies of several weakly bound complexes of the ^{18}OCO isotopomer, it was demonstrated that the r_{CO} bond length is only slightly perturbed by complex formation, if it all. The structures of $\text{N}_2\text{-}^{18}\text{OCO}$ and $\text{Ne-}^{18}\text{OCO}$ were found to be very similar to the main isotopomers. A rigid rotor Hamiltonian was successfully fitted to the observed transitions of $\text{He-}^{18}\text{OCO}$ in spite of the large amplitude internal motions.

A major objective of this thesis was to probe the feasibility of using a molecular beam TDL spectrometer for trace gas sensing. The spectrometer was therefore modified for single line monitoring, and its performance as a gas sensor was evaluated (Chapter 8). The achieved detection limits for ^{18}OCO in air were found to be in the low ppb range, limited by excess laser noise, showing that a molecular beam can be used for trace gas sensing in the IR. The detection limits could have been improved further if a power- and frequency-stabilized laser had been employed.

Much work still needs to be done before a molecular beam spectrometer becomes a viable alternative to traditional gas sampling techniques in the field. Many of remaining challenges are engineering problems, for example the construction of an automated sample introduction and calibration system. For the construction of a miniaturized version to be used in field experiments, the laser power instability and low pulse repetition rate need to be addressed. In my opinion, this will require a new frequency- and power-stabilized mid-infrared radiation source, perhaps a TDL with an external Bragg grating or a QC laser, and a more powerful pump. Both laser and pump ideally will not require liquid nitrogen cooling, because transport of liquid nitrogen to the test site poses a logistic problem. The pulse-to-pulse fluctuations of the sample delivery can in principle be reduced to less than 1% using the nozzle head described by Suenram

*et al.*¹¹ The remaining components are adequate for a field instrument. For example, the optical multipass cell was fairly robust and stable over the periods of many months, even though it was not isolated from the vibrations of the pump, and was constructed from readily available components, including off-the-shelf mirrors by Edmund Scientific. Similarly, other components, including lenses, function generator, pre- and lock-in amplifiers, and the TDL dewar and current source, performed well.

A potential problem is the lack of automation and self-calibration. For example, in many direct absorption techniques the concentration can be inferred directly from the observed line shape. The molecular beam spectrometer must be calibrated with real samples, and therefore gas cylinders containing standard gas mixtures must be present at the field site. An alternative solution would be to employ internal standard calibration, which is frequently used in gas chromatography, using permeation tubes, or fast switches. However, reduced performance in the field must still be expected because of miniaturization effects.¹¹⁶

The main advantage of the molecular beam technique is the very high selectivity and suppression of many high J impurity lines, which makes much larger regions of the mid-infrared accessible. For example, routine measurements of SO₂ and H₂S in the fundamental absorption regions near 1360 and 1100 cm⁻¹ are hindered by overlap with atmospheric water lines. As such, there may be a niche for a molecular beam spectrometer as a point sensor for highly toxic SO₂ and/or H₂S, for example near sour gas wells, because the overlapping atmospheric water lines in question are high J transitions which would be quenched in a molecular beam.

REFERENCES

- (1) *Chronicle of the World*; Mercer, D., Ed.; DK Publishing: New York, 1996.
- (2) Finlayson-Pitts, B. J.; Pitts, J. N. *Chemistry of the upper and lower atmosphere*; Academic Press: San Diego, 2000.
- (3) *The Smoake of London. Two Prophecies: Evelyn, J., 1661. Fumifugium: Or the Inconvenience of the Aer and Smoake of London Dissipated and Barr, R., The Doom of London*; Lodge, J. P., Ed.; Maxwell Reprint Co.: Elmsford, NY, 1969.
- (4) Seinfeld, J. H.; Pandis, S. N. *Atmospheric Chemistry and Physics: From Air Pollution to Climate*; John Wiley: New York, 1998.
- (5) Farman, J. C.; Gardiner, B. G.; Shanklin, J. D. *Nature* **1985**, *315*, 207.
- (6) *Handbook for the international treaties for the protection of the ozone layer : the Vienna Convention (1985), the Montreal Protocol (1987)*. 5 ed.; United Nations: Nairobi, Kenya, 2000.
- (7) *Agenda 21, Rio Declaration, Forest Principles*; United Nations: New York, 1992.
- (8) Grubb, M. *The Kyoto Protocol: A Guide and Assessment*; The Royal Institute of International Affairs: London, 1999.
- (9) Scoles, G.; Valbusa, U.; Lane, D. C. *Atomic and Molecular Beam Methods*; Oxford University Press: New York, 1992; Vol. 2.
- (10) Demtröder, W. *Laser Spectroscopy*, 2 ed.; Springer: Berlin, 1998.
- (11) Suenram, R. D.; Grabow, J.-U.; Leonov, Z. A. *Rev. Sci. Instrum.* **1999**, *70*, 2127.

- (12) Townes, C. H.; Schawlow, A. L. *Microwave Spectroscopy*; Dover: New York, 1975.
- (13) van Wijngaarden, J.; Jäger, W. *J. Am. Chem. Soc.* **2003**, *125*, 14631.
- (14) Xu, Y.; Jäger, W.; Tang, J.; McKellar, A. R. W. *Phys. Rev. Lett.* **2003**, *91*, 163401.
- (15) Xu, Y.; Jäger, W. *J. Chem. Phys.* **1997**, *106*, 7968.
- (16) Xu, Y.; Jäger, W. *J. Molec. Spectrosc.* **1998**, *192*, 435.
- (17) Xu, Y.; Jäger, W. *J. Molec. Struct.* **2001**, *599*, 211.
- (18) Markov, V. N.; Xu, Y.; Jäger, W. *Rev. Sci. Instrum.* **1998**, *69*, 4061.
- (19) Mäder, H.; Heineking, N.; Stahl, W.; Jäger, W.; Xu, Y. *J. Chem. Soc., Faraday Trans.* **1996**, *92*, 901.
- (20) Tang, J.; Xu, Y.; McKellar, A. R. W.; Jäger, W. *Science* **2002**, *297*, 2030.
- (21) Liu, Y.; Jäger, W. *J. Chem. Phys.* **2003**, *119*, 8449.
- (22) Bernath, P. *Spectra of Atoms and Molecules*; Oxford University Press: New York, 1995.
- (23) Atkins, P. *Physical Chemistry*, 5 ed.; W. H. Freeman: New York, 1994.
- (24) McQuarrie, D. A.; Simon, J. D. *Physical Chemistry - A Molecular Approach*; University Science Books: Sausalito, CA, 1997.
- (25) *Air Monitoring by Spectroscopic Techniques*; Sigrist, M. W., Ed.; John Wiley: New York, 1994; Vol. 127.
- (26) *SPEC-DILAS-IR data sheet*. **2004**,
<http://www.lasercomponents.com/pdf/lc/irserie.pdf>
- (27) Chin, G.; Senesac, L. R.; Blass, W. E.; Hillman, J. J. *Science* **1996**, *274*, 1498.

- (28) Gordy, W.; Cook, R. L. *Microwave Molecular Spectra*, 2 ed.; John Wiley: New York, 1984; Vol. 18.
- (29) Herzberg, G. *Infrared and Raman Spectra of Polyatomic Molecules*; D. van Nostrand Co.: Princeton, NJ, 1966.
- (30) Skoog, D. A.; Leary, J. J. *Principles of Instrumental Analysis*, 4 ed.; Saunders College: Fort Worth, 1992.
- (31) Patel, K. *Phys. Rev. Lett.* **1964**, *12*, 588.
- (32) Patel, C. K. N.; Faust, W. L.; McFarlane, R. A. *Bull. Am. Phys. Soc.* **1964**, *9*, 500.
- (33) Butler, J. F.; Calawa, A. R.; Phelan, R. J.; Harmon, T. C.; Strauss, A. J.; Rediker, R. H. *Appl. Phys. Lett.* **1964**, *5*, 75.
- (34) Butler, J. F.; Calawa, A. R.; Harman, T. C. *Appl. Phys. Lett.* **1966**, *9*, 427.
- (35) Mantz, A. W. *Spectrochim. Acta A* **1995**, *51*, 2211.
- (36) Fehér, M.; Martin, P. A. *Spectrochim. Acta A* **1995**, *51*, 1579.
- (37) Werle, P. *Spectrochim. Acta A* **1996**, *52*, 805.
- (38) Hall, R. N.; Fenner, G. E.; Kingsley, J. D.; Soltys, T. J.; Carlson, R. O. *Phys. Rev. Lett.* **1962**, *9*, 366.
- (39) Vogel, P.; Ebert, V. *Appl. Phys. B* **2001**, *72*, 127.
- (40) Faist, J.; Capasso, F.; Sivco, D. L.; Sirtori, C.; Hutchinson, A. L.; Cho, A. Y. *Science* **1994**, *264*.
- (41) Richter, D.; Lancaster, D. G.; Curl, R. F.; Neu, W.; Tittel, F. K. *Appl. Phys. B* **1998**, *67*, 347.
- (42) Richter, D.; Fried, A.; Wert, B. P.; Walega, J. G.; Tittel, F. K. *Appl. Phys. B* **2002**, *75*, 281.

- (43) Seiter, M.; Sigrist, M. W. *Appl. Opt.* **1999**, *38*, 4691.
- (44) Seiter, M.; Sigrist, M. W. *Infrared Phys. Tech.* **2000**, *41*, 259.
- (45) Werle, P. *Spectrochim. Acta A* **1998**, *54*, 197.
- (46) Winnewisser, G.; Drascher, T.; Giesen, T.; Pak, I.; Schmülling, F.; Schieder, R. *Spectrochim. Acta A* **1999**, *55*, 2121.
- (47) Werle, P. Diode-Laser Sensors for in-situ Gas Analysis. In *Lasers in Environmental and Life Sciences - Modern Analytical Methods*; Hering, P., Lay, P., Stry, S., Eds.; Springer: Heidelberg, 2004; pp 223.
- (48) Williams, R. M.; Kelly, J. F.; Hartman, J. S.; Sharpe, S. W.; Taubman, M. S.; Hall, J. L.; Capasso, F.; Gmachl, C.; Sivco, D. L.; Baillargeon, J. N.; Cho, A. Y. *Opt. Lett.* **1999**, *24*, 1844.
- (49) Werle, P.; Jänker, B. *Opt. Eng.* **1996**, *35*, 2051.
- (50) De Piante, A.; Campbell, E. J.; Buelow, S. J. *Rev. Sci. Instrum.* **1989**, *60*, 858.
- (51) Carlisle, C. B.; Cooper, D. E.; Preier, H. *Appl. Opt.* **1989**, *28*, 2567.
- (52) Cooper, D. E.; Carlisle, C. B. *Opt. Lett.* **1988**, *13*, 719.
- (53) Cooper, D. E.; Warren, R. E. *J. Opt. Soc. Am. B* **1987**, *4*, 470.
- (54) Ajili, L.; Scalari, G.; Hofstetter, D.; Beck, M.; Faist, J.; Beere, H.; Davies, G.; Linfield, E.; Ritchie, D. *Electron. Lett.* **2002**, *38*, 1675.
- (55) Rochat, M.; Ajili, L.; Willenberg, H.; Faist, J.; Beere, H.; Davies, G.; Linfield, E.; Ritchie, D. *Appl. Phys. Lett.* **2002**, *81*, 1381.
- (56) Herriott, D.; Kogelnik, H.; Kompfner, R. *Appl. Opt.* **1964**, *3*, 523.
- (57) Altmann, J.; Baumgart, R.; Weitkamp, C. *Appl. Opt.* **1981**, *20*, 995.
- (58) McManus, J. B.; Keabian, P. L. *Appl. Opt.* **1990**, *29*, 898.

- (59) White, J. U. *J. Opt. Soc. Am.* **1942**, *32*, 285.
- (60) White, J. U. *J. Opt. Soc. Am.* **1976**, *66*, 411.
- (61) McManus, J. B.; Kebabian, P. L.; Zahniser, M. S. *Appl. Opt.* **1995**, *34*, 3336.
- (62) Hao, L.-Y.; Qiang, S.; Wu, G.-R.; Qi, L.; Feng, D.; Zhu, Q.-S.; Hong, Z. *Rev. Sci. Instrum.* **2002**, *73*, 2079.
- (63) Scherer, J. J.; Paul, J. B.; O'Keefe, A.; Saykally, R. J. *Chem. Rev.* **1997**, *97*, 25.
- (64) Mürtz, M.; Frech, B.; Urban, W. *Appl. Phys. B* **1999**, *68*, 243.
- (65) Dahnke, H.; Kleine, D.; Urban, W.; Hering, P.; Mürtz, M. *Appl. Phys. B* **2001**, *72*, 121.
- (66) Engeln, R.; Berden, G.; Peeters, R.; Meijer, G. *Rev. Sci. Instrum.* **1998**, *69*, 3763.
- (67) Peeters, R.; Berden, G.; Apituley, A.; Meijer, G. *Appl. Phys. B* **2000**, *71*, 231.
- (68) He, Y.; Orr, B. J. *Chem. Phys. Lett.* **2000**, *319*, 131.
- (69) O'Keefe, A. *Chem. Phys. Lett.* **1998**, *293*, 331.
- (70) O'Keefe, A.; Scherer, J. J.; Paul, J. B. *Chem. Phys. Lett.* **1999**, *307*, 343.
- (71) Hoffstetter, D.; Beck, M.; Faist, J.; Nägele, M.; Sigrist, M. W. *Opt. Lett.* **2001**, *26*, 887.
- (72) Nägele, M.; Sigrist, M. W. *Appl. Phys. B* **2000**, *70*, 895.
- (73) Sigrist, M. W. *Rev. Sci. Instrum.* **2003**, *74*, 486.
- (74) Blasing, T. J.; Jones, S. *Current Greenhouse Gas Concentrations*. **2003**, http://cdiac.esd.ornl.gov/pns/current_ghg.html.
- (75) *Atmospheric Chemistry and global change*; Brasseur, G. P.; Orlando, J. J.; Tyndall, G. S., Eds.; Oxford University Press: New York, 1999.

- (76) Flanagan, L. B.; Brooks, J. R.; Varney, G. T.; Ehleringer, J. R. *Global Biogeochem. Cycles* **1997**, *11*, 83.
- (77) *J. Phys. Chem. Ref. Data* **1984**, *13*, 809.
- (78) Rothman, L. J. *Quant. Spectrosc. Radiat. Transfer* **2003**, *82*, 1.
- (79) Pfeilsticker, K.; Lotter, A.; Peters, C.; Bösch, H. *Science* **2003**, *300*, 2078.
- (80) *Chem. Rev.* **1994**, *94*.
- (81) *Chem. Rev.* **2000**, *100*.
- (82) *Chem. Rev.* **1988**, *88*.
- (83) Solomon, S.; Portmann, R. W.; Sanders, R. W.; Daniel, J. S. *J. Geophys. Res. - Atm.* **1998**, *103*, 3847.
- (84) Headrick, J. E.; Vaida, V. *Phys. Chem. Earth C* **2001**, *26*, 479.
- (85) Walsh, M. A.; England, T. H.; Dyke, T. R.; Howard, B. J. *Chem. Phys. Lett.* **1987**, *142*, 265.
- (86) Randall, R. W.; Walsh, M. A.; Howard, B. J. *Faraday Discuss. Chem. Soc.* **1988**, *85*, 13.
- (87) Walsh, M. A.; Dyke, T. R.; Howard, B. J. *J. Molec. Spectrosc.* **1988**, *189*, 111.
- (88) Randall, R. W.; Summersgill, J. P. L.; Howard, B. J. *J. Chem. Soc., Faraday Trans.* **1990**, *86*, 1943.
- (89) Legon, A. C.; Suckley, A. P. *J. Chem. Phys.* **1989**, *91*, 4440.
- (90) Sharpe, S. W.; Sheeks, R.; Wittig, C.; Beaudet, R. A. *Chem. Phys. Lett.* **1988**, *151*, 267.
- (91) Sharpe, S. W.; Reifschneider, D.; Wittig, C.; Beaudet, R. A. *J. Chem. Phys.* **1991**, *94*, 233.

- (92) Sharpe, S. W.; Zeng, Y. P.; Wittig, C.; Beaudet, R. A. *J. Chem. Phys.* **1990**, *92*, 943.
- (93) Dutton, C.; Sazonov, A.; Beaudet, R. A. *J. Phys. Chem.* **1996**, *100*, 17772.
- (94) Sazonov, A.; Beaudet, R. A. *J. Phys. Chem. A* **1998**, *102*, 2792.
- (95) Dutton, C. C.; Dows, D. A.; Eikey, R.; Evans, S.; Beaudet, R. A. *J. Phys. Chem. A* **1998**, *102*, 6904.
- (96) Block, P. A.; Marshall, M. D.; Pedersen, L. G.; Miller, R. E. *J. Chem. Phys.* **1992**, *96*, 7321.
- (97) Bernish, R. J.; Block, P. A.; Pedersen, L. G.; Miller, R. E. *J. Chem. Phys.* **1995**, *103*, 7788.
- (98) Oudejans, L.; Olson, D.; Miller, R. E. *J. Chem. Phys.* **1996**, *105*, 8515.
- (99) Layton, D. C.; Pedersen, L. G.; Miller, R. E. *J. Chem. Phys.* **1990**, *93*, 4560.
- (100) Weida, M. J.; Sperhac, J. M.; Nesbitt, D. J. *J. Chem. Phys.* **1995**, *103*, 7685.
- (101) Weida, M. J.; Nesbitt, D. J. *J. Chem. Phys.* **1996**, *105*, 10210.
- (102) Sperhac, J. M.; Weida, M. J.; Nesbitt, D. J. *J. Chem. Phys.* **1996**, *104*, 2202.
- (103) Weida, M. J.; Sperhac, J. M.; Nesbitt, D. J. *J. Chem. Phys.* **1994**, *101*, 8351.
- (104) Ozaki, Y.; Horiai, K.; Konno, T.; Uehara, H. *Chem. Phys. Lett.* **2001**, *335*, 188.
- (105) Sun, L.; Ioannou, I. I.; Kuczkowski, R. L. *Mol. Phys.* **1996**, *88*, 225.
- (106) Leopold, K. R.; Fraser, G. T.; Klemperer, W. *J. Chem. Phys.* **1983**, *80*, 1039.
- (107) McKellar, A. R. W. *J. Chem. Phys.* **1997**, *108*, 1811.
- (108) McKellar, A. R. W.; Roth, D. A.; Pak, I.; Winnewisser, G. *J. Chem. Phys.* **1999**, *110*, 9989.
- (109) Tang, J.; McKellar, A. R. W. *J. Chem. Phys.* **2001**, *115*, 3053.

- (110) Tang, J.; McKellar, A. R. W. *J. Chem. Phys.* **2002**, *116*, 646.
- (111) Wangler, M.; Roth, D. A.; Winnewisser, G.; Pak, I.; McKellar, A. R. W. *Can. J. Phys.* **2001**, *79*, 423.
- (112) Xia, C.; Walker, K. A.; McKellar, A. R. W. *J. Chem. Phys.* **2001**, *114*, 4824.
- (113) Balle, T. J.; Flygare, W. H. *Rev. Sci. Instrum.* **1981**, *52*, 33.
- (114) Wang, Z.; Eliades, M.; Carron, K.; Bevan, J. W. *Rev. Sci. Instrum.* **1991**, *62*, 21.
- (115) Hu, T. A.; Chappell, E. L.; Munley, J. T.; Sharpe, S. W. *Rev. Sci. Instrum.* **1993**, *64*, 3380.
- (116) Pak, I.; Hepp, M.; Roth, D. A.; Winnewisser, G. *Rev. Sci. Instrum.* **1996**, *68*, 1668.
- (117) Kaur, D.; de Souza, A. M.; Wanna, J.; Hammad, S. A.; Mercorelli, L.; Perry, D. S. *Appl. Opt.* **1990**, *29*, 119.
- (118) Sun, H. C.; Whittaker, E. A. *Appl. Opt.* **1992**, *31*, 4998.
- (119) Kagawa, N.; Wada, O.; Koga, R. *Opt. Eng.* **1997**, *36*, 2586.
- (120) Lovejoy, C. M.; Nesbitt, D. J. *Rev. Sci. Instrum.* **1987**, *58*, 807.
- (121) Walker, K. A.; McKellar, A. R. W. *J. Mol. Spectrosc.* **2000**, *205*, 331.
- (122) Silver, J. A. *Appl. Opt.* **1992**, *31*, 707.
- (123) Supplee, J. M.; Whittaker, E. A.; Lenth, W. *Appl. Opt.* **1994**, *33*, 6294.
- (124) Bomse, D. S.; Stanton, A. C.; Silver, J. A. *Appl. Opt.* **1992**, *31*, 718.
- (125) Modugno, G.; Corsi, C.; Gabrysch, M.; Marin, E.; Inguscio, M. *Appl. Phys. B* **1998**, *67*, 289.
- (126) Weida, M. J.; Nesbitt, D. J. *J. Chem. Phys.* **1999**, *110*, 156.
- (127) *Handbook of Chemistry and Physics*; 54th ed.; Lide, D. R., Ed.; CRC Press: Boca Raton, FL, 1995.

- (128) Pine, A. S.; Fraser, G. T. *J. Chem. Phys.* **1988**, *89*, 100.
- (129) McKellar, A. R. W., personal communication, **2003**.
- (130) Watson, J. K. G. *Vibrational Spectra and Structure*; Elsevier: New York, 1977; Vol. 6.
- (131) Bunker, P.; Jensen, P. *Molecular Symmetry and Spectroscopy*, 2nd ed.; NRC Research Press: Ottawa, Canada, 1998.
- (132) Columberg, G.; Bauder, A.; Heineking, N.; Stahl, W.; Makarewicz, J. *Mol. Phys.* **1998**, *93*, 215.
- (133) Soldán, P.; Spirko, V.; Kraemer, W. P. *J. Mol. Spectrosc.* **1997**, *183*, 212.
- (134) Soldán, P. *J. Math. Chem.* **1996**, *20*, 331.
- (135) Soldán, P. *J. Molec. Spectrosc.* **1996**, *180*, 249.
- (136) Brown, R. D.; Burdon, F. R.; Mohay, G. M. *Aust. J. Chem.* **1969**, *22*, 251.
- (137) Pickett, H. M. *J. Molec. Spectrosc.* **1991**, *148*, 371.
- (138) Amos, R. D.; Bernhardsson, A.; Berning, A.; Celani, P.; Cooper, D. L.; Deegan, M. J. O.; Dobbyn, A. J.; Eckert, F.; Hampel, C.; Hetzer, G.; Knowles, P. J.; Korona, T.; Lindh, R.; Lloyd, A. W.; McNicholas, S. J.; Manby, F. R.; Meyer, W.; Mura, M. E.; Nicklaß, A.; Palmieri, P.; Pitzer, R.; Rauhut, G.; Schütz, M.; Schumann, U.; Stoll, H.; Stone, A. J.; Tarroni, R.; Thorsteinsson, T.; Werner, H.-J. <http://www.molpro.net>; 2002.3 ed., 2002.
- (139) Boys, S. F.; Bernadi, F. *Mol. Phys.* **1970**, *19*, 553.
- (140) Dunning, T. H. *J. Chem. Phys.* **1989**, *90*, 1007.
- (141) Tao, F. M.; Klemperer, W. *J. Chem. Phys.* **1994**, *101*, 1129.

- (142) Guelachvili, G.; Rao, K. N. *Handbook of infrared standards*; Academic Press: New York, 1986.
- (143) Legon, A. C.; Roberts, B. P.; Wallwork, A. L. *Chem. Phys. Lett.* **1990**, *173*, 107.
- (144) Atkins, M. J.; Legon, A. C.; Wallwork, A. L. *Chem. Phys. Lett.* **1992**, *192*, 368.
- (145) Ohshima, Y.; Endo, Y. *J. Chem. Phys.* **1990**, *93*, 6256.
- (146) Legon, A. C.; Wallwork, A. L. *J. Chem. Soc., Faraday Trans.* **1992**, *88*, 1.
- (147) Wangler, M.; Roth, D. A.; Krivtsun, V. M.; Pak, I.; Winnewisser, G.; Geleijns, M.; Wormer, P. E. S.; van der Avoird, A. *Spectrochim. Acta A* **2002**, *58*, 2499.
- (148) Pak, I.; Roth, D. A.; Yamada, K. M. T.; Winnewisser, G.; Scouteris, D.; Howard, B. J.; Yamada, K. M. T. *Z. Naturforsch. A: Phys. Sci.* **1998**, *53*, 725.
- (149) Brookes, M. D.; Hughes, D. J.; Howard, B. J. *J. Chem. Phys.* **1996**, *104*, 5391.
- (150) Brookes, M. D.; Hughes, D. J.; Howard, B. J. *J. Chem. Phys.* **1997**, *107*, 2738.
- (151) Randall, R. W.; Ibbotson, J. B.; Howard, B. J. *J. Chem. Phys.* **1993**, *100*, 7051.
- (152) Suenram, R. D.; Fraser, G. T.; Lovas, F. J.; Kawashima, Y. *J. Chem. Phys.* **1994**, *101*, 7230.
- (153) Walker, A. R. H.; Fraser, G. T.; Suenram, R. D.; Lovas, F. J. *J. Chem. Phys.* **2000**, *113*, 2139.
- (154) Dore, L.; Cohen, R. C.; Schmuttenmaer, C. A.; Busarow, K. L.; Elrod, M. J.; Loeser, J. G.; Saykally, R. J. *J. Chem. Phys.* **1994**, *100*, 863.
- (155) Randall, R. W.; Ibbotson, J. B.; Howard, B. J. *J. Chem. Phys.* **1994**, *100*, 7042.
- (156) Hutson, J. M.; Thornley, A. E. *J. Chem. Phys.* **1994**, *100*, 2505.
- (157) Hearn, J. P. I.; Howard, B. J. *Mol. Phys.* **2002**, *100*, 2679.

- (158) Kawashima, Y.; Suenram, R. D.; Fraser, G. T.; Lovas, F. J.; Hirota, E. *J. Mol. Spectrosc.* **1999**, *197*, 232.
- (159) Korona, T.; Moszynski, R.; Thibault, F.; Launay, J.-M.; Bussery-Honvault, B.; Boissoles, J.; Wormer, P. E. S. *J. Chem. Phys.* **2001**, *115*, 3074.
- (160) Fraser, G. T.; Pine, A. S.; Suenram, S. D. *J. Chem. Phys.* **1988**, *88*, 6157.
- (161) Watson, J. K. G. *J. Chem. Phys.* **1968**, *48*, 4517.
- (162) Kraitichman, J. *Am. J. Phys.* **1953**, *21*.
- (163) Taylor, J. R. *An introduction to error analysis*; University Science Books: Mill Valley, CA, 1982.
- (164) Werle, P.; Scheumann, B.; Schandl, J. *Opt. Eng.* **1994**, *33*, 3093.
- (165) Riris, H.; Carlisle, C. B.; Warren, R. E. *Appl. Opt.* **1994**, *33*, 5506.
- (166) Riris, H.; Carlisle, C. B.; Warren, R. E.; Cooper, D. E.; Martinelli, R. U.; Menna, R. J.; York, P. K.; Garbuzov, D. Z.; Lee, H.; Abeles, J. H.; Morris, N.; Connolly, J. C.; Narayan, S. Y. *Spectrochim. Acta A* **1996**, *52*, 843.
- (167) Leleux, D. P.; Claps, R.; Chen, W.; Tittel, F. K.; Harman, T. L. *Appl. Phys. B* **2001**, *74*, 85.
- (168) Kalman, R. E. *J. Basic Eng.* **1960**, *82*, 35.
- (169) Wiener, N. *Extrapolation, Interpolation, and Smoothing of Stationary Time Series*; Wiley: New York, 1949.
- (170) Savitzky, A.; Golay, M. J. E. *Anal. Chem.* **1964**, *36*, 1627.
- (171) Morel, F. M. M.; Hering, J. G. *Principles and Applications of Aquatic Chemistry*; John Wiley & Sons: New York, 1993.
- (172) Stryer, L. *Biochemistry*, 4 ed.; W. H. Freeman: New York, 1995.

- (173) Kerstel, E. R. T.; Gagliardi, G.; Gianfrani, L.; Meijer, H. A. J.; van Trigt, R.; Ramaker, R. *Spectrochim. Acta A* **2002**, *58*, 2389.
- (174) Gagliardi, G.; Restieri, R.; Casa, G.; Gianfrani, L. *Opt. Las. Eng.* **2002**, *37*, 131.
- (175) Güllük, T.; Wagner, H. E.; Slemr, F. *Rev. Sci. Instrum.* **1997**, *68*, 230.
- (176) Mihalcea, R. M.; Webber, M. E.; Baer, D. S.; Hanson, R. K.; Feller, G. S.; Chapman, W. B. *Appl. Phys. B* **1998**, *67*, 283.
- (177) Werle, P.; Mücke, R.; D'Amato, F.; Lancia, T. *Appl. Phys. B* **1998**, *67*, 307.
- (178) Gianfrani, L.; De Natale, P.; De Natale, G. *Appl. Phys. B* **2000**, *70*, 467.
- (179) Webber, M. E.; Claps, R.; Englich, F. V.; Tittel, F. K.; Jeffries, J. B.; Hanson, R. K. *Appl. Opt.* **2001**, *40*, 4395.
- (180) Gagliardi, G.; Restieri, R.; De Biasio, G.; De Natale, P.; Cotrufo, F.; Gianfrani, L. *Rev. Sci. Instrum.* **2001**, *72*, 4228.
- (181) Mazzotti, D.; Giusfredi, G.; Cancio, P.; De Natale, P. *Opt. Las. Eng.* **2002**, *37*, 2002.
- (182) Roller, C.; Namjou, K.; Jeffers, J. *Opt. Lett.* **2002**, *27*, 107.
- (183) Kidd, G. *Spectrochim. Acta A* **2002**, *58*, 2373.
- (184) Osthoff, H. D.; Walls, J.; van Wijngaarden, W. A.; Jäger, W. *Rev. Sci. Instrum.* **2004**, *75*, 46.
- (185) Senesac, L. R.; Blass, W. E.; Chin, G.; Hillman, J. J.; Lobell, J. V. *Rev. Sci. Instrum.* **1999**, *70*, 1719.
- (186) Brown, R. G. *Introduction to random signal analysis and Kalman filtering*; Wiley: New York, 1983.
- (187) Spaink, H. A.; Lub, T. T.; Smit, H. C. *Anal. Chim. Acta* **1990**, *241*, 83.

(188) Werle, P.; Mücke, R.; Slemr, F. *Appl. Phys. B* **1993**, *57*, 131.

(189) Allan, D. W. *Proceed. IEEE* **1966**, *54*, 221.

APPENDIX

A. Supplementary data.

Table A3.1

Coding of CO₂ vibrational levels in Hitran.⁷⁸

Hitran code	v_1, v_2, l, v_3, r
1	00001
2	01101
3	10002
4	02201
5	10001
6	11102
7	03301
8	11101
9	00011
16	01111
23	10012
24	02211
25	10011
36	11112
37	03311
38	11111
39	00021

Note: l is the angular momentum associated with the v_2 bending mode, and r is a ranking index for members of a Fermi resonance.

Table A3.2

Observed transitions (source: Hitran⁷⁸) using the diode F-2462-GMP as the laser source.

E'' is the energy of the lower state, v' and v'' are coding parameters in Hitran (see Table A3.1).

Isotope	Frequency /cm ⁻¹	Intensity @296K /cm molecule ⁻¹	E'' /cm ⁻¹	v'	v''	Transition
¹² C ¹⁶ O ₂	2347.575924	6.81E-19	2.3	9	1	P 2
¹² C ¹⁶ O ₂	2347.632652	1.35E-19	749.5	16	2	R 14
¹² C ¹⁶ O ₂	2347.675570	2.16E-21	1751.0	25	5	R 30
¹² C ¹⁶ O ₂	2347.717248	1.90E-21	1801.0	24	4	R 34
¹² C ¹⁶ O ¹⁷ O	2347.948783	1.11E-21	41.6	9	1	R 10
¹² C ¹⁶ O ¹⁸ O	2348.040053	5.83E-21	203.2	9	1	R 23
¹² C ¹⁶ O ₂	2348.279107	1.71E-21	1828.4	24	4	R 35
¹² C ¹⁶ O ₂	2348.301904	1.37E-19	761.1	16	2	R 15
¹² C ¹⁶ O ¹⁸ O	2348.630696	5.57E-21	220.9	9	1	R 24
¹² C ¹⁶ O ¹⁷ O	2348.634219	1.17E-21	50.0	9	1	R 11
¹² C ¹⁶ O ₂	2348.667939	3.63E-21	1648.4	23	3	R 30
¹² C ¹⁶ O ₂	2348.827351	1.81E-21	1800.1	25	5	R 32
¹² C ¹⁶ O ₂	2348.837689	1.54E-21	1856.6	24	4	R 36
¹² C ¹⁶ O ₂	2348.994596	1.37E-19	773.8	16	2	R 16
¹² C ¹⁶ O ¹⁸ O	2349.215476	5.30E-21	239.3	9	1	R 25
¹² C ¹⁶ O ¹⁷ O	2349.313654	1.21E-21	59.1	9	1	R 12
¹² C ¹⁶ O ₂	2349.386898	1.37E-21	1885.5	24	4	R 37
¹² C ¹⁶ O ₂	2349.650289	1.36E-19	786.9	16	2	R 17
¹² C ¹⁶ O ¹⁸ O	2349.794388	5.02E-21	258.4	9	1	R 26
¹² C ¹⁶ O ₂	2349.838622	3.05E-21	1697.6	23	3	R 32

Table A3.2 (cont'd)

Isotope	Frequency /cm⁻¹	Intensity @296K /cm molecule⁻¹	E'' /cm⁻¹	v'	v''	Transition
¹² C ¹⁶ O ₂	2349.917232	3.44E-19	0.0	9	1	R 0
¹² C ¹⁶ O ₂	2349.933490	1.22E-21	1915.3	24	4	R 38
¹² C ¹⁶ O ₂	2349.953803	1.49E-21	1852.3	25	5	R 34
¹² C ¹⁶ O ¹⁷ O	2349.987083	1.24E-21	68.9	9	1	R 13
¹² C ¹⁶ O ₂	2350.331808	1.34E-19	801.2	16	2	R 18
¹² C ¹⁶ O ¹⁸ O	2350.367430	4.73E-21	278.3	9	1	R 27
¹² C ¹⁶ O ₂	2350.469986	1.08E-21	1945.8	24	4	R 39
¹² C ¹⁶ O ¹⁷ O	2350.654505	1.26E-21	79.5	9	1	R 14
¹² C ¹⁶ O ¹⁸ O	2350.934600	4.43E-21	298.9	9	1	R 28
¹² C ¹⁶ O ₂	2350.974076	1.31E-19	815.8	16	2	R 19
¹² C ¹⁶ O ₂	2350.984956	2.51E-21	1749.9	23	3	R 34
¹² C ¹⁶ O ₂	2351.004634	9.51E-22	1977.1	24	4	R 40
¹² C ¹⁶ O ₂	2351.054909	1.21E-21	1907.7	25	5	R 36
¹² C ¹⁶ O ₂	2351.110165	1.35E-23	3015.4	39	9	R 41

Table A3.3

Observed transitions (source: Hitran⁷⁸) using the diode IR-2333 as a laser source.

Isotope	Frequency /cm ⁻¹	Intensity @296K /cm molecule ⁻¹	E'' /cm ⁻¹	v'	v''	Transition
¹² C ¹⁶ O ₂	2331.596954	2.59E-22	2130.6	36	6	R 22
¹² C ¹⁶ O ₂	2331.640097	4.18E-21	1370.4	24	4	R 9
¹² C ¹⁶ O ₂	2331.756632	5.98E-23	1188.3	16	2	Q 36
¹² C ¹⁶ O ₂	2331.801075	1.30E-22	2321.8	37	7	R 28
¹² C ¹⁶ O ₂	2331.845411	7.29E-20	683.8	16	2	P 6
¹² C ¹⁶ O ₂	2331.885055	2.60E-21	1404.6	25	5	R 6
¹² C ¹⁶ O ₂	2331.928461	1.11E-22	2330.6	38	8	R 25
¹² C ¹⁶ O ¹⁸ O	2332.022789	2.73E-22	775.2	16	2	R 17e
¹² C ¹⁶ O ¹⁸ O	2332.037538	2.72E-22	775.3	16	2	R 17f
¹² C ¹⁶ O ¹⁷ O	2332.173436	1.01E-21	41.6	9	1	P 10
¹² C ¹⁶ O ₂	2332.204875	2.48E-22	2148.1	36	6	R 23
¹² C ¹⁶ O ₂	2332.369047	3.12E-18	163.9	9	1	P 20
¹² C ¹⁶ O ₂	2332.552978	1.04E-22	2351.5	38	8	R 26
¹² C ¹⁶ O ₂	2332.665028	6.14E-20	679.1	16	2	P 5
¹² C ¹⁶ O ₂	2332.732140	4.36E-21	1301.8	23	3	R 6
¹² C ¹⁶ O ₂	2332.766517	1.13E-22	1080.4	16	2	Q 32
¹² C ¹⁶ O ₂	2332.811146	3.61E-23	1276.4	16	2	Q 39
¹²C¹⁶O¹⁸O	2332.842883	6.53E-22	0.0	9	1	R 0
¹² C ¹⁶ O ₂	2332.869001	2.36E-22	2167.4	36	6	R 24
¹² C ¹⁶ O ¹⁷ O	2332.984223	9.46E-22	34.1	9	1	P 9

Table A3.3 (cont'd).

Isotope	Frequency /cm ⁻¹	Intensity @296K /cm molecule ⁻¹	E'' /cm ⁻¹	v'	v''	Transition
¹² C ¹⁶ O ₂	2333.001591	1.11E-22	2368.0	37	7	R 30
¹² C ¹⁶ O ₂	2333.066954	4.70E-21	1386.8	24	4	R 11
¹² C ¹⁶ O ₂	2333.153260	9.78E-23	2371.9	38	8	R 27
¹² C ¹⁶ O ₂	2333.188460	5.09E-23	1216.4	16	2	Q 37
¹² C ¹⁶ O ₂	2333.227618	1.53E-22	1031.1	16	2	Q 30
¹² C ¹⁶ O ¹⁸ O	2333.272252	2.66E-22	802.4	16	2	R 19e
¹² C ¹⁶ O ¹⁸ O	2333.288040	2.65E-22	802.6	16	2	R 19f
¹² C ¹⁶ O ₂	2333.339361	3.15E-21	1416.3	25	5	R 8
¹² C ¹⁶ O ₂	2333.465505	4.89E-20	675.2	16	2	P 4
¹² C ¹⁶ O ₂	2333.546153	7.07E-23	1159.4	16	2	Q 35
¹²C¹⁶O¹⁸O	2333.567658	1.30E-21	0.7	9	1	R 1
¹² C ¹⁶ O ₂	2333.592706	1.02E-22	2392.3	37	7	R 31
¹² C ¹⁶ O ₂	2333.659481	2.05E-22	985.0	16	2	Q 28
¹² C ¹⁶ O ₂	2333.771266	4.88E-21	1396.2	24	4	R 12
¹² C ¹⁶ O ¹⁷ O	2333.789071	8.69E-22	27.3	9	1	P 8
¹² C ¹⁶ O ¹⁸ O	2333.888289	2.60E-22	817.2	16	2	R 20e
¹² C ¹⁶ O ¹⁸ O	2333.904551	2.60E-22	817.4	16	2	R 20f
¹² C ¹⁶ O ₂	2334.156486	3.25E-18	133.4	9	1	P 18

Table A3.3 (cont'd).

Isotope	Frequency /cm ⁻¹	Intensity @296K /cm molecule ⁻¹	E'' /cm ⁻¹	v'	v''	Transition
¹² C ¹⁶ O ₂	2334.270182	3.53E-20	672.1	16	2	P 3
¹² C ¹⁶ O ¹⁷ O	2334.278937	1.29E-24	1603.3	25	5	R 24
¹²C¹⁶O¹⁸O	2334.286631	1.94E-21	2.2	9	1	R 2
¹² C ¹⁶ O ₂	2334.353428	8.46E-23	2416.4	38	8	R 29
¹² C ¹⁶ O ₂	2334.375241	8.00E-23	2419.6	39	9	R 13
¹² C ¹⁶ O ₂	2334.435463	3.55E-22	902.1	16	2	Q 24
¹² C ¹⁶ O ₂	2334.469412	5.02E-21	1406.4	24	4	R 13
¹² C ¹⁶ O ¹⁸ O	2334.498526	2.53E-22	832.6	16	2	R 21e
¹² C ¹⁶ O ¹⁸ O	2334.515232	2.52E-22	832.9	16	2	R 21f
¹² C ¹⁶ O ¹⁷ O	2334.587978	7.83E-22	21.2	9	1	P 7

Table A4.1

Single point calculations on the potential energy surface of CO₂-SO₂. Cut 1: Normal input structure (see Fig. 4.1).

r_{cm} /Å	Interaction Energy /cm ⁻¹	r_{cm} /Å	Interaction Energy /cm ⁻¹
2.34	4657	3.69	-577
2.44	2855	3.74	-551
2.54	1580	3.79	-526
2.64	696	3.84	-501
2.74	100	3.89	-477
2.84	-288	3.94	-454
2.94	-528	3.99	-431
3.04	-664	4.04	-410
3.14	-728	4.14	-369
3.19	-741	4.24	-332
3.24	-744	4.34	-299
3.29	-740	4.44	-269
3.34	-730	4.54	-242
3.39	-715	4.64	-218
3.44	-696	5.14	-133
3.49	-675	5.64	-85
3.54	-652	6.14	-57
3.59	-627	6.64	-40
3.64	-602	7.14	-29
		7.64	-21

Table A4.2

Single point calculations on the potential energy surface of CO₂-SO₂. Cut 2: SO₂-inverted input structure.

r_{cm} /Å	Interaction Energy /cm ⁻¹	r_{cm} /Å	Interaction Energy /cm ⁻¹
2.56	12144	3.71	-87
2.66	8716	3.76	-107
2.76	6151	3.81	-121
2.81	5132	3.86	-129
2.86	4259	3.96	-136
2.91	3515	4.06	-132
2.96	2882	4.16	-123
3.01	2347	4.26	-110
3.06	1894	4.36	-96
3.11	1515	4.86	-38
3.16	1197	5.36	-8
3.21	932	5.86	4
3.26	713	6.36	8
3.31	531	7.36	8
3.36	383	8.36	7
3.41	262	8.36	6
3.46	165	9.36	5
3.51	87	10.36	4
3.56	25	15.36	1
3.61	-23	45.36	0
3.66	-59		

Table A4.3

Calculations on the potential energy surface of CO₂-SO₂ in order to estimate the internal rotation barrier height. r_{cm} was fixed at 3.24Å. τ is the torsional angle.

τ_{tor} /°	Interaction Energy /cm ⁻¹
0	-736
5	-730
10	-710
15	-678
20	-635
25	-580
30	-516
35	-443
40	-364
45	-280
50	-195
55	-110
60	-28
65	48
70	115
75	170
80	211
85	237
90	246

Table A5.1

Intermolecular *ab initio* interaction energy (in mH) of surface A as a function of α (in degrees) and r_{cm} (in Å).

α	90°	80°	70°	60°	50°	40°	30°	20°	10°	0°
r_{cm}										
3.0Å	9.385	11.070	16.757	28.541	50.587	128.63	163.78	257.27	-	-
3.3Å	2.296	2.923	5.065	9.607	18.342	34.170	60.385	136.52	175.9	-
3.4Å	1.238	1.675	3.179	6.402	12.676	24.146	43.195	69.957	97.437	-
3.5Å	0.539	0.837	1.873	4.124	8.571	16.787	30.484	49.599	68.888	115.88
3.6Å	0.090	0.289	0.985	2.526	5.630	11.443	21.185	34.728	48.227	54.063
3.7Å	-0.185	-0.058	0.394	1.423	3.550	7.605	14.456	23.966	33.364	37.384
4.0Å	-0.454	-0.436	-0.357	-0.128	0.443	1.667	3.857	6.948	9.980	11.249
4.3Å	-0.400	-0.414	-0.447	-0.469	-0.413	-0.164	0.397	1.265	2.142	2.507
4.5Å	-0.328	-0.346	-0.398	-0.468	-0.524	-0.504	-0.344	-0.033	0.309	0.451
5.0Å	-0.176	-0.190	-0.234	-0.303	-0.391	-0.484	-0.562	-0.607	-0.622	-0.625
5.5Å	-0.093	-0.101	-0.126	-0.168	-0.222	-0.285	-0.348	-0.400	-0.433	-0.445
6.0Å	-0.051	-0.056	-0.070	-0.093	-0.123	-0.159	-0.194	-0.225	-0.245	-0.252
10 Å	-0.001	-0.002	-0.003	-0.003	-0.004	-0.005	-0.006	-0.007	-0.007	-0.007

Figure A5.1

Cut A through the potential energy surface of $\text{CO}_2\text{-CH}_4$. The minimum potential energy in this cut (which may or may not be a true minimum on the higher-dimensional potential energy surface) is located at $r_{\text{cm}}=5.0\text{\AA}$ and $\alpha=0^\circ$.

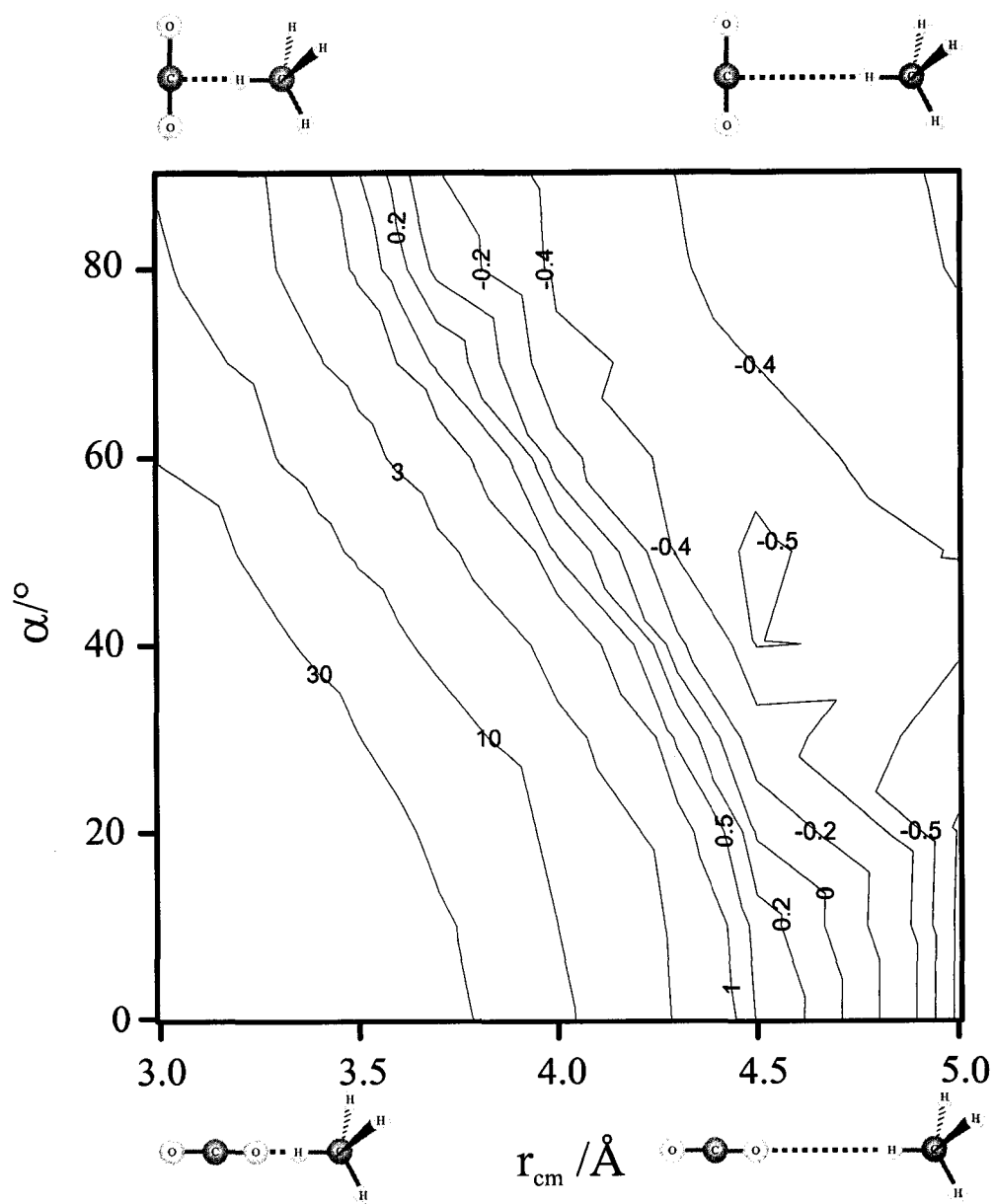


Table A5.2

Intermolecular *ab initio* interaction energy (in mH) of surface B as a function of α (in degrees) and r_{cm} (in Å). The data are plotted in Fig. 5.3.

α	90°	80°	70°	60°	50°	40°	30°	20°	10°	0°
r_{cm}										
3.0Å	-0.439	0.150	2.298	6.892	15.556	30.261	51.753	76.896	97.707	-
3.3Å	-1.483	-1.282	-0.570	0.974	3.937	9.034	16.550	25.401	32.805	-
3.4Å	-1.498	-1.362	-0.884	0.162	2.185	5.691	10.883	17.016	22.158	-
3.5Å	-1.443	-1.352	-1.038	-0.344	1.018	3.399	6.948	11.155	14.691	15.960
3.6Å	-1.348	-1.290	-1.089	-0.639	0.261	1.856	4.251	7.105	9.513	10.369
3.7Å	-1.234	-1.198	-1.075	-0.792	-0.211	0.837	2.431	4.343	5.964	6.532
4.0Å	-0.884	-0.880	-0.866	-0.821	-0.703	-0.453	-0.041	0.477	0.928	1.070
4.3Å	-0.606	-0.609	-0.622	-0.638	-0.645	-0.625	-0.562	-0.463	-0.369	-0.353
4.5Å	-0.468	-0.472	-0.487	-0.510	-0.537	-0.559	-0.566	-0.556	-0.538	-0.547
5.0Å	-0.249	-0.252	-0.261	-0.276	-0.299	-0.326	-0.355	-0.380	-0.398	-0.413
5.5Å	-0.139	-0.140	-0.144	-0.151	-0.161	-0.174	-0.189	-0.203	-0.213	-0.223
6.0Å	-0.081	-0.081	-0.083	-0.086	-0.090	-0.095	-0.101	-0.107	-0.112	-0.117
10 Å	-0.004	-0.004	-0.004	-0.004	-0.003	-0.003	-0.003	-0.003	-0.002	-0.003

Table A5.3

Intermolecular *ab initio* interaction energy (in mH) of surface C as a function of α (in degrees) and r_{cm} (in Å).

α	90°	80°	70°	60°	50°	40°	30°	20°	10°	0°
r_{cm}										
3.0Å	0.581	1.374	4.063	9.686	20.285	38.911	68.321	107.02	143.91	-
3.3Å	-0.983	-0.701	0.264	2.314	6.245	13.240	24.316	38.738	52.192	57.884
3.4Å	-1.104	-0.909	-0.242	1.186	3.947	8.890	16.731	26.917	36.369	40.350
3.5Å	-1.129	-0.999	-0.546	0.433	3.086	5.798	11.292	18.420	25.009	27.774
3.6Å	-1.097	-1.010	-0.712	-0.054	1.250	3.628	7.434	12.375	16.930	18.836
3.7Å	-1.030	-0.976	-0.785	-0.355	0.515	2.129	4.732	8.120	11.241	12.544
4.0Å	-0.766	-0.758	-0.728	-0.643	-0.434	0.001	0.750	1.755	2.691	3.082
4.3Å	-0.528	-0.533	-0.549	-0.564	-0.559	-0.497	-0.345	-0.109	0.124	0.223
4.5Å	-0.406	-0.413	-0.435	-0.467	-0.502	-0.520	-0.501	-0.443	-0.373	-0.342
5.0Å	-0.210	-0.216	-0.233	-0.261	-0.299	-0.344	-0.389	-0.425	-0.447	-0.455
5.5Å	-0.113	-0.116	-0.126	-0.142	-0.164	-0.191	-0.219	-0.245	-0.263	-0.270
6.0Å	-0.064	-0.065	-0.071	-0.079	-0.091	-0.105	-0.120	-0.133	-0.143	-0.147
10 Å	-0.002	-0.003	-0.003	-0.003	-0.003	-0.004	-0.004	-0.004	-0.004	-0.004

Figure A5.2

Cut C through the potential energy surface of $\text{CO}_2\text{-CH}_4$. The minimum potential energy in this cut (which may or may not be a true minimum on the higher-dimensional potential energy surface) is located at $r_{\text{cm}} = 3.5\text{\AA}$ and $\alpha = 90^\circ$.

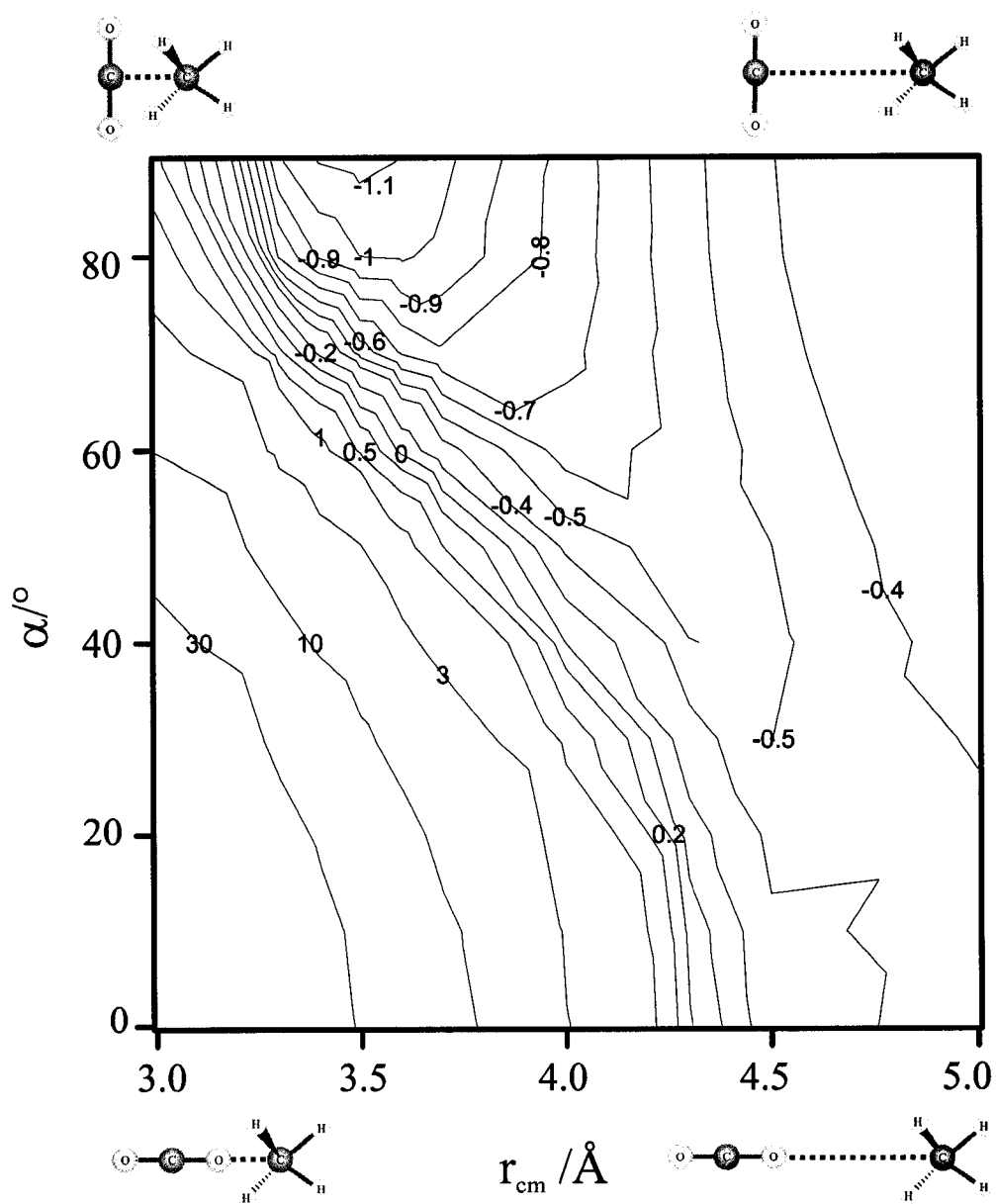


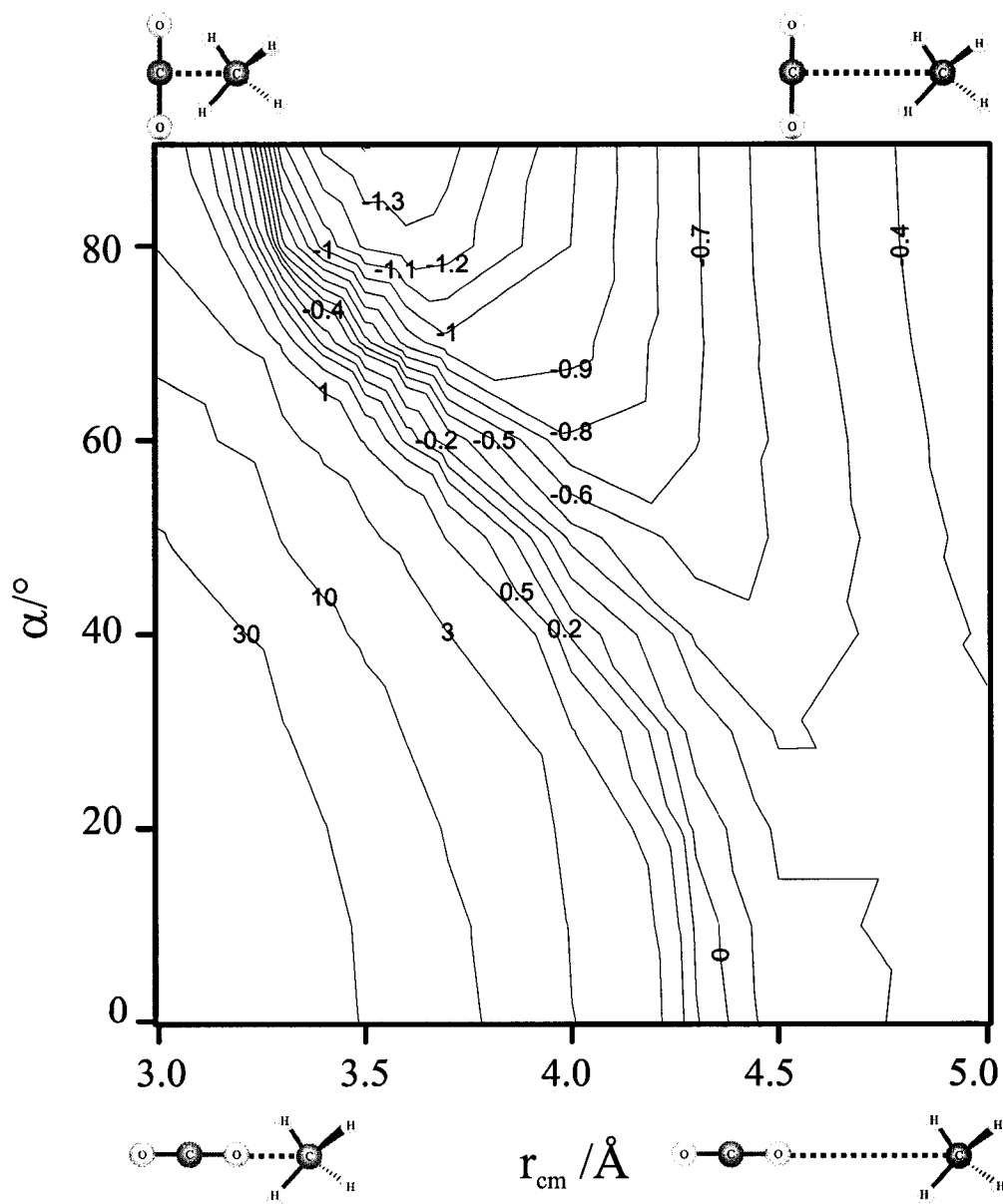
Table A5.4

Intermolecular *ab initio* interaction energy (in mH) of surface D as a function of α (in degrees) and r_{cm} (in Å).

α	90°	80°	70°	60°	50°	40°	30°	20°	10°	0°
r_{cm}										
3.0Å	1.611	2.796	6.884	15.540	31.462	57.092	91.243	126.16	150.87	-
3.3Å	-1.075	-0.669	0.747	3.796	9.486	18.754	31.298	44.492	54.315	57.884
3.4Å	-1.317	-1.040	-0.067	2.044	6.012	12.509	21.350	30.720	37.769	40.350
3.5Å	-1.406	-1.220	-0.561	0.883	3.622	8.138	14.319	20.918	25.927	27.774
3.6Å	-1.398	-1.275	-0.838	0.136	2.004	5.113	9.396	14.003	17.529	18.836
3.7Å	-1.333	-1.255	-0.971	-0.326	0.931	3.047	5.986	9.171	11.628	12.544
4.0Å	-1.014	-0.999	-0.941	-0.787	-0.450	0.157	1.036	2.016	2.705	3.082
4.3Å	-0.707	-0.710	-0.715	-0.706	-0.653	-0.524	-0.313	-0.061	0.145	0.223
4.5Å	-0.546	-0.552	-0.568	-0.586	-0.593	-0.571	-0.514	-0.436	-0.368	-0.342
5.0Å	-0.287	-0.291	-0.305	-0.327	-0.355	-0.385	-0.413	-0.435	-0.450	-0.455
5.5Å	-0.156	-0.159	-0.166	-0.178	-0.194	-0.213	-0.234	-0.252	-0.264	-0.270
6.0Å	-0.089	-0.091	-0.094	-0.100	-0.108	-0.118	-0.128	-0.137	-0.144	-0.147
10 Å	-0.003	-0.004	-0.004	-0.003	-0.004	-0.004	-0.004	-0.004	-0.004	-0.004

Figure A5.3

Cut D through the potential energy surface of $\text{CO}_2\text{-CH}_4$. The minimum potential energy in this cut (which may or may not be a true minimum on the higher-dimensional potential energy surface) is located at $r_{\text{cm}} = 3.5 \text{ \AA}$ and $\alpha = 90^\circ$.

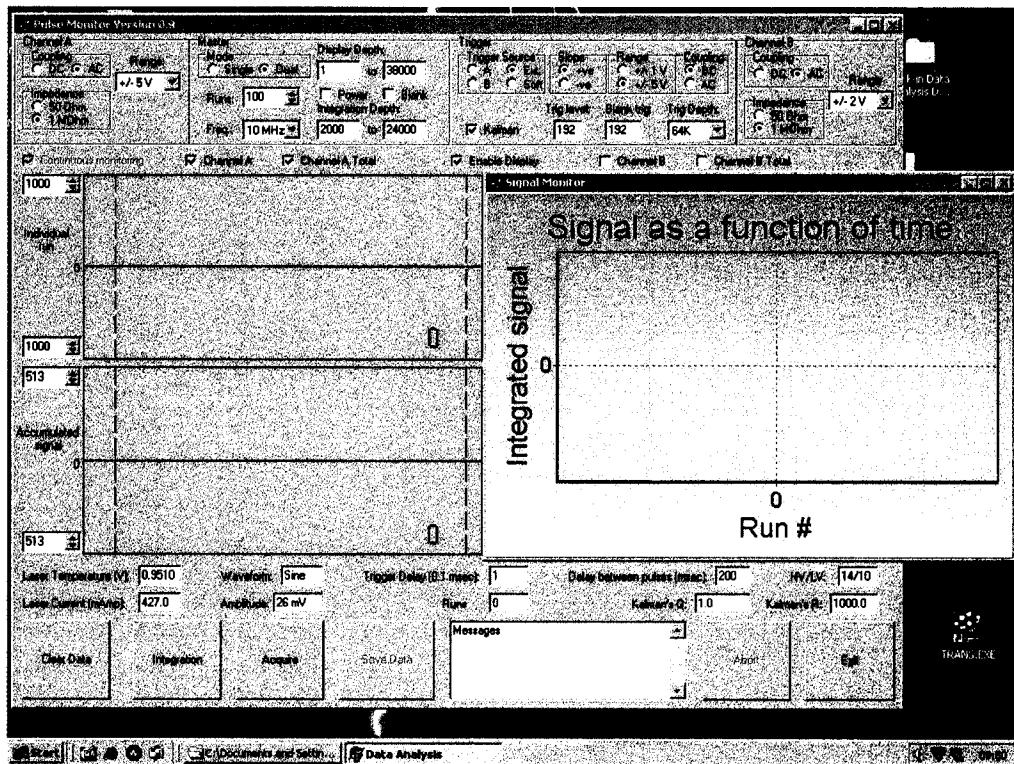


Appendix B

Maple 9.0 input file for line shape model (Section 3.3.4).

```
> restart;sigmatheta:=Pi/20:sigmav:=50: vavg := 1500: step_size := 1:
> for vinp from 1 by step_size to vavg+4*sigmav do result[vinp] := 0: od:
> density := distance ->
evalf(exp(-(arctan(radius(distance)/distance)*arctan(radius(distance)/distance)))/(2*sigma
theta*sigmatheta))*(distance)^(-2));
> pv:=vinp->sqrt(1/(2*Pi*sigmav^2))*exp(-((vinp-vavg)^2)/(2*sigmav^2));
> radius:=distance->0.05:
Alternative: Radius (d) = 0.01 - d/50
> for vinp from vavg-4*sigmav by step_size to vavg+4*sigmav do
> soln:=solve(veff=vinp*cos(arctan(radius(distance)/distance)),distance):
> for v from 1 by step_size to (vinp-step_size) do
> result[v]:=result[v]+evalf(pv(vinp)*(subs(veff=v,density(soln[1])))):
> od:
> printf("vinp = %f\n", vinp);
> od:
> for v from 1 by step_size to (vavg+4*sigmav-1) do printf("%f\n",result[v]): od;
```

C. Screen shot of data acquisition software.



D. Photograph of the laboratory.

